5-6-2014 12:00 AM

Electrical Resistivity Tomography for Mapping Subsurface Remediation

Christopher Power
The University of Western Ontario

Supervisor
Dr. Jason Gerhard
The University of Western Ontario

Graduate Program in Civil and Environmental Engineering
A thesis submitted in partial fulfillment of the requirements for the degree in Doctor of Philosophy

ELECTRICAL RESISTIVITY TOMOGRAPHY FOR MAPPING SUBSURFACE REMEDIATION

(Thesis format: Integrated Article)

by

Christopher Anthony Power

Graduate Program in Civil and Environmental Engineering

A thesis submitted in partial fulfillment
of the requirements for the degree of
Doctor of Philosophy

The School of Graduate and Postdoctoral Studies
The University of Western Ontario
London, Ontario, Canada

ABSTRACT

Cleaning up sites contaminated with dense non-aqueous phase liquids (DNAPLs) remains a challenging geoenvironmental problem. The performance of site remediation methods is difficult to assess without a practical, non-destructive technique to map where and how quickly DNAPL mass is being reduced. The promise of electrical resistivity tomography (ERT) in this context has not been realized, in part because traditional ERT methods were used to solve the near-impossible problem of mapping the initial DNAPL outline. However, new developments in ERT have emerged that focus on resolving subsurface changes over time. The objective of this work was to evaluate the potential of time-lapse ERT for mapping DNAPL mass reduction during remediation.

A new numerical model was developed to explore this potential at the field scale, generating realistic DNAPL scenarios and predicting the response of an ERT survey. Central to the model was the development of a novel linkage between hydrogeological and geoelectrical properties. Sensitivity studies conducted at a variety of scales demonstrated that the linkage routine is robust and the DNAPL-ERT model is a valuable research tool. Moving forward to consider site applications, a new time-lapse method, four-dimensional (4D, three spatial dimensions plus time) ERT, was identified as highly promising. A laboratory experiment was conducted that demonstrated, for the first time, the effectiveness of 4D ERT applied at the surface for mapping an evolving DNAPL distribution. Independent simulation of the experiment demonstrated the reliability of the DNAPL-ERT model for simulating real systems. The numerical model was then used to explore the 4D surface ERT approach at the field scale for monitoring a range of realistic DNAPL remediation scenarios. The approach showed excellent potential for mapping shallow DNAPL changes but deeper changes were not as well resolved. To overcome this limitation, a new surface-to-horizontal borehole (S2HB) ERT configuration was proposed. The potential benefit of this innovation was first demonstrated by using the numerical model to compare surface ERT to S2HB ERT for a realistic, field scale DNAPL scenario with remediation at depth. A second laboratory experiment then demonstrated that this new configuration does better resolve changes in DNAPL

distribution relative to surface ERT, particularly at depth. Independent simulation of the experiment showed that S2HB ERT is reliably modelled.

Overall, this research has substantially advanced ERT in the context of DNAPL sites, with novel contributions to theory, modelling, demonstrations with physical systems, and simulations of realistic field scenarios. As a whole, this work demonstrates that, with these innovations, ERT exhibits significant potential as a DNAPL remediation site monitoring tool.

Keywords: Hydrogeophysics, groundwater contamination, remediation, non-aqueous phase liquids, multiphase flow, electrical resistivity tomography, numerical modelling, petrophysics, inverse problem, time-lapse monitoring, four-dimensional inversion.

CO-AUTHORSHIP STATEMENT

The thesis was written in accordance with the guidelines and regulations for an integrated-article format stipulated by the School of Graduate and Postdoctoral Studies at The University of Western Ontario, Canada. The candidate designed and conducted all simulations and laboratory experiments presented in this thesis, analyzed all data, and formed the conclusions presented. The work was conducted at Western under the supervision of Dr. Jason Gerhard. The candidate wrote the thesis and was the lead author on the manuscript drafts of the following chapters:

Chapter 3: A new coupled model for simulating dense non-aqueous phase liquids by electrical resistivity tomography

A version of this chapter has been published: Power, C., J.I. Gerhard, P. Tsourlos, and A. Giannopoulos. 2013. A new coupled model for simulating the mapping of dense non-aqueous phase liquids using electrical resistivity tomography. Geophysics, 78(4): EN1-EN15. doi: 10.1190/geo2012-0395.1

Chapter 4: Evaluating four-dimensional time-lapse electrical resistivity tomography for monitoring DNAPL source zone remediation

A version of this chapter has been published: Power, C., J.I. Gerhard, M. Karaoulis, P. Tsourlos, and A. Giannopoulos. 2014. Evaluating four-dimensional time-lapse electrical resistivity tomography for monitoring DNAPL source zone remediation. Journal of Contaminant Hydrology, 162-163: 27-46. doi: 10.1016/j.jconhyd.2014.04.004

Chapter 5: Improved time-lapse electrical resistivity tomography monitoring of dense non-aqueous phase liquids with surface-to-horizontal borehole arrays

A version of this chapter has been prepared for publication: Power, C., J.I. Gerhard, P. Tsourlos, P. Soupios, K. Simyrdanis, and M. Karaoulis. Improved time-lapse electrical resistivity tomography monitoring of dense non-aqueous phase liquids with surface-to-horizontal borehole arrays. Journal of Applied Geophysics. In preparation.

Contributions:

Christopher Power: research topic lead; developed and programmed the linkage methodology; designed, conducted and analyzed all laboratory experiments and numerical simulations; wrote all manuscript chapters.

Jason Gerhard: financial support and guidance on the research topic; assisted design of laboratory experiments and numerical simulations; assisted interpretation of all results; reviewed/revised drafts of all manuscript chapters.

Panagiotis Tsourlos: assisted design of laboratory experiments and numerical simulations; assisted interpretation of all results; reviewed/revised drafts of all manuscript chapters.

Antonios Giannopoulos: assisted design and interpretation of numerical simulations and results; reviewed/revised drafts of two manuscript chapters.

Marios Karaoulis: assisted design and interpretation of numerical simulations and results with respect to four-dimensional ERT algorithms; reviewed/revised drafts of two manuscript chapters.

Pantelis Soupios: provided access and part financial support to experimental facility; assisted preparation and execution of laboratory experiments; assisted interpretation of laboratory results; reviewed/revised draft of one manuscript chapter.

Kleanthis Simyrdanis: assisted preparation and execution of laboratory experiments; assisted with analysis of laboratory results; reviewed/revised draft of one manuscript chapter.

ACKNOWLEDGEMENTS

Financial support for this research was provided by the Natural Sciences and Engineering Research Council of Canada (NSERC) in the form of an Industrial Postgraduate Scholarship to the author, supported with industrial contributions from Geosyntec Consultants, and a Discovery Grant to the author's supervisor, Dr. J. I. Gerhard.

I would like to express my extreme gratitude to my supervisor Dr. Jason Gerhard for your continuous support, guidance, patience and friendship. I will always be grateful to you for believing in me and providing me with the opportunity to further my studies, work on an interesting topic with amazing people, and travel. The journey I have taken in these past 6 years has changed my life and I have experienced nothing but positive times. Thank you for your massive contribution to my life so far.

I am so fortunate to have worked with and become friends with all members of the 'Greek research family'. I am extremely grateful to Dr. Panos Tsourlos for your invaluable guidance, support and friendship. I can't thank you enough for all your help over the years, especially the many late nights you spent on Skype with me (I am sure you will miss all those powerpoint slides). Thanks to Dr. Antonis Giannopoulos for being there since you first set me on my way with geophysics in Edinburgh. Thanks to Dr. Pantelis Soupios for providing me with the opportunity to visit Crete and conduct laboratory experiments. You were an amazing host and I am still taken aback by the kindness of everyone I encountered during my stay in Crete. I would like to thank Dr. Marios Karaoulis and Dr. Kleanthis Simyrdanis for all your time and support over the years.

I am thankful to Dr. Denis O'Carroll and Dr. Clare Robinson for their general guidance over the years and for creating a wonderful atmosphere within the RESTORE research group. I came to Canada as a complete stranger and from the very first day, this group has provided me with enormous support and close friendships. I am grateful to each and every one of you for helping me along this journey. Thank you in particular to Ahmed Chowdury who was always there to help me whenever I asked and also to Laura Kinsman and Tarek Rashwan for your help in the laboratory. I have to also give a very special thanks to all the staff in the Engineering and Earth Sciences departments who helped me

in different ways throughout my time at Western. In particular, I'd like to thank Stephanie Laurence, Cynthia Quintus, Whitney Barrett, Tim Stephens and Barry Price.

Thank you to everyone at Geosyntec Consultants for providing me with the opportunity to obtain field work experience and gain a more practical mindset to better appreciate the relevance and ultimate end-goal of this research topic. Thanks to Clayton Inculet and Tarek Rashwan for supporting me during my field work and for making those long drives to New Jersey enjoyable. A very special thanks to Panagiotis Kyrmizakis, Theodore Papadoulis and Stella Kirkou for your generosity, support and friendship during my time in Crete. Thank you to Baolai Ge for all your help with utilizing the SHARCNET supercomputers that supported a crucial component of my research.

I have to acknowledge the Djibouti soccer team for playing a major part in my life at Western. It has been an unforgettable experience managing and playing on this team for most of my time at Western. I am grateful for the many great friends I have gained from this team. There are too many friends I would like to acknowledge that have been there for me over the years but I would especially like to thank Navid Baktash, Brett Lubbock, Stephanie MacPhee, Mark Migueis, Clayton Inculet and Andrew Ross.

I would like to thank all of my friends and family back home in Ireland for your constant support and encouragement, especially at the beginning when I decided to move to Canada. Thank you Pat Walsh, Darren O'Driscoll and Niall Brophy for always helping me to switch off and enjoy my trips home. I am extremely grateful to my family for their encouragement and support over the years and their sheer happiness at seeing me enjoying my life. A very special thanks to my amazing mother for supporting me every step of the way throughout this educational marathon. This thesis is dedicated to you, Mam. On top of this, I can't have asked for a more wonderful family-in-law and I am so grateful for their support in the latter years of this journey.

Finally, words cannot express my feelings of love and gratitude to my wife, Lori-Beth. The completion of this thesis would not have been possible without your monumental love, support and patience. You have been my anchor during the accomplishment of this work.

TABLE OF CONTENTS

LIST OF TABLES

LIST OF FIGURES

NOTATION

Typical units are presented in brackets. [-] denotes a dimensionless parameter.

C spatial second-derivative operator [-]

Cl volumetric clay content [-]

C_f ionic concentration associated with salinity [mol/L]

C_n aqueous phase concentration for non-wetting phase [mol/L]

C_κ aqueous phase concentration for species κ [mg/L]

$C_{\kappa,s}$ concentration of the source or sink flux for species κ [mg/L]

d_{sd} mean grain diameter of sand [m]

D recorded data vector [-]

D_{ij} hydrodynamic dispersion coefficient tensor [m]

E electric field intensity [Newton/Coulomb]

g gravitational constant [m/s^2]

G forward operator [-]

G_f geometrical factor [-]

h hydraulic head [m]

I_c electric current [Amps]

J Jacobian matrix [-]

J_c current density [A/m^2]

k intrinsic permeability [m^2]

k_{sd} intrinsic permeability of sand [m^2]

k_{ij} second-order intrinsic permeability tensor [m^2]

k_r relative permeability [-]

$k_{r,w}$ wetting phase relative permeability [-]

$k_{r,n}$ non-wetting phase relative permeability [-]

K_{ij} hydraulic conductivity [m/s]

m cementation exponent [-]

m_{sd} cementation exponent of sand [-]

m_{cl} cementation exponent of clay [-]

m_{cs} cementation exponent of clayey sand [-]

m_j exponent of disperse element j [-]

M temporal first-derivative operator [-]

n saturation exponent [-]

P_c capillary pressure [Pa]

P_w wetting phase pressure [Pa]

$P^*_{w,b}$ wetting phase pressure at boundary b [Pa]

P_n non-wetting phase pressure [Pa]

q number of disperse elements [-]

q_s volumetric flow rate per unit volume of aquifer [m/s]

q_w wetting phase flux [m/s]

q_n non-wetting phase flux [m/s]

Q_w wetting phase source/sink flux [s^{-1}]

Q_n non-wetting phase source/sink flux [s^{-1}]

R_n chemical reaction term [-]

s number of incremental steps [-]

S_s specific storage [L^{-1}]

S_w wetting phase saturation [-]

$S^*_{w,b}$ wetting phase saturation at boundary b [-]

S_n non-wetting phase saturation [-]

t time [sec/day/year]

T temperature of pore water [°C]

v_i seepage of linear pore water velocity [m/s]

V_{nr} DNAPL volume remediated [m^3]

V_{cl} bulk volume fraction of clay [-]

V_{sd} bulk volume fraction of sand [-]

V_w bulk volume fraction of water [-]

V_d bulk volume fraction of DNAPL [-]

V_a bulk volume fraction of air [-]

$V_{i,j}$ volume sum at increment i and disperse element j [-]

V_p bulk volume of each respective disperse element j [-]

V_j bulk volume of disperse element j [-]

X subsurface model parameter vector [-]

ϕ porosity [-]

ϕ_{sd} porosity of sand [-]

ϕ_{cl} porosity of clay [-]

$\phi_{i,j}$ porosity for increment *i* at disperse element *j* [-]

ϕ_t total water volume [-]

θ water content [-]

μ_w wetting phase viscosity [Pa.s]

μ_n non-wetting phase viscosity [Pa.s]

ς_w wetting phase density [kg/m^3]

ς_n non-wetting phase density [kg/m^3]

ρ electrical resistivity [ohm-m]

ρ_w pore water electrical resistivity [ohm-m]

ρ_a apparent resistivity [ohm-m]

ρ_t ERT-inverted electrical resistivity [ohm-m]

σ electrical conductivity [S/m]

σ_{bulk} bulk electrical conductivity [S/m]

σ_m matrix conductivity [S/m]

σ_w electrical conductivity of water [S/m]

σ_s electrical conductivity of soil [S/m]

σ_o^* complex mixture electrical conductivity [S/m]

σ_w^* complex water electrical conductivity [S/m]

σ_m^* complex matrix electrical conductivity [S/m]

$\sigma_{o_{i,j}}$ electrical conductivity of the mixture at increment *i* and disperse element *j* [S/m]

σ_{d_j} electrical conductivity of disperse element *j* [S/m]

δ Dirac delta function [-]

α Lagrangian multiplier in time [-]

λ Lagrangian multiplier in space [-]

Λ space-domain Lagrangian as a variable diagonal matrix [-]

A time-domain Lagrangian as a variable diagonal matrix [-]

Φ voltage potential [Volts]

Φ_d data misfit vector [-]

Φ_m regularization function in space [-]

Φ_t regularization function in time [-]

1 INTRODUCTION

1.1 Background

The remediation of sites contaminated with dense non-aqueous phase liquids (DNAPLs) represents a major technical, economic and environmental challenge. DNAPLs such as creosote, coal tar and chlorinated solvents are among the most common and persistent organic contaminants polluting the environment (Pankow et al., 1996). DNAPLs are hazardous organic liquids that are immiscible in water but exhibit aqueous solubilities sufficient to contaminate large volumes of soil and groundwater, posing unacceptable risk to human health and ecosystems. Years of research have been devoted to examining the processes governing the fate and transport of DNAPLs in the subsurface, including controlled spill field experiments (e.g., Kueper et al., 1993), laboratory experiments (e.g., Illangasekare et al., 1995; O'Carroll et al., 2004) and numerical simulations (e.g., Kueper and Gerhard, 1995; Dekker and Abriola, 2000). Following a near-surface release, DNAPLs penetrate the subsurface as an immiscible 'oil' phase migrating in response to gravity and capillary forces. The behaviour of DNAPL is site specific and governed by many factors including the properties of the DNAPL and porous media (e.g., Kueper and Gerhard, 1995). As a result, the DNAPL source zone can exhibit a wide range of forms, from a laterally extensive pool to a complex, heterogeneous distribution of both pools and residual (e.g., Gerhard et al., 2007).

Robust characterization and monitoring of DNAPL source zones is an essential and challenging component for the successful implementation of a remediation strategy. Identifying the volume and extent of DNAPL, both initially and over time, is necessary to inform site conceptual models and the subsequent design, monitoring and performance assessment of remedial strategies (Kavanaugh et al., 2003). Conventional site investigations, which tend to rely on a sparse network of intrusive sampling points (e.g., coring, direct-push sampling and monitoring wells), can be insufficient, as spatial information is restricted to vertical profiles at discrete intervals. Geophysical methods have long been recognized as an attractive approach at DNAPL sites as they can provide

non-invasive and spatially continuous information on subsurface variability leading to potentially more complete site characterization (e.g., Brewster et al., 1995).

In particular, electrical resistivity tomography (ERT) exhibits significant potential. DNAPLs typically have a high electrical resistivity (Lucius et al., 1992) and their presence in the pore space can provide a distinct electrical contrast with the surrounding groundwater that is amenable to ERT detection. ERT is one of the most well established and widely applied techniques in near-surface geophysics (e.g., Revil et al., 2012; Loke et al., 2013). Over the last 10 years, significant improvements have occurred in many aspects of the ERT technique, including field instrumentation, data acquisition and inversion (e.g., Ogilvy et al., 2009; Nenna et al., 2011; Loke et al., 2014), and ERT is now firmly established as a popular technique across a broad variety of applications in the field of hydrogeology. ERT has been used to investigate moisture content mapping (e.g., Zhou et al., 2001), groundwater flow patterns (e.g., Coscia et al., 2012), CO_2 migration (e.g., Schmidt-Hattenberger et al., 2013), salt-tracer transport (e.g., Doetsch et al., 2012), saline water intrusion (e.g., de Franco et al., 2009) and contaminant degradation (e.g., Atekwana et al., 2005).

ERT has been used in the context of DNAPL scenarios with some success. Chambers et al. (2004) performed time-lapse resistivity imaging to identify DNAPL flow through a saturated porous medium in a laboratory column. Daily and Ramirez (1995) used cross-hole ERT at a chlorinated solvent site to monitor changes in subsurface resistivity properties associated with in situ soil remediation processes, specifically air sparging and water infiltration. Newmark et al. (1998) used cross-hole ERT to monitor the removal of DNAPL during groundwater pumping. Goes and Meekes (2004) used cross-hole ERT to delineate DNAPL at two contaminated field sites, demonstrating a correlation between DNAPL presence and high electrical resistivity. Chambers et al. (2010) used high-resolution, cross-hole ERT in a pilot-scale experiment to map groundwater chemistry changes associated with the bioremediation of a DNAPL source zone.

While laboratory based ERT has invariably shown accurate delineation of DNAPL presence, field application of ERT to map DNAPLs is not commonly practiced. This is due, in part, to the difficulty in interpreting data from real contaminated sites. It is also

because ERT has traditionally been advocated and evaluated as a site characterization technique for static detection of the DNAPL source zone (e.g., Goes and Meekes, 2004; Cardarelli and Di Filippo, 2009). DNAPL sites are often highly heterogeneous with a tortuous DNAPL distribution superimposed upon a heterogeneous soil matrix, thereby presenting a complex electrical target. As a result, the relatively few field studies conducted at existing contaminated sites demonstrate mixed results. Moreover, it is not currently understood the range of site conditions under which ERT can be a valuable DNAPL investigation site tool.

The application of time-lapse ERT for monitoring changes in DNAPL mass and distribution over time demonstrates greater potential than static DNAPL detection. This is because the background heterogeneity, which is constant with time, is removed; thus, the evolving ERT response directly corresponds to changes in DNAPL (e.g., Newmark et al., 1998). This potential has not yet been properly evaluated due to the difficulty of performing controlled remediation experiments in the field and the difficulty of knowing the actual changes occurring during site remediation activities. Time-lapse ERT monitoring is now one of the most innovative and strongly emerging areas of applied geophysics (e.g., Supper et al., 2014) with recent developments such as optimized monitoring survey design (e.g., Wilkinson et al., 2013) and four-dimensional (4D, three spatial dimensions plus time) inversion algorithms (e.g., Karaoulis et al., 2013). These advancements are providing more reliable and higher quality information, with ERT now firmly establishing itself as a popular monitoring technique across a broad variety of applications in the field of hydrogeology (Loke et al., 2013). This provides new potential for ERT as a DNAPL site tool, particularly for monitoring time-lapse changes such as DNAPL remediation.

Exploring the complexity of field scale systems is typically accomplished with numerical models; field experiments with DNAPLs are now generally prohibited and field scale heterogeneity cannot be recreated in the laboratory. Numerous multiphase flow models have been developed in the field of contaminant hydrogeology to simulate DNAPL behaviour in groundwater systems (e.g., Abriola and Pinder, 1985; Grant and Gerhard, 2007a,b). Similarly, a number of ERT models have been developed in the field of

geophysics to predict the response from an ERT survey given a subsurface distribution of electrical resistivity (e.g., Spitzer, 1995; Tsourlos and Ogilvy, 1999; Rücker et al., 2006). A few studies have simulated the geophysical response from a simple DNAPL block in homogeneous porous media (e.g., Orlando and Renzi, 2013; Karaoulis et al., 2014). However, no numerical model exists that predicts the electrical response from a realistic DNAPL distribution generated by a multiphase flow model. As a result, no numerical modelling studies have been performed for investigating ERT mapping of DNAPL or DNAPL remediation at the field scale.

1.2 Research Objectives

The overall goal of this research is to explore the potential of ERT for application as a non-invasive DNAPL site investigation tool with specific emphasis on evaluating the potential of 4D time-lapse ERT for monitoring the remediation of DNAPL source zones.

The first objective was to develop a coupled DNAPL-ERT numerical model that would provide a platform for the evaluation of ERT for realistic, field scale DNAPL scenarios. The coupled model integrated a three-dimensional (3D) multiphase flow model, which can generate realistic DNAPL scenarios, with a 3D ERT forward model that can calculate the corresponding resistivity response. Central to the coupling was a new linkage between key hydrogeological parameters and the resulting local bulk electrical resistivity by integration of a variety of published relationships. Sensitivity studies were conducted at a variety of scales to evaluate the robustness of the linkage model and its sensitivity to heterogeneity in both DNAPL distribution and soil structure.

The second objective was to explore the potential of 4D time-lapse surface ERT to monitor DNAPL source zone remediation. A laboratory experiment was conducted to evaluate 4D ERT for mapping a changing NAPL distribution over time. The developed DNAPL-ERT numerical model was then employed to independently simulate the experiment which would provide confidence that the DNAPL-ERT model was a reliable tool for simulating real systems. The numerical model was then used to evaluate the

potential for 4D ERT at the field scale. Four DNAPL source zones, exhibiting a range of complexity, were then simulated, followed by modelled time-lapse ERT monitoring of complete DNAPL remediation by enhanced dissolution. 4D ERT inversion provided estimates of the regions of the source zone experiencing mass reduction with time and the volumes remediated.

The third objective was to evaluate the potential of a new ERT array configuration, surface-to-horizontal borehole (S2HB), to overcome limitations of tracking DNAPL mass reduction at depth. A field scale simulation of a DNAPL remediation scenario, monitored by both surface and S2HB ERT, was first conducted to provide an initial, theoretical estimate of the potential benefit of the S2HB ERT approach. A laboratory experiment was then performed to validate the S2HB ERT approach mapping evolving NAPL distributions in a physical system. Independent simulation of the experiment with the DNAPL-ERT model allowed direct comparison of the model to a more complex, known system under controlled conditions; this would provide further confidence in the model for reliably simulating real systems. 4D ERT inversion was employed for both numerical and experimental investigations to generate time-lapse resistivity images of the subsurface regions experiencing NAPL changes.

1.3 Thesis Outline

The following is a brief description of each subsequent chapter presented in this thesis:

- Chapter 2: summarizes the scientific literature relevant to the characterization and monitoring of DNAPLs by ERT.
- Chapter 3: focuses on the development of the coupled DNAPL-ERT model and includes all relevant theory and numerical simulation results.
- Chapter 4: evaluates the potential of time-lapse, surface-based ERT monitoring of DNAPL source remediation and includes all relevant background, laboratory and numerical simulation results.

- Chapter 5: examines the improved time-lapse monitoring of DNAPL remediation using surface-to-horizontal borehole (S2HB) ERT and includes all relevant background, laboratory and numerical simulation results.

- Chapter 6: summarizes the findings in this research as well as recommendations for future work on DNAPL mapping by ERT.

- Appendices: provide supplemental information, referenced throughout the thesis, that was not included in the manuscript chapters.

1.4 References

Abriola L.M., and G.F. Pinder. 1985. A multiphase approach to the modelling of porous media contamination by organic compounds: 1. Equation development. Water Resources Research, 21(1): 11-18.

Atekwana, E.A., E. Atekwana, F.D. Legall, and R.V. Krishnamurthy. 2005. Biodegradation and mineral weathering controls on bulk electrical conductivity in a shallow hydrocarbon contaminated aquifer. Journal of Contaminant Hydrology, 80: 149-167.

Brewster, M.L., A.P. Annan, J.P. Greenhouse, B.H. Kueper, and G.R. Olhoeft. 1995. Observed migration of a controlled DNAPL release by geophysical methods. Ground Water, 33: 977-987.

Cardarelli, E., and G. Di Filippo. 2009. Electrical resistivity and induced polarization tomography in identifying the plume of chlorinated hydrocarbons in sedimentary formation: a case study in Rho (Milan—Italy). Waste Man. & Research, 27: 595–602.

Chambers J.E., M.H. Loke, R.D. Ogilvy, and P.I. Meldrum. 2004. Noninvasive monitoring of DNAPL migration through a saturated porous medium using electrical impedance tomography. Journal of Contaminant Hydrology, 68: 1–22.

Chambers, J.E., P.B. Wilkinson, G.P. Wealthall, M.H. Loke, R. Dearden, R. Wilson, D. Allen, and R.D. Ogilvy. 2010. Hydrogeophysical imaging of deposit heterogeneity and groundwater chemistry changes during DNAPL source zone bioremediation. Journal of Contaminant Hydrology, 118: 43-61.

Coscia, I., N. Linde, S. Greenhalgh, T. Vogt, and A. Green. 2012. Estimating traveltimes and groundwater flow patterns using 3D time-lapse crosshole ERT imaging of electrical resistivity fluctuations induced by infiltrating river water. Geophysics, 77(4): E239-E250.

Daily, W., and A. Ramirez. 1995. Electrical resistance tomography during in-situ trichloroethylene remediation at the Savannah River Site. Journal of Applied Geophysics, 33: 239–249.

de Franco, R., G. Biella, L. Tosi, P. Teatini, et al. 2009. Monitoring the saltwater intrusion by time lapse electrical resistivity tomography: the Chioggia test site (Venice Lagoon, Italy). Journal of Applied Geophysics, 69(3-4): 117–130.

Dekker, T.J., and L.M. Abriola. 2000. The influence of field-scale heterogeneity on the surfactant-enhanced remediation of entrapped nonaqueous phase liquids. Journal of Contaminant Hydrology, 42: 219-251.

Doetsch, J., N. Linde, T. Vogt, A. Binley, and A.G. Green. 2012. Imaging and quantifying salt-tracer transport in a riparian groundwater system by means of 3D ERT monitoring. Geophysics, 77(5): B207-B218.

Gerhard, J.I., T. Pang, and B.H. Kueper. 2007. Time scales of DNAPL migration in sandy aquifers. Ground Water, 45: 147-157.

Goes, B.J.M., and J.A.C. Meekes. 2004. An effective electrode configuration for the detection of DNAPLs with electrical resistivity tomography. Journal of Environmental and Engineering Geophysics, 9(3): 127-141.

Grant, G.P., and J.I. Gerhard. 2007a. Simulating the dissolution of a complex dense non-aqueous phase liquid source zone: 1. model to predict interfacial area. Water Resources Research, 43: W12410.

Grant, G.P., and J.I. Gerhard. 2007b. Simulating the dissolution of a complex dense non-aqueous phase liquid source zone: 2. experimental validation of an interfacial area-based mass transfer model. Water Resources Research, 43.

Illangasekare T.H., J.L. Ramsey Jr., K.H. Jensen, and M.B. Butts. 1995. Experimental study of the movement and distribution of dense organic contaminants in heterogeneous aquifer. Journal of Contaminant Hydrology, 20: 1–25.

Karaoulis, M., A. Revil, P. Tsourlos, D.D. Werkema, and B.J. Minsley. 2013. IP4DI: A software for time-lapse 2D/3D DC-resistivity and induced polarization tomography. Computers & Geosciences, 54(0): 164-170.

Karaoulis, M., P. Tsourlos, J.H. Kim, and A. Revil. 2014. 4D time-lapse ERT inversion: introducing combined time and space constraints. Near Surface Geophysics, 12(1): 25-34.

Kavanaugh, M.C., P.S.C. Rao, L. Abriola, C. Newell, J. Cherry, T. Sale, G. Destouni, S. Shoemaker, R. Falta, R. Siegrist, D. Major, G. Teutsch, J. Mercer, and K. Udell. 2003. The DNAPL remediation challenge: is there a case for source depletion?. US Environmental Protection Agency, Washington DC.

Kueper, B.H., J.D. Redman, R.C. Starr, S. Reitsma, and M. Mah. 1993. A field experiment to study the behavior of tetrachloroethylene below the water table: spatial distribution of residual and pooled DNAPL. Ground Water, 31: 756-766.

Kueper, B.H., and J.I. Gerhard. 1995. Variability of point source infiltration rates for two-phase flow in heterogeneous porous media. Water Resources Research, 31: 2971-2980.

Loke, M.H., J.E. Chambers, D.F. Rucker, O. Kuras, and P.B. Wilkinson. 2013. Recent developments in the direct-current geoelectrical imaging method. Journal of Applied Geophysics, 95: 135-156.

Loke, M.H., T. Dahlin, and D.F. Rucker. 2014. Smoothness-constrained time-lapse inversion of data from 3-D resistivity surveys. Near Surface Geophysics, 12(1): 5-24.

Lucius, J.E., G.R.Olhoeft, P.L. Hill, and S.K. Duke. 1992. Properties and hazards of 108 selected substances - 1992 edition. Open-File Report 92-527, U. S. Geological Survey.

Nenna, V., A. Pidlisecky, and R. Knight. 2011. Informed experimental design for electrical resistivity imaging. Near Surface Geophysics, 9: 469-482.

Newmark R.L., W.D. Daily, K.R. Kyle, and A.L. Ramirez. 1998. Monitoring DNAPL pumping using integrated geophysical techniques. Journal of Environmental and Engineering Geophysics, 3: 7–13.

O'Carroll, D.M., S.A. Bradford, and L.M. Abriola. 2004. Infiltration of PCE in a system containing spatial wettability variations. Journal of Contaminant Hydrology, 73: 39-63.

Ogilvy R.D., O. Kuras, P.I. Meldrum, P.B. Wilkinson, J.E. Chambers, M. Sen, A. Pulido-Bosch, J. Gisbert, S. Jorreto, I. Frances, and P. Tsourlos. 2009. Automated monitoring of coastal aquifers with electrical resistivity tomography. Near Surface Geophysics, 7: 367–375.

Orlando, L., and B. Renzi. 2013. Time-lapse monitoring of DNAPL in a controlled cell. Near Surface Geophysics, 11: 129-142.

Pankow, J.F., S. Feenstra, J.A. Cherry, and M.C. Ryan. 1996. Dense chlorinated solvents in groundwater: Background and history of the problem. In: Pankow, J.F., and J.A. Cherry (Eds.), Dense Chlorinated Solvents and other DNAPLs in Groundwater, History, Behavior, and Remediation. Waterloo Press, Portland, Oregon, United States, pp. 1-52.

Revil, A., M. Karaoulis, T. Johnson, and A. Kemna. 2012. Review: Some low-frequency electrical methods for subsurface characterization and monitoring in hydrogeology. Hydrogeology Journal, 20: 617-658.

Rücker, C., T. Günther, and K. Spitzer. 2006. Three-dimensional modelling and inversion of dc resistivity data incorporating topography – I. Modelling. Geophysical Journal International, 166(2): 495-505.

Schmidt-Hattenberger, C., P. Bergmann, D. Bösing, T. Labitzke, M. Möller, S. Schröder, F. Wagner, and H. Schütt. 2013. Electrical resistivity tomography (ERT) for monitoring of CO_2 migration – from tool development to reservoir surveillance at the Ketzin pilot site. Energy Procedia, 37: 4268-4275.

Spitzer, K. 1995. A 3-D finite-difference algorithm for DC resistivity modelling using conjugate gradient methods. Geophysical Journal International, 123: 903-914.

Supper, R., J. Chambers, P. Tsourlos, and J.H. Kim. 2014. Foreword on the Special Topic of Geoelectrical Monitoring. Near Surface Geophysics, 12(1): 1-3.

Tsourlos, P., and R. Ogilvy. 1999. An algorithm for the 3-D inversion of tomographic resistivity and induced polarization data: preliminary results. Journal of the Balkan Geophysical Society, 2: 30-45.

Wilkinson, P.B., S.S. Uhlemann, J.E. Chambers, P.I. Meldrum, L.S. Oxby, and O. Kuras. 2013. Optimised sequential experimental design for geoelectrical resistivity monitoring surveys. Near Surface Geoscience 2013, 19th European Meeting of Environmental and Engineering Geophysics, Bochum, Germany, September 2013.

Zhou, Q.Y., J. Shimada, and A. Sato. 2001. Three-dimensional spatial and temporal monitoring of soil water content using electrical resistivity tomography. Water Resources Research, 37(2): 273–285.

2 LITERATURE REVIEW

This chapter summarizes the literature relevant to the characterization and monitoring of dense non-aqueous phase liquids (DNAPLs) by electrical resistivity tomography (ERT). This review first examines the behaviour and distribution of DNAPLs in the subsurface and the challenges facing successful remediation of sites contaminated with DNAPL. The ERT technique has been well-established for many years but has evolved significantly in recent years with a large amount of research documenting numerous advancements. This review will examine the current state of knowledge with respect to ERT. Although the focus of this work is the application of ERT to DNAPL investigations, the scientific literature relevant to hydrogeological studies is also presented to demonstrate the more widespread utilization and increasing popularity of ERT in this field. A key component of this work, and the basis for the development of a coupled DNAPL-ERT model, is related to the various hydraulic-electric relationships in the literature and specific emphasis will be placed on these relationships. A summary is then presented which identifies research gaps and opportunities.

2.1 Dense Non-aqueous Phase Liquids

2.1.1 Introduction

Tens of thousands of sites worldwide exhibit groundwater contamination by hazardous organic and inorganic chemicals (NRC, 2005). Dense non-aqueous phase liquids (DNAPLs) are a class of hazardous organic liquids that have been widely used in a variety of industrial applications and/or are the byproducts of industrial activities often introduced into the subsurface by uncontrolled releases (Pankow et al., 1996). Common types of DNAPLs include wood treating oils such as creosote, transformer and insulating oils containing polychlorinated biphenyls (PCBs), coal tar and a variety of chlorinated solvents such as tetrachloroethylene (PCE) and trichloroethylene (TCE). DNAPLs are denser than water with most DNAPLs being highly volatile and toxic. Although these compounds are considered immiscible in water in the context of their physical behaviour,

they have finite solubilities sufficient to generate levels of dissolved contamination orders of magnitude greater than drinking water standards (Kueper et al., 2003). Therefore, even relatively small concentrations of DNAPLs have the capacity to act as a long-term source of pollution and contaminate large amounts of groundwater, posing unacceptable risk to human health and ecosystems.

2.1.2 DNAPL Migration

The migration of DNAPLs in the subsurface is a complex multiphase flow problem. Most of the existing information regarding DNAPL behaviour and its influencing factors has been obtained by a few controlled spill field experiments (e.g., Kueper et al., 1993), laboratory experiments (e.g., Illangasekare et al., 1995; O'Carroll et al., 2004) and numerical simulations (e.g., Kueper and Gerhard, 1995; Dekker and Abriola, 2000; Gerhard and Kueper, 2003a,b,c). The process of DNAPL migration is not only controlled by the flow of groundwater, but also by geological structures, soil properties and gravity. DNAPL migration demonstrates substantial sensitivity to even subtle variations in porous media properties, particularly intrinsic permeability (e.g., Poulsen and Kueper, 1992; Kueper and Gerhard, 1995).

Figure 2-1 provides an illustration of a typical DNAPL distribution following a near-surface release. Following release to the subsurface, the DNAPL spreads and migrates downward, penetrating the subsurface as an immiscible 'oil' phase. In many circumstances, DNAPL is non-wetting on the soil grains with respect to water (NRC, 2005). In such scenarios, locally a sufficient DNAPL pressure is needed to overcome the soil entry capillary pressure in order to displace pore water. Entry pressures are, in turn, a function of soil permeability (Dekker and Abriola, 2000). The result is that DNAPL migration pathways at the field scale are dictated by the subsurface distribution of permeability. The DNAPL will continue to redistribute, following pathways of least capillary resistance until coming to rest either as disconnected, hydraulically trapped ganglia known as 'residual' or in the form of potentially mobile 'pools' perched upon capillary barriers (e.g., Kueper et al., 2003). The timescale for this process of DNAPL

migration and redistribution can be on the order of months to decades, depending on the fluid properties and site characteristics (Gerhard et al., 2007). The final distribution of DNAPL can be in the form of a laterally extensive layer near the surface (e.g., Gerhard et al., 2001) or a complex distribution of residual and pools distributed widely and penetrating to significant depth (e.g., Gerhard et al., 2007). The 'DNAPL body' is composed of the pooled and residual DNAPL in the subsurface, while the total extent of subsurface surrounding the DNAPL body is considered the 'source zone'. The DNAPL source zone is so named because its contact with the flowing groundwater results in its slow dissolution, forming dissolved-phase plumes which can act as a source of groundwater contamination for many decades.

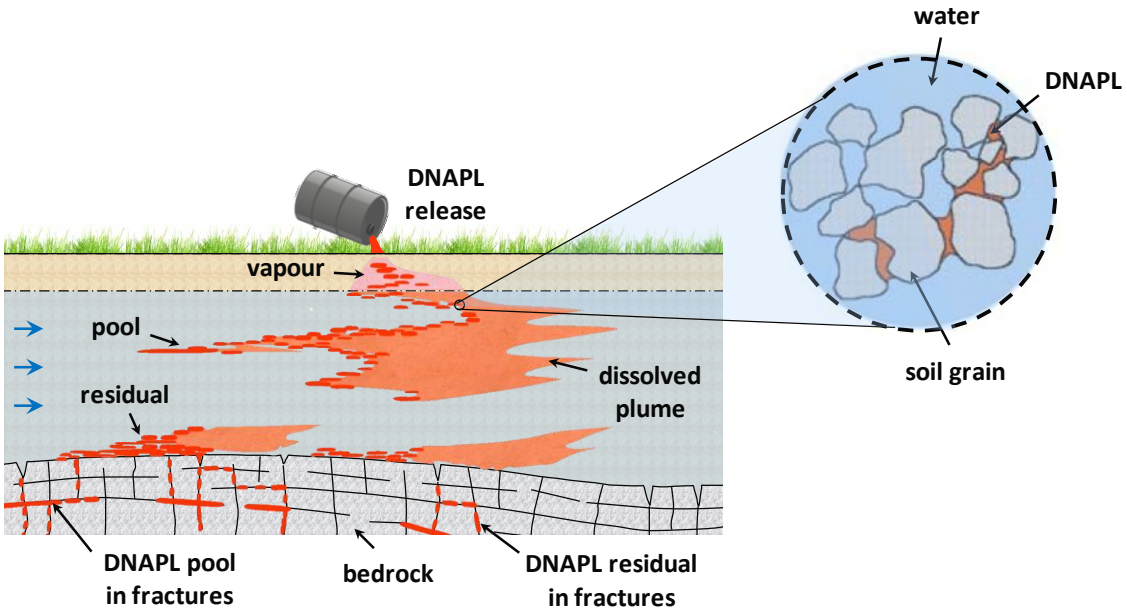

Figure 2-1: DNAPL distribution in the subsurface (modified from Kueper et al., 2003). This figure indicates the complex distribution of DNAPL in the form of pools and residual DNAPL. The magnified image illustrates the residual DNAPL in the saturated porous media.

2.1.3 DNAPL Remediation

The remediation of sites contaminated with DNAPLs remains a major environmental challenge. Over the past 25 years, a wide variety of remediation strategies have been

deployed at DNAPL sites including containment of the source zone, management of the dissolved plume and aggressive source zone depletion technologies. Hundreds of pilot-scale site trials have been conducted to evaluate innovative in situ technologies, while a much smaller number of full-scale source zone remediation projects have been reported (Kavanaugh et al., 2003). In addition to a vast number of journal papers, a number of documents with compiled information on various remediation technologies have been presented (e.g., NRC, 2005; ITRC, 2011).

Previously, the treatment strategy of choice usually involved the containment of the source zone and/or management of the dissolved plume rather than aggressive source zone depletion technologies. Source zone containment strategies, coupled with long-term monitoring, have been adopted at a number of DNAPL sites, including groundwater pump-and-treat, cut-off walls, and permeable reactive barriers (PRBs) (e.g., Mackay and Cherry, 1989; Pearlman, 1999). Although containment has been effective at limiting the spread of contaminants and significantly reducing the risk of human and ecological exposures, the failure to remove the DNAPL source means that long-term stability and monitoring is required along with significant financial resources (Kavanaugh et al., 2003).

A number of aggressive ex situ and in situ technologies, both conventional and innovative, have also been deployed at sites to focus on obtaining substantial DNAPL mass reduction in the source zone (e.g., NRC, 2005). The more aggressive DNAPL removal technologies include fluid flushing, thermal, bioremediation and chemical oxidation. Waterflooding (also known as hydraulic displacement) involves the injection of water to mobilize DNAPL towards an extraction well and also enhance dissolution rates (e.g., Alexandra et al., 2012). Surfactant and co-solvent flushing technologies significantly increase the aqueous solubility of DNAPL components and reduce interfacial tension to provide increased mobilization of the DNAPL for extraction (e.g., Saenton and Illangasekare, 2013). Steam enhanced extraction is a thermal technology that utilizes steam to heat the subsurface and recover vapors, contaminated water and DNAPL through associated extraction systems (e.g., Udell, 1997). Smoldering combustion of NAPLs involves the ignition and propagation of a smoldering combustion reaction in contaminated porous media to achieve contaminant destruction (e.g., Pironi et

al., 2009; Switzer et al., 2009). Enhanced bioremediation technologies deliver electron donors to the source zone to encourage microbial growth as close as possible to the DNAPL (e.g., Carr et al., 2000; Cope and Hughes, 2001). Chemical oxidation relies on rapid chemical reactions between an injected chemical oxidant and the chemical constituents in DNAPLs (e.g., Seol et al., 2003).

In addition to DNAPL mass reduction, additional subsurface processes may occur during site remediation that combine to make it more difficult for site characterization and monitoring techniques to discern DNAPL mass changes from other changes. Most technologies involve the delivery of amendment fluids to the contaminated region and the reaction of these additives with the groundwater and contaminants may also generate subsurface changes. For example, the injection of an emulsified vegetable oil (EVO) electron donor for enhanced bioremediation results in groundwater chemistry changes (e.g., Chambers et al., 2010). Smoldering combustion results in significantly increased subsurface temperatures and dewatering in advance of the combustion front (e.g., Switzer et al., 2009).

Despite years of research and experience in deploying various technologies for DNAPL cleanup, the ability to completely remediate contaminated sites is still in doubt. Such uncertainty is not only caused by the performance of the remediation technique, but also uncertainties in site characterization (e.g., aquifer heterogeneity and the location and amount of DNAPL), predicting the beneficial and adverse impacts of partial source zone depletion, and attaining regulatory targets (Kavanaugh et al., 2003). As discussed in Section 2.1.2, geologic heterogeneity is one of the primary factors controlling the migration and distribution of DNAPL in the subsurface (e.g., Kueper and Gerhard, 1995; Dekker and Abriola, 2000). It also complicates characterization of the source zone (e.g., Nelson et al., 1999) and effectiveness of remediation (e.g., Saenton et al., 2002; NRC, 2005). For instance, most remediation technologies that rely on the delivery of remedial agents to the source zone are strongly affected by the geologic heterogeneity.

Characterization of the DNAPL distribution in the source zone is essential for the purposes of selection, design, and performance assessment of DNAPL remediation technologies (NRC, 2005). Typically, the progress of source zone remediation is

measured indirectly by evaluating dissolved contaminant concentrations at locations downgradient of the source zone. However, depending on the aquifer heterogeneity, a very large fraction of DNAPL mass may have to be removed from the source zone to make any significant impact on those concentrations (e.g., Sale and McWhorter, 2001; Saenton and Illangasekare, 2013). Alternatively, significant concentration reductions may be observed with little source zone mass reduction, for example due to a shifting groundwater gradient (Inculet, 2011). Therefore, it is preferable to implement characterization techniques at the source zone to directly and more effectively monitor DNAPL mass removal.

Another problem facing remediation strategies at contaminated sites is the required cleanup target. Regulatory agencies have gravitated to the Maximum Contaminant Level (MCL) as the key criterion for subsurface remediation at all sites. Several studies have evaluated the ability of remediation technologies to achieve MCLs in the source zone. Kavanaugh et al. (2003) concluded that MCLs are not likely to be achieved within a reasonable time frame in source zones at the vast majority of DNAPL sites. McGuire et al. (2006) investigated the performance of remedial efforts at 59 chlorinated solvents sites and demonstrated that no site reached MCLs. NRC (2005) reported that no cases exist of large DNAPL sites being fully restored to the MCL criteria. The years of research and experience in this area has now provided a much better understanding of the key contaminant processes and of what remediation systems can realistically achieve. This has led a number of studies to recommend more realistic and attainable goals for source zone remediation to replace the rigid MCLs-everywhere approach (e.g., ITRC, 2011; Newell et al., 2011; Hadley and Newell, 2012). More flexible or intermediate performance goals provide a more encouraging climate for implementing innovative remediation technologies. For instance, a new technology that achieves ‘only’ partial DNAPL source depletion would be acceptable as an intermediate goal as part of a phased site cleanup (Kavanaugh et al., 2003).

2.1.4 Numerical Modelling

2.1.4.1 Multiphase flow

Numerical modelling studies have become the primary method for studying field scale DNAPL behaviour as field experiments are generally prohibited and field scale heterogeneity is rarely recreated in laboratory experiments. Numerous multiphase flow models have been developed to simulate the behaviour of organic contaminants in groundwater systems (e.g., Kaluarachchi and Parker, 1990; Kueper and Frind, 1991a,b; Sleep and Sykes, 1993; Dekker and Abriola, 2000; Gerhard and Kueper, 2003a,b,c).

The migration of a non-wetting phase through an initially wetting phase saturated porous medium may be represented mathematically as a case of two-phase flow. Assuming no mass transfer between the phases, the continuity equations for mass balance of a wetting (subscript '*w*') and non-wetting (subscript '*n*') phase can be written as (Bear, 1972):

$$-\frac{\partial}{\partial x_i}\left[\varsigma_w q_{w,i}\right] + Q_w = \frac{\partial}{\partial t}\left[\phi \varsigma_w S_w\right], \qquad i = x,y,z \tag{2-1}$$

$$-\frac{\partial}{\partial x_i}\left[\varsigma_n q_{n,i}\right] + Q_n = \frac{\partial}{\partial t}\left[\phi \varsigma_n S_n\right], \qquad i = x,y,z \tag{2-2}$$

where ς_w and ς_n are the wetting and non-wetting phase densities, respectively, $q_{w,i}$ and $q_{n,i}$ are the respective fluxes, Q_w and Q_n are the respective source/sink terms, t is the time, *x*, *y*, *z* are the spatial coordinates, ϕ is the porosity of the porous medium, and S_w and S_n are the respective phase saturations.

The multiphase extension of Darcy's law can be used to describe the fluid fluxes (e.g., Bear, 1972):

$$q_{w,i} = -\frac{k_{ij}k_{r,w}}{\mu_w}\left(\frac{\partial P_w}{\partial x_j} + \varsigma_w g \frac{\partial z}{\partial x_j}\right), \qquad i = x,y,z \tag{2-3}$$

$$q_{n,i} = -\frac{k_{ij}k_{r,n}}{\mu_n}\left(\frac{\partial P_n}{\partial x_j} + \varsigma_n g \frac{\partial z}{\partial x_j}\right), \qquad i = x,y,z \tag{2-4}$$

where k_{ij} is the second-order tensor defining porous media intrinsic permeability, $k_{r,w}$ and $k_{r,n}$ are the relative permeabilities to the wetting and non-wetting phases, respectively, μ_w and μ_n are the respective phase viscosities, P_w and P_n are the respective phase pressures, g is the acceleration due to gravity, z is the vertical direction.

Substituting the multiphase extension of Darcy's law into Equations 2-1 and 2-2, assuming that both the fluids and the porous medium are incompressible, and ignoring the source/sink terms, the problem reduces to the simultaneous differential equations (Kueper and Frind, 1991a):

$$\frac{\partial}{\partial x_i}\left[\frac{-k_{ij}k_{r,w}}{\mu_w}\left(\frac{\partial P_w}{\partial x_j} + \varsigma_w g \frac{\partial z}{\partial x_j}\right)\right] - \phi\frac{\partial S_w}{\partial t} = 0, \qquad i,j = x,y,z \tag{2-5}$$

$$\frac{\partial}{\partial x_i}\left[\frac{-k_{ij}k_{r,n}}{\mu_n}\left(\frac{\partial P_n}{\partial x_j} + \varsigma_n g \frac{\partial z}{\partial x_j}\right)\right] + \phi\frac{\partial S_n}{\partial t} = 0, \qquad i,j = x,y,z \tag{2-6}$$

Equations 2-5 and 2-6 are coupled through the relationship for capillary pressure:

$$P_c(S_w) = P_n - P_w, \tag{2-7}$$

where P_c is the capillary pressure, and subject to

$$S_w + S_n = 1 \tag{2-8}$$

The capillary pressure relationship and the saturation constraint are substituted into Equation 2-6 to arrive at a set of equations formulated in terms of the two primary unknowns P_w and S_w (Kueper and Frind, 1991a):

$$\frac{\partial}{\partial x_i}\left[\frac{-k_{ij}k_{r,w}}{\mu_w}\left(\frac{\partial P_w}{\partial x_j} + \varsigma_w g \frac{\partial z}{\partial x_j}\right)\right] - \phi\frac{\partial S_w}{\partial t} = 0, \qquad i,j = x,y,z \tag{2-9}$$

$$\frac{\partial}{\partial x_i}\left[\frac{-k_{ij}k_{r,n}}{\mu_n}\left(\frac{\partial (P_c + P_w)}{\partial x_j} + \varsigma_n g \frac{\partial z}{\partial x_j}\right)\right] + \phi\frac{\partial S_w}{\partial t} = 0, \quad i,j = x,y,z \tag{2-10}$$

These equations are highly non-linear due to the dependence of the relative permeabilities $k_{r,w}$ and $k_{r,n}$ on the wetting phase saturation, and the dependence of the capillary pressure P_c on the wetting phase saturation. Constitutive relationships describing these dependencies – $k_{r,w}(S_w)$, $k_{r,n}(S_w)$ and $P_c(S_w)$ – are required in order to solve these equations. Widely used and basic forms of these constitutive relations are described by Brooks and Corey (1964) and van Genuchten (1980). Numerous studies have investigated hysteretic constitutive relations governing multiphase flow (e.g., Lenhard and Parker, 1987; Parker and Lenhard, 1987; Gerhard and Kueper, 2003a,b).

Numerical methods, such as finite difference or finite element, are normally employed to obtain an approximate solution to the governing multiphase equations (e.g., Kueper and Frind, 1991a,b). Equations 2-9 and 2-10 are discretized into a solution domain with the unknown variables at discrete points, or nodes. The non-linear nature of the governing equations is handled with numerical techniques to linearize the problem. For example,

the Newton-Raphson technique, which is generally regarded as the most robust (Huyakorn and Pinder, 1983), involves replacing the non-linear system of equations with a linear approximation using Newton's Method and then minimizing the resulting error with an iterative solution scheme.

Model verification, validation and calibration steps are frequently performed to ensure that a numerical model is an accurate and credible representation of a real system (Rykiel, 1996). Model verification is a process used to confirm that the model formalism is correct; this process determines that the inputs and calculations are correctly implemented. Model validation compares the simulated system output with real system observations to check that the model, within a satisfactory range of accuracy, represents the real system (Rykiel, 1996). Model calibration is an iterative process that compares the model to the actual system behaviour and uses the discrepancies between the two, and the insights gained, to improve the model. Model calibration can occur as part of either verification or validation procedures (Rykiel, 1996).

2.1.4.2 Boundary conditions

The partial differential equations (Equations 2-9 and 2-10) must be coupled with boundary and initial conditions to specify a solvable mathematical model. Source/sink terms are added into the mass balance equations (2-9) and (2-10) only for chosen boundary nodes. By manipulating the form of these additional flux terms, all physically possible boundary configurations can be specified.

For each phase that is mobile through a boundary node (i.e., able to enter or leave the domain via that boundary), the model indirectly solves for the appropriate mass flux such that the boundary condition is maintained. For a constant wetting pressure (Dirichlet type) boundary condition, for example, the model is forced to solve $\Delta P_w = 0$ at boundary node b. If both phases are mobile through the node, this is accomplished by adding source/sink terms to the wetting and non-wetting equations respectively:

$$Q_{w,b} = W_I (P^*_{w,b} - P_{w,b}) k_{r,w,b}\,, \tag{2-11}$$

$$Q_{n,b} = W_J (P^*_{w,b} - P_{w,b}) k_{r,n,b}\,, \tag{2-12}$$

where W_I and W_J are very large, but unequal numbers (e.g., 10^{25} and 10^{30}), and $P^*_{w,b}$ is the specified wetting pressure at boundary node b. The presence of such large numbers forces the model, in this case, to always solve $P_{w,b} \cong P^*_{w,b}$. To specify a constant saturation at node b with both phases mobile, a similar formulation of the flux terms is needed:

$$Q_{w,b} = W_J (S^*_{w,b} - S_{w,b}) k_{r,w,b}\,, \tag{2-13}$$

$$Q_{n,b} = W_I (S^*_{w,b} - S_{w,b}) k_{r,n,b}\,, \tag{2-14}$$

where $S^*_{w,b}$ is the specified wetting saturation at boundary node b. Furthermore, both boundary conditions can be specified at a single node by combining the flux terms. Thus, for a constant wetting pressure and saturation at boundary node b with both phases mobile, the required source/sink terms are given by:

$$Q_{w,b} = k_{r,w,b}\left[W_I (P^*_{w,b} - P_{w,b}) + W_J (S^*_{w,b} - S_{w,b})\right] \tag{2-15}$$

$$Q_{n,b} = k_{r,n,b}\left[W_J (P^*_{w,b} - P_{w,b}) + W_I (S^*_{w,b} - S_{w,b})\right] \tag{2-16}$$

In any of these cases, the boundary condition may restrict flux into or out of the domain to only one fluid. If only the wetting phase is mobile across the boundary node, then the non-wetting flux term, $Q_{n,b}$, would be zero. Consequently, for a no-flow boundary and for a non-boundary node, the source/sink terms can be ignored altogether (i.e., $Q_{w,i} = 0$

and $Q_{n,i} = 0$ for all i, unless otherwise specified). All other possible boundary conditions, such as constant flux, injection and extraction wells can be similarly specified at any node in the domain.

2.1.4.3 Multiphase flow models

A number of multiphase flow models have been developed which solve the system of equations described above (e.g., Abriola and Pinder, 1985; Kaluarachchi and Parker, 1990; Kueper and Frind, 1991a,b; Abriola et al., 1992; Sleep and Sykes, 1993). These models have been used to study DNAPL migration (e.g., Kueper and Gerhard, 1995), impacts of wettability changes (e.g., O'Carroll et al., 2004), DNAPL dissolution (e.g., Dekker and Abriola, 2000; Saenton and Illangasekare, 2013), and various remediation strategies (e.g., Rathfelder et al., 2000; Christ and Abriola, 2006; Chen et al., 2013).

The model that is used extensively in this thesis is DNAPL3D. DNAPL3D is a finite-difference, multiphase fluid flow model that simulates the infiltration, redistribution, and immobilization of DNAPL in heterogeneous porous media at the field scale. The initial formulation of the model in two-dimensions (2D) was provided by Kueper and Frind (1991a,b). Gerhard and Kueper (2003a,b) incorporated capillary pressure-saturation and non-wetting phase relative permeability-saturation relationships into the numerical model, which was then validated against one-dimensional (1D) laboratory experiments in both space and time. Gerhard and Kueper (2003c) demonstrated that the details of the constitutive model incorporated into a two-phase flow code profoundly influence the details of the DNAPL scenario, including the proportion of DNAPL pools to residual, the extent of the source zone, and the time required for DNAPL migration to occur. Grant et al. (2007) validated the model for DNAPL redistribution in heterogeneous porous media in 2D.

DNAPL3D, and similar models, provide an effective tool for designing field and laboratory-scale experiments and can be used to perform sensitivity analysis in the study of DNAPL migration. Kueper and Gerhard (1995) demonstrated that source location,

source size and source strength all have a profound influence on the infiltration rate of DNAPL into the subsurface. Gerhard et al. (2007) utilized DNAPL3D to examine the time scales of the migration of six different DNAPLs in sandy aquifers, and demonstrated that the density and viscosity of DNAPL and the mean permeability of the aquifer are the key parameters that affect the time scale; the higher the DNAPL mobility and aquifer permeability, the lower the cessation times. The release volume, strength of the source, ambient ground water hydraulic gradient, mean aquifer porosity, and DNAPL-water interfacial tension are not found to significantly affect cessation times, but they do significantly affect the spatial distribution of the DNAPL.

2.1.4.4 Contaminant transport

The partial differential equation describing the fate and transport of dissolved phase contaminants of species κ in 3D, transient groundwater flow systems can be written as follows (Freeze and Cherry, 1979):

$$\frac{\partial}{\partial t}(\phi C_\kappa) = \frac{\partial}{\partial x_i}\left(\phi D_{ij}\frac{\partial C_\kappa}{\partial x_j}\right) - \frac{\partial}{\partial x_i}(\phi v_i C_\kappa) + q_s C_{\kappa,s} + \sum R_n , \qquad i,j = x,y,z \qquad (2\text{-}17)$$

where C_κ is the aqueous phase concentration, D_{ij} is the hydrodynamic dispersion coefficient tensor, v_i is the seepage of linear pore water velocity (it is related to the specific discharge or Darcy flux through the relationship $v_i = q_i / \phi$), q_s is the volumetric flow rate per unit volume of aquifer representing fluid sources (positive) and sinks (negative), $C_{\kappa,s}$ is the concentration of the source or sink flux for species κ, and $\sum R_n$ is the chemical reaction term.

The transport equation is related to the groundwater flow equation through Darcy's law (Bear, 1972):

$$v_{\kappa,j} = \frac{q_{\kappa,j}}{\phi} = -\frac{K_{ij}}{\phi}\frac{\partial h}{\partial x_j} \quad , \tag{2-18}$$

where K_{ij} is the hydraulic conductivity and h is hydraulic head, calculated from the solution of the groundwater flow equation (Bear, 1972):

$$\frac{\partial}{\partial x_j}\left(K_{ij}\frac{\partial h}{\partial x_j}\right) + q_s = S_s\frac{\partial h}{\partial t} \quad , \tag{2-19}$$

where S_s is the specific storage of the aquifer.

The chemical reaction term, R_n, in Equation 2-17 can be used to include the effects of general biochemical and geochemical reaction (e.g., sorption and decay) which are generally expressed as functions of aqueous phase concentration. Therefore, the governing equations for each component require the solution of only one unknown (i.e., C_κ) for each equation.

A number of numerical models have been developed to simulate contaminant transport. MT3D is a 3D transport model for simulating the advection, dispersion and chemical reactions of soluble contaminants in groundwater systems (Zheng, 1990). The MT3D code is widely used in contaminant transport modelling and remediation assessment studies (e.g., Saba and Illangasekare, 2000; Saenton et al., 2002; Oostrom et al., 2006; Grant and Gerhard, 2007a,b). RT3D is a solute transport code derived from MT3D but with greatly expanded reaction capabilities, including simulation of inorganic reactions, geochemistry reactions, colloid transport and heat transport (Clement, 1997). This model has also seen wide application in the literature (e.g., Tartakovsky et al., 2002; Clement et al., 2004; Phanikumar and McGuire, 2004; West et al., 2008). Other solute transport models include MISER (Abriola et al., 1997), FEMWATER (Lin et al., 1997) and TOUGHREACT (Xu et al., 2012).

2.1.4.5 DNAPL mass removal

In addition to simulating the realistic infiltration and redistribution of DNAPL at a contaminated site, numerical models have also been developed to simulate the mass removal of DNAPL. Numerical models are a widely used and cost-effective avenue for predicting the performance of various DNAPL remediation technologies such as natural dissolution (e.g., Grant and Gerhard, 2007a,b), surfactant-enhanced dissolution (e.g., Saenton and Illangasekare, 2013) and chemical oxidation (e.g., West et al., 2008).

The DNAPL mass removal method used throughout this thesis is natural groundwater dissolution. As discussed, the components of DNAPL dissolve into groundwater to some degree. Partitioning from the DNAPL phase to groundwater has been examined by a number of studies and a number of mass transfer expressions have been developed (e.g., Miller et al., 1990; Powers et al., 1992; Imhoff et al., 1993; Saba and Illangasekare, 2000; Nambi and Powers, 2003; Grant and Gerhard, 2007a,b). A number of numerical modelling studies have been conducted to investigate the removal of entrapped DNAPL either from natural or enhanced dissolution (e.g., Park and Parker, 2005; Grant and Gerhard, 2007a,b; Saenton and Illangasekare, 2013).

Grant and Gerhard (2007a,b) developed DNAPL3D-MT to simulate DNAPL infiltration and redistribution below the water table as well as DNAPL dissolution and transport of dissolved phase species in groundwater. DNAPL3D-MT couples the multiphase flow model DNAPL3D (Gerhard and Kueper, 2003a,b,c) and the dissolved phase transport model MT3D (Zheng, 1990) through a novel mass transfer routine based on the interfacial area between immiscible phases (Grant and Gerhard, 2007a,b). A standard split operator approach (e.g., Barry et al., 2002) was used to link the two sub-models. Within a time step, DNAPL migration is initially simulated using DNAPL3D. The appropriate amount of contaminant mass introduced locally into the aqueous phase at nodes with DNAPL present is then determined by the mass transfer routine. MT3D is then employed within the same time step to simulate the advection and dispersion of the dissolved phase in groundwater. Finally the phase saturations are updated at the end of the time step in accordance with the amount of mass transferred from the DNAPL to the aqueous phase. The DNAPL3D-MT model was validated for the complete dissolution of

a DNAPL source zone in 2D heterogeneous porous media. Figure 2-2 presents an example of a simulated DNAPL source zone undergoing mass removal via dissolution by groundwater flowing from left to right.

DNAPL3D-MT has also been used to examine the effectiveness of hydraulic displacement for the removal of pooled DNAPL through the use of injection and extraction wells (e.g., Alexandra et al., 2012). The hydraulic displacement simulations demonstrated an increase in the amount of the residual DNAPL present, which in turn resulted in increased solute concentrations in groundwater and enhanced DNAPL dissolution. DNAPL3D has also been coupled with a combustion front expansion model to develop an In Situ Smoldering Model (ISSM) that simulates the expansion of a smoldering front in heterogeneous porous media (MacPhee et al., 2012).

DNAPL3D-RX was developed by West et al. (2008) by coupling DNAPL3D to the reactive transport model RX3D (Clement, 1997). DNAPL3D-RX simulates DNAPL infiltration and redistribution, mass transfer between the non-aqueous and aqueous phases, and advective-dispersive aqueous phase reactive transport in groundwater. The mass transfer module and standard split operator used by Grant and Gerhard (2007a,b) in DNAPL3D-MT is also employed in this model. DNAPL3D-RX is calibrated to published 1D column experiments. West et al. (2008) employed DNAPL3D-RX to study the efficacy of the chemical oxidation treatment process on DNAPL source zone removal.

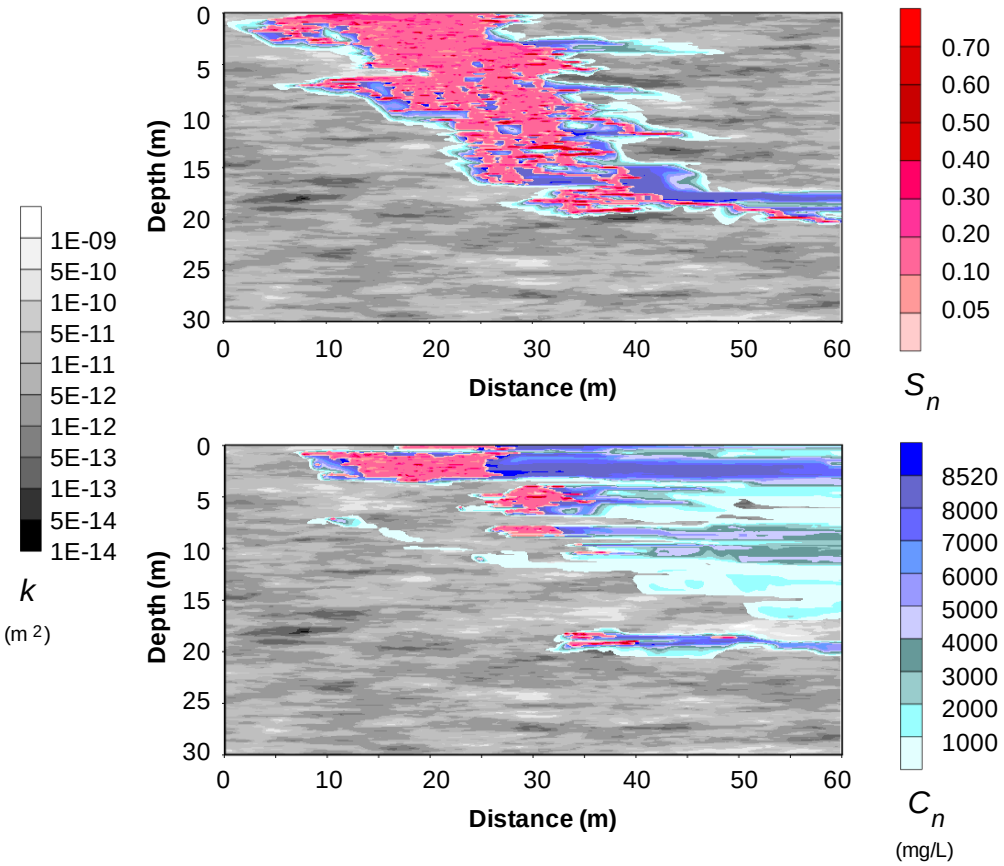

Figure 2-2: Numerical simulation of a DNAPL source zone undergoing mass removal via natural groundwater dissolution (modified from Grant, 2005): (a) initial DNAPL source zone with ~0% DNAPL mass removed, and (b) DNAPL source zone after 77% DNAPL mass removal. DNAPL saturations shown in pink-to-red scale (minimum saturation = 0.01) and dissolved phase concentrations shown in light-to-dark blue scale (minimum concentration = 100 mg/L).

Other studies have linked reactive transport models to multiphase flow models to investigate DNAPL remediation processes. The MISER model (e.g., Abriola et al., 1997) is a reactive transport model that has been linked to the two-phase immiscible flow model M-VALOR (Abriola et al., 1992) to simulate soil vapour extraction, bioventing and surfactant flushing at both the laboratory and field scale (e.g., Dekker and Abriola, 2000; Rathfelder et al., 2000, 2001). Christ and Abriola (2006) adapted the MISER model to simulate dissolution enhancement due to metabolic reductive dechlorination in field scale DNAPL source zones.

2.2 DNAPL Source Zone Characterization

2.2.1 Introduction

A review of the literature in the previous section has shown that the migration of DNAPL is a very complex multiphase flow process resulting in a heterogeneous distribution of DNAPL in the subsurface. This presents a significant challenge for effective characterization of DNAPL source zones which is an essential component for successful remediation of contaminated sites. Subsurface information, both initially and over time, is required to inform site conceptual models and the subsequent design, monitoring and performance assessment of remedial strategies (Kavanaugh et al., 2003; NRC, 2005). A variety of invasive and non-invasive techniques have demonstrated potential for successful characterization and monitoring of DNAPL source zones and numerous studies present and compare the different techniques (e.g., Kram et al., 2001, 2002; NRC, 2005).

2.2.2 Invasive Techniques

Traditionally, DNAPL site characterization and monitoring has relied on a sparse network of intrusive sampling points consisting of test pits, direct push sampling, coring and monitoring wells (e.g., Griffin and Watson, 2002; NRC, 2005). Coring technologies, such as rotasonic drilling, provide large diameter, relatively undisturbed cores of soil for characterization. Methods to characterize the soil cores above ground include hydrophobic dye shake testing, ultraviolet (UV) fluorescence, and chemical analyses. Down-hole methods, such as cone penetrometer technology (CPT) and laser induced fluorescence (LIF), can be used to provide real-time characterization of stratigraphy and fluorescent contamination. Groundwater quality profiling, using direct push technology or multi-level wells, measures the downgradient dissolved concentrations to ‘backtrack’ and locate the DNAPL source zone. Although these techniques have been widely implemented at contaminated sites, a number of limitations exist; these techniques are costly, time-consuming and suffer from low sampling density, relying on data from a limited number of locations, sometimes widely spaced, with the spatial distribution of DNAPL interpolated between the sample points (Chambers et al., 2010).

2.2.3 Non-Invasive Techniques

For a considerable time, geophysical techniques have been touted for characterizing and monitoring DNAPLs source zones. These non-invasive techniques have the advantage of producing spatially continuous information on subsurface variability that leads to potentially more complete site characterization (e.g., Brewster et al., 1995). The geophysical properties of DNAPLs, including electric, dielectric and acoustic, are generally distinct from the surrounding groundwater in the subsurface (Ajo-Franklin et al., 2006). Generally, DNAPLs are much more electrically resistive than groundwater (Lucius et al., 1992), exhibit low dielectric permittivities (2.2 to 10.9) relative to water (81) and low P-wave velocities (938 to 1217 m/s) relative to water (1480 m/s) (Ajo-Franklin et al., 2006). Therefore, the presence of DNAPL in the pore space should theoretically provide a geophysical target amenable to detection.

Over the years, a number of geophysical techniques have been proposed for the detection and monitoring of DNAPL distribution in the subsurface, including ground penetrating radar (GPR) (e.g., Brewster and Annan, 1994), seismic reflection (e.g., Temples et al., 2001), ERT (e.g., Newmark et al., 1998), induced polarization (IP) (e.g., Olhoeft, 1985) and self-potential (SP) (e.g., Minsley et al., 2007). Despite significant potential, geophysical techniques have not become commonly used tools at DNAPL sites, due, in part, to the highly heterogeneous nature of contaminated sites, the complexity of a typical DNAPL distribution and the limited understanding of the relationship between hydrogeological and geophysical properties.

In recent years, however, hydrogeophysics has become a rich field of research and significant advancements have occurred in many techniques. In particular, geoelectrical methods have become increasingly popular in environmental and hydrogeological applications (e.g., Slater and Lesmes, 2002; Binley and Kemna, 2005; Revil et al., 2012; Loke et al., 2013). Geoelectrical methods such as ERT, IP and GPR obtain measurements of subsurface electrical characteristics, including electrical resistivity, electrochemical activity and dielectric permittivity. These methods have been used across a wide range of hydrogeological investigations, including the mapping of moisture content (Zhou et al., 2001; Turesson, 2006), groundwater quality (Ogilvy et al., 2009), salt tracer transport

(e.g., Slater et al., 2000), distribution of injected amendment fluids (e.g., Lane et al., 2006), and changes associated with contaminant biodegradation (e.g., Atekwana et al., 2005; Sogade et al., 2006; Flores Orozco et al., 2011). More recently, geoelectrical monitoring has significantly developed and is now a strongly emerging branch in applied geophysics (Supper et al., 2014a).

2.3 Electrical Resistivity Tomography

2.3.1 Introduction

Electrical resistivity tomography (ERT) is one of the oldest and most commonly used geophysical methods and measures the variation of electrical resistivity in the subsurface (Dahlin, 2001). The ERT technique has evolved significantly from its basic form as 1D electrical prospecting method that was used to map vertical or horizontal layers or anomalies in the subsurface (e.g., Slichter, 1933). Over the past two decades, coupled with the significant advancements in computers, there have been revolutionary improvements in ERT and it is now one of the most widely researched and applied techniques in geophysics (e.g., Revil et al., 2012; Loke et al., 2013). This section examines the basic principles of ERT, data acquisition and processing and the use of ERT in hydrogeological and DNAPL applications.

2.3.2 Principles of ERT

2.3.2.1 Basic resistivity theory

The fundamental physical law used in resistivity surveys is Ohm's law that governs the flow of electrical current in the earth. The equation for Ohm's law in vector form for current flow in a continuous medium is given by (Tsourlos, 1995):

$$J_c = \sigma E, \tag{2-20}$$

where σ is the electrical conductivity of the medium, J_c is the current density and E is the electric field intensity. In practice, what is measured is the electric field potential Φ. The relationship between the electric potential and the field intensity is given by:

$$E = -\nabla\Phi \tag{2-21}$$

Combining Equations 2-20 and 2-21, we get:

$$J_c = -\sigma\nabla\Phi \tag{2-22}$$

In almost all surveys, the current sources are in the form of point sources. In this case, over an elemental volume ∇V surrounding a current source I_c located at (x_s, y_s, z_s), the relationship between the current density and the current is given by (Dey and Morrison, 1979):

$$\nabla J_c = \left(\frac{I}{\nabla V}\right)\delta(x-x_s)\delta(y-y_s)\delta(z-z_s)\,, \tag{2-23}$$

where δ is the Dirac delta function. Equation 2-23 can then be rewritten as:

$$-\nabla\bullet\left[\sigma(x,y,z)\nabla\Phi(x,y,z)\right] = \left(\frac{I}{\nabla V}\right)\delta(x-x_s)\delta(y-y_s)\delta(z-z_s) \tag{2-24}$$

This partial differential equation gives the subsurface potential distribution in an isotropic, non-uniform 3D medium due to a point current source. Numerous techniques have been developed to solve this equation. This is the 'forward' modelling problem which determines the potential that would be observed over a given subsurface structure, and is incorporated in both forward models and inversion algorithms as discussed in Sections 2.3.2.5 and 2.3.2.7.

2.3.2.2 ERT data acquisition

The ERT method employs an artificial source of current injected into the subsurface through point electrodes and the resulting potential difference is measured at other electrode positions in the vicinity of the current flow. Figure 2-3 illustrates a single point source of current on the surface of a semi-infinite conducting layer of uniform resistivity (i.e., a homogeneous and isotropic medium).

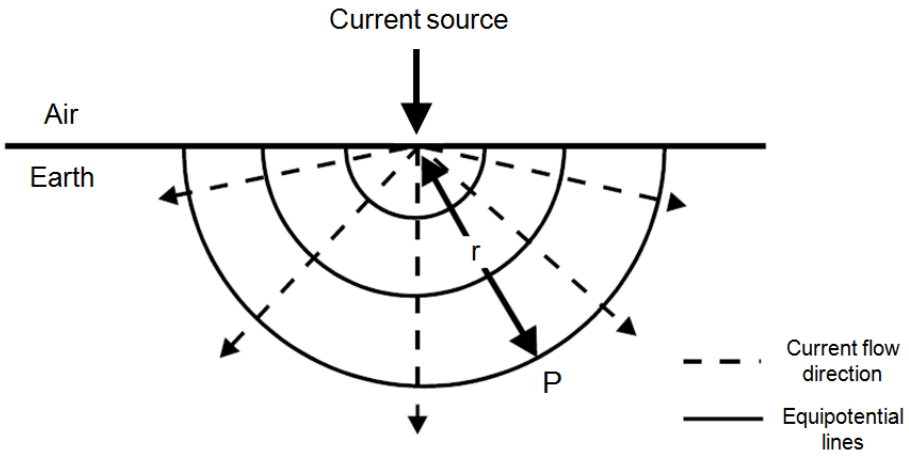

Figure 2-3: Current from a point source and the resulting equipotential surfaces

The current I_c injected from the point source will flow radially outwards and its distribution will be uniform over a hemispherical shell of resistivity ρ. At a distance r from the point source, the surface area of the hemispherical shell is $2\pi r^2$ so that the potential at the point P for the homogeneous half space is given by (Tsourlos, 1995):

$$\Phi_P = \frac{\rho I_c}{2\pi r} \tag{2-25}$$

In practice, two current electrodes are normally used. One of the electrodes (A) is positive and sends current into the ground (source) while the other electrode (B) is negative and collects the returning current (sink), as illustrated in Figure 2-4.

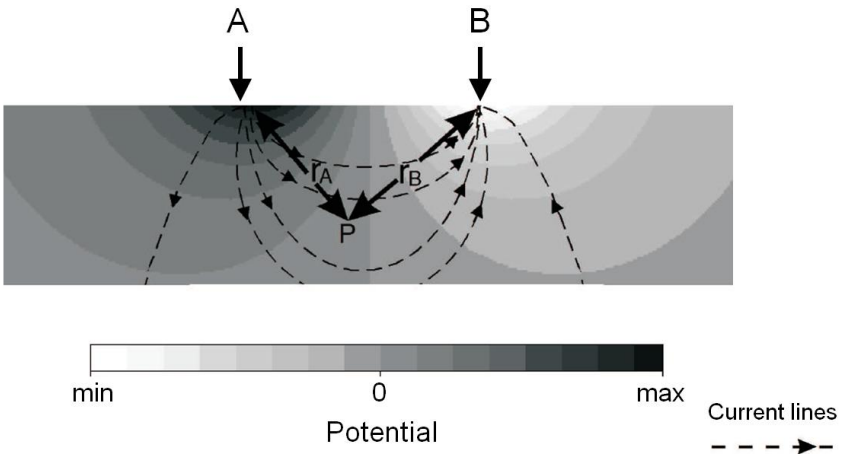

Figure 2-4: The equipotential surfaces and the current lines for two point source electrodes

The potential at a point P, which is at a distance r_A and r_B from A and B, respectively, is measured as:

$$\Phi_P = \frac{\rho I_c}{2\pi}\left(\frac{1}{r_A} - \frac{1}{r_B}\right) \tag{2-26}$$

ERT surveys determine the spatial variation of electrical resistivity through four-electrode measurements. The two current electrodes, A and B, inject constant electrical current I_c into the subsurface, while two potential electrodes, M and N, measure the difference in the resulting voltage Φ. Figure 2-5 illustrates a four-electrode station with current electrodes A,B and potential electrodes M,N over a homogeneous, isotropic medium with resistivity ρ. The potential at M and N can be determined using Equation 2-26 as follows:

$$\Phi_M = \frac{\rho I_c}{2\pi}\left(\frac{1}{AM} - \frac{1}{BM}\right) \tag{2-27}$$

$$\Phi_N = \frac{\rho I_c}{2\pi}\left(\frac{1}{AN} - \frac{1}{BN}\right) \tag{2-28}$$

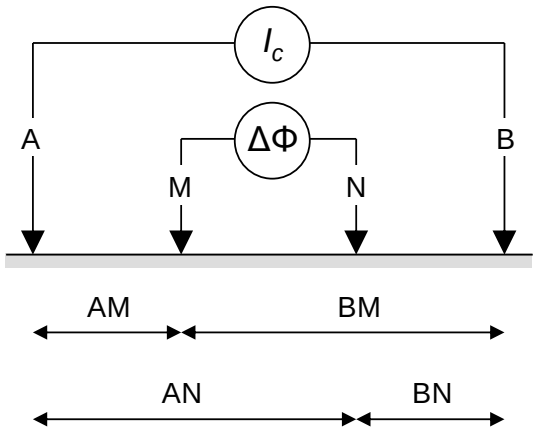

Figure 2-5: Illustration of a four-electrode station containing current and potential electrodes

Therefore, the potential difference is given by:

$$\Delta\Phi = \Phi_M - \Phi_N = \frac{\rho I_c}{2\pi}\left(\frac{1}{AM} - \frac{1}{BM} - \frac{1}{AN} + \frac{1}{BN}\right) \tag{2-29}$$

This equation gives the potential that would be observed over a homogeneous half space with a typical four-electrode configuration. The subsurface is typically heterogeneous so that the resistivity observed is 'apparent'. The apparent resistivity is only the true resistivity of the subsurface when it consists of a completely homogeneous and isotropic medium. Apparent resistivity can be seen as a weighted average of the resistivities of the subsurface volume. The apparent resistivity depends on the configuration of the electrodes and is determined as follows:

$$\rho_a = G_f \frac{\Delta\Phi}{I_c}, \tag{2-30}$$

where G_f is the geometrical factor that depends on the configuration of the current and potential electrodes, and is given by:

$$G_f = 2\pi \Big/ \left(\frac{1}{AM} - \frac{1}{BM} - \frac{1}{AN} + \frac{1}{BN} \right) \tag{2-31}$$

A large number of electrode configurations exist (e.g., Dahlin and Zhou, 2004) and these are discussed in more detail in Section 2.3.2.3. This four-electrode approach to resistivity surveys, historically used for 1D vertical electrical sounding and lateral profiling, remains the basis for the 2D and 3D surveys employed today.

Previously, one of the inherent limitations of ERT was the time-consuming and laborious task of acquiring these four-electrode measurements along a survey line. Over the years, significant improvements in field instrumentation have occurred ranging from an initial multi-electrode system with manual switching (e.g., Barker, 1981) to the fast automated multi-channel systems now commonly used (e.g., Stummer et al., 2004; Ogilvy et al., 2009). ERT surveys are now being carried out in a range of challenging environments from under-water (e.g., Day-Lewis et al., 2006; Mansoor and Slater, 2007) to active landslides (e.g., Supper et al., 2014b).

To obtain 2D apparent resistivity measurements, electrodes are placed along a survey line using a range of different electrode separations and midpoints defined by the survey configuration. The resistivity of the 2D model is assumed to vary both vertically and laterally along the survey line but constant in the direction perpendicular to the survey line (e.g., Oldenburg and Li, 1999). However, all geological structures and spatial distribution of subsurface electrical properties are inherently 3D in nature. The 3D effects of subsurface structures are more pronounced in hydrogeological investigations where the geology is highly heterogeneous and 2D surveys conducted in these environments can lead to misinterpretation of the recorded data (e.g., Bentley and Gharibi, 2004). Hence a 3D survey gives the most accurate and reliable results (e.g., Papadopoulos et al., 2007).

A 3D survey can be conducted in various forms. To obtain a complete 3D data set, the measurements should ideally be made in all possible directions (Loke and Barker, 1996). The electrodes are placed in square and rectangular grids and each time current is injected, potential can be measured at all remaining electrodes (e.g., Chambers et al.,

1999) or only those electrodes at 45-degrees from the current electrode (e.g., Loke and Barker, 1996). Although required to obtain an ideal 3D data set, these methods are usually impractical, time-consuming and cumbersome. The most commonly used and practical method to obtain 3D data involves collecting data along sets of parallel and/or orthogonal 2D lines (e.g., Bentley and Gharibi, 2004). This method allows more flexible survey design and choice of electrode arrays which were first developed for 2D surveying. The resulting 3D data set can be processed with 2D inversion of each individual 2D survey line which is then compiled into an inverted 'quasi-3D' data set or the complete set of 2D lines can be inverted with 3D inversion. When full 3D inversion algorithms are used to invert a number of parallel 2D lines, Papadopoulos et al. (2007) demonstrated that only parallel lines in either the *x*- or *y*-direction are required to correctly resolve the 3D nature of subsurface targets, whereas both parallel and orthogonal lines (both *x*- and *y*-directions) are required when using quasi-3D inversion.

Time-lapse ERT surveys have become increasingly popular in recent years and can consist of mobile, semi-permanent or permanent electrodes with periodic measurements acquired over time (e.g., Ogilvy et al., 2009). Time-lapse ERT surveys have been applied across a wide range of environments and have recently been successfully applied to monitor processes in challenging transient natural systems such as active landslides (e.g., Supper et al., 2014b). One significant challenge in these environments is the possible movement of electrodes during monitoring and studies have investigated techniques to compensate for potential errors (e.g., Wilkinson et al., 2010). In addition, a number of time-lapse inversion algorithms have recently been developed to provide improved time-lapse images (e.g., Kim et al., 2009; Karaoulis et al., 2011a; Loke et al., 2014). These are discussed in more detail in Section 2.3.2.7.

2.3.2.3 Electrode configurations

ERT surveys are normally identified according to the arrangement of the current and potential electrodes, with the most commonly used arrays including Wenner, Schlumberger, dipole-dipole and pole-dipole arrays (Loke, 2013). The main

characteristic of an electrode array is its geometrical factor which is related to the systematic arrangement and spacing of the electrodes (see Equation 2-31). Each electrode array has different attributes including sensitivity to vertical and lateral variations in subsurface resistivity, depth of investigation and signal strength. Therefore, different arrays are more suitable for different investigations with the choice of a particular array dependent on the geometry and location of the desired target, required resolution and allowable survey time (e.g., Dahlin and Zhou, 2004; Loke, 2013). A number of studies have investigated the effectiveness of different arrays to delineate various targets of interest. Bing and Greenhalgh (2000) investigated the effectiveness of different electrode configurations for cross-hole ERT surveys examining two targets of interest: a dipping conductive strip and a dislocated fault. Dahlin and Zhou (2004) conducted a comprehensive numerical investigation to evaluate the performance of ten different electrode arrays on five different subsurface targets.

In addition to the standard electrode arrays, many studies have investigated non-conventional electrode arrays to optimize the subsurface resistivity information recorded (e.g., Stummer et al., 2004; Wilkinson et al., 2006; Nenna et al., 2011). Comprehensive data sets containing all possible combinations of four-electrode configurations (including every possible conventional and non-conventional array) can be generated to provide increased subsurface information (e.g., Stummer et al., 2004). Due to the large number of measurements and corresponding survey time of comprehensive arrays, subsequent studies utilized optimization procedures to generate smaller, optimal arrays (e.g., Wilkinson et al., 2006; Furman et al., 2007; Athanasiou et al., 2007). The optimization procedure incorporates electrode configurations exhibiting high sensitivities and depth of influence into a successively increasing optimal data set (e.g., Wilkinson et al., 2006). Optimization of electrode arrays deployed for time-lapse monitoring have also been developed which optimize the electrode array sequentially through the monitoring period (e.g., Wilkinson et al., 2013).

2.3.2.4 Borehole ERT

ERT surveys are also characterized by the deployment of the electrodes. Surface ERT, with electrodes deployed along the surface, is minimally invasive and provides relatively fast and large spatial coverage. However, the resolution of surface ERT generally decreases with depth. To overcome this depth limitation and provide higher resolution in regions of interest, ERT electrodes have often been deployed in boreholes in closer proximity to the desired target. The placement of electrodes in boreholes presents several possible configurations, including borehole-to-borehole – also known as cross-hole (e.g., Daily and Owen, 1991; Slater et al., 2000) and surface-to-borehole (e.g., Dhu and Heinson, 2004; Tsourlos et al., 2011). While borehole ERT provides superior depth resolution and imaging, it is more expensive and more difficult to achieve large spatial coverage due to the constraint on borehole spacing: borehole depth / borehole spacing ≈ 1.5; so, for example, a survey relying on 6 m deep boreholes would need to be placed with a maximum separation of 4 m.

In recent years, electrodes have been placed in tunnels (i.e., tunnel-to-tunnel) to image geological conditions in advance of tunnel boring (Danielsen and Dahlin, 2010) and mining (van Schoor and Binley, 2010). Simyrdanis (2013) examined the applicability of surface-to-tunnel ERT for imaging subsurface targets. Various aspects of this ERT arrangement were discussed and explored by means of numerical simulation and experimental tests on various targets with simple geometries. For example, various geometrical shapes with contrasting resistivities were simulated, while various metal and plastic targets (e.g., plastic pipes and metal plates) were placed in a water-filled experimental tank. Although surface-to-tunnel ERT shares many similarities with cross-hole ERT, the major difference relates to the fact that measurements associated with surface electrodes exhibit different sensitivities compared to measurements involving tunnel electrodes. Simyrdanis (2013) examined a number of electrode arrays and proposed a geometrical factor threshold to ensure viable arrays with sufficient signal-to-noise ratios. Simyrdanis (2013) also examined the vertical distance between surface and tunnel electrodes which strongly influences the resolving ability in the areas between the arrays. After a number of tests using synthetic data, an optimum ratio (separation

distance / electrode spacing) of 7/1 was recommended for resistive targets. Simyrdanis (2013) also demonstrated that the tunnel itself can affect the measurements since it is a subsurface 'object' with infinite resistance, and solutions to compensate for this tunnel effect were proposed.

2.3.2.5 Forward modelling

It is possible to mathematically predict the theoretical outcome (i.e., apparent resistivity) of a set of measurements from ERT surveys on a subsurface distribution of electrical resistivity. Forward modelling seeks to find a solution of the differential equation presented in Equation 2-24. There are several methods available to solve the forward problem, including analytical, boundary element, finite-difference and finite-element methods (Loke et al., 2013). The analytical and boundary element methods are more accurate and flexible but are restricted to relatively simple geometries. The finite-difference and finite-element methods are the most viable methods as they permit modelling of large, complex and arbitrary subsurface resistivity distributions (Tsourlos, 1995). The subsurface is subdivided into a large mesh of individual cells, each with a constant, user-specified resistivity and then the potential difference is calculated at nodes of the mesh (Dey and Morrison, 1979). Li and Spitzer (2002) evaluated the performance of both methods for the resistivity forward problem. In general, the finite-element method is preferred and widely used in a number of forward modelling schemes (e.g., Tsourlos and Ogilvy, 1999; Rücker et al., 2006; Karaoulis et al., 2013).

In addition to being an integral part of the inversion process (i.e., calculates the theoretical apparent resistivity values for the models predicted by the inversion), forward modelling has found many applications including the design of field surveys and testing of new inversion algorithms (e.g., Goes and Meekes, 2004; Karaoulis et al., 2014a). As discussed in Section 2.3.2.3, different electrode arrays produce different resistivity results and forward modelling has been used to evaluate various electrode arrays for imaging different subsurface resistivity distributions (e.g., Bing and Greenhalgh, 2000; Dahlin and Zhou, 2004; Simyrdanis et al., 2012). Forward modelling has also been used to evaluate

the effectiveness of 2D and 3D inversion algorithms on ERT data from 3D subsurface structures (e.g., Tsourlos, 2005; Papadopoulos et al., 2007). Karaoulis et al. (2011a; 2014a) and Kim et al. (2013) used synthetic examples and forward modelling to evaluate the performance of newly developed four-dimensional (4D) inversion algorithms.

2.3.2.6 Noise considerations

Some of the major sources in an ERT survey are related to the contact resistance between the electrodes and subsurface, measurements errors, and background/cultural noise (Slater et al., 2000). While noise can never be fully eliminated, techniques such as stacking and reciprocal measurements can minimize and/or quantify the noise. For example, obtaining reciprocal measurements, which involves switching the source and receiver electrode pair in an electrode array, provides a measure of data precision and estimates of standard deviations (Miller et al., 2008). Understanding the noise in the recorded ERT data is crucial for data inversion, and ultimately determines how well we resolve the subsurface structure. Noise results in artifacts in the inverted resistivity model, which is especially problematic at sites with low signal-to-noise ratio, where the inversion artifacts may overwhelm the targets sought. It should be noted that even noise-free data may also produce some inversion artifacts due to numerical errors and constraints (e.g., smoothness) in the inversion.

It is common for numerical modeling studies that simulate ERT surveys to add Gaussian noise to the recorded ERT data to mimic realistic scenarios (e.g., Miller et al., 2008; Karaoulis et al., 2011a; Karaoulis et al., 2014a).

2.3.2.7 Inversion

Inversion is required to invert the apparent electrical values obtained during ERT surveys to obtain the distribution of true electrical properties. Inversion is a very rich field of research and inversion schemes are being continuously improved and developed,

resulting in more accurate and valuable results from electrical measurements. A large number of different inversion codes have been developed and can be applied to the various survey approaches, including 2D and 3D surveys (e.g., Loke and Barker, 1996; Tsourlos and Ogilvy, 1999) for surface and borehole data (e.g., LaBrecque et al., 1996) in static and time-lapse modes (e.g., Karaoulis et al., 2013).

The inverse problem involves determining the subsurface resistivity distribution (model) that explains the set of apparent electrical measurements (recorded survey data) to an acceptable degree (i.e., minimize the difference between measured and calculated values). The widely used L_2-norm inversion scheme involves minimizing the L_2-norm of the following objective function, S:

$$S = \Phi_d + \lambda \Phi_m = \left\| D - G(X) \right\|^2 + \lambda^2 \left\| C\, X \right\|^2, \tag{2-32}$$

where Φ_d denotes the data misfit vector, Φ_m is a regularization function, λ is the Lagrangian multiplier used for controlling this regularization term, X denotes the subsurface model sought from the inversion procedure (i.e., distribution of bulk resistivity that best fits the ERT data), D denotes the recorded ERT data, G is the forward operator, and C is the spatial second-derivative operator. The first term of the right-hand side of Equation (2-32) ensures the convergence of the inverted model generated with respect to the recorded data. The second term is introduced to stabilize the inversion algorithm and produce smooth inverted models that satisfy the data (Constable et al., 1987). The solution to the minimization of this objective function can be found using, for instance, an iterative Gauss-Newton algorithm, which yields the following iterative normal equation:

$$X_{l+1} = X_l + dX = X_l + (J^T J + \lambda C^T C)^{-1} J^T (D - G(X)), \tag{2-33}$$

where l denotes the iteration number, dX denotes the perturbation to the updated model, and J is the Jacobian or sensitivity matrix (i.e., derivatives of the recorded data with respect to changes in the model parameters).

As mentioned, inversion is a very active and rich field of research, with a number of approaches being continuously developed to improve ERT inversion. Hydrogeological or geophysical information can be incorporated into ERT inversion to provide improved imaging (e.g., Miller et al., 2012; Karaoulis et al., 2012; 2014a). Doetsch et al. (2012a) incorporate structural information obtained from GPR data to constrain and improve the inverted ERT images to better characterize mineral deposits. Zhou et al. (2014) similarly incorporate high resolution GPR data to generate an image guide to provide significantly improved ERT imaging. ERT has also been jointly inverted with seismic (e.g., Karaoulis et al., 2012) and hydrogeological data (e.g., Miller et al., 2012).

ERT used in time-lapse mode has developed into one of the most widely applied branches in geophysics today, and a large number of inversion schemes and approaches have been used. The independent inversion approach has been used in time-lapse monitoring where ERT data is collected over time. This traditional approach involves independently recording ERT data at each monitoring step is independently inverted and differential time-lapse images are reconstructed (e.g., Tsourlos et al., 2003). However, as suggested by several researchers, independent time-lapse inversion images may be strongly contaminated with inversion artifacts due to measurement and independent inversion errors (e.g., Kim et al., 2009).

In an attempt to minimize those artifacts, LaBrecque and Yang (2001) presented the difference inversion algorithm where time-lapse resistivity data are processed by inverting for the differences between the background and subsequent data sets (e.g., Miller et al., 2008; de Franco et al., 2009). The resistivity obtained by the inversion of background data serves as the a priori model in the difference inversion. This provides a good initial guess, thereby making convergence faster. Also, systematic errors, such as those due to errors in field configuration and discretization errors in the forward modelling algorithm tend to cancel (LaBrecque and Yang, 2001).

In recent years, significant and ongoing research is being conducted in the area of 4D time-lapse inversion algorithms (e.g., Kim et al., 2009; Karaoulis et al., 2014a; Loke et al., 2014). In these approaches, the subsurface model and the entire monitoring dataset are defined in a space-time domain; monitoring datasets recorded at different times are simultaneously inverted. Regularizations are introduced in both space and time domains which stabilize the inversion and effectively reduce inversion artifacts evident in independent inversion (Kim et al., 2009) while demonstrating improved sensitivity in regions of resistivity changes (Karaoulis et al., 2011a). Inversion artifacts are false resistivity anomalies generated due to the presence of noise in the ERT measurements; these false signals can masks changes of interest or suggest subsurface changes happened where none actually occurred.

The 4D inverted subsurface model X for all monitoring steps is expressed as $X = \left[X_1, ..., X_t\right]^T$, where X_i is the inverted model for the *i*th monitoring step and *t* is the number of monitoring steps. The entire monitoring data are defined as a data vector $D = \left[D_1, ..., D_t\right]^T$, where D_i are the data from the *i*th monitoring step. The objective function S to be minimized by the inversion process can be expressed as follows (Kim et al., 2009):

$$S = \Phi_d + \lambda \Phi_m + \alpha \Phi_t \tag{2-34}$$

where Φ_m and Φ_t are the two regularization functions. The function Φ_m is used to perform the regularization in space using smoothness (second-order derivative) as a regularizer, while the function Φ_t is used to perform the regularization in time using flatness (first-order derivative) as a regularizer. The parameter λ is the Lagrangian multiplier for controlling the regularization in space, while α is the Lagrangian multiplier for controlling the regularization in time. Minimizing the objective function (2-34) with respect to the model perturbation vector $dX = \left[dX_1, ..., dX_t\right]^T$ yields the following normal equation (Karaoulis et al., 2011a):

$$X^{l+1} = X^{l} + dX = X^{l} + (J^{T} J + C^{T} \Lambda C + M^{T} A M)^{-1} \cdot (J^{T} [D - G(X^{l})] - M^{T} A M X^{l}), \quad (2\text{-}35)$$

where J denotes the Jacobian matrix given by $J = diag[J_1, ..., J_t]$, C is the differential operator in the space domain given by $C = diag[C_1, ..., C_t]$, Λ is the space-domain Lagrangian given by $\Lambda = diag[\Lambda_1, ..., \Lambda_t]$, M is the temporal second-derivative operator which takes the form of a square matrix with one non-zero diagonal and one non-zero sub-diagonal, and A is the time-domain Lagrangian given by $A = diag[A_1, ..., A_t]$. The space-domain Lagrangian can be expressed as either a constant value λ ($\Lambda = \lambda I$) or as a variable diagonal matrix Λ that can be optimized with several schemes such as active constraint balancing (ACB) (Yi et al., 2003). In terms of the time-domain Lagrangian, it can also be expressed as either a constant value α ($A = \alpha I$) (Kim et al., 2009) or as a variable diagonal matrix A (Karaoulis et al., 2011a). Using the 4D active time constraint (4D-ATC) method introduced by Karaoulis et al. (2011a), the time Lagrangian varies between different monitoring steps proportionally to the expected degree of spatial resistivity changes occurring (i.e., areas of significant changes are assigned low time regularization values and vice versa). One method proposed by Karaoulis et al., (2011a) to pre-estimate regions of change and assign appropriate time Lagrangian values is based on a preliminary analysis of the data through differential imaging of initial independent inversion; this is the method used in this work. Other methods of pre-estimation are possible, for example using only a priori information such as hydrogeological data or expected remediation patterns. With the appropriate time Lagrangian, the 4D-ATC algorithm was then applied to the entire dataset recorded from all monitoring steps with focus now on the spatial and temporal changes of resistivity. The application and benefits of this algorithm have been demonstrated on a number of synthetic and field data sets, including salt tracer migration, water injection and contamination scenarios (e.g., Karaoulis et al., 2011a,b; 2014a).

The 4D-ATC approach has also been applied to other geophysical techniques including jointly inverted seismic-ERT (Karaoulis et al., 2012), complex conductivity (Karaoulis et

al., 2011b) and gravity (Karaoulis et al., 2014b). To address the problem related to the lack of sensitivity of ERT with depth which may overlook changes at depth, Karaoulis et al. (2014a) extended the active Lagrangian distribution to the spatial domain. The resulting active spatial constraint (4D-ASC) and combined active spatial temporal constraint (4D-ATSC) algorithms demonstrate significant promise for improved resolution of subsurface changes at depth. Additional inversion approaches for time-lapse inversion are continuously been developed, including 4D algorithms with L_1-norm minimization that may help overcome problems with too smoothly varying and diminished model changes (e.g., Kim et al., 2013), and simultaneous inversion of 3D ERT monitoring data (e.g., Hayley et al., 2011; Loke et al., 2014).

2.3.3 Hydrogeological Investigations with ERT

Electrical resistivity tomography (ERT) is now one of the most widely used techniques in hydrogeophysics, owing largely to the recent advancements previously discussed. The close relation between electrical resistivity and hydrogeological parameters such as porosity, saturation and groundwater chemistry, has led to the increased use of ERT for geological and hydrogeological investigations (Loke et al., 2013).

ERT has found wide application in investigating and characterizing unconsolidated saturated sediments (e.g., Froese et al., 2005), with the major lithological effect on resistivity in these types of sediments being the proportion and type of clay minerals. ERT has also been used to study moisture content (Zhou et al., 2001) and groundwater quality (Ogilvy et al., 2009). Zhou et al. (2001) integrated soil sample analysis and ERT to monitor 3D variations of soil water content. Archie's law was used to calculate the 3D distribution of soil water content from the bulk electrical resistivity distribution. Ogilvy et al. (2009) developed an automated time-lapse ERT (ALERT) system for the long-term monitoring of hydrogeologic changes in subsurface aquifers (e.g., seawater intrusion, rising sea levels).

Over the years, ERT has become increasingly popular for monitoring a wide range of dynamic subsurface processes, including landfill leachate migration (Acworth and Jorstad, 2005; Clement et al., 2011), groundwater-surface water interaction (e.g., Cardenas and Markowski, 2010; Johnson et al., 2012), groundwater flow patterns (e.g., Coscia et al., 2012), salt-water intrusion (e.g., Nguyen et al., 2009), transport of saline tracers (e.g., Slater et al., 2002; Perri et al., 2012; Robert et al., 2012), recharge-induced contaminant plume behaviour (e.g., Gasperikova et al., 2012), temperature changes (Hayley et al., 2007), rising and falling water levels (Kuras et al., 2009), vadoze zone water movement (Daily et al., 1992), and contaminant degradation (e.g., Atekwana et al., 2005; Chambers et al., 2010).

2.3.4 DNAPL Investigations with ERT

Of particular interest is the utilization of ERT, either separately or in combination with other geophysical, hydrological, or geochemical techniques, to detect and monitor the spatial and temporal extent of DNAPL and the interactions between remedial processes and the contaminated environment. DNAPLs are typically highly resistive (Lucius et al., 1992) – for example, the resistivity of TCE is 1×10^6 ohm-m – so DNAPL displacement of conductive pore water with insulating DNAPLs results in an increase in resistivity.

ERT surveys have been conducted to obtain the spatial and temporal distribution of electrical properties for characterization and monitoring of DNAPL contamination scenarios. ERT has demonstrated limited success in delineating the distribution of existing DNAPL spills. This is due, in part, to the difficulty in interpreting data from real contaminated sites; DNAPL sites are often highly heterogeneous with a tortuous DNAPL distribution superimposed upon a heterogeneous soil matrix, thereby presenting a complex electrical target. The relatively few field studies conducted at existing contaminated sites demonstrate limited ERT performance for static detection of a DNAPL source zone (e.g., Goes and Meekes, 2004; Cardarelli and Di Filippo, 2009; Naudet et al., 2013). As a result, ERT has been more frequently applied in time-lapse mode for monitoring subsurface changes over time relating to DNAPL migration and

remediation (e.g., Newmark et al., 1998; Chambers et al., 2004) and DNAPL remediation processes (e.g., Daily and Ramirez, 1995; Chambers et al., 2010).

Chambers et al. (2004) used electrical resistivity measurements to monitor the migration of a fluorinated DNAPL through a saturated porous medium within a laboratory column. Differential time-lapse resistivity imaging clearly delineated resistive anomalies associated with the vertical migration and lateral spreading of the DNAPL. Daily and Ramirez (1995) used cross-hole ERT to image subsurface processes (i.e., air sparging and water infiltration) associated with in situ remediation efforts at a TCE contaminated site. Injection of an air-methane mixture increased the formation resistivity as the highly resistive mixture displaced the more conductive pore water, whereas infiltration of water decreased the formation resistivity by increasing the moisture content in the vadose zone. In both processes, the flow paths appeared to be confined to discrete channels defined by the local heterogeneity in the subsurface permeability. Therefore, the ERT images provided valuable information to indicate the nature of flow channeling in the vadose and saturated zones.

Newmark et al. (1998) monitored the removal of DNAPL (primarily TCE, but also containing PCE and methylene chloride) during pumping from the Hill Air Force Base in Utah. The aquifer is composed of interbedded silts, sands and gravels, and fibre optic sensors and neutron logs verified the lithology and presence of the free-product DNAPL pooled on a thick, laminated clay aquitard. Cross-hole ERT was implemented in monitoring boreholes, each containing 20 electrodes, to produce time-lapse images indicating decreasing electrical resistivities over time. This corresponded to the replacement of the highly insulating DNAPL with low resistive groundwater during pumping, with this interpretation being supported by fibre optic sensor results.

Chambers et al. (2010) used high-resolution cross-hole ERT to monitor a field scale bioremediation experiment to suggest that ERT can be an effective technique for monitoring chlorinated solvent degradation and groundwater chemistry changes associated with injected amendment fluids. ERT arrays were installed in closely spaced boreholes and designed to ensure high resolution resistivity images. Baseline ERT images combined with multi-level sampling data effectively detected subsurface

geological variability, while time-lapse ERT spatially and temporally imaged significant resistivity changes associated with the subsurface distribution of the injected biostimulation and pH control fluids, which indicated the presence of a major preferential pathway within the cell. In addition, resistivity signatures possibly resulting from biodegradation products were also detected. A number of LNAPL studies have demonstrated that ERT is a viable technique for monitoring resistivity changes associated with contaminant degradation (e.g., Sauck, 2000; Atekwana et al., 2005).

In addition to mapping subsurface changes induced by DNAPL remediation processes, ERT may be employed to directly monitor the long-term performance of in situ remediation technologies containing granular iron or zero valent metals (e.g., Slater and Binley, 2003, 2006). For example, PRBs are typically composed of highly conductive granular iron to degrade the contaminants. Slater and Binley (2003) demonstrated that cross-hole resistivity can accurately define the geometry of the barrier, which may permit effective long-term monitoring of PRB performance and provide an indirect measure of contaminant reduction.

2.4 Hydraulic-Electrical Relationships

2.4.1 Introduction

A key step in the quantitative interpretation of geophysical data is its conversion into desired hydrogeological parameters. With respect to ERT, a large number of petrophysical relationships have been empirically and theoretically developed to relate the bulk electrical resistivity to the electrical resistivities and volume fractions of the individual conducting phases (soil, water, air, NAPL), and some measure of their distribution or connectivity (e.g., Archie, 1942; Hanai, 1960,1961; Sen et al., 1981). A comprehensive review and evaluation of the theoretical and practical limitations of the petrophysical models used to derive electrical-hydrogeological predictive relationships is provided by Lesmes and Friedman (2005).

As discussed in Chapter 1, such relationships underpin the objectives of this thesis; for example, they are a key component in the development of a coupled DNAPL-ERT model (Chapter 3) and estimation of DNAPL saturation changes from ERT measurements (Chapter 4). This section will review the main petrophysical relationships available to equate them. It is noted that this section is described in terms of electrical conductivity (reciprocal of electrical resistivity), as is typical for studies in this field.

2.4.2 Key Properties

In general, the electrical conductivity of a partially saturated soil is a function of its porosity (ϕ), water saturation (S_w), the electrical conductivity of the pore water (σ_w), and the conductivity of the soil (σ_s) (Urish, 1981). In a non-conducting matrix (e.g., clean sand), the pore water is the only conducting phase making the pore water conductivity and water content ($\theta = \phi \cdot S_w$) the dominant factors affecting the bulk electrical conductivity.

2.4.3 Archie's Law

Archie (1942) developed an empirical relationship to relate the bulk material conductivity to pore fluid conductivity and fractional porosity. The empirical expression for the electrical conductivity of partially saturated rocks is given by:

$$\sigma_{bulk} = \phi^m \cdot S_w{}^n \cdot \sigma_w \ , \tag{2-36}$$

where σ_{bulk} is the bulk electrical conductivity of the fully saturated porous medium, m is the material-dependant empirical exponent related to cementation, and n is the saturation exponent. Archie's law was derived empirically for highly conductive saline solutions (20,000 to 100,000 mg of NaCl per litre) saturating clean, consolidated sandstones and unconsolidated sands, with porosities ranging from 0.1 to 0.4. Therefore, it implicitly

assumes that there is only one conducting phase, which is distributed in some manner within a non-conductive matrix (Archie, 1942).

The classical form of Archie's law is only valid strictly for one conductive phase occupying a non-conducting matrix (i.e., assumes negligible clay content). Numerous studies have been conducted over the years to account for contributions from surface-mediated conduction when clays are present in any significant volume (e.g., Waxman and Smits, 1968; Revil and Glover, 1997; Revil et al., 1998). Archie's law in Equation 2-36 has been modified to include a surface conduction term in parallel with the bulk conduction term resulting from the pore solution. The effects of lithology and solution chemistry on the surface conductivity were accounted for by Waxman and Smits (1968) in the following model:

$$\sigma_{bulk} = \phi^m \cdot S_w^{\,n} \left(\sigma_w + {B \cdot Q_v}/{S_w} \right), \tag{2-37}$$

where B is the equivalent ionic conductance of the clay exchange cations, and Q_v is the cation exchange capacity per unit pore volume which is a measure of the effective clay content. More sophisticated surface conductivity models have been developed in terms of the electrical double layer (EDL) that forms between the mineral grains and the bulk pore solution (e.g., Johnson et al., 1986; Revil and Glover, 1997). For example, surface complexation models can be used to predict the surface conductivity response as a function of geochemical parameters such as mineral surface charge density and effective surface ionic mobility, with these parameters vary with solution type, concentration and mineralogy (e.g., Revil and Glover, 1997; Revil et al., 1998).

In addition to the surface conductivity studies discussed, other studies have modified and extended Archie's law to be applicable for two conducting phases (e.g., Glover et al., 2000). More recently, Glover (2010) presented a generalized form of Archie's law for any number of phases; the law contains a phase conductivity, a phase volume fraction and phase exponent for each of its phases. The connectedness of each of the phases is

considered and a principle of conservation of connectedness in a 3D multiphase mixture is introduced (Glover, 2010).

Despite the empirical development of Archie's law, it has been derived from first principles using a differential effective medium approach in some special cases, such as for granular porous media (e.g., Sen et al., 1981). Archie's law is the most widely used equation in hydrogeological applications and has been used in a large number of studies to estimate desired hydrogeological properties from electrical resistivity distributions, including water content (e.g., Zhou et al., 2001) and salt tracer concentration (e.g., Slater et al., 2000; Doetsch et al., 2012b). Some underestimation does exist which is related to the limited utility and accuracy of Archie's law for providing quantitative estimates of hydraulic parameters from the spatially variable resolution of the inverted resistivity tomograms. Some work has investigated improved petrophysical relationships that compensate for spatially variable resolution and the inversion approach used (e.g., Day-Lewis et al., 2005; Singha and Gorelick, 2006a,b).

2.4.4 Effective Medium Models

A rigorous and widely used theoretical approach to modelling the conductive response of a material is the use of effective medium theory (e.g., Bruggeman, 1935; Hanai, 1960,1961). A comprehensive review of effective medium theory is presented by Cosenza et al. (2009). Bruggeman (1935) and Hanai (1960,1961) developed an equation that relates the electrical properties of a heterogeneous mixture to the properties of the individual components. The Hanai-Bruggeman (HB) equation for complex conductivity of a two-component mixture of matrix and water is given by (Bussian, 1983):

$$\phi = \left(\frac{\sigma_w^*}{\sigma_o^*} \right)^{\frac{(m-1)}{m}} \cdot \left(\frac{\sigma_o^* - \sigma_m^*}{\sigma_w^* - \sigma_m^*} \right), \tag{2-38}$$

where σ_w^* is the complex water (continuous phase) conductivity, σ_o^* is the complex mixture conductivity, σ_m^* is the complex matrix (disperse phase) conductivity. The frequency dependence of the conductivities used in Equation (2-38) can be stated as (Bussian, 1983):

$$\sigma^* = \sigma + i\omega\varepsilon_o K, \tag{2-39}$$

where σ^* is the complex conductivity, σ is the real conductivity, $i = \sqrt{-1}$, ω is the angular frequency, ε_o is the permittivity of free space and K is the dielectric constant. At the low frequencies employed by ERT, the imaginary term of Equation (2-39) is insignificant and the real conductivity can be used. Therefore the HB equation at low-frequencies can be rewritten as:

$$\sigma_b = \sigma_w \cdot S^n \cdot \phi^m \cdot \left(\frac{1 - \sigma_m / \sigma_w}{1 - \sigma_m / \sigma_b} \right)^m \tag{2-40}$$

When the matrix phase conductivity is negligible ($\sigma_m = 0$), the HB equation collapses to Archie's law. Conversely, with a non-zero σ_m, the HB equation can accommodate the mixture of both fluid and grain surface conduction in clayey soils, with the σ_m term representing both the dry mineral grain and surface conductivity effects. The HB equation has been used in a number of approaches to study the conductivity of soils and rocks with the matrix conductivity attributed to laminated and/or dispersed clay (e.g., Bussian, 1983; de Lima and Sharma, 1990; Berg, 1995, 2007).

Bussian (1983) used an approximation of the HB equation to develop a semi-empirical saturation model; the model demonstrated the suitability of the HB equation for the study of conductivity in rocks at low frequencies but the HB equation was approximated for a limited range of conditions, such as high water salinities. Revil et al. (1998) used the

model by Bussian (1983) to account, in a more sophisticated way, for the surface conductivity through the matrix conductivity term in Equation 2-40. Another way of mixing matrix elements is to formulate a relationship to calculate composite grain conductivity and then substitute that grain conductivity along with the fluid conductivity into the HB equation (e.g., de Lima and Sharma, 1990; Berg, 1995). de Lima and Sharma (1990) used a first-principle approach, where the derivation is based on the theory upon which the HB equation is based, to develop a model for adding clay and sand grains in small, but proportional amounts; however, it limits the cementation and saturation exponents for each component to a value of 1.5. Berg (1995) assumed that the disperse phase component of the HB equation can be calculated by a volumetric weighted average (resistors in parallel). The composite matrix (sand and clay) grains and hydrocarbons are both associated with the disperse phase, while the continuous phase includes only the formation water. This equation was successfully proven to work on experimental data under a wide range of frequencies and water conductivities and compared favourably with various petrophysical models derived from other studies (e.g., Waxman and Smits, 1968; Clavier et al., 1984; Bussian, 1983). However, the main limitation of this model is that the host water must have a much higher conductivity than both the matrix and hydrocarbons; this may be true at high salinities but the accuracy of the approach may be affected at low salinities (e.g., freshwater environments). Berg (2007) presented a dispersed-clay algorithmic approach for calculating the electrical conductivity of clayey-sand material that is applicable to all frequencies, water salinities and conductivities. This ‘incremental’ model accommodates simultaneous mixing of any number of disperse elements and accounts for both the exponent and grain conductivity associated with each respective component. Berg (2007) demonstrated that the model worked well on experimental data under a wide range of conditions and produced results that closely matched the results from other published models (e.g., Waxman and Smits, 1968; Bussian, 1983; de Lima and Sharma, 1990).

Overall, the HB equation is advantageous because (i) it reduces to Archie’s law when the matrix conductivity is negligible, (ii) it relates the bulk electrical conductivity to the electrical conductivity and volume fractions of the individual phases of water and matrix (disperse) phases, and provides some measure of their distribution and connectivity, (iii)

the disperse phase can account for several elements including sand, clay and hydrocarbons, (iii) it is formulated to handle complex conductivities and frequency dependencies.

2.5 Summary and Gaps

From this review of the relevant scientific literature, a number of observations can be made that are directly relevant to the scope of this work:

- DNAPL source zone architecture is complex, highly variable, and coupled to site heterogeneity.
- Remediation of sites where DNAPLs are present requires substantial mass reduction of the DNAPL source.
- Successful remediation of DNAPL source zones requires effective characterization and monitoring.
- Numerical modelling is the most effective method for systematically studying DNAPL scenarios at the field scale.
- DNAPLs exhibit favourable electrical properties making them amenable to geoelectrical detection.
- Non-invasive geoelectrical techniques have long been proposed as exhibiting significant potential for DNAPL site characterization and monitoring. However, inconsistent results at sites means that potential has not been realized. Partly this is due to a focus on static DNAPL detection which remains unlikely due to the complexity of the electrical target.
- Electrical resistivity tomography (ERT) has undergone significant improvements in the past 20 years with some key advances recently, including in the areas of field instrumentation, data acquisition and processing. These changes may overcome some of the previous barriers to successful application at DNAPL sites.
- ERT applied in time-lapse mode - monitoring subsurface changes with time - has emerged as one of the dominant fields in applied geophysics. Particularly

promising is the development, over the last 5 years, of a number of four-dimensional inversion schemes.

- Time-lapse ERT is now widely applied in a range of hydrogeological applications including the mapping of salt-water intrusion, groundwater-surface water interactions and wastewater transport.
- Cross-hole ERT, with electrodes deployed in parallel vertical boreholes, has been used in the majority of investigations involving ERT imaging of DNAPLs. This array configuration has limited potential for full scale, site wide monitoring of DNAPL source zones.
- Effective medium theory has recently emerged as a reliable and flexible method for relating hydrogeological properties to bulk electrical resistivity. It permits the inclusion of any number of disperse elements that can account for key phases such as sand, clay, DNAPL and air, allowing each of these phases to be non-zero if necessary. In addition, it is formulated to handle complex conductivities and dielectric permittivities meaning it can be used as a basis to develop relationships between key hydrogeological properties and the key electrical properties of several geoelectrical techniques such as ERT, spectral IP and GPR.
- Despite some limitations, Archie's law is still the most widely used relationship to estimate desired hydrogeological properties from ERT surveys.

From a survey of the literature and the summary provided, it is evident that a number of aspects are yet to be investigated in relation to ERT mapping of DNAPLs:

- Little work has been done on developing or evaluating non-invasive tools specifically for monitoring DNAPL source zone remediation.
- 4D ERT, one of the most promising of many advances in the field, has yet to be considered for application to DNAPL sites.
- Only controlled laboratory experiments and field experiments have previously been used to investigate ERT mapping of DNAPLs. A numerical model that simulates realistic, field scale DNAPL source zones and their remediation and predicts the corresponding response from an ERT survey currently does not exist.

- Surface ERT arrays are promising for DNAPL monitoring because of their ease of deployment, low cost, and ability to remain in place for repeat surveys over time. However, these have not been studied for DNAPL sites.
- Surface-to-tunnel ERT array configuration has been recently proposed for improving resolution at depth but has not been considered before for a horizontal borehole application at environmental sites or been employed in time-lapse mode.

2.6 References

Abriola L.M., and G.F. Pinder. 1985. A multiphase approach to the modelling of porous media contamination by organic compounds: 1. Equation development. Water Resources Research, 21(1): 11-18.

Abriola, L.M., K.M. Rathfelder, S. Yadav, and M. Maiza. 1992. VALOR code version 1.0: a PC code for simulating subsurface immiscible contaminant transport. Electric Power Research Institute.

Abriola, L.M., J.R. Lang, and K. Rathfelder. 1997. Michigan soil–vapor extraction remediation (MISER) model – a computer program to model bioventing of organic chemicals in unsaturated geological material. US Environmental Protection Agency.

Acworth, R.I., and L.B. Jorstad. 2005. Integration of multi-channel piezometry and electrical tomography to better define chemical heterogeneity in a landfill leachate plume within a sand aquifer. Journal of Contaminant Hydrology, 83(3-4): 200-220.

Ajo-Franklin, J.B., J.T. Geller, and J.M. Harris. 2006. A survey of geophysical properties of chlorinated DNAPLs. Journal of Applied Geophysics, 59: 177–189.

Alexandra, R., J.I. Gerhard, and B.H. Kueper. 2012. Hydraulic displacement of dense, nonaqueous phase liquids for source zone stabilization. Ground Water, 50: 765-774.

Archie, G.E. 1942. The electrical resistivity log as an aid in determining some reservoir characteristics. Transactions of the AIME, 146: 54–62.

Atekwana, E.A., E. Atekwana, F.D. Legall, and R.V. Krishnamurthy. 2005. Biodegradation and mineral weathering controls on bulk electrical conductivity in a shallow hydrocarbon contaminated aquifer. Journal of Contaminant Hydrology, 80: 149-167.

Athanasiou, E., P. Tsourlos, and G. Vargemezis. 2007. Optimizing Electrical Resistivity Array Configurations for Hydrogeological Studies. In Coastal Aquifers: Challenges and Solutions, (eds Pulido Bosch, A. ,Lopez-Geta,J.A.& Ramos Gonzalez, G.). Hidrogeologia y agues subterraneas .Instituto Geologico y Minero de Espana, Madrid. n23: 243-252.

Barker, R.D. 1981. The offset system of electrical resistivity sounding and its use with multicore cable. Geophy. Prosp., 29: 128-143.

Barry, D. A., H. Prommer, C. T.Miller, P. Engesgaard, A. Brun, and C. Zheng. 2002. Modeling the fate of oxidizable organic contaminants in groundwater. Water Resour., 25: 945– 983.

Bear, J. 1972. Dynamics of fluids in porous media. Dover, Mineola, New York.

Bentley, L.R., and M. Gharibi. 2004. Two- and three-dimensional electrical resistivity imaging at a heterogeneous site. Geophysics, 69: 674-680.

Berg, C.R. 1995. A simple effective-medium model for water saturation in porous rocks. Geophysics, 60: 1070–1080.

Berg, C. 2007. An effective medium algorithm for calculating water saturations at any salinity or frequency. Geophysics, 72(2): E59-E67.

Bing, Z., and S.A. Greenhalgh. 2000. Cross-hole resistivity tomography using different electrode configuration. Geophy. Prosp., 48: 887-912.

Binley, A., and A. Kemna. 2005. DC resistivity and induced polarization methods. In: Rubin, Y., and S.S. Hubbard (Eds.), Hydrogeophysics. Water and Science Technology Library, Springer, New York, United States, pp. 129-156.

Brewster, M.L., and A.P. Annan. 1994. Ground-penetrating radar monitoring of a controlled DNAPL release: 200 MHz radar. Geophysics, 59: 1211-1221.

Brewster, M.L., A.P. Annan, J.P. Greenhouse, B.H. Kueper, and G.R. Olhoeft. 1995. Observed migration of a controlled DNAPL release by geophysical methods. Ground Water, 33: 977-987.

Brooks, R. H., and A. T. Corey, Hydraulic properties of porous media, Hydrol. Pap. 3, Civ. Eng. Dep., Colo. State Univ., Fort Collins, 1964.

Bruggeman, D.A.G. 1935. The calculation of various physical constants of heterogeneous substances: I. The dielectric constants and conductivities of mixtures composed of isotropic substances. Ann. Phys., 24: 636–664 (in German).

Bussain, A.E. 1983. Electrical conductance in a porous medium. Geophysics, 48: 1258–1268.

Cardarelli, E., and G. Di Filippo. 2009. Electrical resistivity and induced polarization tomography in identifying the plume of chlorinated hydrocarbons in sedimentary formation: a case study in Rho (Milan-Italy). Waste Management & Research, 27: 595–602.

Cardenas, M.B., and M.S. Markowski. 2010. Geoelectrical Imaging of Hyporheic Exchange and Mixing of River Water and Groundwater in a Large Regulated River. Environmental Science & Technology, 45(4): 1407-1411.

Carr, C. S., S. Garg, and J. B. Hughes. 2000. Effect of dechlorinating bacteria on the longevity and composition of PCE-containing nonaqueous phase liquids under equilibrium dissolution conditions. Environ. Sci. Technol., 34: 1088–1094.

Chambers, J.E., R.D. Ogilvy, P.I. Meldrum, J. Nissen. 1999. 3D electrical resistivity imaging of buried oil-tar contaminated waste deposits. Eu. J. Environ. Eng. Geophy., 4: 3-15.

Chambers J.E., M.H. Loke, R.D. Ogilvy, and P.I. Meldrum. 2004. Noninvasive monitoring of DNAPL migration through a saturated porous medium using electrical impedance tomography. Journal of Contaminant Hydrology, 68: 1–22.

Chambers, J.E., P.B. Wilkinson, G.P. Wealthall, M.H. Loke, R. Dearden, R. Wilson, D. Allen, and R.D. Ogilvy. 2010. Hydrogeophysical imaging of deposit heterogeneity and groundwater chemistry changes during DNAPL source zone bioremediation. Journal of Contaminant Hydrology, 118: 43-61.

Chen, M., L. M. Abriola, B. K. Amos, E.J. Suchomel, K. D. Pennell, F. E. Löffler, and J. A. Christ. 2013. Reductive dechlorination by an anaerobic consortium during bioenhanced PCE dissolution: Model validation and sensitivity analysis. Journal of Contaminant Hydrology, 151: 117–130.

Christ, J.A., and L.M. Abriola. 2006. Modeling metabolic reductive dechlorination in dense non-aqueous phase liquid source-zones. Advances in Water Resources, 30: 1547-1561.

Clavier, C., G. Coates, and J. Dumanoir. 1984. Theoretical and experimental bases for the dual-water model for interpretation of shaly sands. Society of Petroleum Engineers Journal, 24: 153–168.

Clement, T.P. 1997. RT3D - A modular computer code for simulating Reactive Multi species Transport in 3 Dimensional Groundwater Systems. PNNL-11720, Pacific Northwest National Laboratory, Richland, Washington, USA.

Clement, T.P., T.R. Gautam, K.K. Lee, M.J. Truex, and G.B. Davies. 2004. Modeling of DNAPL-dissolution, rate-limited sorption and biodegradation reactions in groundwater systems. Bioremediation Journal, 8: 47-64.

Clement, R., L. Oxarango, and M. Descloitres. 2011. Contribution of 3D time-lapse ERT to the study of leachate recirculation in a landfill. Waste Management, 31(3): 457-467.

Coscia, I., N. Linde, S. Greenhalgh, T. Vogt, and A. Green. 2012. Estimating traveltimes and groundwater flow patterns using 3D time-lapse crosshole ERT imaging of electrical resistivity fluctuations induced by infiltrating river water. Geophysics, 77(4): E239-E250.

Constable, S., R. Parker, C. Constable. 1987. Occam's inversion: a practical algorithm for generating smooth models from electromagnetic sounding data. Geophysics, 52:289-300.

Cope, N., and J. B. Hughes. 2001. Biologically-enhanced removal of PCE from NAPL source zones. Environ. Sci. Technol., 35: 2014–2021.

Cosenza, P., A. Ghorbani, C. Camerlynck, F. Rejiba, R. Guérin, and A. Tabbagh. 2009. Effective medium theories for modeling the relationships between electromagnetic properties and hydrological variables: a review. Near Surface Geophysics, 7: 563–578.

Dahlin, T. 2001. The development of DC resistivity imaging techniques. Computer and Geosciences, 27(9): 1019-1029.

Dahlin, T., and B. Zhou. 2004. A numerical comparison of 2D resistivity imaging with 10 electrode arrays. Geophysical Prospecting, 52(5): 379-398.

Daily, W., and E. Owen. 1991. Cross-borehole resistivity tomography. Geophy., 56: 1228-1235.

Daily, W., and A. Ramirez. 1995. Electrical resistance tomography during in-situ trichloroethylene remediation at the Savannah River Site. Journal of Applied Geophysics, 33: 239–249.

Daily, W., A. Ramirez, D. LaBrecque, and J. Nitao. 1992. Electrical Resistivity Tomography of Vadose Zone Water Movement. Water Resources Research, 28(5): 1429-1442.

Danielsen B.E, and T. Dahlin. 2010. Numerical modeling of resolution and sensitivity of ERT in horizontal boreholes. Journal of Applied Geophysics, 70: 245–254.

Day-Lewis, F.D., K. Singha, and A. Binley. 2005. Applying petrophysical models to radar travel time and electrical resistivity tomograms: Resolution-dependent limitations. Journal of Geophysical Research, 110: B08206.

Day-Lewis, F.D., E.A. White, C.D. Johnson, and J.W. Lane. 2006. Continuous resistivity profiling to delineate submarine groundwater discharge –examples and limitations. The Leading Edge, 25: 724-728.

de Franco, R., G. Biella, L. Tosi, P. Teatini, et al. 2009. Monitoring the saltwater intrusion by time lapse electrical resistivity tomography: the Chioggia test site (Venice Lagoon, Italy). Journal of Applied Geophysics, 69(3-4), 117–130.

de Lima, O. A. L., and M. M. Sharma. 1990. A grain conductivity approach to shaly sandstones. Geophysics, 55: 1347–1356.

Dekker, T.J., and L.M. Abriola. 2000. The influence of field-scale heterogeneity on the surfactant-enhanced remediation of entrapped nonaqueous phase liquids. Journal of Contaminant Hydrology, 42: 219-251.

Dey, A., and H.F. Morrison. 1979. Resistivity modelling for arbitrarily shaped three-dimensional structures. Geophysics, 44: 753-780.

Dhu, T., and G. Heinson. 2004. Numerical and laboratory investigations of electrical resistance tomography for environmental monitoring. Expl. Geophy., 35: 33-40.

Doetsch, J., N. Linde, M. Pessognelli, A.G. Green, and T. Günther. 2012a. Constraining 3D electrical resistance tomography with GPR reflection data for improved aquifer characterization. Journal of Applied Geophysics, 78: 68-76.

Doetsch, J., N. Linde, T. Vogt, A. Binley, and A.G. Green. 2012b. Imaging and quantifying salt-tracer transport in a riparian groundwater system by means of 3D ERT monitoring. Geophysics, 77(5): B207-B218.

Flores Orozco, A., K.H. Williams, P.E. Long, S.S. Hubbard, and A. Kemna. 2011. Using complex resistivity imaging to infer biogeochemical processes associated with bioremediation of an uranium-contaminated aquifer. Journal of Geophysical Research: Biogeosciences, 116(G3).

Freeze, R. A., and J. A. Cherry. 1979. Groundwater: Prentice Hall Inc.

Froese, D.G., D.G. Smith, and D.T. Clement. 2005. Characterizing large river history with shallow geophysics: Middle Yukon River, Yukon Territory and Alaska. Geomorphology, 67(3–4): 391–406.

Furman, A., T.P.A. Ferre, and G.L. Heath. 2007. Spatial focusing of electrical resistivity surveys considering geologic and hydrologic layering. Geophysics, 72: 65-73.

Gasperikova, E., S.S. Hubbard, D.B. Watson, G.S. Baker, J.E. Peterson, M.B. Kowalsky, M. Smith, and S. Brooks. 2012. Long-term electrical resistivity monitoring of recharge-induced contaminant plume behavior. Journal of Contaminant Hydrology, 142–143: 33-49.

Gerhard, J.I., B.H. Kueper, G.R. Hecox, and E.J. Schwarz. 2001. Site-specific design for dual phase recovery and stabilization of pooled DNAPL. Ground Water Monitoring and Remediation, Spring: 71-88.

Gerhard, J.I., and B.H. Kueper. 2003a. Capillary pressure characteristics necessary for simulating DNAPL infiltration, redistribution, and immobilization in saturated porous media. Water Resources Research, 39: 1212.

Gerhard, J.I., and B.H. Kueper. 2003b. Relative permeability characteristics necessary for simulating DNAPL infiltration, redistribution, and immobilization in saturated porous media. Water Resources Research, 39: 1213.

Gerhard, J.I., and B.H. Kueper. 2003c. Influence of constitutive model parameters on the predicted migration of DNAPL in heterogeneous porous media. Water Resources Research, 39: 1279.

Gerhard, J.I., T. Pang, and B.H. Kueper. 2007. Time scales of DNAPL migration in sandy aquifers. Ground Water, 45: 147-157.

Glover, P.W.J., M.J. Hole, and J. Pous. 2000. A modified Archie's law for two conducting phases. Earth Planet. Sci. Lett., 180(3–4): 369–383.

Glover, P.W.J. 2010. A generalized Archie's law for *n* phases. Geophysics, 75(6): E247-E265.

Goes, B.J.M., and J.A.C. Meekes. 2004. An effective electrode configuration for the detection of DNAPLs with electrical resistivity tomography. Journal of Environmental and Engineering Geophysics, 9(3):127-141.

Grant, G.P., 2005. The evolution of complex DNAPL releases: rates of migration and dissolution. Ph.D. Thesis, University of Edinburgh, Ediburgh, Scotland, UK, 429 pp.

Grant, G.P., and J.I. Gerhard. 2007a. Simulating the dissolution of a complex dense non-aqueous phase liquid source zone: 1. model to predict interfacial area. Water Resources Research, 43: W12410.

Grant, G.P., and J.I. Gerhard. 2007b. Simulating the dissolution of a complex dense non-aqueous phase liquid source zone: 2. experimental validation of an interfacial area-based mass transfer model. Water Resources Research, 43: W12409.

Grant, G.P., J.I. Gerhard, and B.H. Kueper. 2007. Multidimensional validation of a numerical model for simulating a DNAPL release in heterogeneous porous media. Journal of Contaminant Hydrology, 92: 109-128.

Griffin, T.W., and K.W. Watson. 2002. A comparison of field techniques for confirming dense nonaqueous phase liquids. Ground Water Monitoring Review, 22(2): 48-59.

Hadley, P.W., and C.J. Newell. 2012. Groundwater Remediation: The Next 30 Years. Ground Water, 50(5): 669-678.

Hanai, T. 1960. Theory of the dielectric dispersion due to the interfacial polarization and its application to emulsions. Kolloid-Zeitschrift, 171: 23–31.

Hanai, T. 1961. A remark on "Theory of the dielectric dispersion due to the interfacial polarization and its application to emulsions". Kolloid-Zeitschrift, 175: 61–62.

Hayley, K., L.R. Bentley, M. Gharibi, and M. Nightingale. 2007. Low temperature dependence of electrical resistivity: Implications for near surface geophysical monitoring. Geophysical Research Letters, 34(18).

Hayley, K., A. Pidlisecky, and L.R. Bentley. 2011. Simultaneous time-lapse electrical resistivity inversion. Journal of Applied Geophysics, 75: 401-411.

Huyakorn, P.S., and G.F. Pinder. 1983. Computational Methods in Subsurface Flow. Academic Press, New York, N.Y.

Illangasekare T.H., J.L. Ramsey Jr., K.H. Jensen, and M.B. Butts. 1995. Experimental study of the movement and distribution of dense organic contaminants in heterogeneous aquifer. Journal of Contaminant Hydrology, 20: 1–25.

Imhoff, P.T., P.R. Jaffe, and G.F. Pinder. 1993. An experimental study of complete dissolution of a nonaqueous phase liquid in saturated porous media. Water Resour. Res., 30: 307–320.

Inculet, C.I. 2011. Impact of Varying Groundwater Flow Direction on Monitoring Well Concentrations Downgradient of DNAPL Source Zones. M.Sc. Thesis, The University of Western Ontario, London, Ontario, Canada, 272 pp.

Interstate Technology & Regulatory Council (ITRC). 2011. Integrated DNAPL Site Strategy. IDSS-1. Washington, DC: Interstate Technology & Regulatory Council, Integrated DNAPL Site Strategy Team. www.itrcweb.org.

Johnson, D.L., J. Koplik, and L.M. Schwartz. 1986. New pore-size parameter characterizing transport in porous media. Phys. Rev. Lett., 57: 2564-2567.

Johnson, T.C., L.D. Slater, D. Ntarlagiannis, F.D. Day-Lewis, and M. Elwaseif. 2012. Monitoring groundwater-surface water interaction using time-series and time-frequency analysis of transient three-dimensional electrical resistivity changes. Water Resources Research, 48(7): W07506.

Kaluarachchi, J., and J. Parker. 1990. Modelling multi-component organic chemical transport in three-phase porous media. Journal of Contaminant Hydrology, 5: 349.

Karaoulis, M.C., J.H. Kim, and P.I. Tsourlos. 2011a. 4D active time constrained resistivity inversion. Journal of Applied Geophysics, 73: 25-34.

Karaoulis, M., A. Revil, D.D. Werkema, B.J. Minsley, W.F. Woodruff, and A. Kemna. 2011b. Time-lapse three-dimensional inversion of complex conductivity data using an active time constrained (ATC) approach. Geophysical Journal International, 187: 237-251.

Karaoulis, M., A. Revil, J. Zhang, and D.D. Werkema. 2012. Time-lapse joint inversion of crosswell DC resistivity and seismic data: A numerical investigation. Geophysics, 77(4): D141-D157.

Karaoulis, M., A. Revil, P. Tsourlos, D.D. Werkema, and B.J. Minsley. 2013. IP4DI: A software for time-lapse 2D/3D DC-resistivity and induced polarization tomography. Computers & Geosciences, 54(0): 164-170.

Karaoulis, M., P. Tsourlos, J.H. Kim, and A. Revil. 2014a. 4D time-lapse ERT inversion: introducing combined time and space constraints. Near Surface Geophy., 12(1):25-34.

Karaoulis, M., A. Revil, B. Minsley, M. Todesco, J. Zhang, and D.D. Werkema. 2014b. Time-lapse gravity inversion with active time constraint. Geophysical Journal International, 196(2): 867-884.

Kavanaugh, M.C., P.S.C. Rao, L. Abriola, C. Newell, J. Cherry, T. Sale, G. Destouni, S. Shoemaker, R. Falta, R. Siegrist, D. Major, G. Teutsch, J. Mercer, and K. Udell. 2003. The DNAPL remediation challenge: is there a case for source depletion?. US Environmental Protection Agency, Washington DC.

Kim, J.H., M.J. Yi, S.G. Park, and J.G. Kim. 2009. 4-D inversion of DC resistivity monitoring data acquired over a dynamically changing earth model. Journal of Applied Geophysics, 68: 522-532.

Kim, J.H., R. Supper, P. Tsourlos, and M.J. Yi. 2013. Four-dimensional inversion of resistivity monitoring data through L*p* norm minimizations. Geophysical Journal International, 195(3): 1640-1656.

Kram, M. L., A. A. Keller, J. Rossabi, and L. G. Everett. 2001. DNAPL characterization methods and approaches. I. Performance comparisons. Ground Water Monitoring and Remediation, 21: 109–123.

Kram, M. L., A. A. Keller, J. Rossabi, and L. G. Everett. 2002. DNAPL characterization methods and approaches. II. Cost comparisons. Ground Water Monitoring and Remediation, 22: 46-61.

Kueper, B.H., and E.O. Frind. 1991a. Two-phase flow in heterogeneous porous media, 1 Model development. Water Resources Research, 27(6): 1049–1057.

Kueper, B.H., and E.O. Frind. 1991b. Two-phase flow in heterogeneous porous media, 2 Model application. Water Resources Research, 27(6): 1058–1070.

Kueper, B.H., J.D. Redman, R.C. Starr, S. Reitsma, and M. Mah. 1993. A field experiment to study the behavior of tetrachloroethylene below the water table: spatial distribution of residual and pooled DNAPL. Ground Water, 31: 756-766.

Kueper, B.H., and J.I. Gerhard. 1995. Variability of point source infiltration rates for two-phase flow in heterogeneous porous media. Water Resources Research, 31: 2971-2980.

Kueper, B.H., G.P. Wealthall, J.W.N. Smith, S.A. Leharne, and D.N. Lerner. 2003. An illustrated handbook of DNAPL transport and fate in the subsurface. Environment Agency R&D Publication 133. EA, Bristol.

Kuras, O., J.D. Pritchard, P.I. Meldrum, J.E. Chambers, P.B. Wilkinson, R.D. Ogilvy, and G.P. Wealthall. 2009. Monitoring hydraulic processes with automated time-lapse electrical resistivity tomography (ALERT). Comptes Rendus – Geoscience, 341(10-11): 868-885.

LaBrecque, D.J., M. Miletto, W. Daily, A. Ramirez, and E. Owen. 1996. The effect of noise on Occam inversion of resistivity tomography data. Geophysics, 61: 538-548.

LaBrecque, D.J., Yang, X., 2001. Difference inversion of ERT data: a fast inversion method for 3-D in situ monitoring. Journal of Environmental and Engineering Geophysics, 5: 83–90.

Lane J.W., F.D. Day-Lewis, and C.C. Casey. 2006. Geophysical monitoring of a field-scale biostimulation pilot project. Ground Water, 44(3): 430–443.

Lenhard, R.J., and J.C. Parker. 1987. A model for hysteretic constitutive relations governing multiphase flow, 2, Permeability-saturation relations. Water Resour. Res., 23: 2197-2206.

Lesmes, D.P., and Friedman, S.P. (2005) Relationships between the electrical and hydrogeological properties of rocks and soils. In: Y. Rubin and S. S. Hubbard, eds., Hydrogeophysics, Water Science and Technology Library, Chapter 2, Vol. 50:523, Springer, 87-128.

Li, Y., and K. Spitzer. 2002. Three-dimensional DC resistivity forward modeling using finite elements in comparison with finite-difference solutions. Geophys. J. Int., 151: 924-934.

Lin, H.C., D.R. Richards, G.T. Yeh, J.R. Cheng, H.P. Cheng, and N.L. Jones. 1997. FEMWATER: A Three-Dimensional Finite Element Computer Model for Simulating Density Dependent Flow and Transport in Variably Saturated Media. Technical Report CHL-96-12, U. S. Army Corps of Engineers: Vicksburg, MS; 126 pp.

Loke, M.H., and R.D. Barker. 1996. Practical techniques for 3D resistivity surveys and data inversion. Geophy. Prosp., 44: 499-524.

Loke, M.H. 2013. Tutorial: 2-D and 3-D electrical imaging surveys. http://www.geotomosoft.com/downloads.php, accessed 20 August 2013.

Loke, M.H., J.E. Chambers, D.F. Rucker, O. Kuras, and P.B. Wilkinson. 2013. Recent developments in the direct-current geoelectrical imaging method. Journal of Applied Geophysics, 95: 135-156.

Loke, M.H., T. Dahlin, and D.F. Rucker. 2014. Smoothness-constrained time-lapse inversion of data from 3-D resistivity surveys. Near Surface Geophysics, 12(1): 5-24.

Lucius, J.E., G.R.Olhoeft, P.L. Hill, and S.K. Duke. 1992. Properties and hazards of 108 selected substances - 1992 edition. Open-File Report 92-527, U. S. Geological Survey.

Mackay, D. M., and J. A. Cherry. 1989. Ground water contamination: Pump-and-Treat remediation. Environmental Science and Technology, 23(6): 620-636.

MacPhee, S.L., J.I. Gerhard, and G. Rein. 2012. A novel method for simulating smoldering propagation and its application to STAR (Self-sustaining treatment for active remediation). Environmental Modelling and Software, 31: 84-98.

Mansoor, N., and L. Slater. 2007. Acquatic electrical resistivity imaging of shallow-water wetlands. Geophysics, 72(5): F211-F221.

McGuire, T. M., J. M. McDade, and C. J. Newell. 2006. Performance of DNAPL source depletion technologies at 59 chlorinated solvent-impacted sites. Ground Water Monitoring and Remediation, 26(1): 73-84.

Miller, C.T., M.M. Poirier-McNeill, and A.S. Mayer. 1990. Dissolution of trapped nonaqueous phase liquids: Mass transfer characteristics. Water Resour. Res., 26: 2783-2796.

Miller, C.R., P.S. Routh, T.R. Brosten, and J.P. McNamara. 2008. Application of time-lapse ERT imaging to watershed characterization. Geophysics, 73(3): G7-G17.

Miller, E., L.M. Abriola, and A. Aghasi. 2012. Environmental remediation and restoration: Hydrological and geophysical processing methods. IEEE Signal Processing Magazine, 29(4): 16-26.

Minsley, B.J., J. Sogade, and F.D. Morgan. 2007. Three-dimensional self-potential inversion for subsurface DNAPL contaminant detection at the Savannah River Site, South Carolina. Water Resources Research, 43(4): W04429.

Nambi, I.M., and S.E. Powers. 2003. Mass transfer correlations for nonaqueous phase liquid dissolution from regions with high initial saturations. Water Resour. Res., 39(2): 1030.

National Research Council (NRC). 2005. Contaminants in the Subsurface: Source Zone Assessment and Remediation. The National Academies Press, Washington D.C.

Naudet, V., J.C. Gourry, F. Girard, F. Mathieu, and A. Saada. 2013. 3D electrical resistivity tomography to locate DNAPL contamination around a housing estate. Near Surface Geophysics, (In Press).

Nelson, N.T., M. Oostrom, T.W. Wietsma, and M.L. Brusseau. 1999. Partitioning tracer method for the in situ measurement of DNAPL saturation: Influence of heterogeneity and sampling method. Environmental Science Technology, 33: 4046–4053.

Nenna, V., A. Pidlisecky, and R. Knight. 2011. Informed experimental design for electrical resistivity imaging. Near Surface Geophysics, 9: 469–482.

Newell, C. J., S. K. Farhat, D. T. Adamson, and B. B. Looney. 2011. Contaminant plume classification system based on mass discharge. Ground Water, 49: 914–919.

Newmark R.L., W.D. Daily, K.R. Kyle, and A.L. Ramirez. 1998. Monitoring DNAPL pumping using integrated geophysical techniques. Journal of Environmental and Engineering Geophysics, 3: 7–13.

Nguyen, F., A. Kemna, A. Antonsson, P. Engesgaard, O. Kuras, R. Ogilvy, J. Gisbert, S. Jorreto, and A. Pulido-Bosch. 2009. Characterization of seawater intrusions using 2D electrical imaging. Near Surface Geophysics, 7: 377–390.

O'Carroll, D.M., S.A. Bradford, and L.M. Abriola. 2004. Infiltration of PCE in a system containing spatial wettability variations. J. Cont. Hydrology, 73: 247–270.

Ogilvy R.D., O. Kuras, P.I. Meldrum, P.B. Wilkinson, J.E. Chambers, M. Sen, A. Pulido-Bosch, J. Gisbert, S. Jorreto, I. Frances, and P. Tsourlos. 2009. Automated monitoring of coastal aquifers with electrical resistivity tomography. Near Surface Geophysics, 7: 367–375.

Oldenburg, D.W., and Y. Li. 1999. Estimating depth of investigation in dc resistivity and IP surveys. Geophysics, 64: 403-416.

Oldenborger, G.A., M.D. Knoll, P.S. Routh, and D.J. LaBrecque. 2007. Time-lapse ERT monitoring of an injection/withdrawal experiment in a shallow unconfined aquifer. Geophysics, 72(4): F177–F187.

Olhoeft,G.R. 1985. Low-frequency electrical properties. Geophysics, 50(12): 2492-2502.

Oostrom, M., J.H. Dane, and T.W. Wietsma. 2006. A Review of Multidimensional, Multifluid Intermediate Scale Experiments Nonaqueous Phase Liquid Dissolution and Enhanced Remediation. Vadose Zone Journal.

Pankow, J.F., S. Feenstra, J.A. Cherry, and M.C. Ryan. 1996. Dense chlorinated solvents in groundwater: Background and history of the problem. In: Pankow, J.F., and J.A. Cherry (Eds.), Dense Chlorinated Solvents and other DNAPLs in Groundwater, History, Behavior, and Remediation. Waterloo Press, Portland, Oregon, United States, pp. 1-52.

Papadopoulos N.G., P. Tsourlos, G.N. Tsokas, and A. Sarris. 2007. Efficient ERT measuring and inversion strategies for 3D imaging of buried antiquities. Near Surface Geophysics, 5: 349–362.

Park, E., and J.C. Parker. 2005. Evaluation of an upscaled model for DNAPL dissolution kinetics in heterogeneous aquifers. Adv Water Resour, 28(12): 1280–1291

Parker, J. C., and R. J. Lenhard. 1987. A model for hysteretic constitutive relations governing multiphase flow, 1, Saturation-pressure relations. Water Resour. Res., 23: 2187-2196.

Pearlman, L. 1999. Subsurface containment and monitoring systems: barriers and beyond. U.S. Environmental Protection Agency, Office of Solid Waste and Emergency Response, Washington, USA.

Perri, M.T., G. Cassiani, I., Gervasio, R., Deiana, A. and Binley. 2012. A saline tracer test monitored via both surface and cross-borehole electrical resistivity tomography: Comparison of time-lapse results. Journal of Applied Geophysics, 79(0): 6-16.

Phanikumar, M.S. and J.T. McGuire. 2004. A 3D partial-equilibrium model to simulate coupled hydrogeological, microbiological, and geochemical processes in subsurface systems. Geophysical Research Letters, 31(11): L11503.

Pironi, P., C. Switzer, G. Rein, J.I. Gerhard, and J.L. Torero. 2009. Small-scale forward smouldering experiments for remediation of coal tar in inert media. Proceedings of the Combustion Institute, 32 (2): 1957-1964.

Poulsen, M.M., and B.H. Kueper. 1992. A field experiment to study the behaviour of tetrachloroethylene in unsaturated porous media. Environmental Science and Technology, 26(5): 889-895.

Powers, S.E., L.M. Abriola, and W.J. Weber Jr. 1992. An experimental investigation of NAPL dissolution in saturated subsurface systems: Steady state mass transfer rates. Water Resour. Res., 28: 2691–2706.

Rathfelder, K.M., J.R. Lang, and L.M. Abriola. 2000. A numerical model (MISER) for the simulation of coupled physical, chemical, and biological processes in soil vapor extraction and bioventing systems. Journal of Contaminant Hydrology, 43: 239-270.

Rathfelder, K., L.M. Abriola, T.P. Taylor, and K.D. Pennell. 2001. Surfactant enhanced recovery of tetrachloroethylene from a porous medium containing low permeability lenses. 2. Numerical simulation. Journal of Contaminant Hydrology, 48: 351-374.

Revil, A., and P.W.J. Glover. 1997. Theory of ionic-surface electrical conduction in porous media. Physical Review B, 55(3): 1757-1773.

Revil, A., L.M. Cathles III, S. Losh, and J.A. Nunn. 1998. Electrical conductivity in shaly sands with geophysical applications. Journal of Geophysical Research, 103: 23.925-23.936.

Revil, A., M. Karaoulis, T. Johnson, and A. Kemna. 2012. Review: Some low-frequency electrical methods for subsurface characterization and monitoring in hydrogeology. Hydrogeology Journal, 20(4): 617-658.

Robert, T., D. Caterina, J. Deceuster, O. Kaufmann, and F. Nguyen. 2012. A salt tracer test monitored with surface ERT to detect preferential flow and transport paths in fractured/karstified limestones. Geophysics, 77(2): B55-B67.

Rücker, C., T. Günther, and K. Spitzer. 2006. Three-dimensional modelling and inversion of dc resistivity data incorporating topography – I. Modelling. Geophysical Journal International, 166(2): 495-505.

Rykiel, E.J., Jr. 1996. Testing ecological models: the meaning of validation. Ecological Modeling, 90: 229-244.

Saba, T., and T.H. Illangasekare. 2000. Effect of groundwater flow dimensionality on mass transfer from entrapped nonaqueous phase liquid contaminants. Water Resour. Res.

Saenton, S., T. Illangasekare, K. Soga, and T. Saba. 2002. Effect of source zone heterogeneity on surfactant enhanced NAPL dissolution and resulting remediation endpoints. J Contam Hydrol, 53(1–2): 27–44.

Saenton, S., and T.H. Illangasekare. 2013. Effects of incomplete remediation of NAPL-contaminated aquifers: experimental and numerical modeling investigations. Appl Water Sci, 3: 401-414.

Sale, T., and D. McWhorter. 2001. Steady-state mass transfer from singlecomponent dense non-aqueous phase liquids in uniform flow fields. Water Resour Res, 37(2): 393–404

Sauck, W.A. 2000. A model for the resistivity structure of LNAPL plumes and their environs in sandy sediments. Journal of Applied Geophysics, 44: 151-165.

Seol Y, H. Zhang, F. Schwartz. 2003. A review of in situ chemical oxidation and heterogeneity. Environ Eng Geosci., 9(1): 37–49.

Sen, P.N., Scala, C., Cohen, M.H., 1981. A self similar model for sedimentary rocks with application to the dielectric constant of fused glass beads. Geophysics, 46: 781-795.

Simyrdanis, K. 2013. Development of surveying geophysical techniques for the study of geotechnical and environmental problems. PhD thesis. Aristotle University of Thessaloniki, Greece.

Simyrdanis, K., P. Tsourlos, P. Soupios, and J.H. Kim. 2012. Optimizing surface-to-tunnel ERT measurements. Near Surface Geoscience 2012, 18th European Meeting of Environmental and Engineering Geophysics, Paris, France, September 2012.

Singha, K., and S.M. Gorelick. 2006a. Hydrogeophysical tracking of three-dimensional tracer migration: The concept and application of apparent petrophysical relations. Water Resources Research 42(6): W06422.

Singha, K., and S.M. Gorelick. 2006b. Effects of spatially variable resolution on field-scale estimates of tracer concentration from electrical inversions using Archie's law. Geophysics, 71(3): G83-G91.

Slater, L., A. Binley, W. Daily, and R. Johnson. 2000. Cross-hole electrical imaging of a controlled saline tracer injection. Journal of Applied Geophysics, 44: 85-102.

Slater, L., A. Binley, R. Versteeg, G. Cassiani, R. Birken, and S. Sandberg. 2002. A 3D ERT study of solute transport in a large experimental tank. Journal of Applied Geophysics, 49: 211-229.

Slater, L., and D. Lesmes. 2002. IP interpretation in environmental investigations. Geophysics, 67(1): 77-88.

Slater, L., and A. Binley. 2003. Evaluation of permeable reactive barrier (PRB) integrity using electrical imaging methods. Geophysics, 68(3): 911-921.

Slater, L., and A. Binley. 2006. Synthetic and field-based electrical imaging of a zerovalent iron barrier: Implications for monitoring long-term barrier performance. Geophysics, 71(5): B129-B137.

Sleep, B., and J. Sykes. 1993. Compositional simulation of groundwater contamination by organic compounds. Water Resources Research, 29(6): 1697–1708.

Slichter, L.B. 1933. The interpretation of the resistivity prospecting method for horizontal structures, J Appl Phys, v4, pp 307–322.

Sogade, J.A., F. Scira-Scappuzzo, Y. Vichabain, W. Shi, W. Rodi, D.P. Lesmes, and F.D. Morgan. 2006. Induced-polarisation detection and mapping of contaminant plumes. Geophysics, 71(3): B75–B84.

Stummer, P., H. Maurer, and A. Green. 2004. Experimental design: electrical resistivity data sets that provides optimum subsurface information. Geophysics, 69: 120-139.

Supper, R., J. Chambers, P. Tsourlos, and J.H. Kim. 2014a. Foreword on the Special Topic of Geoelectrical Monitoring. Near Surface Geophysics, 12(1): 1-3.

Supper, R. D. Ottowitz, B. Jochum, J-H. Kim, A. Römer, I. Baron, S. Pfeiler, M. Lovisolo, S. Gruber, and F. Vecchiotti. 2014b. Geoelectrical monitoring: an innovative method to supplement landslide surveillance and early warning. Near Surface Geophysics, 12(1): 133-150.

Switzer, C., P. Pironi, J.I. Gerhard, G. Rein, J.L. Torero. 2009. Self-sustaining smoldering combustion: a novel remediation process for non-aqueous-phase liquids in porous media. Environmental Science & Technology, 43(15): 5871-5877.

Tartakovsky, B. D., Millette, S. Delisle, and S.R. Giuot. 2002. Ethanol-stimulated bioremediation of nitrate-contaminated ground water. Ground Water Monitoring Remediation, 22: 78-87.

Temples, T., Waddel, M., Domoracki, W., Eyer, J., 2001. Noninvasive determination of the location and distribution of DNAPLs using advanced seismic reflection techniques. Ground Water 39: 465–474.

Tsourlos P. (1995). Modeling, Interpretation and Inversion of Multielectrode Resistiv-ity Data. D.Phil. Thesis, University of York, 315 pp.

Tsourlos, P. (2005) Inversion of Electrical Resistivity Tomography Data Deriving From 3D Structures. Bulletin of the Geological Society of Greece, 36, 1289-1297.

Tsourlos, P., and R. Ogilvy. 1999. An algorithm for the 3-D inversion of tomographic resistivity and induced polarization data: preliminary results. Journal of the Balkan Geophysical Society, 2: 30-45.

Tsourlos, P., R.D. Ogilvy, P.I. Meldrum, G.M. Williams. 2003. Time-lapse monitoring in single boreholes using electrical resistivity tomography. Journal of Environmental and Engineering Geophysics, 8(1): 1–14.

Tsourlos, P., R. Ogilvy, C. Papazachos, and P. Meldrum. 2011. Measurement and inversion schemes for single borehole-to-surface electrical resistivity tomography surveys. Journal of Geophysics and Engineering, 8: 487

Turesson, A. 2006. Water content and porosity estimated from ground-penetrating radar and resistivity. Journal of Applied Geophysics, 58: 99-111.

Udell, K.S. 1997. Thermally enhanced removal of liquid hydrocarbon contaminants from soils and groundwater, In: Subsurface Restoration. Ward, C.H., J. Cherry, and M. Scalf (Eds). Ann Arbor Press, Chelsea MI. pp. 251-270.

Urish, D.W. 1981. Electrical resistivity—hydraulic conductivity relationships in glacial outwash aquifers. Water Resour. Res., 17(5): 1401–1408.

van Genuchten, M.T. 1980. A closed form equation for predicting the hydraulic conductivity of unsaturated soils. Soil Sci. Soc. Am. J., 44: 892-898.

van Schoor, M., and A. Binley. 2010. In-mine (tunnel-to-tunnel) electrical resistance tomography in South African platinum mines. Near Surface Geophysics, 8: 563-574.

Waxman, M.H., and L.J.M. Smits. 1968. Electrical conductivities and oil-bearing shaly sands. Society of Petroleum Engineers, 8: 107–122.

West, M.R., G.P. Grant, J.I. Gerhard, and B.H. Kueper. 2008. The influence of precipitate formation on the chemical oxidation of TCE DNAPL with potassium permanganate. Advances in Water Resources, 31: 324-338.

Wilkinson, P.B., P.I. Meldrum, J.E. Chambers, O. Kurus, and R.D. Ogilvy. 2006. Improved strategies for the automatic selection of optimized sets of electrical resistivity tomography measurement configurations. Geophy. J. Int., 169: 1119-1126.

Wilkinson, P.B., J.E. Chambers, P.I. Meldrum, D.A. Gunn, R.D. Ogilvy, and O. Kuras. 2010. Predicting the movements of permanently installed electrodes on an active landslide using time-lapse geoelectrical resistivity data only. Geophysical Journal International, 183: 543-556.

Wilkinson, P.B., S.S. Uhlemann, J.E. Chambers, P.I. Meldrum, L.S. Oxby, and O. Kuras. 2013. Optimised sequential experimental design for geoelectrical resistivity monitoring surveys. Near Surface Geoscience 2013, 19th European Meeting of Environmental and Engineering Geophysics, Bochum, Germany, September 2013.

Xu, T., E. Sonnenthal, N. Spycher, and K. Pruess. 2004. TOUGHREACT User's Guide: A Simulation Program for Nonisothermal Multiphase Reactive Geochemical Transport in Variably Saturated geologic Media, Lawrenc Berkeley National Laboratory.

Yi, M.J., J.H. Kim, and S.H. Chung. 2003. Enhancing the resolving power of least-squares inversion with active constraint balancing. Geophysics, 68: 931-941.

Zheng, C. 1990. MT3D, A Modular Three-Dimensional Transport Model for Simulation of Advection, Dispersion and Chemical Reactions of Contaminants in Groundwater Systems, 170 pp., U.S. Environ. Prot. Agency, Washington, D. C.

Zhou, Q. Y., J. Shimada, and A. Sato. 2001. Three-dimensional spatial and temporal monitoring of soil water content using electrical resistivity tomography. Water Resources Research, 37: 273–285.

Zhou, J. A. Revil, M. Karaoulis, D. Hale, J. Doetsch, and S. Cuttler. 2014. Image-guided inversion of electrical resistivity data. Geophysical Journal International, 197(1): 292-309.

3 A NEW COUPLED MODEL FOR SIMULATING THE MAPPING OF DENSE NON-AQUEOUS PHASE LIQUIDS USING ELECTRICAL RESISTIVITY TOMOGRAPHY [1]

3.1 Introduction

Successful remediation of sites contaminated with dense non-aqueous phase liquids (DNAPLs) is a major challenge. DNAPLs are a class of industrial organic liquids, including chlorinated solvents, coal tar and polychlorinated biphenyl (PCB) oils, that are among the most hazardous and frequently detected contaminants detected in soil and groundwater (Kavanaugh et al., 2003). Upon release to the subsurface (e.g., due to rupture of a pipeline or tank), DNAPLs penetrate the pore space as an immiscible 'oil' phase. With a density greater than water, they routinely penetrate the water table and occupy the saturated zone. Their low solubility and high resistance to degradation relative to many groundwater contaminants means that a "DNAPL source zone" is typically expected to remain in the subsurface for decades, posing health risks to humans and ecosystems (Kueper et al., 2003).

Numerous studies have been conducted in recent years to understand the expected distribution of DNAPLs in the subsurface, including physical experiments at the bench (e.g., Illangasekare et al., 1995) and field scales (e.g., Kueper et al., 1993; Brewster et al., 1995), and numerical modelling studies (e.g., Dekker and Abriola, 2000; Gerhard & Kueper, 2003c). In fact, numerical models have become an essential tool for studying field scale DNAPL behaviour as field experiments are generally prohibited and laboratory experiments cannot reproduce the field scale heterogeneity that is critical to DNAPL

[1] A version of this chapter has been published: Power C., J.I. Gerhard, P. Tsourlos, and A. Giannopoulos. 2013. A new coupled model for simulating the mapping of dense non-aqueous phase liquids using electrical resistivity tomography. Geophysics, 78(4): EN1-EN15.

migration. From these studies, it is known that DNAPL source zones can exhibit a wide range of forms, from a laterally extensive layer near the surface (e.g., Gerhard et al., 2001) to a complex distribution of residual (trapped blobs) and pools (highly saturated accumulations) distributed widely and penetrating to significant depth (e.g., Gerhard et al., 2007). The configuration of a particular DNAPL source zone is site specific and usually unknown in advance, since it depends on many factors including characteristics of the release and the detailed distribution of sands, silt and clay lenses at the release location (Kueper and Gerhard, 1995; Gerhard et al., 2007).

Successful remediation of DNAPL sites depends on effective site investigation and monitoring strategies. Currently, DNAPL mapping typically relies on a sparse network of intrusive sample points (e.g., wells, cores and test-pits) that are costly and provide limited spatial and temporal resolution. Identifying the volume and distribution of soil impacted by DNAPL in this manner, both initially and over time during remedial efforts, can be challenging, since direct, conclusive evidence is often absent at most sampling locations (Kueper and Davies, 2009). It has long been recognized that geophysical methods have the potential to significantly improve DNAPL site investigation and remediation monitoring (e.g., Brewster et al., 1995; Wilson et al., 2009). Electrical resistivity tomography (ERT), a well-established and widely employed hydrogeophysics technique – e.g. for mapping moisture content (Zhou et al., 2001) and hydraulic conductivity (Slater, 2007) – is promising since DNAPLs are typically much more resistive than groundwater (Lucius et al., 1992). The dissolved phase plume produced during natural dissolution of DNAPL is generally not considered of consequence for geo-electrical studies due to the small quantities of dissolved molecules (parts per million) and lack of charge carriers (organic molecules are electrically neutral) (e.g., Sauck et al., 1998; Redman, 2009). However, it is noted that, in some instances, chlorinated solvent plumes may exhibit increased electrical conductivity over time (e.g., Atekwana and Atekwana, 2009); this elevated conductivity has been attributed to increased dissolved ion concentrations in groundwater from mineral weathering occurring as a byproduct of biodegradation of the dissolved solvent compounds (e.g., Sauck, 2000; Atekwana et al., 2005). In contrast, there is no evidence that the resistive nature of DNAPLs changes with time. Thus, a

resistive DNAPL source zone beneath the water table presents a potential electrical target at sites whether or not significant dissolution or biodegradation is occurring.

The potential of ERT to detect DNAPL has been suggested by a number of controlled laboratory studies (e.g., Dhu and Heinson, 2004); for example, Chambers et al. (2004) used differential time-lapse resistivity imaging to monitor the movement of DNAPL through a saturated porous medium in a laboratory column. Applications at a handful of research sites have provided mixed results. Daily and Ramirez (1995) applied cross-hole ERT at a chlorinated solvent site to track changes in resistivity associated with a subsurface remediation program which included the injection of an electron donor and infiltration of water. Newmark et al. (1998) used time-lapse cross-hole resistivity images to monitor the removal of a mixed DNAPL during groundwater pumping. Cardarelli and Di Filippo (2009) used surface ERT with induced polarization (IP) to identify anomalies associated with the presence of DNAPL, while Chambers et al. (2010) used high-resolution, cross-hole ERT in a pilot-scale experiment to not detect DNAPL directly but rather to map the groundwater chemistry changes associated with bioremediation.

ERT has not become a standard DNAPL site investigation tool due, in part, to the challenge of interpreting data from real contaminated sites. Most sites present a complex electrical target, including an unknown, often tortuous contaminant distribution superimposed upon an uncertain, heterogeneous distribution of soil properties. Moreover, unlike field experiments, real applications typically do not have the benefit of having a background image of the uncontaminated subsurface. It is not currently known under what circumstances ERT can be a valuable site investigation tool at DNAPL sites. It is expected that there exists a range of scenarios for which ERT would be a cost-effective strategy, and this will be a function of: (i) the degree of heterogeneity in the subsurface, (ii) the depth and geometry of the DNAPL source zone, and (iii) the extent of DNAPL mass removal during remediation. Moreover, this envelope of favourable conditions is likely dependent on the ERT survey design and processing methodology, neither of which have been optimized for DNAPL sites. It is possible that recent advances in ERT imaging (e.g., data acquisition and time-lapse monitoring), may be beneficial in this context (e.g., Ogilvy et al., 2009; Karaoulis et al., 2011a; Nenna et al., 2011). The

systematic, controlled studies required to explore these questions at the field scale are not available from field trials or laboratory studies.

The objective of this study is to develop a numerical model able to determine the conditions under which ERT is able to map realistic DNAPL source zones within realistic subsurface environments at the field scale. This paper presents the development of such a model, which couples a simulator for DNAPL evolution under release and remediation conditions with a simulator for the corresponding ERT response of the subsurface. Central to the model coupling is the linking of hydrogeological to geoelectrical parameters, and presented is a sensitivity to key elements of the chosen methodology. Finally, the paper presents the model's application to an example scenario. As a whole, the work provides a new, comprehensive model for ERT of DNAPL sites and demonstrates the potential of the model as a tool for better understanding the range of site conditions under which ERT may assist site remediation activities.

3.2 Model Development

3.2.1 Model Components

To simulate the electrical resistivity response of complex DNAPL architecture at the field scale, a novel coupling was developed between a model that simulates DNAPL contamination and remediation scenarios and one that simulates an ERT survey of the subsurface. Figure 3-1 highlights the key parameters that link the two models.

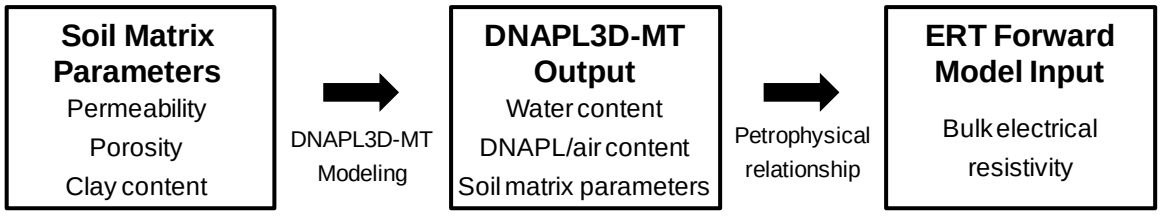

Figure 3-1: Schematic illustration of the parameters and steps considered during the coupled model development

DNAPL3D-MT (Grant and Gerhard, 2007a,b) is a three-dimensional, finite-difference, multiphase flow model that is well established for simulating the migration and dissolution of DNAPL in heterogeneous porous media. The model solves the mass conservation equations for the simultaneous flow of DNAPL and groundwater; air is considered a passive phase at atmospheric pressure throughout the vadose zone. Implicit solution of these equations with Newton-Raphson iteration provides the distribution of hydraulic head and DNAPL saturation (i.e., fraction of porosity occupied by DNAPL) throughout the domain at each timestep. These, in turn, provide local values of groundwater velocity and DNAPL-groundwater interfacial area, which are integrated with the solution of the advection-dispersion equation to provide DNAPL dissolution rates and contaminant concentrations in groundwater. The model, therefore, simulates a realistic initial distribution of DNAPL at a contaminated site and the complex pattern of DNAPL removal as it is dissolved by groundwater flowing through the site. Complete details on the model formulation and solution methods are provided in Gerhard and Kueper (2003a,b,c), Grant and Gerhard (2007a,b) and Grant et al. (2007a,b). The model has been used for numerous studies of DNAPL migration and dissolution at the field scale, including in three-dimensional (3D), heterogeneous domains (e.g., Alexandra et al., 2012). Although not considered for this work, the DNAPL model can also be employed to investigate reactive transport processes, including, chemical oxidation and bioremediation (e.g., West et al., 2008), and to simulate fractured rock environments (e.g., Pang et al., 2007).

While DNAPL3D-MT provides the distribution of DNAPL at each timestep during the evolution of a contaminated site, an ERT model is employed to simulate an ERT survey applied at the surface at regular intervals. Forward geoelectrical modelling was performed using a proven 3D algorithm which is fully described in Tsourlos and Ogilvy (1999). The forward model uses the finite element method to numerically solve Poisson's equation and mathematically predict the theoretical outcome (apparent resistivity) of a set of measurements from an ERT survey given a subsurface distribution of electrical resistivity. This particular forward modelling scheme has been used as a base in a number of modelling studies, including archeological investigations and salt tracer transport mapping (e.g., Papadopoulos et al., 2006; 2011; Karaoulis et al., 2011b).

As noted in Figure 3-1, the DNAPL model requires as input both intrinsic hydraulic permeability (k) and total porosity (ϕ), defined at the same spatial resolution as the finite difference grid. Heterogeneity of k, in particular, has long been known to be the dominant influence on the migration of DNAPL in soil and transport of dissolved contaminants in groundwater because k values naturally vary over at least 9 orders of magnitude (e.g., Freeze and Cherry, 1979). In previous modelling with DNAPL3D-MT, clay content was not explicitly identified; rather its effects on DNAPL, groundwater, and aqueous contaminant movement were implicitly accounted for in soil properties such as k, ϕ, retardation coefficients, etc. However, explicit clay content is important in this context since the porosity, bound water and specific surface area of clay significantly affects the electrical properties of soil. Moreover, as illustrated in Figure 3-1, the spatial distributions of air, DNAPL and water volumetric contents have a major influence on electrical resistivity (Archie, 1942). Therefore, central to linking the numerical models, was establishing a reliable set of relationships that provide an electrical resistivity field (input parameter for the ERT forward model) that accounts for the spatial heterogeneity of subsurface soils (including clay) and the evolving spatial distributions of fluids in the soil porosity (air, DNAPL, and water).

3.2.2 Model Linkage

The linkage methodology for this work is illustrated and detailed in Figure 3-2 and summarized in the following steps. Note that the methodology is described as applied to a single representative elementary volume of soil (i.e., single subsurface location, single node) but that it is applied to all locations in the domain simultaneously, once per timestep.

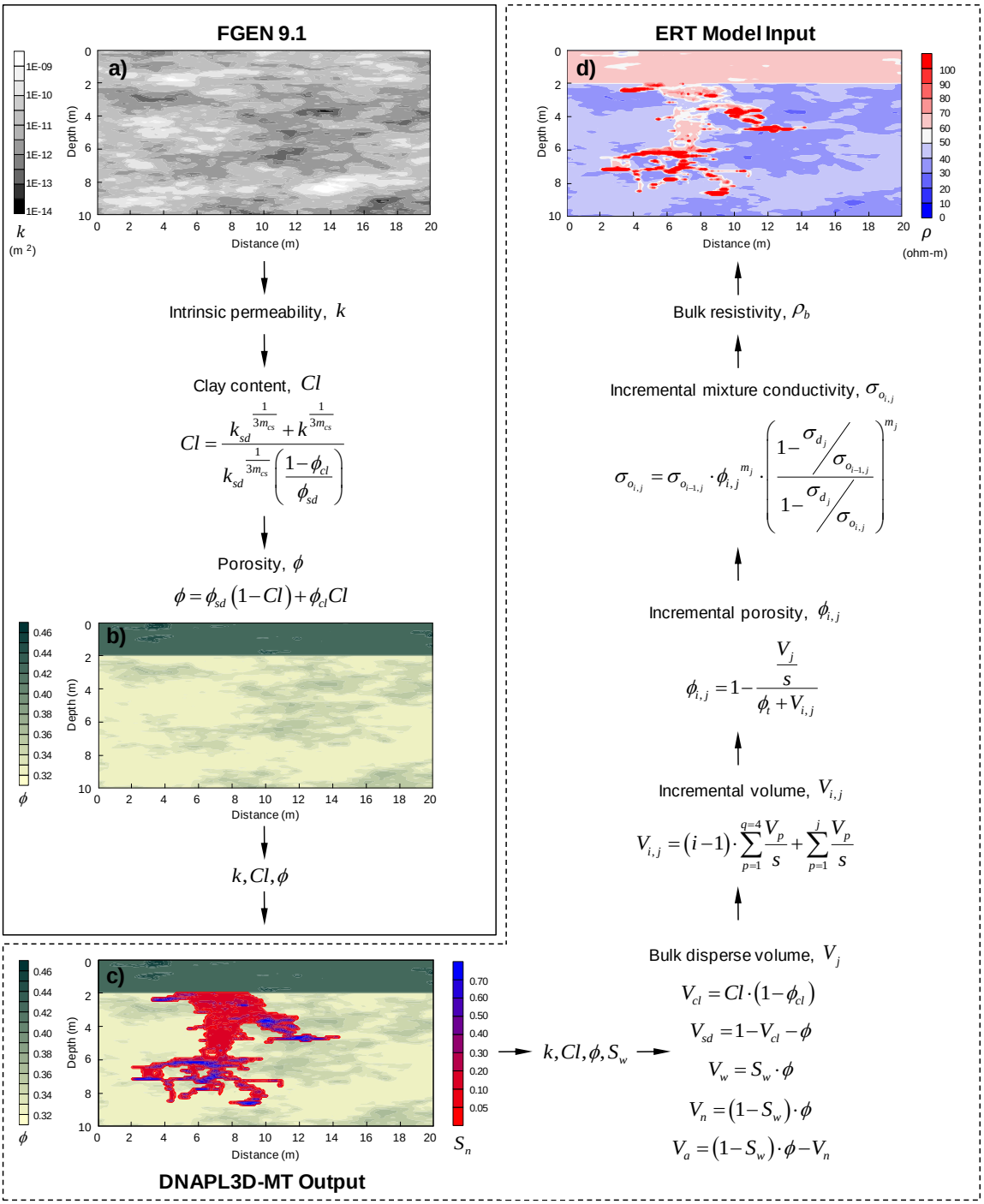

Figure 3-2: Schematic illustration of the methodology linking the multiphase flow model DNAPL3D-MT and the ERT forward model. The solid box encloses steps carried out once (at *time* = 0), whereas the dashed box encloses the linkage steps that are done repeatedly, once for each air/water/DNAPL configuration (i.e., at each timestep). A full description of the equations and images shown is provided in the text.

(i) Specify intrinsic hydraulic permeability

A random, spatially-correlated, intrinsic hydraulic permeability field is generated to provide a realistic subsurface distribution of k. For this work, the Field Generator (FGEN) algorithm of Robin et al. (1991) was used as it has been demonstrated to avoid the diagonal artifacts found in other methods and has been used widely in hydrogeological studies (e.g., Attinger et al., 2009; Alexandra et al., 2012). The value of k at each location is assumed to represent the total permeability resulting from a combination of clay and sand (volumetric fractions to be determined in subsequent steps).

(ii) Determine volumetric clay content

First, the lower threshold permeability of clean, clay-free sand, k_{sd}, is calculated (Revil and Cathles, 1999):

$$k_{sd} = \frac{{d_{sd}}^2 \left(\phi_{sd}\right)^{3m_{sd}}}{24}, \tag{3-1}$$

where d_{sd} is the mean grain diameter of sand [m], ϕ_{sd} is the porosity of sand and m_{sd} is the cementation exponent for sand. The values for these parameters are obtained from laboratory measurements and literature values. Note that k_{sd} is a single number for the entire domain and is invariant in time. For example, in this work, d_{sd} =2 x10^{-4} m, ϕ_{sd} =0.32, and m_{sd} =1.8, which provides k_{sd} = 3.6 x10^{-12} m^2, which corresponds to a fine sand. All k values greater than k_{sd} are taken as clay-free sand/gravel whereas k values below k_{sd} are indicative of sand containing a fraction of clay. It should be noted that k_{sd} can be determined using a number of methods, including laboratory and field measurements and empirical relationships such as the Kozeny-Carman equation (Bear, 1972).

Numerous studies of clay-sand mixtures have shown that an increase in clay content results in a decrease in permeability (e.g., Revil and Cathles, 1999; Schön and Georgi, 2003). Revil and Cathles (1999) developed an equation that determines the permeability of clay-sand mixtures as a function of volumetric clay content, and the porosities and permeabilities of pure sand and pure clay (the end members). Revil and Cathles (1999) demonstrated close agreement between predicted permeabilities and those measured over 11 orders of magnitude from available laboratory and core measurements. For this study, the equation by Revil and Cathles (1999) is rearranged to determine volumetric clay content Cl (ratio of clay, including water, to the whole soil volume) in terms of known parameters:

$$Cl = \frac{k_{sd}^{\frac{1}{3m_{cs}}} + k^{\frac{1}{3m_{cs}}}}{k_{sd}^{\frac{1}{3m_{cs}}}\left(\frac{1-\phi_{cl}}{\phi_{sd}}\right)}, \tag{3-2}$$

where m_{cs} is the cementation exponent corresponding to the clayey sand domain and ϕ_{cl} is the porosity of pure clay. Equation 3-2 determines the volume of clay based on the sand/clay mixture permeability, k, and the threshold sand permeability, k_{sd}, computed in Equation 3-1; for all locations where $k < k_{sd}$, the permeability is the result of a mixture of sand exhibiting a volume of clay Cl. Note that $Cl = 0$ for all nodes where $k > k_{sd}$. This model, with sand and clay co-existing at each macroscopic location, is valid as long as $Cl \le \phi_{sd}$; this is representative of clayey-sand mixtures relevant to hydrogeological studies (Giroux and Chouteau, 2008).

(iii) Determine total porosity and sand and clay volume fractions

The relationship between clay content and total porosity is influenced by the clay volume and its distribution within the porous matrix. Marion et al. (1992) derived a micro-

geometrical model based on adding clay such that it replaces sand porosity (i.e., pore-filling); the relationship for clay/sand mixtures exhibits a maximum clay content equal to the sand porosity and predicts decreasing electrical conductivity as clay content increases in a clayey sand (adding clay reduces total porosity). Alternatively, clay grains can be added in such a manner as to replace sand grains (e.g., de Lima and Sharma, 1990; Berg, 1995), such that total porosity is calculated:

$$\phi = \phi_{sd}\left(1 - Cl\right) + \phi_{cl} Cl \tag{3-3}$$

Equation 3-3 exhibits the property that electrical conductivity increases as clay content increases, which matches expectations. Equation 3-3 has been used in numerous studies for incorporating clay fractions in predictions of electrical resistivity (e.g., de Lima and Sharma, 1990; Berg, 2007). It is therefore adopted here to compute total porosity at each location in the domain, and the subsurface volume comprising each fraction of the soil matrix at each location is then given by:

$$V_{cl} = Cl \cdot \left(1 - \phi_{cl}\right) \tag{3-4}$$

$$V_{sd} = 1 - V_{cl} - \phi \tag{3-5}$$

where V_{cl} is the volume fraction of clay and V_{sd} is the volume fraction of sand.

(iv) Determine volume fractions of DNAPL and water

At each timestep, the DNAPL model solves for the fraction of pore space occupied by water, DNAPL and air. Therefore, the bulk volume occupied by each phase is:

$$V_w = S_w \cdot \phi \tag{3-6}$$

$$V_n = (1 - S_w) \cdot \phi \tag{3-7}$$

$$V_a = (1 - S_w) \cdot \phi - V_n \tag{3-8}$$

where V_w is the bulk water volume, V_n is the bulk DNAPL volume, V_a is the bulk air volume and S_w is the water saturation (fraction of pore space containing water). It is noted that while steps (i) to (iii) of this linking methodology are only executed once at the start of a new scenario, step (iv) is conducted once per timestep: after the DNAPL3D-MT model completes and before the ERT forward model is used.

(v) Modify the pore water resistivity to account for salinity and temperature

The electrical resistivity of natural waters is dependent on the concentration and mobility of dissolved ions present in the pore fluid. The solution resistivity decreases with (i) increasing ionic concentrations, with pore water resistivities ranging from ~100 ohm-m for freshwater aquifers to ~0.5 ohm-m for salt water (e.g., Loke, 2010), and (ii) increasing temperature, since the ionic mobility and degree of dissociation are temperature dependent. The effect of ionic concentration and temperature upon the electrical resistivity of the pore water is accounted for by using the model of Sen and Goode (1992):

$$\rho_w = 1 \Bigg/ \left[\left(5.6 + 0.27T - 1.5x10^{-4}T^2\right) \cdot C_f - \left(\frac{2.36 + 0.099T}{1.0 + 0.214C_f} \right) \cdot C_f^{\frac{3}{2}} \right], \tag{3-9}$$

where T is the temperature (ºC) and C_f is the ionic concentration (mol/L) associated with salinity. It is straightforward for the model to employ alternative relationships between electrical resistivity of pore water and concentration of a wider range of ions

(e.g., total dissolved solids, Schön, 1996). Thus, the model is well equipped to consider reactive transport processes that affect subsurface resistivity via dissolved ions such as biodegradation (e.g., Atekwana et al., 2005). This can be accomplished presently in an indirect manner by specifying elevated groundwater conductivity where dissolved phase solvent is present or, in future, directly by coupling biodegradation reactions in the plume to groundwater conductivity.

(vi) Determine overall resistivity

A variety of petrophysical relationships have been empirically and theoretically developed to relate electromagnetic to hydrogeological properties. Differential effective medium theories, which are reviewed by Cosenza et al. (2009), provide a rigorous and widely used theoretical approach. Bruggeman (1935) and Hanai (1960, 1961) considered the macroscopic electrical properties of a heterogeneous mixture based on the properties of its components. The Hanai-Bruggeman (HB) equation for complex conductivity (electrical resistivity is described in this section in terms of its reciprocal, electrical conductivity) of a two-component mixture of matrix and water is (Bussian, 1983):

$$\phi = \left(\frac{\sigma_w^*}{\sigma_o^*} \right)^{\frac{(m-1)}{m}} \cdot \left(\frac{\sigma_o^* - \sigma_m^*}{\sigma_w^* - \sigma_m^*} \right), \tag{3-10}$$

where σ_w^* is the complex water (continuous phase) conductivity [S/m], σ_o^* is the complex mixture conductivity [S/m], σ_m^* is the complex matrix (disperse phase) conductivity [S/m] and m is the cementation exponent. At low frequencies (i.e., dc resistivity), the imaginary term of the complex conductivity is insignificant and the real conductivity can be used; therefore, the complex conductivity notation will be dropped for this study. The HB equation is advantageous because (i) it reduces to Archie's law (Archie, 1942) at zero matrix conductivity, (ii) it permits the inclusion of a conductive matrix, with some approaches also permitting a non-zero sand and non-zero hydrocarbon conductivity (e.g.,

Berg, 1995; 2007), and (iii) it is formulated to handle frequency dependencies, complex conductivities and dielectric permittivities, which can be extended to study complementary geoelectrical techniques such as radar and spectral IP (e.g., Giroux and Chouteau, 2008; Revil, 2012).

Equation 3-10 has been the basis for a number of studies on the conductivity of clayey soils and rocks. Bussian (1983) developed a semi-empirical saturation model to demonstrate the suitability of the HB equation for the study of conductivity in rocks at low frequencies but it was approximated for a limited range of conditions. de Lima and Sharma (1990) used a first-principle approach to develop a model for adding clay and sand grains in small, but proportional amounts; however, it limits the cementation exponents for each component to a value of 1.5. Berg (1995) used volumetric-weighted averaging to associate hydrocarbons, in addition to the composite matrix (sand and clay) grains, with the disperse phase component of the HB equation. The main limitation of this particular model is that the host water must have a much higher conductivity than both the matrix and hydrocarbons; this may be true at high salinities but the accuracy of the approach may be affected at low water salinities and saturations (Berg, 2007). Revil et al. (1998) used the model by Bussian (1983) to account, in a more sophisticated way, for the surface conductivity of the electrical double layer at the grain/water interface; however a number of complex electrochemical variables were used and other studies treat surface conductance as an equivalent clay volume conductance (e.g., de Lima and Sharma, 1990). Berg (2007) presented a dispersed-clay algorithmic approach that accommodates simultaneous mixing of any number of disperse elements and is applicable to all frequencies, salinities and conductivities. This 'incremental' model uses discrete integration of the HB calculation to add tiny, but proportional, amounts of disperse elements into the disperse phase (matrix) component, including clay, sand and hydrocarbons (Berg, 2007). This method overcomes order-of-addition problems associated with a number of disperse components while also accommodating independent exponents for each disperse phase and their associated conductivities. Berg (2007) demonstrated that the model worked well on experimental data under a wide range of conditions and produced results very close to the results from other published models (e.g., Waxman and Smits, 1968; Bussian, 1983; de Lima and Sharma, 1990).

The incremental model by Berg (2007) was selected for this work as it is the most versatile and applicable to the wide range of conditions that are typically present in aquifers of primary interest in DNAPL studies. The disperse element associated with hydrocarbons in Berg (2007) will be used to account for the DNAPL and air components in this model. In the iterative inclusion process, the calculated mixture conductivity from the current iteration constitutes the fluid conductivity for the next iteration. The volumes for the four disperse elements (clay, sand, DNAPL and air) are divided into equal portions for each increment s. The disperse volume sum at each step is given by (Berg, 2007):

$$V_{i,j} = (i-1)\cdot\sum_{p=1}^{q=4}\frac{V_p}{s} + \sum_{p=1}^{j}\frac{V_p}{s}, \tag{3-11}$$

where $V_{i,j}$ is the volume sum at increment i and disperse element j, q is the number of disperse elements (q=4) and V_p is the bulk volume of each respective disperse element j. The porosity for each increment i at disperse element j is then given by (Berg, 2007):

$$\phi_{i,j} = 1 - \frac{\frac{V_j}{s}}{\phi_t + V_{i,j}}, \tag{3-12}$$

where V_j is the bulk volume of disperse element j, and ϕ_t is the total water volume ($\phi_t = S_w \cdot \phi$). The routine to calculate each incremental σ_o is based on Equation 3-10 which can be rearranged:

$$\sigma_{o_{i,j}} = \sigma_{o_{i-1,j}} \cdot \phi_{i,j}^{\,m_j} \cdot \left(\frac{1 - \sigma_{d_j} / \sigma_{o_{i-1,j}}}{1 - \sigma_{d_j} / \sigma_{o_{i,j}}} \right)^{m_j}, \tag{3-13}$$

where $\sigma_{o_{i,j}}$ is the electrical conductivity of the mixture at increment i and disperse element j, $\sigma_{o_{i-1,j}}$ is the electrical conductivity of the mixture of the previous increment which becomes the fluid conductivity for the current iteration, σ_{d_j} is the electrical conductivity of disperse element j, and m_j is the exponent related to disperse element j (cementation exponents m_{sd} and m_{cl} used for sand and clay inclusions, respectively, and saturation exponent n used for DNAPL and air inclusions). The routine computing Equation 3-13 is called $s \cdot q$ times, and each time the small volume portions are added to the mix. The 'final' incremental σ_o at increment s and disperse element q provides the overall bulk electrical conductivity of the heterogeneous mixture. This is computed once per timestep, after DNAPL3D-MT has provided the fluid saturation values, and before the ERT forward model is used.

The linkage methodology described in steps (i) – (vi) was written in MATLAB code that efficiently combined the FGEN, DNAPL3D-MT and ERT models. Solving the HB routine in Equation 3-13 for σ_o at each increment was accomplished using the Newton-Raphson technique for finding roots. The number of increments, s, was set to 100 as this provides sufficient accuracy (Berg, 2007). Effective medium models have a tendency to calculate different mixture conductivities depending on the order that the disperse elements are added; reversing the order of input of the disperse elements on each successive step of the incremental method overcomes this problem and further improves accuracy (Berg, 2007).

3.2.3 Sensitivity Analysis

The linkage methodology presented in this paper accounts for a number of hydrogeological and electrical parameters, each exhibiting an influence on the generated bulk electrical resistivity. Here, the sensitivity of predicted resistivity is considered as a function of assumptions used in the model, first at the scale of a single node and then at the scale of an entire domain. Figure 3-3a plots the predicted bulk resistivity value of a

single node as a function of DNAPL saturation and clay content (see curves labelled "Berg 07", presenting calculations with Equations 3-11 – 3-13 of the presented model). The node considered is below the water table, where $S_w + S_n$ = 1. The figure illustrates that, as expected, bulk resistivity increases with increasing DNAPL saturation, with the sensitivity becoming more pronounced as DNAPL saturation increases beyond 50%. Moreover, as expected, the addition of conductive clay decreases predicted resistivity. The presence of significant amounts of clay reduces the sensitivity to DNAPL saturation in the region S_n > 50% because this corresponds to low water content and thus the relative contribution of clay to the bulk resistivity is higher. A variety of geochemical processes and in situ conditions can influence the resistivity of groundwater. Figure 3-3b illustrates the sensitivity of predicted bulk resistivity to the assumed resistivity of groundwater and clay content in the absence of DNAPL. As expected, higher resistivity groundwater corresponds to increased bulk resistivity in the model. However, here too the sensitivity is diminished with increasing clay content.

In addition, Figure 3-3 compares this sensitivity of the presented model with that achieved when other formulations are used in place of Equations 3-11 – 3-13 (i.e., Waxman and Smits, 1968; de Lima and Sharma, 1990; Berg, 1995). It is evident that this model produces similar results to alternative models for the parameters used. The models are indistinguishable for the case of zero clay in both Figures 3-3a and 3-3b. Increased clay fractions produce some differences in the predicted bulk resistivity at very high DNAPL saturations (Figure 3-3a) and high water resistivities (Figure 3-3b); this is expected as these conditions approach or exceed the limiting condition implicit in de Lima and Sharma (1990, Equation 18) and Berg (1995) models which requires the water resistivity to be much less than the matrix resistivity. It is noted that Equation 3-13, used for this study, does not exhibit the same limitation.

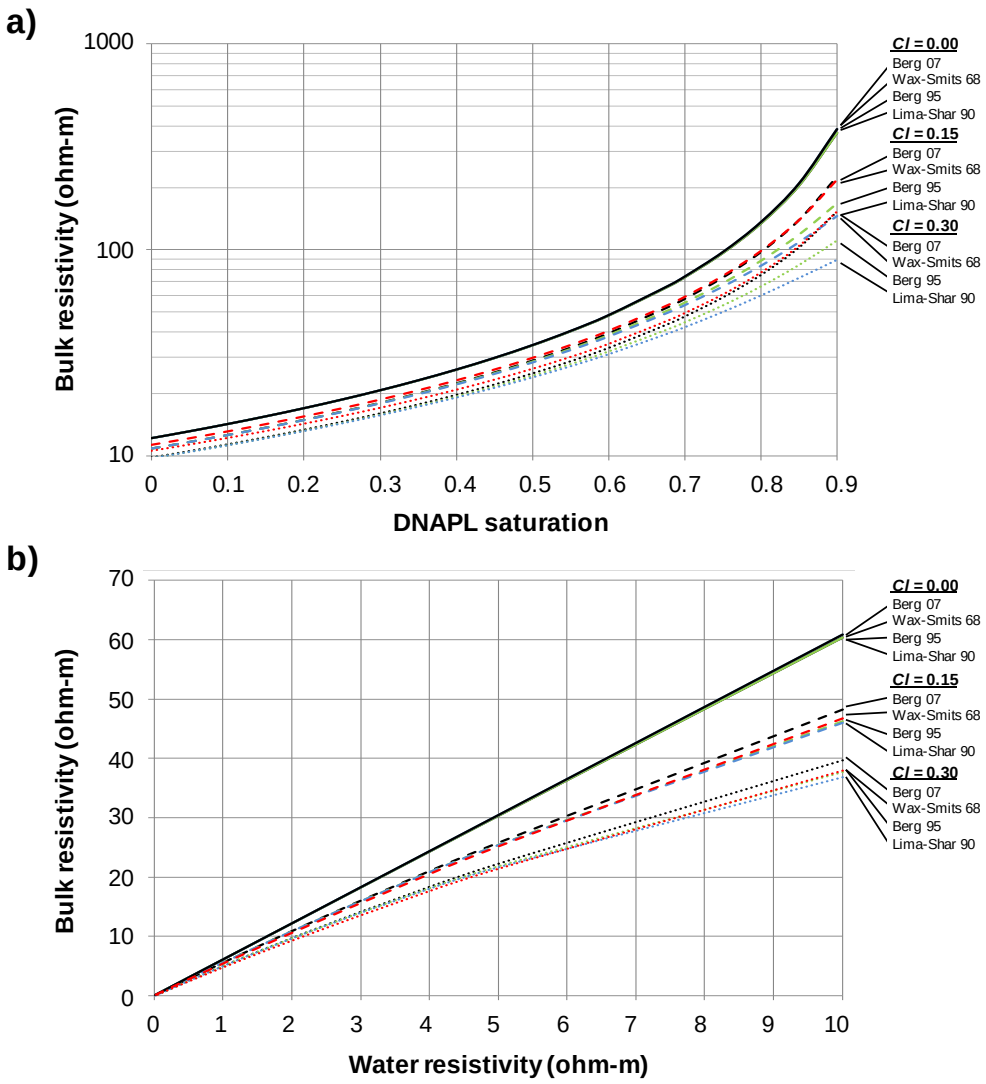

Figure 3-3: Bulk resistivity variation with (a) DNAPL saturation and (b) water resistivity, as a function of clay content (Cl = 0.0 (solid line); Cl = 0.15 (dashed); Cl = 0.3 (dotted)). Model used in this paper (Berg (2007); see Equations 3-11 – 3-13) compared to other published models. The input variables were: ρ_w = 2 ohm-m (Figure 3-3a), ρ_{cl} = 40 ohm-m, ρ_{sd} = 1000 ohm-m, ρ_n = 1.79 x 10^{11} ohm-m (Brewster and Annan, 1994), m_{sd} = m_{cl} = 1.5, S_n = 0.0 (Figure 3-3b), ϕ_{sd} = 0.30 and ϕ_{cl} = 0.40; values selected to meet the constraints of the other petrophysical models (i.e., exponents = 1.5 for Equation 18 of de Lima and Sharma (1990), $\rho_w < \rho_{cl} / \rho_{sd} / \rho_n$ for de Lima and Sharma (1990) and Berg (1995)). The cation exchange capacity of clay for Waxman and Smits (1968) comparison = 0.03 meq/g (i.e., kaolinite). Note that the vertical axis of Figure 3-3a employs a logarithmic scale.

To consider the model sensitivity at the domain scale, a DNAPL release scenario was simulated in a two-dimensional domain 20 m x 10 m deep, with a nodal spacing of 0.1 m in each direction resulting in 20,000 nodes. The *k*-field was generated with a mean *k* of 8.91 x10^{-11} m^2 (mean ln(*k*) = -25.4 m^2), variance ln(*k*) = 2.97 and an exponential auto-correlation structure of 5.0 m horizontally and 0.5 m vertically; the distribution of *k* for the single realization used is illustrated in Figure 3-2a (grey scale image where darker shades of grey correspond to lower permeability). Considering the saturated zone (20 m x 8 m deep, 16,000 nodes), the distribution of *k* values is illustrated by the histogram shown in Figure 3-4a. As discussed earlier, all *k* values less than the sand permeability threshold correspond to clay-containing soil (Equation 3-1); here k_{sd} = 3.6 x10^{-12} m^2 and Figure 3-4a illustrates that this corresponds to 4,913 nodes (31%) for this *k*-field. Figure 3-4b shows the corresponding distribution of clay content in the domain (Equation 3-2), with 4,913 nodes exhibiting $Cl > 0$ (mean Cl = 0.09, max Cl = 0.32). The distribution of total porosity is plotted in Figure 3-4c, illustrating that total porosity is equal to sand porosity at the 11,087 nodes containing zero clay and total porosity increases with increasing clay content (Equation 3-3). The spatial distribution of porosity is illustrated in Figure 3-2b (green scale with darker shades corresponding to higher clay content), revealing that higher clay content regions correspond to the low permeability lenses of Figure 3-2a.

The permeability, clay content and total porosity fields constitute the soil matrix domain into which a 1 m^3 release of trichloroethylene DNAPL (a common subsurface contaminant) was simulated. Figure 3-2c presents the spatial distribtuion of the DNAPL 10 days after the release, at which time the DNAPL has formed a complex source zone. As expected, DNAPL primarily occupies the higher permeability regions (i.e, low clay content) since these represent the least resistive flow pathways. Figure 3-4d demonstrates that the DNAPL occupies 2,313 nodes (14%) and exhibits saturations from 1% to 94% of the pore space (mean S_n = 25%).

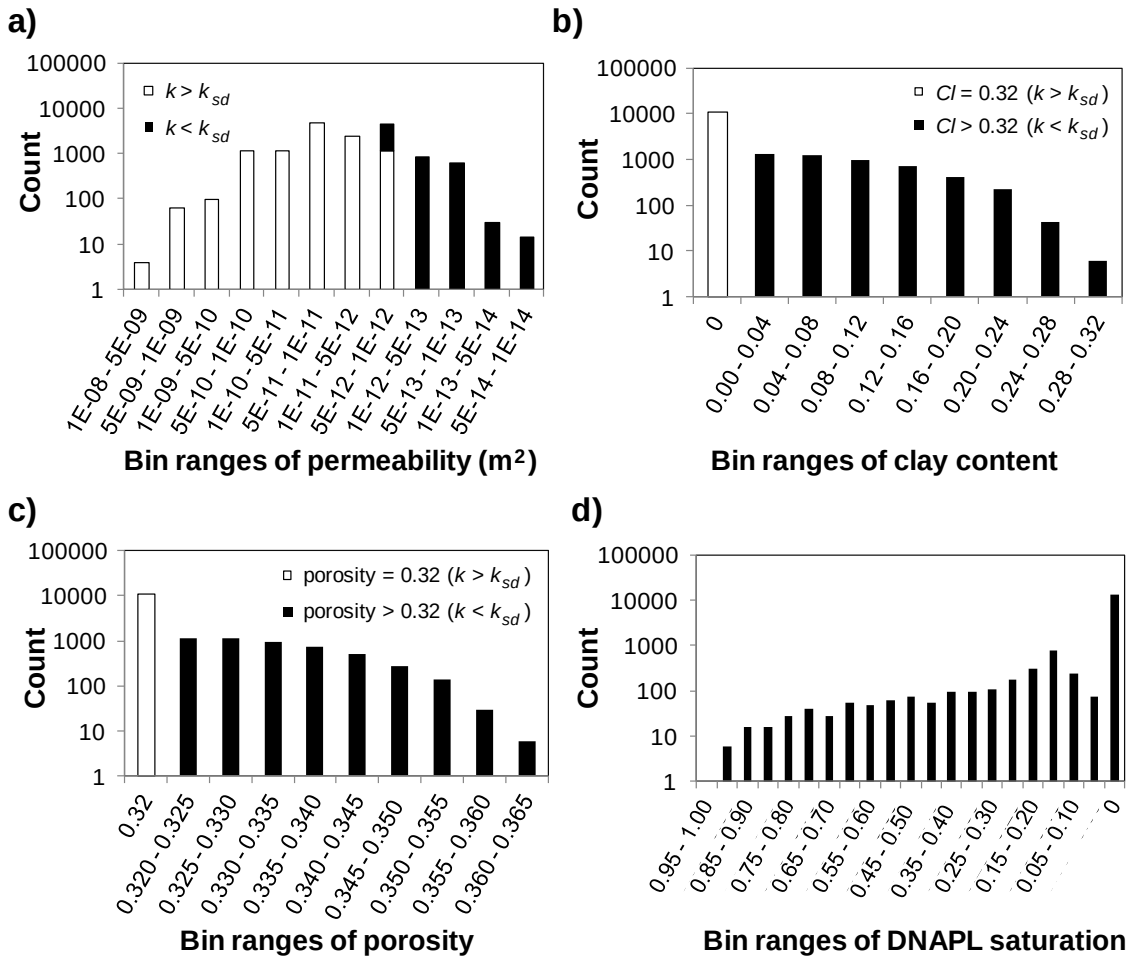

Figure 3-4: Histograms illustrating the distributions of the key model parameters for all of the nodes in the saturated zone for the example model domain illustrated in Figure 3-2: (a) intrinsic hydraulic permeability; (b) clay content; (c) total porosity; (d) DNAPL saturation values at t = 10 days. In all cases, counts are presented on a logarithmic axis.

As illustrated in Figure 3-2, in order for the model to predict bulk resistivity at each node, it is necessary to specify the concentration of ions in groundwater and the resistivity of the DNAPL; in this example, values of 900 ppm (e.g., Giroux and Chouteau, 2008) and 1.79 x 10^{11} ohm-m (e.g., Brewster and Annan, 1994) were used. Figure 3-5a reveals that the predicted bulk resistivities for the soil matrix only ranges from 48.17 ohm-m (clay-free soil) to 30.61 ohm-m (Cl = 0.3) (mean = 46.3 ohm-m). It further demonstrates that the presence of the DNAPL source zone (Figure 3-2c) results, as expected, in a wider

distribution of predicted values, ranging from 4228.7 ohm-m (Cl = 0.0, S_n = 0.94) to 30.6 ohm-m (mean = 58.7 ohm-m). The predicted spatial distribution of bulk resistivity is provided in Figure 3-2d, in which the strong contrast between the DNAPL and the background is evident; in addition, the variability predicted within the soil matrix is clear.

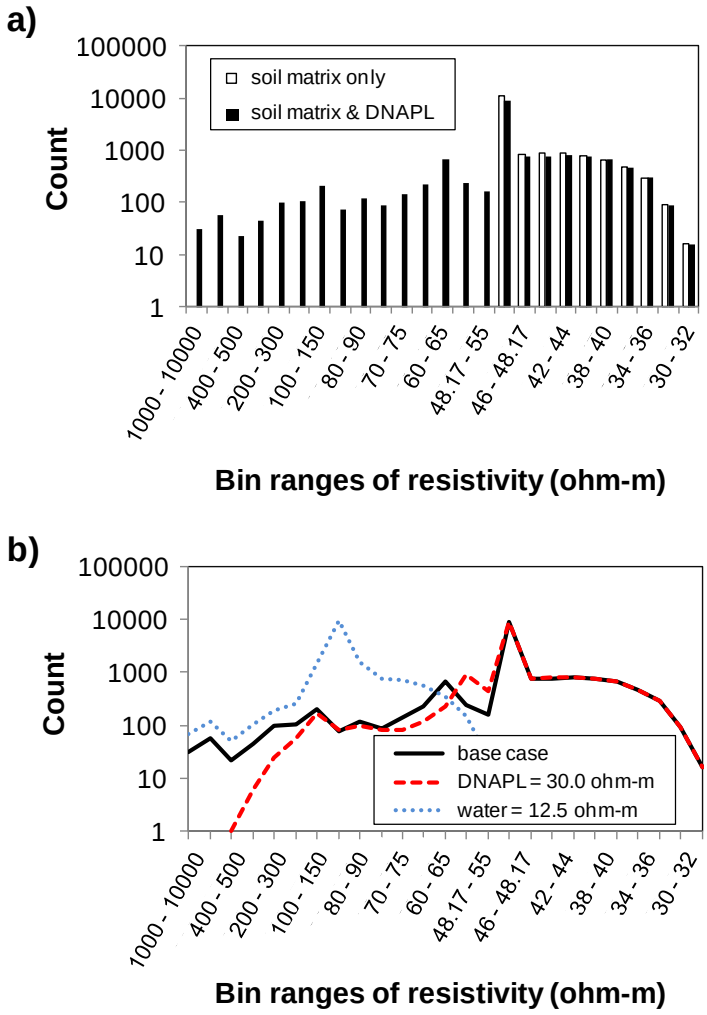

Figure 3-5: Histograms of predicted resistivity values for the saturated zone of the example model domain presented in Figure 3-2: (a) soil matrix only (white bars) versus soil matrix plus DNAPL (black bars); (b) soil matrix plus DNAPL (black line; identical to black bars in 3-5a) for base case (DNAPL = 1.79 x 10^{11} ohm-m, ionic concentration in water = 900 ppm)) compared to case with less resistive DNAPL (dashed gray line; DNAPL = 30 ohm-m, ionic concentration = 900 ppm) and case with increased water resistivity (dotted black line; DNAPL = 1.79 x 10^{11} ohm-m, ionic concentration = 450 ppm).

The sensitivity of the predicted bulk resistivity field to a number of key model parameters was investigated. Figure 3-5b again presents the distribution of resistivities related to the base case (DNAPL = 1.79 x 10^{11} ohm-m, ionic concentration in water = 900 ppm, and compares it to the case of a less resistive DNAPL (DNAPL = 30 ohm-m, ionic concentration = 900 ppm). It is evident that, as expected, the most significant influence is on the upper limit of predicted bulk resistivity values (i.e., highest DNAPL saturations) which reduced from 4,228.7 ohm-m to 406.4 ohm-m; less impact is observed in the middle range while, of course, no change is observed in DNAPL-free soil, resulting overall in a decrease in the mean bulk resistivity from 58.7 ohm-m to 49.6 ohm-m. A second comparison is made against a case in which the concentration of ions in the groundwater was decreased (DNAPL = 1.79 x 10^{11} ohm-m, ionic concentration = 450 ppm), thereby increasing the groundwater resistivity. Figure 3-5b illustrates that this resulted, as expected, in increased predicted resistivity values at all locations, with the range becoming 6,208.3 to 51.1 ohm-m and the mean increasing from 58.7 ohm-m to 111.7 ohm-m. It is evident from the variations in the distribution of resistivities that the coupled model is handling changes in key model parameters as expected.

3.3 Demonstration Simulation

3.3.1 DNAPL Spill Scenario

A field scale contamination scenario was simulated in a three-dimensional model domain with a surface area of 12 m long (*x*-direction) by 12 m wide (*y*-direction), and a depth of 4 m (*z*-direction). The domain was discretized into 73,728 nodes with a nodal spacing of 0.250 m in the *x*- and *y*-directions and 0.125 m in the *z*-direction. The domain used a random, spatially-correlated, k field generated using FGEN to represent the heterogeneous subsurface. The permeability generator used an exponential autocorrelation function with the statistics provided in Table 3-1, based on an aquifer in Canada on which a detailed geostatistical analysis was conducted (Sudicky et al., 2010). The corresponding clay content and total porosity at each node was determined from the presented linkage methodology (Equations 3-2 – 3-3). 26% (19,063 nodes) were

determined to exhibit $Cl > 0$, with a mean $Cl = 0.08$ and variance of $Cl = 0.003$. For the entire domain, the mean total porosity = 0.33 and the variance of porosity = 0.001. The result was a domain with unconsolidated porous media dominated by horizontal lenses exhibiting a distribution of permeability, porosity, and clay content representative of an aquifer characterized, on average, by a medium sand and encompassing soils ranging from clay to gravel.

Table 3-1: Hydrogeological parameters

Parameter	**Value**	**Units**
Mean (ln *k*) [1]	-25.4	m^2
Variance (ln *k*) [1]	1.94	-
Correlation lengths [1]	4.0 (horizontal); 0.5 (vertical)	m
Sand porosity [2]	0.32 (saturated); 0.46 (vadoze)	-
Clay porosity [2]	0.42 (sat.); 0.56 (vadoze)	-
Particle diameter for sand [2]	2×10^{-4} (sat.); 6×10^{-5} (vadoze)	m
Water density [3]	1000	kg/m^3
Water viscosity [3]	0.001	Pa·s
DNAPL density [3]	1170	kg/m^3
DNAPL viscosity [3]	0.0005	Pa·s
DNAPL solubility [4]	5100	mg/L
DNAPL-water interfacial tension [4]	0.04	N/m

[1] Grant and Gerhard (2007a)

[2] Bear (1972)

[3] Gerhard et al. (2007)

[4] Mercer and Cohen (1990)

The water table was established at 0.250 m below ground surface, below which the domain was initially fully saturated with water ($S_w = 1$). Above the water table, the domain was partially saturated ($S_w = 0.7$). The near surface soils in the vadose zone contained higher porosity and smaller particle sizes than deeper soils (e.g., Revil and

Cathles, 1999). In this simulation, the capillary fringe is assumed to be negligible; while it is acknowledged that explicitly incorporating a capillary fringe may provide a more gradual transition in electrical properties, it is not expected to significantly impact the conclusions of this work. The side boundaries were characterized by fixed, hydrostatic water pressures that established an ambient hydraulic gradient of 0.01 from left to right across the domain and the bottom boundary was set as impermeable to both DNAPL and water.

The release of a chlorinated solvent DNAPL commonly found at contaminated sites, 1,1 dichloroethylene (1,1 DCE) (note that TCE was used in the sensitivity analysis above), was simulated through a 1.0 m^2 patch area located centrally in the domain (in plan view) and located coincident with the water table. Table 3-1 provides the fluid properties used. The aim was to mimic a leaking underground storage tank or the bottom of a waste lagoon. To achieve this in the model, a constant DNAPL flux was assigned to each node within the patch area, with the value assigned weighted according to the node's *k* and ensuring the sum achieved a total flux of 1.3 m^3/day (Grant et al., 2007a). The source was initiated at time $t = 0$ and was turned off at $t = 1$ day, representing the release of 1.3 m^3 (1,300 litres) of DNAPL. In order to achieve a realistic initial distribution of DNAPL in the subsurface, the DNAPL was allowed to continue to migrate under gravity and capillary forces for 6 days after the source was turned off. During this time, no DNAPL was permitted to dissolve and, at $t = 7$ days – coinciding with the start of the ERT survey – the resulting DNAPL distribution was "immobilized" so that no further DNAPL migration occurred. The purpose of these modelling steps were (a) to ensure that the full 1300 litres was retained as the initial DNAPL volume, and (b) to ensure that the only signal available for subsequent geophysical detection was DNAPL disappearance. These simplifying assumptions are reasonable considering the focus of this paper is on demonstrating a DNAPL-ERT resistivity model linkage. Note that a subsequent publication will focus on using the developed model to evaluate the ability of ERT to track DNAPL remediation for a range of DNAPL release scenarios, soil types, and soil distributions.

At t = 7 days, DNAPL dissolution was enabled, and the simulation was then continued until t = 1.3 years by which time all of the released DNAPL mass had dissolved into the ambient groundwater flowing through the source zone. It is acknowledged that 1,1 DCE has a relatively high solubility in groundwater (Table 3-1), and complete natural dissolution of a DNAPL source zone could require decades (Kueper et al., 2003). Engineered remediation of DNAPL source zones, however, can substantially accelerate DNAPL mass removal rates. The rate of mass removal is independent of the objectives of this work.

The electrical properties assigned to each soil and fluid constituent are presented in Table 3-2. In this study, the pore water was at a temperature of 20 ºC and composed of Na^+ and Cl^- ions at 900 ppm concentration, which is within the range usually characterized as fresh water. The resistivity values assigned to each soil type are assumed to be independent of temperature variations. The resistivity of clay could be calculated to account for the surface conductivity at the grain water interface (e.g., Revil et al., 1998); however, for this demonstration, an equivalent clay volume conductance is obtained from the literature.

Table 3-2: Electrical parameters

Parameter	Value	Units
Water resistivity [5]	6.5	ohm-m
DNAPL resistivity [6]	1.79×10^{11}	ohm-m
Air resistivity [6]	1.79×10^{11}	ohm-m
Sand resistivity [7]	500	ohm-m
Clay resistivity [7]	30	ohm-m
Saturation exponent [8]	2.0	-
Cementation exponent for sand [9]	1.8	-
Cementation exponent for clay [9]	2.7	-

[5] Calculated from Equation 3-9 in this chapter

[6] Brewster and Annan (1994)

[7] Loke (2010)

[8] Berg (2007)

[9] Revil and Cathles (1999)

3.3.2 ERT Modelling and Inversion

Site investigation and remediation of DNAPL sites invariably begins subsequent to a known or discovered release. For this study, it was assumed that site investigation by ERT was initiated at t = 7 days. ERT surveys were simulated at intervals corresponding to 10% reductions of DNAPL mass to obtain 10 time-lapsed images of the site remediation during the source zone lifespan (corresponding to t = 9, 15, 24, 35, 50, 72, 100, 144, 226, 474 days). The geoelectrical modelling finite element mesh, employing hexahedral elements, was designed with the same resolution as the DNAPL model finite difference grid, thereby permitting the underlying hydrogeological parameters of the latter to be directly assigned 1:1 (i.e., no interpolation necessary) as a total resistivity value to each finite element block (as determined by the linkage methodology described in Equations 3-1 – 3-13). Each three-dimensional ERT survey was simulated using dense, parallel survey lines traversing only in the x-direction (e.g., Papadopoulos et al., 2006; 2007); the pole-dipole configuration in a combined forward and reverse mode (A-

MN and NM-A) was used, with an inline electrode spacing of 0.5 m (25 electrodes along each survey line) and an interline spacing of 0.5 m (25 survey lines). Furthermore, to render modelling results more realistic, random noise with a Gaussian distribution of 3 mV/A peak-to-peak amplitude was added to the synthetic potential difference data.

An inversion algorithm is required to invert the (observed) apparent resistivity values in order to obtain the "true" subsurface resistivity distribution. The ERT inversion program DC_3DPro (Yi et al., 2001; Kim and Yi, 2010) was utilized for this study; DC_3DPro performs three-dimensional, iterative smoothness constrained inversion and uses the active constraint balancing technique in order to calculate efficiently the Lagrangian multiplier vector for each iteration (Yi et al., 2003). Independent inversion of each ERT survey was used. Future work will consider a detailed study of time-lapse monitoring and the optimal array configuration, inversion algorithm and processing methodology for tracking DNAPL remediation.

3.3.3 ERT Detection of DNAPL Source Zone

Figure 3-6a illustrates the three-dimensional hydrogeological model domain at the start of the ERT investigation (i.e., 100% DNAPL remaining), while Figures 3-6c and 3-6e show cross-sectional and plan-view images of the subsurface, respectively. The figures reveal that DNAPL has penetrated to 3 m depth in the subsurface and spread to cover an area approximately 4 m × 4 m in plan view. The DNAPL is observed to consist of a complex network of pools and residual, exhibiting a range of DNAPL saturations from 1% to 74% of the pore space. Three distinct pools of high DNAPL saturation exist at 0.5 m, 1.5 m and 2.5 m depths (see Figure 3-6c), hereafter named Pool 1, Pool 2 and Pool 3, respectively. Qualitative consideration of the corresponding true (inverted) resistivity distribution (see Figures 3-6b, 3-6d and 3-6f) suggests that the combined DNAPL-ERT simulation produced realistic ERT images of both (i) the subsurface heterogeneity, and (ii) the DNAPL body.

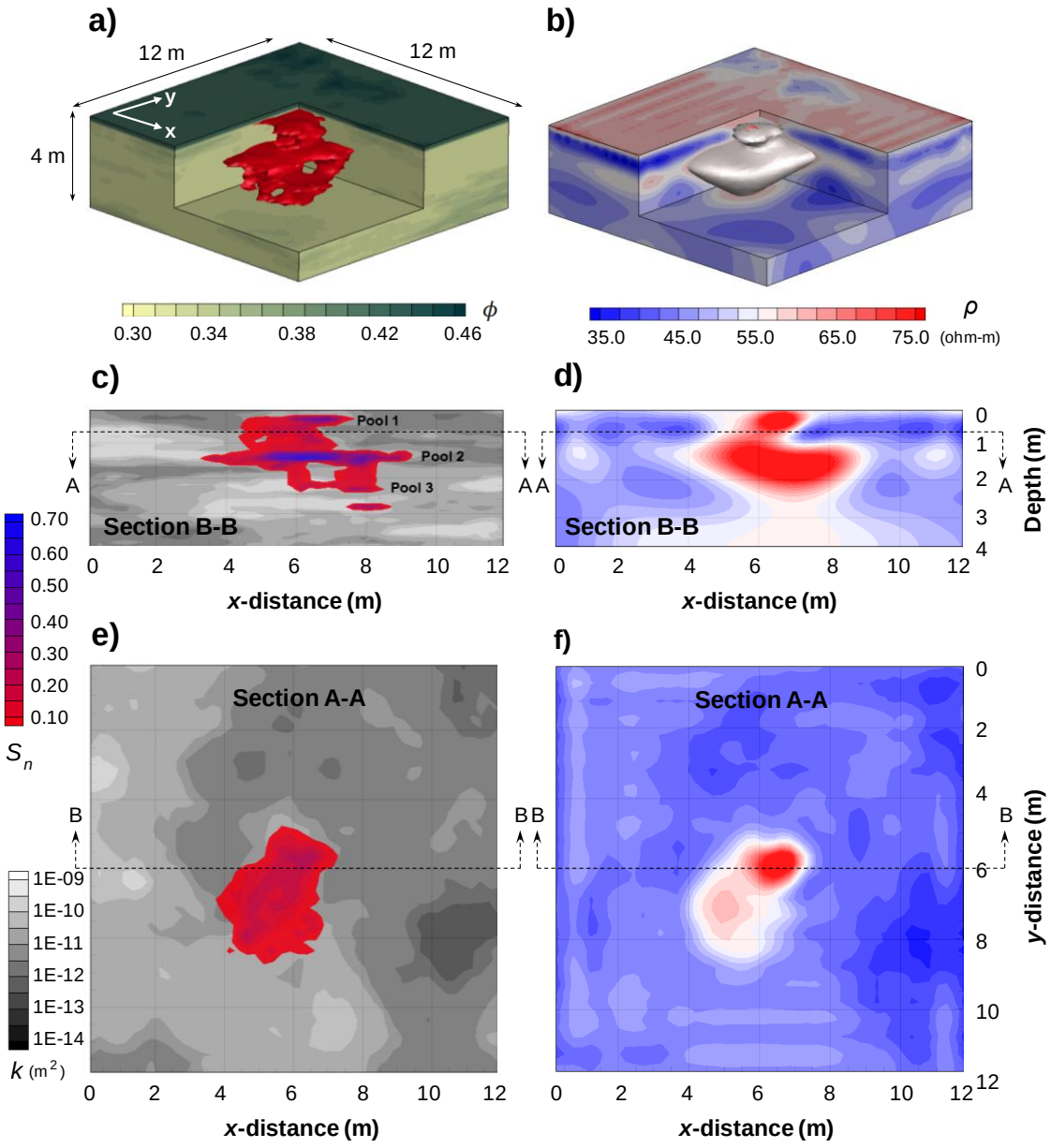

Figure 3-6: Field scenario 7 days after DNAPL release: (a) 10% DNAPL saturation isosurface, (b) 56 ohm-m resistivity isosurface; (c, e) DNAPL saturation distribution in cross-section and plan view; (d, f) corresponding resistivity distribution. A threshold DNAPL saturation of 10% corresponds to a threshold resistivity of 56 ohm-m, as determined by the linkage model.

In Figure 3-6b, the higher resistivity (red), near-surface response corresponds to the vadose zone. Notice that within the vadose zone there happened to exist a lower

resistivity (blue) region corresponding to the higher porosity (and higher clay content) region shown in Figure 3-6a (dark green). The hydrogeological and resistivity plan-view images at 0.5 m depth (Section A-A) presented in Figures 3-6e and 3-6f, respectively, again demonstrate that the soil matrix variability is realistically simulated in the ERT response; for example, the lowest resistivities (dark-blue) in Figure 3-6f correspond to higher clay contents associated with the lowest permeabilities (dark-grey) in Figure 3-6e. Figures 3-6c and 3-6d, which present the cross-sectional images at 6 m in the y-direction (Section B-B), reveal that the ERT response reasonably accounts for the soil matrix variability in the near-surface soil (top 1 m), but is unable to detect variability at larger depths, which is expected since ERT sensitivity reduces with depth.

The strongest contrasts in the ERT response are representative of the water-DNAPL distinction, and it is evident that the DNAPL distribution is reasonably imaged by the simulated ERT survey. For example, the true resistivity distribution in Figure 3-6d indicates two distinct zones of high resistivity (red) at depths intervals of 0.2 – 0.5 m and 1.0 – 2.5 m, respectively. These zones correspond to the DNAPL pools: ERT resolved Pool 1 from Pool 2, but was unable to resolve the deeper Pool 3, instead enveloping both Pool 2 and Pool 3. This is expected due to the reduced sensitivity of ERT with depth and the fact that shallow targets can interfere with the detection of deeper targets. Thus, it is not surprising that the detailed distribution of pools characteristic of a complex DNAPL may be challenging to resolve.

A number of methods can be used to provide optimum subsurface information, including informed ERT survey design (e.g., Nenna et al., 2011), and future work will explore these techniques in the context of DNAPL investigations. However, overall, Figure 3-6 suggests that, at favourable sites, ERT may be suitable for determining the outer boundaries of the location and depth of a DNAPL body in heterogeneous porous media, with increased resolution towards the surface as expected.

3.3.4 Mapping DNAPL Remediation

It is acknowledged that a number of factors may change the magnitude of the DNAPL signal relative to the background, including an increase in the soil matrix heterogeneity and clay content, and evolving resistivity of the DNAPL plume (e.g., enhanced conductivity due to biodegradation). However, time-lapse monitoring of DNAPL remediation may remain promising even in such scenarios, since the background heterogeneity is constant and the evolving signal directly corresponds to changes in DNAPL mass and distribution. As mentioned, ERT surveys were simulated at intervals corresponding to ~10% reductions of the DNAPL mass. While difference or four-dimensional inversion routines (e.g., Kim et al., 2009; Karaoulis et al., 2011a) may best take advantage of the differences detected, such optimization of the ERT analysis for DNAPL remediation is the subject of future work.

Figures 3-7a and 3-7c reveal that, as expected, DNAPL mass was removed from the source zone in a heterogeneous manner (compare to Figure 3-6c). For example, the majority of the residual DNAPL was dissolved first, as is common (e.g., Grant and Gerhard, 2007b). As well, Pool 3 disappeared relatively early since it resided in a relatively high permeability zone that experienced significant groundwater flux. With 58% of the DNAPL removed, the remaining source zone was dominated by Pools 1 and 2. Figures 3-7b and 3-7d reveal that the ERT response changed correspondingly to the mass reduction of DNAPL. In fact, since the parts of the source zone first remediated were, coincidentally, the low saturations and the deepest pool (i.e., the DNAPL that was the least well-resolved by ERT), the inverted images became more effective at characterizing the source zone during remediation.

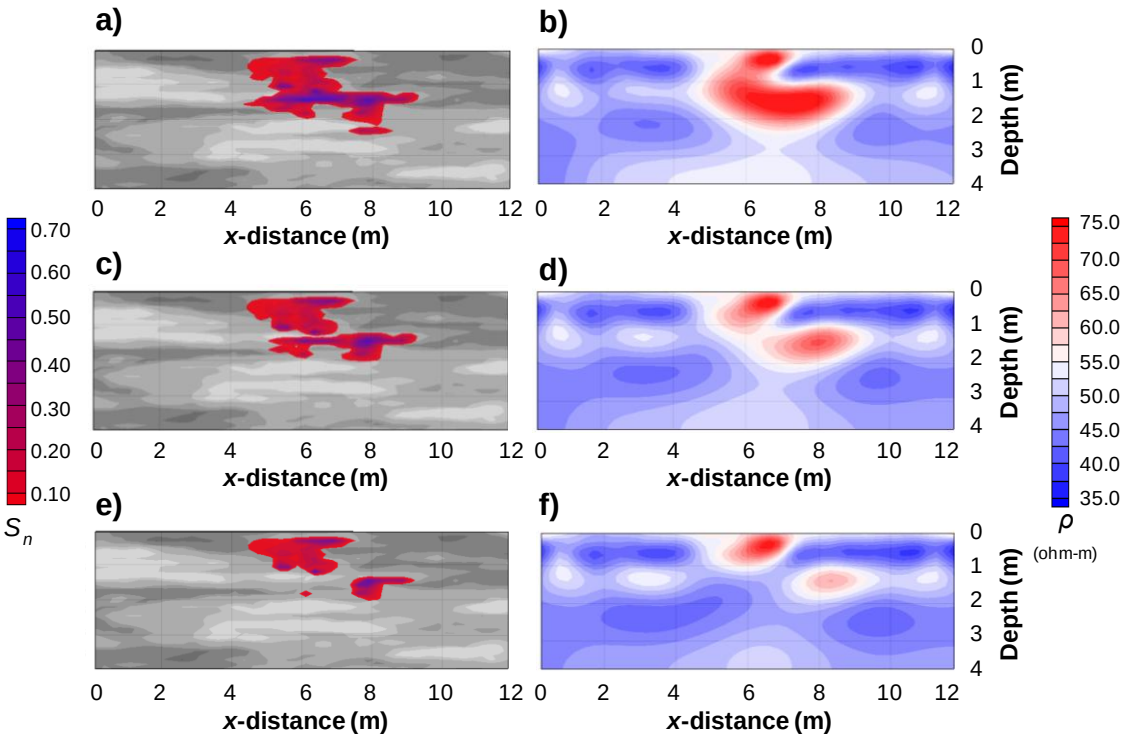

Figure 3-7: Cross-section of spill scenario after (a) 28%, and (c) 58%, and (e) 78% of the original DNAPL mass has been removed; and the corresponding resistivity distribution after (b) 28%, (d) 58%, and (f) 78% of the DNAPL mass has been removed.

While it is not possible to extrapolate generally based on a single case, and the 'fortuitous' removal of the deepest pool will not always occur, it is generally true that DNAPL source zone geometry simplifies with time and become characterized by isolated, substantial DNAPL pools. This may lead to continual improvement of the ERT response as remediation progresses. Overall, this work suggests that ERT may be promising in revealing reductions in DNAPL mass over time.

3.4 Discussion

The coupled multiphase-geophysics numerical model presented is able to account for various hydrogeophysical parameters, including groundwater quality (e.g., salinity, temperature), soil matrix (e.g., heterogeneity, clay content) and electrical (e.g., conductivities, survey design, inversions) properties. This universal linkage model permits simultaneous mixing of any number of disperse elements and accommodates geometric factors, such as sand and clay porosity exponents and saturation exponents, for each disperse element and its associated resistivity. In addition, the model can handle complex conductivities and complex dielectric permittivities which may permit future modelling work on complementary geoelectrical methods (e.g., spectral induced polarization and ground penetrating radar).

A sensitivity analysis of the predicted bulk resistivity, conducted at the scale of a single location and an entire domain, provided confidence in the linkage methodology presented. As expected, bulk resistivity increases with (i) increasing DNAPL saturation, (ii) higher resistivity groundwater (corresponding to reduced groundwater salinity), and (iii) reduced clay fraction. Furthermore, the relative contribution of clay to the bulk resistivity is higher in regions of high DNAPL saturation and/or high water resistivity. Analysis of the model sensitivity for a 2D case demonstrated that a realistic distribution and correlation of hydrogeological parameters, including hydraulic permeability, clay content and porosity, were generated and (with the addition of the DNAPL distribution) subsequently mapped to a realistic distribution of bulk electrical resistivity. The presented model was demonstrated to provide a good match to other published models across a range of key parameters within the bounds to which those other models can be applied. However, the presented model can also be applied outside these bounds and can work at all water salinities and tool frequencies.

A three-dimensional, field scale, surface release of a chlorinated solvent DNAPL into heterogeneous clayey sand, including complete DNAPL remediation and its mapping by time-lapsed surface ERT surveys, demonstrated realistic ERT responses that were sensitive to heterogeneity in both soil properties and DNAPL saturations. While static

detection of the initial DNAPL distribution appears possible under ideal circumstances, it is expected to be challenging in most sites due to the difficulty in distinguishing these two complex signals. However, the simulated ERT response appears sensitive to changes in the mass and distribution of DNAPL, suggesting that ERT has the potential for tracking the time-lapsed remediation of a DNAPL source zone. Such a non-invasive tool, which could map where and how quickly DNAPL mass changes with time during site cleanup, would be a major step forward in remediation practice.

A number of simplifying assumptions in the demonstration case were used for the purposes of this initial, exploratory work. The water table was relatively shallow for an unconfined aquifer and contained moderate water saturations with no capillary fringe effects. A resistive DNAPL was assumed in the presence of groundwater exhibiting constant, moderate conductivity. It is acknowledged that some biogeochemical reactions, including those associated with biodegradation, occurring within the contaminant plume emanating from a DNAPL source zone may raise groundwater conductivity. Such reactions may increase the water-DNAPL electrical contrast when substantial DNAPL remains but may also complicate the mapping of DNAPL disappearance if bulk resistivity is decreasing due to both effects concurrently. Future simulations will examine this by prescribing elevated groundwater conductivity where dissolved phase solvent is present in the subsurface. Moreover, the model, which can simulate biodegradation directly, can be enhanced further in future to link degradation byproducts to groundwater conductivity directly to evaluate the potential impacts of these transformations on the ability of ERT to track DNAPL remediation.

With respect to the presented linkage methodology, this work considers clayey-sand mixtures where the maximum volume of clay added to the model domain is constrained by the porosity of sand; however, this is not considered a restrictive constraint for many materials relevant to hydrogeological studies. Each of the published relationships associated with the linkage methodology have been independently validated against experimental data. However, it is acknowledged that the presented model as a whole has not been validated against experiments and potential uncertainties may exist in the underlying petrophysical relationships or their cumulative predictions.

3.5 Conclusions

A numerical model was presented that creates a novel and robust link between a multiphase flow model, which generates realistic DNAPL release scenarios, and an ERT model, which simulates the corresponding resistivity response. Sensitivity studies and a field scale simulation demonstrated the performance of the model and its sensitivity to both variations in DNAPL distribution and subsurface heterogeneity. Results suggest that the coupled model can be a valuable and reliable research tool and provide a cost-effective means to develop and evaluate optimum ERT data acquisition, inversion and interpretative tools for contaminated sites. This initial study will be a basis for future work, concentrating on (i) site characteristics most suited to ERT success (ii) detailed time-lapse monitoring of DNAPL remediation, (iii) validating the synthetic ERT data with field results, and (iv) extending the work to examine the benefits of complementary geoelectrical surveys.

3.6 References

Alexandra, R., J.I. Gerhard, and B.H. Kueper. 2012. Hydraulic displacement of dense, nonaqueous phase liquids for source zone stabilization. Ground Water, 50: 765-774.

Archie, G.E. 1942. The electrical resistivity log as an aid in determining some reservoir characteristics. Transactions of the AIME, 146: 54–62.

Atekwana, E.A., E. Atekwana, F.D. Legall, and R.V. Krishnamurthy. 2005. Biodegradation and mineral weathering controls on bulk electrical conductivity in a shallow hydrocarbon contaminated aquifer. Journal of Contaminant Hydrology, 80: 149-167.

Atekwana, E.A., and E.A. Atekwana. 2009. Geophysical signature of microbial activity at hydrocarbon contaminated sites: a review. Surveys in Geophysics, 31: 247-283.

Attinger, S., J. Dimitrova, and W. Kinzelbach. 2009. Homogenization of the transport behavior of nonlinearly adsorbing pollutants in physically and chemically heterogeneous aquifers. Advances in Water Resources, 32: 767

Bear, J. 1972. Dynamics of fluids in porous media. Dover, Mineola, New York.

Berg, C.R. 1995. A simple effective-medium model for water saturation in porous rocks. Geophysics, 60: 1070–1080.

Berg, C. 2007. An effective medium algorithm for calculating water saturations at any salinity or frequency. Geophysics, 72(2): E59-E67.

Brewster, M.L., and A.P. Annan. 1994. Ground-penetrating radar monitoring of a controlled DNAPL release: 200 MHz radar. Geophysics, 59: 1211-1221.

Brewster, M.L., A.P. Annan, J.P. Greenhouse, B.H. Kueper, and G.R. Olhoeft. 1995. Observed migration of a controlled DNAPL release by geophysical methods. Ground Water, 33: 977-987.

Bruggeman, D.A.G. 1935. The calculation of various physical constants of heterogeneous substances: I. The dielectric constants and conductivities of mixtures composed of isotropic substances. Ann. Phys., 24: 636–664 (in German).

Bussain, A.E. 1983. Electrical conductance in a porous medium. Geophysics, 48: 1258–1268.

Cardarelli, E., and G. Di Filippo. 2009. Electrical resistivity and induced polarization tomography in identifying the plume of chlorinated hydrocarbons in sedimentary formation: a case study in Rho (Milan-Italy). Waste Management & Research, 27: 595–602.

Chambers J.E., M.H. Loke, R.D. Ogilvy, and P.I. Meldrum. 2004. Noninvasive monitoring of DNAPL migration through a saturated porous medium using electrical impedance tomography. Journal of Contaminant Hydrology, 68: 1–22.

Chambers, J.E., P.B. Wilkinson, G.P. Wealthall, M.H. Loke, R. Dearden, R. Wilson, D. Allen, and R.D. Ogilvy. 2010. Hydrogeophysical imaging of deposit heterogeneity and groundwater chemistry changes during DNAPL source zone bioremediation. Journal of Contaminant Hydrology, 118: 43-61.

Cosenza, P., A. Ghorbani, C. Camerlynck, F. Rejiba, R. Guérin, and A. Tabbagh. 2009. Effective medium theories for modeling the relationships between electromagnetic properties and hydrological variables: a review. Near Surface Geophysics, 7: 563–578

Daily, W., and A. Ramirez. 1995. Electrical resistance tomography during in-situ trichloroethylene remediation at the Savannah River Site. Journal of Applied Geophysics, 33: 239–249.

Dekker, T.J., and L.M. Abriola. 2000. The influence of field-scale heterogeneity on the surfactant-enhanced remediation of entrapped nonaqueous phase liquids. Journal of Contaminant Hydrology, 42: 219-251.

de Lima, O. A. L., and M. M. Sharma. 1990. A grain conductivity approach to shaly sandstones. Geophysics, 55: 1347–1356.

Dhu, T., and G. Heinson. 2004. Numerical and laboratory investigations of electrical resistance tomography for environmental monitoring. Exploration Geophysics, 35: 33–40.

Freeze, R. A., and J. A. Cherry. 1979. Groundwater: Prentice Hall Inc.

Gerhard, J. I., B.H. Kueper, G.R. Hecox, and R. Schwarz. 2001. Site-specific design for dual phase recovery and stabilization of pooled DNAPL. Ground Water Monitoring and Remediation, 21: 71-88.

Gerhard, J.I., and B.H. Kueper. 2003a. Capillary pressure characteristics necessary for simulating DNAPL infiltration, redistribution, and immobilization in saturated porous media. Water Resources Research, 39: 1212.

Gerhard, J.I., and B.H. Kueper. 2003b. Relative permeability characteristics necessary for simulating DNAPL infiltration, redistribution, and immobilization in saturated porous media. Water Resources Research, 39: 1213.

Gerhard, J.I., and B.H. Kueper. 2003c. Influence of constitutive model parameters on the predicted migration of DNAPL in heterogeneous porous media. Water Resources Research, 39: 1279.

Gerhard, J.I., T. Pang, and B.H. Kueper. 2007. Time scales of DNAPL migration in sandy aquifers. Ground Water, 45: 147-157.

Giroux, B., and M. Chouteau. 2008. A hydrogeophysical synthetic model generator: Computers and Geosciences, 34: 1080-1092.

Grant, G.P., and J.I. Gerhard. 2007a. Simulating the dissolution of a complex dense non-aqueous phase liquid source zone: 1. model to predict interfacial area. Water Resources Research, 43: W12410.

Grant, G.P., and J.I. Gerhard. 2007b. Simulating the dissolution of a complex dense non-aqueous phase liquid source zone: 2. experimental validation of an interfacial area-based mass transfer model. Water Resources Research, 43: W12409.

Grant, G.P., J.I. Gerhard, and B.H. Kueper. 2007a. Field scale impacts of spatially correlated relative permeability in heterogeneous multiphase systems. Advances in Water Resources, 30: 1144-1159.

Grant, G.P., J.I. Gerhard, and B.H. Kueper. 2007b. Multidimensional validation of a numerical model for simulating a DNAPL release in heterogeneous porous media. Journal of Contaminant Hydrology, 92: 109-128.

Hanai, T. 1960. Theory of the dielectric dispersion due to the interfacial polarization and its application to emulsions. Kolloid-Zeitschrift, 171: 23–31.

Hanai, T. 1961. A remark on "Theory of the dielectric dispersion due to the interfacial polarization and its application to emulsions". Kolloid-Zeitschrift, 175: 61–62.

Illangasekare T.H., J.L. Ramsey Jr., K.H. Jensen, and M.B. Butts. 1995. Experimental study of the movement and distribution of dense organic contaminants in heterogeneous aquifer. Journal of Contaminant Hydrology, 20: 1–25.

Karaoulis, M.C., J.H. Kim, and P.I. Tsourlos. 2011a. 4D active time constrained resistivity inversion. Journal of Applied Geophysics, 73: 25-34.

Karaoulis, M., A. Revil, D.D. Werkema, B.J. Minsley, W.F. Woodruff, and A. Kemna. 2011b. Time-lapse three-dimensional inversion of complex conductivity data using an active time constrained (ATC) approach. Geophysical Journal International, 187: 237-251.

Kavanaugh, M.C., P.S.C. Rao, L. Abriola, C. Newell, J. Cherry, T. Sale, G. Destouni, S. Shoemaker, R. Falta, R. Siegrist, D. Major, G. Teutsch, J. Mercer, and K. Udell. 2003. The DNAPL remediation challenge: is there a case for source depletion?. US Environmental Protection Agency, Washington DC.

Kim, J.H., M.J. Yi, S.G. Park, and J.G. Kim. 2009. 4-D inversion of DC resistivity monitoring data acquired over a dynamically changing earth model. Journal of Applied Geophysics, 68: 522-532.

Kim, J.H., and M.J. Yi. 2010. DC_3DPro: user's manual. Geoelectric Imaging Laboratory, Korea Institute of Geoscience and Mineral Resources (KIGAM).

Kueper, B.H., J.D. Redman, R.C. Starr, S. Reitsma, and M. Mah. 1993. A field experiment to study the behavior of tetrachloroethylene below the water table: spatial distribution of residual and pooled DNAPL. Ground Water, 31: 756-766.

Kueper, B.H., and J.I. Gerhard. 1995. Variability of point source infiltration rates for two-phase flow in heterogeneous porous media. Water Resources Research, 31: 2971-2980.

Kueper, B.H., G.P. Wealthall, J.W.N. Smith, S.A. Leharne, and D.N. Lerner. 2003. An illustrated handbook of DNAPL transport and fate in the subsurface. Environment Agency R&D Publication 133. EA, Bristol.

Kueper, B.H., and K.L. Davies. 2009. Assessment and delineation of DNAPL source zones at hazardous waste sites. United States Environmental Protection Agency, Publication EPA/600/R-09/119.

Loke, M.H. 2010. Tutorial: 2-D and 3-D electrical imaging surveys. http://www.geotomosoft.com/downloads.php, accessed 12 July 2012.

Lucius, J.E., G.R.Olhoeft, P.L. Hill, and S.K. Duke. 1992. Properties and hazards of 108 selected substances - 1992 edition. Open-File Report 92-527, U. S. Geological Survey.

Marion, D., A. Nur, H. Yin, and D. Han. 1992. Compressional velocity and porosity in sand-clay mixtures. Geophysics, 57: 554-563.

Mercer, J.W., and R.M. Cohen. 1990. A review of immiscible fluids in the subsurface: properties, models, characterization, and remediation. Journal of Contaminant Hydrology, 6: 107-163.

Nenna, V., A. Pidlisecky, and R. Knight. 2011. Informed experimental design for electrical resistivity imaging. Near Surface Geophysics, 9: 469-482.

Newmark R.L., W.D. Daily, K.R. Kyle, and A.L. Ramirez. 1998. Monitoring DNAPL pumping using integrated geophysical techniques. Journal of Environmental and Engineering Geophysics, 3: 7–13.

Ogilvy R.D., O. Kuras, P.I. Meldrum, P.B. Wilkinson, J.E. Chambers, M. Sen, A. Pulido-Bosch, J. Gisbert, S. Jorreto, I. Frances, and P. Tsourlos. 2009. Automated monitoring of coastal aquifers with electrical resistivity tomography. Near Surface Geophysics, 7: 367–375.

Pang, T.W., J.I. Gerhard, M. West, and B.H. Kueper. 2007. Numerical simulation of ISCO to remediate DNAPL in fractured rock. Proceedings of the 2007 U.S. EPA/NGWA Fractured Rock Conference: State of the Science and Measuring Success in Remediation, 133-147.

Papadopoulos N.G., P. Tsourlos, G.N. Tsokas, and A. Sarris. 2006. Two-dimensional and three-dimensional resistivity imaging in archaeological site investigation. Archaeological Prospection, 13: 163–181.

Papadopoulos N.G., P. Tsourlos, G.N. Tsokas, and A. Sarris. 2007. Efficient ERT measuring and inversion strategies for 3D imaging of buried antiquities. Near Surface Geophysics, 5: 349–362.

Papadopoulos, N.G., P. Tsourlos, C. Papazachos, G.N. Tsokas, A. Sarris, and J.H. Kim. 2011. An algorithm for fast 3D inversion of surface electrical resistivity tomography data: application on imaging buried antiquities. Geophysical Prospecting, 59: 557-575.

Redman, D. 2009. Contaminant mapping, *in* H. Jol, ed., Ground penentrating radar, theory and applications, Chapter 8. Elsevier, 247-269.

Revil, A., L.M. Cathles III, S. Losh, and J.A. Nunn. 1998. Electrical conductivity in shaly sands with geophysical applications. Journal of Geophysical Research, 103: 23.925-23.936.

Revil, A., and L.M. Cathles. 1999. Permeability of shaly sands. Water Resources Research, 35: 651-662.

Revil, A. 2012. Spectral induced polarization of shaly sands: influence of the electrical double layer Water Resources Research, 48: W02517.

Robin, M. J. L., E.A. Sudicky, R.W. Gillham, and R.G. Kachanowski 1991. Spatial variability of Strontium distribution coefficients and their correlation with hydraulic conductivity in the Canadian Forces Base Borden aquifer. Water Resources Research, 27: 2619–2632.

Sauck, W.A., E.A. Atekwana, and M.S. Nash. 1998. Elevated conductivities associated with an LNAPL plume imaged by integrated geophysical techniques. Journal of Environmental and Engineering Geophysics, 2-3: 203-212.

Sauck, W.A. 2000. A model for the resistivity structure of LNAPL plumes and their environs in sandy sediments. Journal of Applied Geophysics, 44: 151-165.

Schön, J.H. 1996. Physical properties of rocks – fundamentals and principles of petrophysics: Elsevier Science Ltd., Handbook of Geophysical Exploration, Seismic Exploration, 18: 379-478.

Schön, J.H., and D.T. Georgi. 2003. Dispersed shale, shaly-sand permeability – a hydraulic analog to the Waxman-Smits equation. SPWLA 44th Annual Logging Symposium.

Sen, P. N., and P.A. Goode. 1992. Influence of temperature on electrical conductivity on shaly sands.: Geophysics, 57: 89–96.

Slater, L. 2007. Near surface electrical characterization of hydraulic conductivity: from petrophysical properties to aquifer geometries — a review. Surveys in Geophysics, 28: 169–197.

Sudicky, E. A., W. A. Illman, I. K. Goltz, J. J. Adams, and R. G. McLaren. 2010. Heterogeneity in hydraulic conductivity and its role on the macroscale transport of a solute plume: from measurements to a practical application of stochastic flow and transport theory. Water Resources Research, 46: W01508.

Tsourlos, P., and R. Ogilvy. 1999. An algorithm for the 3-D inversion of tomographic resistivity and induced polarization data: preliminary results. Journal of the Balkan Geophysical Society, 2: 30-45.

Waxman, M.H., and L.J.M. Smits. 1968. Electrical conductivities and oil-bearing shaly sands. Society of Petroleum Engineers, 8: 107–122.

West, M.R., G.P. Grant, J.I. Gerhard, and B.H. Kueper. 2008. The influence of precipitate formation on the chemical oxidation of TCE DNAPL with potassium permanganate. Advances in Water Resources, 31: 324-338.

Wilson, V.C., C. Power. A. Giannopoulos, J.I. Gerhard, and G.P. Grant. 2009. DNAPL mapping by ground penetrating radar examined via numerical simulation. Journal of Applied Geophysics, 69: 140-149.

Yi., M.J., J.H. Kim, Y. Song, S.J. Cho, S.H. Chung, and J.H. Suh. 2001. Three-dimensional imaging of subsurface structures using resistivity data. Geophysical Prospecting, 49: 483-497.

Yi, M.J., J.H. Kim, and S.H. Chung. 2003. Enhancing the resolving power of least-squares inversion with active constraint balancing. Geophysics, 68: 931-941.

Zhou, Q. Y., J. Shimada, and A. Sato. 2001. Three-dimensional spatial and temporal monitoring of soil water content using electrical resistivity tomography. Water Resources. Research, 37: 273–285.

4 EVALUATING FOUR-DIMENSIONAL TIME-LAPSE ELECTRICAL RESISTIVITY TOMOGRAPHY FOR MONITORING DNAPL SOURCE ZONE REMEDIATION [2]

4.1 Introduction

The remediation of sites contaminated by non-aqueous phase liquids (NAPLs), and in particular denser-than-water NAPLs (DNAPLs) residing below the water table, represents a challenging geoenvironmental problem. DNAPLs extensively polluting the environment include chlorinated solvents, coal tar and polychlorinated biphenyls (PCB) oils. Once released to the subsurface, DNAPLs tend to follow a tortuous migration pathway, penetrating the saturated zone as an immiscible 'oil' phase in response to gravity and capillary forces. Their complex behaviour and distribution within the subsurface is site specific and governed by many factors including the nature of the hydrogeologic environment, properties of the DNAPL, and subsequent mass transfer and transformation processes (Kueper et al., 2003). As a result, DNAPL source zones can exhibit a wide range of forms, from a laterally extensive pool near the surface or at depth to a complex distribution of residual and pools covering many elevations (Gerhard et al., 2007). DNAPL source zones can serve as a persistent source of groundwater contamination posing unacceptable risk to humans and ecosystems.

A variety of remediation technologies have been applied to DNAPL source zones including various thermal, chemical, extraction and biological treatment methods (Hadley and Newell, 2012). In addition to effective delineation of the DNAPL source zone, temporal monitoring is an essential component of successful remediation, informing

[2] A version of this chapter has been published: Power, C., J.I. Gerhard, M. Karaoulis, P. Tsourlos, and A. Giannopoulos. 2014. Evaluating four-dimensional time-lapse electrical resistivity tomography for monitoring DNAPL source zone remediation. Journal of Contaminant Hydrology, 162-163: 27-46.

remedial strategies and assessing remedial performance (Kavanaugh et al., 2003). Traditional methods, including monitoring wells and soil borings, are expensive and suffer from low sampling density, providing limited spatial and temporal information. Non-invasive geophysical methods have the potential to significantly improve DNAPL site assessments and remediation monitoring (Brewster et al., 1995; Wilson et al., 2009). In particular, electrical resistivity tomography (ERT) exhibits significant potential since DNAPLs are typically highly resistive (Lucius et al., 1992) and in many scenarios will provide sufficient electrical contrast between DNAPL and groundwater. ERT is well-established and widely employed in hydrogeological applications (e.g., Loke et al., 2013). ERT used in time-lapse mode, measuring temporal changes in resistivity, has become increasingly popular to monitor dynamic, aqueous phase processes including groundwater-surface water interaction (e.g., Johnson et al., 2012), salt-water intrusion (e.g., Nguyen et al., 2009), transport of saline tracers (e.g., Robert et al., 2012), wastewater transport (e.g., Seferou et al., 2013), recharge-induced contaminant plume behaviour (e.g., Gasperikova et al., 2012) and contaminant degradation (e.g., Atekwana et al., 2005).

The application of ERT to delineating DNAPL source zones has been suggested by a number of studies (e.g., Cardarelli and Di Filippo, 2009; Naudet et al., 2013) but progress towards a practical, reliable field technique has been impeded by several issues. The first is the difficulty of static (i.e., time-invariant) detection of the complex electrical target presented by an intricate, unknown DNAPL distribution in a heterogeneous, unknown permeability field. This is not easily remedied. However, it is hypothesized that ERT applied in time lapse mode can provide valuable information during DNAPL source zone remediation: the shrinking volume of the resistive DNAPL body (and replacement in the pore space by more conductive groundwater) should provide – over time – a signal that can be mapped. Chambers et al. (2004) used differential resistivity imaging (i.e., subtracting one static image from another to get the resistivity change with time) to monitor the movement of DNAPL through water-saturated sand in a laboratory column. Daily and Ramirez (1995) used cross-hole ERT (i.e., from one vertical borehole to another) to image the injection of gas at a trichloroethylene (TCE) site. Newmark et al. (1998) used time-lapse cross-hole ERT to monitor decreasing resistivity changes

associated with the pumping of pooled TCE, while Chambers et al. (2010) used high-resolution, cross-hole ERT in a pilot-scale experiment to map groundwater chemistry changes associated with the bioremediation of a DNAPL source zone.

The second issue impeding ERT usage on sites is the reliability of the interpretation. Converting ERT data into a representation of subsurface resistivity, a process known as inversion, is a rich field of research (e.g., Loke and Barker, 1996; Loke et al., 2013). All of the cited time-lapse studies inverted the ERT data recorded at each monitoring step independently and subtracted successive static ERT images to identify the differences (e.g., Oldenborger et al., 2007). However, these independent time-lapse inversion images are nearly always contaminated by inversion artifacts (i.e., false resistivity anomalies generated due to independent inversion errors and the presence of noise in the ERT measurements). These false signals, which can mask changes of interest or suggest that subsurface changes happened where none actually occurred, are exacerbated in the presence of subsurface heterogeneity (Karaoulis et al., 2011a). Recently, new four-dimensional (4D, three spatial dimensions plus time) inversion algorithms have provided significant improvements, reducing inversion artifacts and improving the stability of the inversion problem (Kim et al., 2013; Karaoulis et al., 2014). Such algorithms, by jointly inverting datasets from multiple times, provide much more reliable interpretations of subsurface resistivity changes.

The third issue limiting ERT field applications is that most pilot field demonstrations of ERT have used cross-borehole surveys, which are not only invasive, but expensive. Since typical borehole spacing must be on the order of a few meters, coverage of significant area can be challenging. A number of recent advancements in time-lapse ERT, in both data acquisition and array configurations are making surface surveys more reliable and data rich (e.g., Ogilvy et al., 2009; Nenna et al., 2011). Surface electrodes installed prior to site remediation and surveyed at regular intervals would provide surveys with significant areal coverage that are practical, inexpensive, and rapid. The availability of (i) improved surface survey techniques, (ii) more reliable 4D inversion methods, and (iii) strategies that focus on the changes occurring during remediation provides a new opportunity to consider ERT as a site monitoring tool.

The objective of this study is to explore the potential of 4D time-lapse ERT implemented with surface-mounted electrodes to monitor the remediation of DNAPL source zones in the near subsurface (i.e., upper 4 m). First, because this is a new application integrating several research advances, a laboratory experiment was performed to demonstrate the approach for mapping a changing NAPL distribution over time. Those results were then compared to an independent simulation of the experiment using a published DNAPL-ERT numerical model. The coupled model, which (i) simulates NAPL migration/remediation, and (ii) predicts the results of ERT surveys, needed to perform both steps accurately in order to reproduce the experiment and thereby provide confidence that the model is a reliable tool for exploring these scenarios. The numerical model was then used to evaluate the potential for ERT mapping of remediation at the field scale. Four DNAPL source zones, ranging from simple to complex, were simulated and complete DNAPL mass removal over time was predicted. During the remediation period, the model also simulated the results of periodic ERT surface surveys of the site. These surveys were analyzed with a recently published 4D ERT inversion algorithm to provide estimates of DNAPL distribution with time. Qualitative and quantitative comparisons between the known DNAPL volume reductions and those estimated by ERT are shown, providing insight into the potential and the limitations of this technique to map DNAPL remediation at field sites.

4.2 Modelling Approach

The numerical modelling approach is presented first because it explains the relationship between NAPL distribution changes and ERT estimates of those changes. This work integrated a number of published numerical models. Figure 4-1 conceptually illustrates the coupling performed between the 3D DNAPL-ERT model developed in Chapter 3 (i.e., Power et al., 2013) and a 4D time-lapse inversion algorithm (Karaoulis et al., 2011a). Details on each component and their integration are provided below.

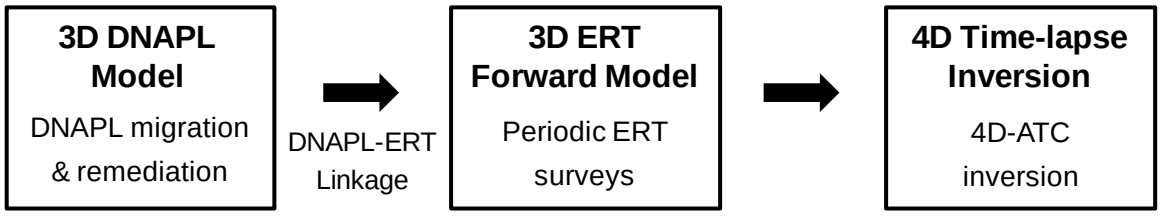

Figure 4-1: Schematic illustration of the numerical components and sequence of data passing involved in the modelling approach. 'Forward' in this context means that an ERT survey data set is predicted based upon an input electrical resistivity domain; 'inversion' means an estimate of the electrical resistivity domain is predicted based upon the ERT survey data.

4.2.1 Coupled DNAPL-ERT Modelling

The DNAPL-ERT model developed in Chapter 3 is a coupling of DNAPL3D-MT, a simulator for DNAPL evolution under release and remediation conditions, and IP4DI, an ERT model that conducts both (a) forward simulation, which predicts the response of the subsurface to an ERT survey, and (b) inversion, which estimates the distribution of resistivity changes given sequential ERT response data sets.

DNAPL3D-MT (Grant and Gerhard, 2007a,b) is a 3D multiphase flow and contaminant transport code, which simulates DNAPL infiltration and redistribution below the water table as well as DNAPL dissolution and transport of the dissolved phase species in groundwater. It permits as input heterogeneous distributions of permeability and porosity. It couples the multiphase flow model DNAPL3D (Gerhard and Kueper, 2003a,b,c) and the dissolved phase transport model MT3D (Zheng, 1990) through a mass transfer module based on interfacial area between the immiscible phases (Grant and Gerhard, 2007a,b). DNAPL3D-MT employs a seven-point node-centered finite difference scheme to discretize the 3D multiphase flow equations, formulated in terms of the two primary variables: water pressure, P_W, and water saturation, S_W (Kueper and Frind, 1991a,b). A sophisticated constitutive relationship model accounts for the hysteretic dependence of capillary pressure and relative permeability on saturation and fully accounts for DNAPL entrapment (Gerhard and Kueper, 2003a,b). At each DNAPL migration time step, implicit solution of these equations with Newton-Raphson iteration

provides the distribution of hydraulic head and DNAPL saturation throughout the domain. This, in turn, provides local values of groundwater velocity and DNAPL-groundwater interfacial area throughout the source zone. Coupled with the solution of the advection-dispersion equation, this provides rate-limited DNAPL dissolution and the distribution of contaminant concentrations in groundwater. The model, therefore, simulates a realistic initial distribution of DNAPL at a contaminated site and the complex pattern of DNAPL removal as it is dissolved by groundwater flowing through the site. Complete details on the model formulation, and the validation of all of its processes against multidimensional, heterogeneous laboratory experiments, are provided by the cited references and Grant et al. (2007a,b). Although not employed in this study, the DNAPL model can also be employed for reactive transport and other remediation processes, including chemical oxidation, bioremediation, and in situ smoldering destruction (e.g., West et al., 2008; MacPhee et al., 2012).

Central to the development of the coupled DNAPL-ERT model was the comprehensive linking of the local, spatially variable hydrogeological properties from DNAPL3D-MT to the local, spatially variable electrical resistivity (shown as "DNAPL-ERT Linkage" in Figure 4-1). This was achieved by a novel integration of a variety of established petrophysical and geoelectrical relationships (e.g., Revil and Cathles, 1999; Berg, 2007), with the electrical resistivity field accounting for both the spatial heterogeneity of subsurface soils (intrinsic permeability, porosity and clay content) and the local volume fractions of fluids in the pore space (water, DNAPL, air) predicted by DNAPL3D-MT at each time step. The resulting 3D electrical representation of the hydrogeological domain is then used as input to the IP4DI forward model. A full description of the development and testing of the coupled DNAPL-ERT model is provided in Chapter 3.

IP4DI was employed to simulate periodic ERT surveys during DNAPL remediation and estimate the change of resistivity in both space and time. IP4DI is a MATLAB® package developed by Karaoulis et al. (2013) that performs both steps of forward geoelectrical modelling and time-lapse inversion. The forward modelling component uses the finite element method with hexahedral elements to numerically solve Poisson's equation and mathematically predict the response from an ERT survey (Tsourlos and Ogilvy, 1999). A

single electrical resistivity measurement uses an array of four electrodes to measure the local subsurface resistivity; a known current (I_c) is injected between two electrodes and the voltage difference ($\Delta\Phi$) is measured across two other electrodes. The current and voltage measurements are then converted into an apparent resistivity ($\rho_a = G_f \cdot \Delta\Phi / I_c$) where G_f is a geometrical factor that depends on the configuration of the electrode array (Loke et al., 2013). Surface ERT is the rapid collection of many electrical resistivity measurements from a regular network of electrodes arranged across the site, providing a 3D distribution of apparent resistivity values. The forward modelling scheme used in IP4DI is based on a well established 3D algorithm fully described by Tsourlos and Ogilvy (1999) and has been used in a number of modelling studies, including archeological investigations and salt tracer mapping (e.g., Papadopoulos et al., 2007; Karaoulis et al., 2011b).

4.2.2 Time-lapse Inversion

Inversion is a well-established process that essentially estimates the subsurface resistivity distribution that gave rise to the recorded apparent resistivity values. Starting from a simple initial domain (usually a homogeneous half-space), an optimization method is used to iteratively change the resistivity of the domain cells to minimize the difference between the recorded and calculated apparent resistivity values. Regularization constraints (e.g., smoothness) are usually incorporated to condition and stabilize the inversion problem.

The traditional approach to time-lapse inversion uses independent inversion, where the ERT data recorded at each monitoring step is inverted independently of any other information and differential time-lapse images are reconstructed by subtracting them from each other (e.g., Tsourlos et al., 2003). Recently, advances are being made in the area of 4D time-lapse inversion (e.g., Kim et al., 2013; Karaoulis et al., 2014). In these approaches, the subsurface model and the entire monitoring datasets are defined in a space-time domain and monitoring datasets recorded at numerous times are simultaneously inverted. Regularizations introduced in both space and time domains

further stabilize the inversion and effectively reduce inversion artifacts (Kim et al., 2009), while demonstrating improved sensitivity in regions of resistivity changes (Karaoulis et al., 2011a). For this study, the 4D active time constraint (4D-ATC) method developed by Karaoulis et al. (2011a) was used. In this method, the temporal Lagrangian varies between different monitoring steps proportionally to the expected degree of spatial resistivity changes occurring (i.e., areas of significant changes are assigned low time regularization values and vice versa). To pre-estimate regions of change and assign appropriate time Lagrangian values, a preliminary analysis of the recorded data is performed through differential imaging of independent inversion (Karaoulis et al., 2011a). With the appropriate time Lagrangian, the 4D-ATC inversion scheme can be applied to an entire dataset recorded from all monitoring steps with increased focus now on areas where the expected changes are likely to occur. The final resistivity distribution estimated by this method will be referred to as that 'measured' by ERT. The application and benefits of this algorithm have been demonstrated on a number of datasets, including salt tracer migration and water injection (Karaoulis et al., 2011a,b).

4.2.3 Estimation of DNAPL Volume Remediated

Many studies have used petrophysical relationships to translate resistivity measurements into hydrogeological properties of interest such as water content and solute concentration (e.g., Zhou et al., 2001; Oldenborger et al., 2007). Although the nonuniqueness and spatially variable resolution of the inverted ERT images generally results in estimates of hydrogeological variables with limited accuracy (Singha and Gorelick, 2006), traditional relationships such as Archie's law (Archie, 1942) continue to be widely used (e.g., Slater et al., 2002; Breen et al., 2012). In this paper, estimates of DNAPL saturation (S_n) changes from 4D-ATC inverted resistivity fields were obtained using Archie's law, which relates the resistivity of a partially saturated porous medium to the water content of the medium. In this study, water saturation was variable in space and time, and equals one minus the local DNAPL saturation below the water table. Archie's law was then

modified to infer the DNAPL saturation, S_n^{ERT}, at each node from the measured resistivity:

$$S_n^{ERT} = 1 - \left(\frac{1}{\phi^m} \frac{\rho_w}{\rho_t} \right)^{1/n}, \tag{4-1}$$

where ϕ is the porosity of the medium, ρ_w is the pore water resistivity, ρ_t is the ERT-measured resistivity of the medium, m is the cementation exponent, and n is the saturation exponent. The cementation exponent and saturation exponent values typically used are 1.5 and 2.0, respectively (e.g., Archie, 1942). The pore water resistivity and porosity can be determined directly from the physical or numerical system, with an average value applied to Equation 4-1.

Differential images were reconstructed by subtraction of the DNAPL saturation distribution at each successive monitoring step from the baseline distribution prior to remediation. The results are local DNAPL saturation changes, ranging from 2% to 100%, with respect to the initial saturation in the source zone. A saturation change threshold of 2% was implemented across all monitoring steps (i.e., saturation changes < 2% were considered insignificant); it is normal practice to implement such a threshold on inverted ERT data to ignore small changes related to artifacts (e.g., Doetsch et al., 2012; Robert et al., 2012). The total volume remediated was calculated by:

$$V_{nr}^{\ i} = \sum_{i=1}^{nz} \sum_{j=1}^{nx} \sum_{k=1}^{ny} S_n^{\ i} \phi \cdot \Delta x \Delta y \Delta z, \tag{4-2}$$

where the superscript i denotes either actual or ERT-measured, Δx, Δy and Δz are the dimensions of the nodes in the *x*-, *y*- and *z*-directions, respectively, and nx, ny, nz are the number of nodes in the *x*-, *y*- and *z*-directions, respectively. Equation 4-2, modified by integrating only over j and k, was used to calculate the volume of DNAPL remediated for each horizontal depth slice of thickness Δz.

4.2.4 Modelling Approach Demonstration

To demonstrate the complete modelling approach taken in this study, this section illustrates the internal workings of the model for time-lapse ERT monitoring of two monitoring steps of a DNAPL remediation scenario. Figure 4-2 presents a schematic to summarize the modelling approach and corresponding images. The simulated scenario involves the release of the chlorinated solvent chlorobenzene (CB) in a two-dimensional (2D) domain (32 m wide x 6 m deep) characterized by a heterogeneous distribution of intrinsic permeability. 1.2 m^3 of CB was released over 5 days into an initially water-saturated domain, allowed to redistribute, and the final distribution of DNAPL corresponds to Time 1 (i.e., when the first ERT scan was obtained, T1). CB was then subject to enhanced dissolution in groundwater flowing from left to right across the domain and a second ERT scan was conducted when the initial DNAPL mass had depleted by 20% (i.e., Time 2, T2).

As illustrated in Box 1 (Figure 4-2), DNAPL3D-MT provides the evolving distribution of DNAPL. Although not part of the modelling approach, to illustrate the difference in the interval between T1 and T2, the time-lapse saturation change (i.e., the "true" DNAPL removed) is also shown in Box 1. The DNAPL-ERT linkage methodology described in Section 2.1 converts the hydrogeological domains at T1 and T2 into their corresponding bulk electrical resistivity domains, as illustrated in Box 2. This represents the "true" distribution of resistivity in the subsurface. The differential resistivity image between the two electrical domains is shown on the right of Box 2. In this ratio image, areas with a ratio value of 1.0 (yellow) indicate no resistivity changes between T1 and T2, areas with a ratio value less than 1.0 (green-blue) indicate decreasing resistivity changes, while areas with a ratio value greater than 1.0 (orange-red) indicate increasing resistivity changes. As expected, the only changes occurring between T1 and T2 are decreasing resistivity changes (green-blue), and correspond to the changes in DNAPL saturation (Box 1).

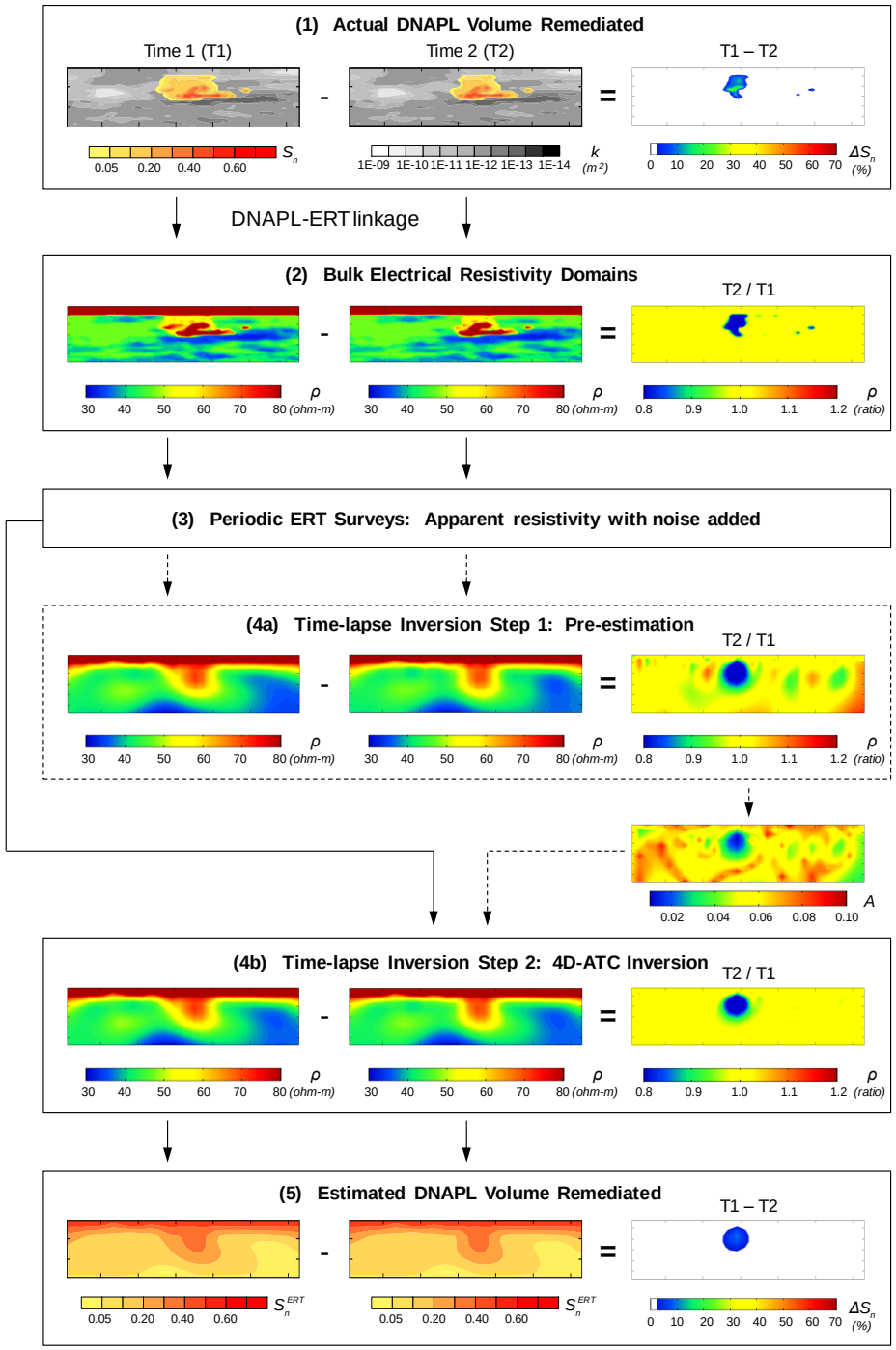

Figure 4-2: The time-lapse modelling approach adopted in this study to monitor DNAPL source zone remediation. Each domain is 32 m (marked at 5 m intervals) x 6 m (marked at 2 m intervals). The colour scale bars represent different parameters at each step, identified below each figure. The right hand figure in each case represents the change between the left two images, with some presented as a difference and some as a ratio, following common practice for each. A full description of the steps and subfigures is provided in the text.

The ERT forward model then simulated a surface ERT survey at each of the two times (Box 3). In this case, the survey used the dipole-dipole electrode array with an inline electrode spacing of 1 m. The apparent resistivity data generated for T1 and T2 are not visualized as inversion is required for its interpretation. To render modelling results more realistic, the recorded synthetic data was contaminated by levels of Gaussian noise. As discussed, the 4D-ATC inversion is conducted in two steps: pre-estimation and 4D inversion. The pre-estimation of expected subsurface changes (dotted box and arrows) is obtained from differential imaging between independently inverted images of each time step (Box 4a). This ratio image, shown in the right side of Box 4a, illustrates the changes between T1 and T2. It is evident from comparison to the "true" resistivity changes in Box 2 that additional areas of resistivity changes (both decreasing and increasing changes) occur in the ratio image in Box 4a due to the artifacts (i.e., false anomalies) typically introduced by independent inversion. The ratio image is then used to formulate the outputted temporal Lagrangian matrix *A* (image between boxes 4a and 4b), where low values (green-blue) correspond to areas with large expected change and large values (orange-red) correspond to areas with little expected change.

The second step of the inversion process (Box 4b) then revisits the original apparent resistivity data and performs simultaneous time-lapse inversion on all monitoring steps; note that all 11 monitoring steps, tracking the complete removal of the DNAPL, were simultaneously inverted although only two are shown. The differential image on the right hand side of Box 4b provides the 4D ERT measurement of the DNAPL region remediated. Comparison of the difference images for the 4D-ATC (Box 4b, right) and independent inversions (Box 4a, right) illustrates that the 4D-ATC scheme eliminates the majority of artifacts evident in the independently inverted image.

This is important for remediation monitoring of DNAPL, where artifacts can be falsely interpreted as regions that are either (a) invaded with remobilized DNAPL or (b) cleaned up. Moreover, note the difficulty in deducing the static DNAPL distribution at T1 (Box 1, left) from either ERT interpretation (Box 4a or Box 4b, left). A number of tests (not shown) similarly highlighted the difficulty of static detection of complex targets such as DNAPL source zones. All of the examples reveal (like Box 4b, right) the greater

potential of time-lapse ERT for monitoring DNAPL removal. Estimation of time-lapse DNAPL saturation changes from the 4D-ATC inverted resistivity fields were obtained using Archie's law (Box 5). The differential image on the right hand side of Box 5 is the ERT-measured estimate of the true DNAPL change (Box 1, right). How well this result compares to the actual changes is explored in Section 5 using a variety of 3D scenarios. First, confidence in the geophysical method and the coupled model is developed with an analog laboratory experiment described in the following section.

4.3 4D ERT NAPL Experiment

In order to demonstrate this new technique for mapping changes in NAPL distributions with time in a physical system, a 3D controlled laboratory experiment was conducted. The experiment was also independently simulated with the DNAPL-ERT model to develop confidence in the model for simulating these systems, particularly the model's ability to reconstruct NAPL changes with time from simulated ERT surveys.

4.3.1 Experimental Procedure

The experiment was performed in a 3D experimental tank (1 m x 1 m x 1 m) constructed of plexiglass (e.g., Seferou et al., 2013). As illustrated in Figure 4-3, only a subvolume of the tank, measuring 0.60 m and 0.20 m long in the *x* and *y* dimensions and 0.20 m in the vertical dimension and located in the center of the tank, was monitored by ERT so as to minimize possible boundary effects on the electrodes. As shown, the tank was packed with a 0.22 m by 0.16 m by 0.07 m deep homogeneous block of medium sand surrounded by fine sand. The medium quartz sand (sieved to retain only a single mesh size) exhibited a mean grain size of 0.58 mm and a narrow particle size distribution (coefficient of uniformity of 1.36). The fine quartz sand exhibited a mean grain size of 0.23 mm and a narrow particle size distribution (coefficient of uniformity = 1.56). After careful packing of the dry sands in 0.01 m lifts, they were saturated by the slow injection of tap water (with salt added to provide moderate water conductivity, 7 ohm-m) into the base of the

tank over 24 hours. A number of photographs illustrating the preparation of the tank experiment are shown in Appendix A.

Corn oil (Minerva, Greece) was the NAPL injected into the center of the medium sand block. The key property relevant to this study is that the corn oil, like most NAPLs, is an insulating fluid that displaces the more conductive water in the pores of the saturated domain, thereby providing time-lapse changes amenable to ERT monitoring. The corn oil was dyed with Oil Blue N powder (Sigma-Aldrich) to permit mapping the NAPL distribution during tank excavation. The properties of the water, oil and sand used in this experiment are shown in Table 4-1 (note that all tabulated parameters without superscripts were measured directly).

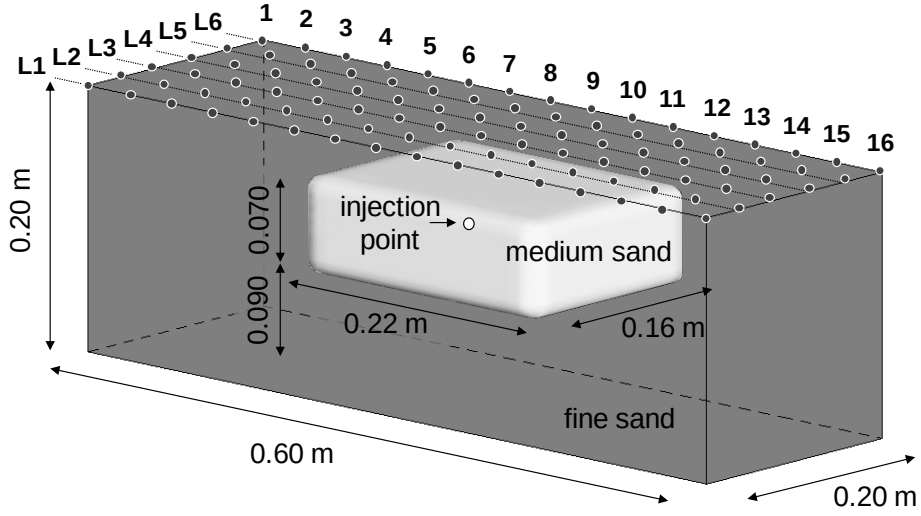

Figure 4-3: Schematic diagram of the 3D experimental domain showing the medium sand block (white) surrounded by fine sand (dark gray). Six parallel ERT survey lines are deployed along the surface (indicated L1 – L6) with each survey line containing 16 electrodes (numbered 1 – 16 on survey line L6).

NAPL was injected through the end of a 5 mm diameter PTFE tube located in the center of the medium sand block using a syringe pump at a constant injection rate of 2 mL/min. The injection was stopped at 4 times, after 50 mL, 100 mL, 250 mL and 500 mL total volume injected. At each time, the injection was stopped for 60 min to permit ERT data

acquisition. Because the sand was homogeneous and the NAPL density was close to that of water, the NAPL was expected to migrate outwards in a uniform, spherical manner from the injection point. The high entry pressure of the fine sand was expected to ensure NAPL containment within the medium sand block. The short interval required for ERT data acquisition and the low density contrast between the fluids suggests that NAPL movement was minimal during these pump-off intervals.

Table 4-1: Experimental parameters

Parameter	**Value**	**Units**
Hydrogeological parameters		
Medium sand porosity	0.40	-
Medium sand permeability	2.35×10^{-11}	m^2
Medium sand mean grain size	0.00058	m
Fine sand porosity	0.43	-
Fine sand permeability	8.07×10^{-13}	m^2
Fine sand mean grain size	0.00023	m
Water density	1000	kg/m^3
Water viscosity	0.001	Pa·s
NAPL density	920	kg/m^3
NAPL viscosity	0.065	Pa·s
NAPL-water interfacial tension[1]	0.0233	N/m
Electrical parameters		
Water resistivity	7	ohm-m
NAPL resistivity	1×10^6	ohm-m
Sand resistivity[2]	1000	ohm-m
Cementation exponent[3]	1.5	-
Saturation exponent[3]	2.0	-

[1] Gaonkar (1989)

[2] Loke (2013)

[3] Berg (2007)

The 3D ERT surveys conducted in this experiment used an array configuration realistic for field application: parallel survey lines traversing only in the *x*-direction (e.g., Papadopoulos et al., 2007). The dipole-dipole electrode array was used with 16 electrodes along each survey line and an inline electrode spacing of 0.04 m. There was a total of 6 survey lines in the survey with an interline spacing of 0.04 m. Each survey line employed a polyvinyl chloride pipe to accommodate all 16 electrodes and cables. A resistivity system (Syscal R1 Plus, Iris Instruments) recorded the ERT measurements. 3D ERT surveys were conducted at time zero (no NAPL) as well as at each injected DNAPL volume interval to provide time-lapse monitoring of the increasing NAPL volume. Preliminary tests were conducted prior to the NAPL experiment to investigate the effects of possible noise sources from the finite tank boundaries. The high repeatability, stability and lack of artifacts in the inversion results suggested that the tank, with the specified tank subvolume, array configuration and experimental procedure (i.e., time-lapse), can be adequately modelled using the standard 'infinite' Dirichlet boundary condition.

Following the injection of 500 mL of NAPL, the tank was excavated to confirm the actual distribution of NAPL. At each excavation depth (top of block, 0.06 m and 0.09 m from top of block, bottom of block), photographs were taken of the plan-view extent of blue-dyed NAPL invasion.

It is acknowledged that the overall aim of this work is to monitor NAPL removal with time rather than NAPL injection. However, the principle of 4D time-lapse ERT is identical for both processes: mapping the temporal changes in NAPL distribution. The change for a given time interval is identical whether the NAPL is added or removed from the subsurface. NAPL injection was chosen for the laboratory experiment because (i) NAPL injection occurs more quickly, (ii) an inert, non-toxic NAPL can be employed, and (iii) this approach provides the ability to excavate at the end of the test to visually confirm the final NAPL distribution. However, the comparison between modelling and experiments is identical if the data is considered as a sequential NAPL addition or if the time intervals are considered in reverse as sequential NAPL removal. Therefore, for the purposes of presenting the results in a manner consistent with the rest of this work, the last monitoring step (500 mL NAPL volume injected) will be taken as the time-zero

scenario (i.e., “prior to NAPL reduction”), with the 250 mL, 100 mL, 50 mL and 0 mL volume injected intervals taken as the 250 mL, 400 mL, 450 mL and 500 mL “volume reduced” scenarios (i.e., 50%, 80%, 90% and 100% NAPL reduced, respectively).

4.3.2 Numerical Simulation of the Experiment

The DNAPL-ERT model and associated modelling approach described in Section 4.2.4 was employed to simulate the experiment. The numerical model simulated both the NAPL migration and results of the ERT surveys. A numerical domain was constructed identical to Figure 4-3 using a grid resolution of 0.02 m in the *x*- and *y*-directions and 0.01 in the *z*-direction, while fluid, sand, and electrical properties were equal to Table 4-1. The domain was initially water-saturated and a constant flux boundary condition specifying 2 mL/min at a single node in the center of the medium sand block was employed for NAPL injection. Side boundaries were constant water pressure and constant water saturation (allowing water displaced by NAPL to flow out of the domain) and the top and bottom boundaries were no flux. No model calibration was employed; the experiment was simulated strictly independently and the simulated ERT survey used the simulated NAPL distribution as input (see Section 2.4).

4.3.3 Experiment and Modelling Results

4.3.3.1 Spatial comparison

The observed extent of NAPL invasion in the 2D cross-section along the center (*y*-distance = 0.10 m) of the experimental subvolume is shown in Figure 4-4a. The excavation confirmed that the NAPL was completely contained within the medium sand, with a small fraction of un-invaded medium sand furthest away from the NAPL injection point (e.g., *x*-distance = 0.20 m). At 0.06 m depth, two soil samples taken 0.05 m either side of the central injection point (i.e., *x*-distance = 0.25 m and 0.35 m) were used to calculate NAPL saturations of 57% and 68% at these locations.

The numerical simulation of the experiment describes the progressive invasion of NAPL into the medium sand pore space. At each volume injected interval (i.e., 50 mL, 100 mL, 250 mL, 500 mL), the percentage of medium sand pores invaded was 14%, 23%, 55% and 91%, respectively. Figure 4-4b illustrates the distribution of NAPL along the central cross-section following the release of the full 500 mL of NAPL, with a mean NAPL saturation of 62%. As expected, the simulated NAPL distribution has spread uniformly from the central NAPL injection point, with both the left and right hand side of the NAPL front equidistant from the injection point and invading the majority of the medium sand. It is evident that the simulated NAPL outline (black dotted line in Figure 4-4b) accurately predicts the actual distribution of NAPL at the 500 mL NAPL volume monitoring step (black dashed line in Figure 4-4a).

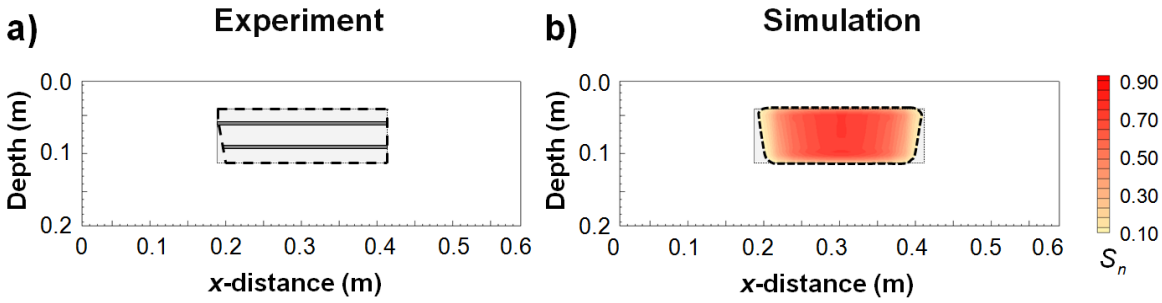

Figure 4-4: (a) Actual extent of NAPL invasion (black dashed line) along the central 2D cross-section (y-distance = 0.10 m) after the injection of 500 mL of NAPL into the experimental tank (note: the horizontal shaded lines are the measured extent of NAPL invasion for two of the excavated depths); (b) simulated NAPL distribution along the 2D cross-section, with the black dotted line indicating the extent of predicted NAPL invasion (cutoff NAPL saturation of 10%).

Figure 4-5a presents the measured 3D resistivity distribution produced from the experimental ERT survey of the 500 mL NAPL source zone (the corresponding central 2D cross-sectional image is given in Figure 4-5b). The figures show a significant contrast in the ERT response which is representative of the insulating NAPL that has invaded the medium sand. It is evident that the ERT survey provides a reliable delineation of the actual extent of NAPL invasion (overlaid in Figure 4-5b), although as expected, the sharp boundaries of the distribution are not captured due to the volume averaging nature of

ERT. The resistivity images show little variation in the soil matrix background, which is expected due to the homogeneity of the fine sand. As noted above, ERT (and other geophysical methods) are not usually reliable for detecting static NAPL distributions, particularly in heterogeneous scenarios (e.g., Daily and Ramirez, 1995); however, it is not surprising that ERT can be successful in more simple domains with favourable conditions (e.g., Chambers et al., 2004).

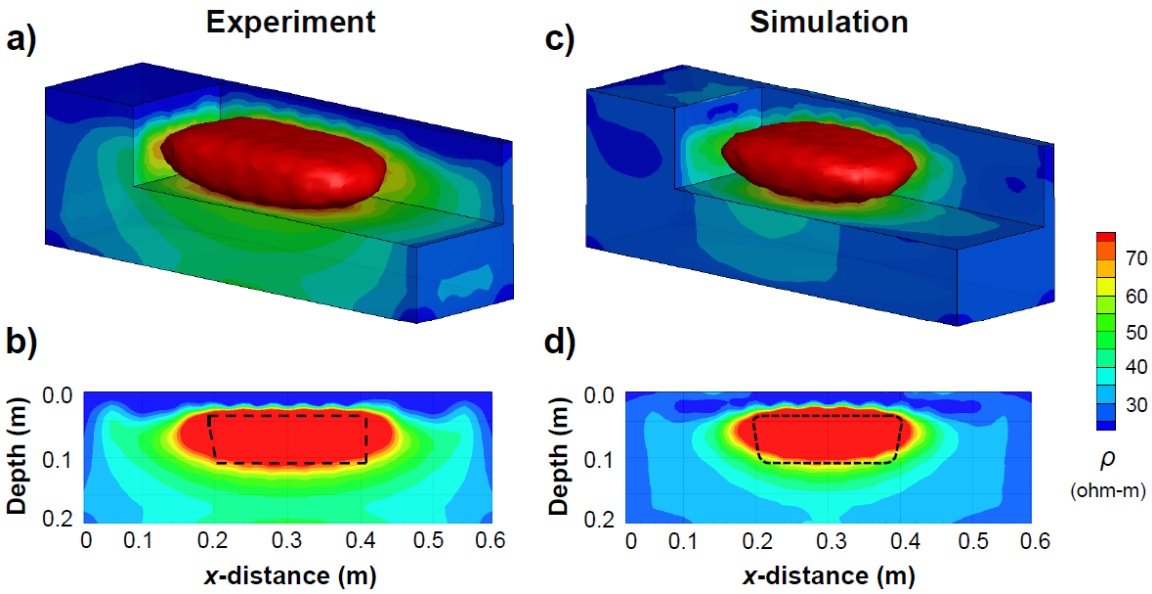

Figure 4-5: Experimental measured and numerically predicted inverted resistivity images at 500 mL NAPL volume. 3D resistivity distribution obtained from (a) laboratory experiment, and (c) numerical simulation. Cross-sectional resistivity distribution (*y*-distance = 0.10 m) from (b) laboratory experiment, and (d) numerical simulation. The 3D isosurfaces (80 ohm-m) in (a,c) illustrate the inferred extent of NAPL invasion. The black dashed line corresponding to the actual extent of NAPL invasion (from Figure 4-4a) is superimposed here in (b), while the black dotted line corresponding to the simulated extent of NAPL invasion (from Figure 4-4b) is superimposed here in (d).

Figures 4-5c and 4-5d show the corresponding inverted resistivity images predicted by the simulated ERT survey using the simulated NAPL distribution (see Figure 4-4b). It is evident that the numerically simulated inverted resistivity distribution provides a reliable

delineation of the simulated NAPL distribution (superimposed on Figure 4-5d) and also reasonably simulates the actual ERT survey results (Figure 4-5, left).

4.3.3.2 Temporal comparison

A comparative analysis of the experimental and numerically predicted ERT responses was also performed on changes in NAPL distribution over time. Following the methodology in Section 2.3, estimates of time-lapse NAPL saturation changes from the 4D-ATC inverted resistivity distributions from each monitoring step were obtained using Archie's law and differential imaging between monitoring steps.

Figure 4-6 illustrates the time-lapse monitoring responses from both experimental (left column in Figure 4-6) and numerical simulation (right column) measurements. Each sub image depicts the NAPL 'volume removed' body between each volume interval. For example, Figure 4-6a presents the ERT-measured initial 50% NAPL volume reduction. Recalling that this is NAPL injection from a central point shown in reverse order, the initial NAPL body is shrinking laterally and vertically over time with NAPL volume being progressively removed at its outer edge. It is evident from Figures 4-6a to 4-6d that experimental time-lapse ERT reasonably resolves these expected time-lapse changes in NAPL distribution. For instance, the elongated nature of the 50% NAPL volume removed body in Figure 4-6a corresponds to NAPL volume being predominantly removed at the left and right hand edges in the *x*-direction during the first volume interval. Similarly, Figure 4-6d captures the spherical time-lapse change corresponding to the final 10% NAPL volume removed around the central injection point. Each sequential change related to the discrete interval of % total NAPL volume reduced (shown in Figures 4-6a to 4-6d) is then assigned an isosurface colour and combined in Figure 4-6e, which shows all of the sequential changes superimposed. Similarly, Figures 4-6f to 4-6i illustrate the time-lapse ERT changes predicted from numerical simulations of the experiment. The simulated time-lapse changes again correspond to the expected pattern and location of NAPL volume removal, while also showing close correlation to the experimental time-lapse changes.

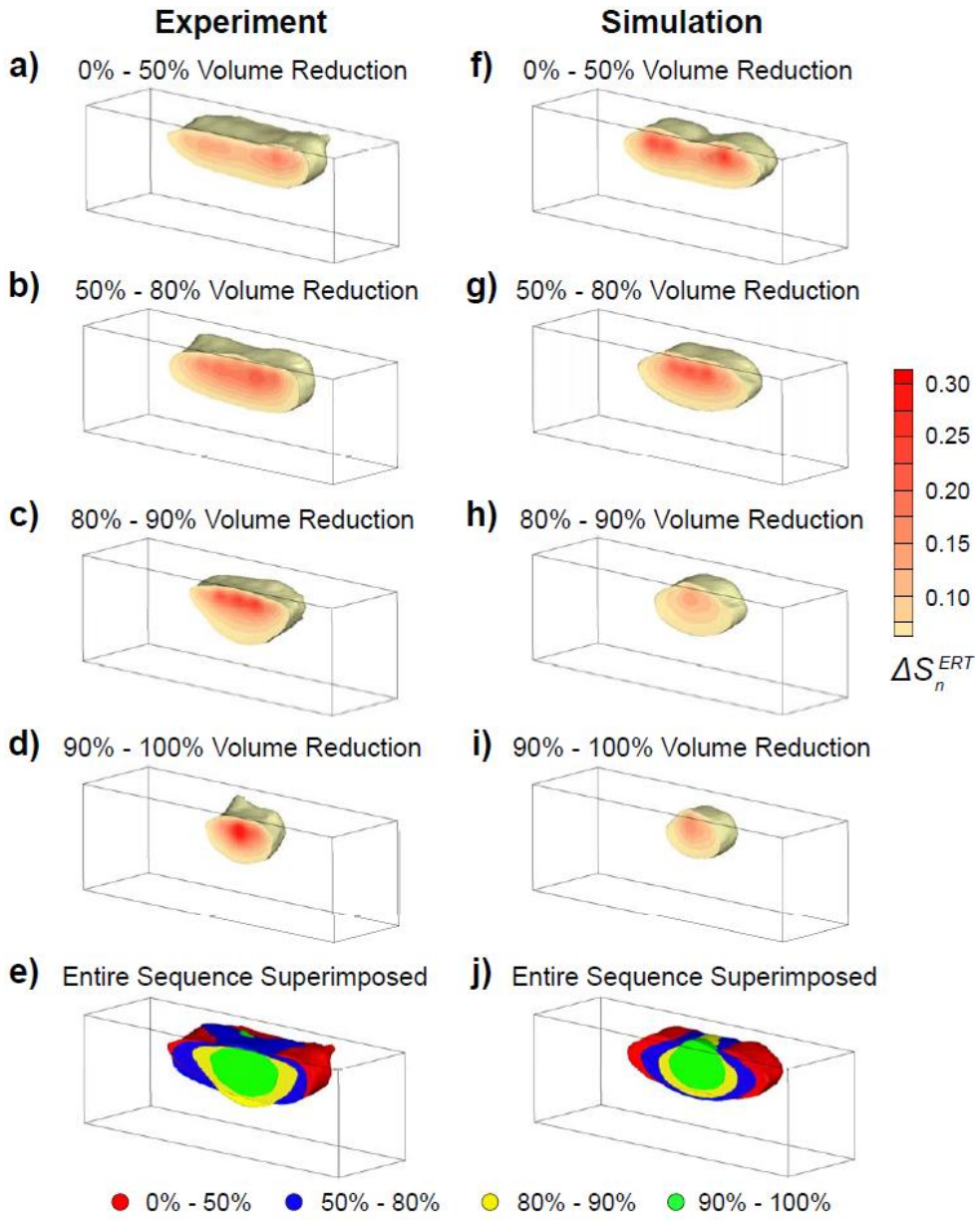

Figure 4-6: ERT-measured time-lapse changes of NAPL volume reduction for the experimental scenario. The outer isosurface encompasses NAPL saturation changes greater than 3% between ERT surveys. The left column provides a 3D view of each sequential NAPL volume change measured from the experiment (a-d) with the front cut away to reveal the NAPL saturation distribution. The right column provides a 3D view of each sequential change predicted by the model using the simulated evolving NAPL distribution (f-i). In (e) and (j) all of the sequential changes above are superimposed with all distinction of the saturation gradient removed for clarity; here isosurface colours correspond to (numbers indicating discrete interval of NAPL volume reduced): 0-50% (red), 50-80% (blue), 80-90% (yellow), 90-100% (green).

The cumulative NAPL volume change as a function of depth, measured from both the experimental and numerical ERT surveys, is presented in Figure 4-7. The actual NAPL volume removed at each monitoring step is indicated, with the corresponding quantities measured by experimental ERT and simulated ERT (i.e., the integrated area under the shown plots) shown in the legend. In all cases, the largest changes correspond to the location of the medium sand block and associated NAPL invasion (i.e., 0.04 m – 0.11 m depth), as expected. It is evident that the numerically predicted cumulative NAPL volume change generally shows good agreement with the experimentally measured changes.

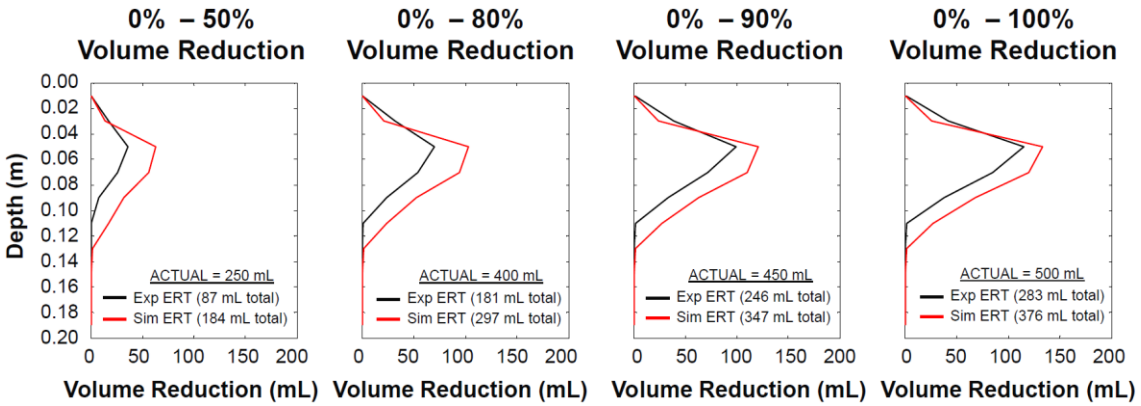

Figure 4-7: Plots of ERT-derived experimental and numerically predicted cumulative volume change as a function of depth (calculated as horizontal slices in the 3D domain) for the four monitoring 'volume reduction' steps.

It is evident from this validation experiment that spatial and temporal comparisons demonstrate confidence in the 4D ERT approach for identifying changes in NAPL distribution. It also provides confidence in the DNAPL-ERT model to simulate the coupled process of subsurface changes and ERT surveys of those changes. It is acknowledged that this experimental apparatus does not contain the complexity of a field site. Nevertheless, it provides confidence that the technique and the model are valuable tools for exploring ERT response to changing NAPL distributions. The model is used to study 4D ERT at the field scale in the following section.

4.4 ERT Mapping of DNAPL Remediation: Field Scale Simulations

4.4.1 DNAPL Release Scenarios

Four field scale releases of chlorinated solvent DNAPLs were generated for this study. Using a combination of two different heterogeneous clayey sand environments and two different DNAPL types, a range of source zone architectures was achieved. All simulations used a model domain that was 22 m long in both lateral dimensions (*x*, *y*) and 4 m in the vertical dimension (*z*). A nodal spacing of 0.50 m in the lateral directions and 0.25 m in the vertical direction discretized the DNAPL model domain into 30,976 nodes. In all cases, the water table was established at 0.5 m below ground surface, below which the domain was initially fully saturated with water. The capillary fringe is assumed to be negligible and the vadose zone was assigned a single (average) water content of 40%. While explicitly incorporating a capillary fringe would provide a more gradual transition in electrical properties, it is not expected to impact the conclusions of this work. In all cases, the side boundaries were characterized by fixed, hydrostatic water pressures such that an average hydraulic gradient of 0.01 was established across the domain in the positive *x* direction. The groundwater was 20 ºC and composed of Na^+ and Cl^- ions at 900 ppm concentration, which is representative of relatively fresh groundwater. The bottom boundary employed in the multiphase flow model is set as impermeable to all fluids, representative of a low permeability clay or bedrock layer.

Two intrinsic permeability fields with contrasting degrees of heterogeneity were employed. The first employed a single aquifer characterized by a random, spatially-correlated permeability field generated using the algorithm of Robin et al. (1991). This domain employed a mean permeability of 4.8 $x10^{-12}$ m^2 and variance of ln(*k*) of 2.9, representing an aquifer with significant heterogeneity characterized by grain sizes from coarse sand to clay. Exponential autocorrelation was employed to define average correlation lengths of 8 m for the horizontal dimensions (16 nodes) and 1 m for the vertical dimension (4 nodes), providing a horizontally laminated structure. This permeability field, hereafter referred to as the ‘heterogeneous domain’, was employed for two of the DNAPL release scenarios as imaged in Figures 4-8a and 4-8b.

The second permeability field contains two laminar, homogeneous aquifers separated by a clay aquitard. The two aquifers were composed of medium sand with a uniform permeability of 4.8 x10^{-12} m^2 (i.e., mean permeability of the heterogeneous domain). The shallow, unconfined aquifer was 2 m thick while the deeper aquifer was 1.5 m thick and they were separated by a 0.5 m thick clay layer with a permeability of 1.0 x10^{-14} m^2. All of the units extended the full width and breadth of the domain. This permeability field, hereafter referred to as the 'layered domain', was used for two DNAPL release scenarios as imaged in Figures 4-8c and 4-8d. Table 4-2 summarizes additional hydrogeological properties employed for all simulations. Using the DNAPL-ERT linkage methodology, the spatial distribution of clay content fraction, Cl, and total porosity, ϕ, within the soil matrix domains were determined. In the heterogeneous domain, 47.9 % (14,831 nodes) exhibited $Cl > 0$, with a mean Cl = 0.085 and variance of Cl = 0.003, while mean ϕ = 0.33 and variance ϕ = 0.001. In the layered domain, 12.5 % (3,872 nodes) exhibited Cl = 0.113 and ϕ = 0.34 (i.e., all the aquitard nodes).

Two different chlorinated solvent DNAPLs were employed: chlorobenzene (CB) and tetrachloroethylene (PCE). Their fluid properties are shown in Table 4-3, revealing that they span a wide range of DNAPL mobility (i.e., DNAPL density divided by viscosity). As a result, they were expected to provide a range of DNAPL source zone architectures with varying complexities and depths of penetration (Gerhard et al., 2007). CB and PCE released into the heterogeneous domain are hereafter named 'CB_het' and 'PCE_het', while CB and PCE released into the layered domain are hereafter named 'CB_lay' and 'PCE_lay'. All releases simulated a leaking lagoon located at the water table.

Table 4-2: Numerical model parameters for field scale simulations

Parameter	Value	Units
Hydrogeological parameters		
Sand porosity [a]	0.32 (saturated); 0.46 (vadose)	-
Clay porosity [a]	0.42 (saturated); 0.56 (vadose)	-
Water density [b]	1000	kg/m^3
Water viscosity [b]	0.001	Pa·s
Electrical parameters		
Sand resistivity [c]	1000	ohm·m
Clay resistivity [c]	30	ohm·m
Water resistivity [d]	6.5	ohm·m
DNAPL and air resistivity [e]	1.0×10^6	ohm·m

[a] Bear (1972)

[b] Gerhard et al. (2007)

[c] Loke (2013)

[d] Calculated from Equation 3-9 in Chapter 3

[e] Chambers et al. (2004)

The release boundary was specified by a constant total DNAPL flux (1 m^3/day) through a 3 m^2 patch area located between 8.5 m and 11.5 m in both horizontal directions. In the layered domain the flux through each node in the patch area was identical; however, in the heterogeneous domain the fraction of total DNAPL flux through each source node was weighted according to the node's permeability in order to mimic the realistic inflow of DNAPL (Grant et al., 2007a). The source was activated at time t = 0 days and terminated at t = 5 days, representing the release of 5 m^3 (1,321 gallons) of DNAPL. The infiltrated DNAPL was allowed to redistribute for 6 months to create a realistic initial subsurface distribution of DNAPL prior to remediation and time-lapse ERT monitoring. At this point, all DNAPL had stopped moving or moved very slowly and the final architectures were essentially evolved. To ensure that the full 5 m^3 of DNAPL was retained, no DNAPL was permitted to dissolve prior to the end of this redistribution stage.

Table 4-3: DNAPL properties for field scale simulations

Compound	**Density (kg/m^3) [e]**	**Viscosity (Pa·s) [e]**	**Interfacial Tension (N/m) [f]**	**Mobility (s/m^2)**
Chlorobenzene	1100	0.000800	0.0374	125000
Tetrachloroethylene	1630	0.000900	0.0444	700000

[e] Pankow et al. (1996)

[f] Mercer and Cohen (1990)

Figure 4-8 illustrates the spatial distribution of the 5 m^3 DNAPL for each of the four release scenarios at t = 6 months (i.e., prior to remediation). The low-density CB source zones shown in Figures 4-8a and 4-8c were characterized by high lateral spreading and limited vertical migration. The CB_lay spill (Figure 4-8c) was unable to overcome the entry pressure of the clay and thus 100% of the DNAPL was retained above 2 m. The CB_het spill (Figure 4-8a) spread laterally and found a low resistance pathway to permit deeper migration, although 85% of the mass still resided within the top 2 m. The high-density PCE_het and PCE_lay releases shown in Figures 4-8b and 4-8d, respectively, exhibited reduced lateral spreading and more substantial vertical migration, as expected. Both PCE releases formed high saturation pools on the impermeable base of the domain, with only 44% and 50% of the DNAPL mass (for PCE_het and PCE_lay, respectively) retained in the upper 2 m.

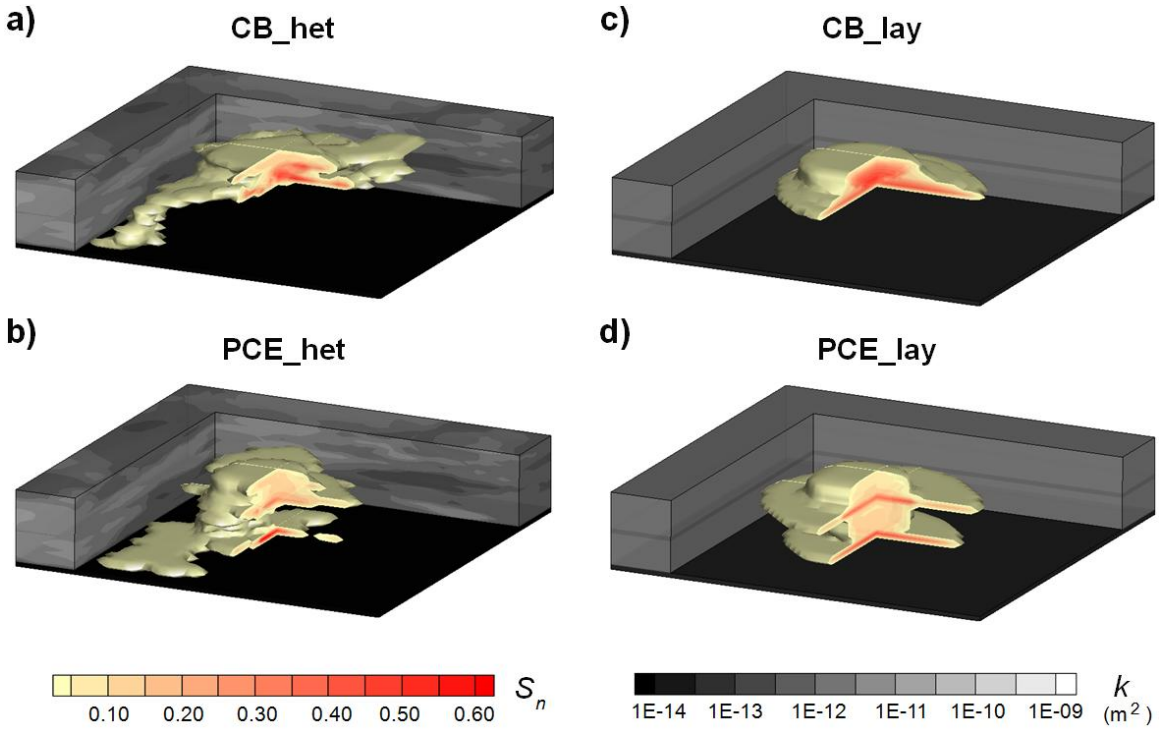

Figure 4-8: DNAPL distributions corresponding to t = 6 months (i.e., prior to remediation) following the release of 5 m3 of (a) chlorobenzene, (b) tetrachloroethylene into the heterogeneous domain, and (c) chlorobenzene, (d) tetrachloroethylene into the layered domain. Shown are DNAPL saturations above 1%, with deeper red corresponding to higher DNAPL saturations. The permeability field is shown in grayscale with darker shades of gray representing lower permeability. Both DNAPL and permeability fields are partially cutaway to assist visibility.

The DNAPL bodies were characterized by a network of both high saturation pools and residual zones. The layered spills exhibited mean DNAPL saturations of 20% and 13%, for CB_lay and PCE_lay, respectively, with a relatively narrow range of DNAPL saturation (1% to 54%); this was indicative of the relatively cohesive distribution of DNAPL. In contrast, the heterogeneous spills exhibit mean DNAPL saturations of 16% and 14% for CB_het and PCE_het, respectively and exhibited a wider range of DNAPL saturations (1% to 73%). The four DNAPL scenarios, with the range of source zone architecture and variety of subsurface soil structures, provided a variety of complex electrical targets. The subsequent sections describe the evolving remediation of these source zones and the ability of ERT surveys to monitor their remediation.

4.4.2 Remediation of Spill Scenarios

For all simulations, the configuration of DNAPL at the end of the release/redistribution period (i.e., Figure 4-8) represented the initial DNAPL source zone subject to remediation. Moreover, the DNAPL configuration at this time was "immobilized" so that no further DNAPL migration occurred, ensuring that ERT monitoring focused on DNAPL disappearance. While the model can simulate a number of types of remedial processes, remediation via enhanced dissolution in groundwater was chosen for this work. In all cases, a DNAPL solubility of 8520 mg/L (i.e., solubility of a relatively highly soluble DNAPL such as 1,2 dichloroethane) was used in order to limit the differences between simulations to DNAPL architecture alone while accelerating DNAPL mass removal rates similar to engineered remediation such as surfactant or cosolvent flushing. The hydraulic gradient of 0.01 represents engineered groundwater pumping across the source zone. Each simulation was continued until all of the DNAPL mass had reduced to zero.

Figure 4-9 illustrates the dissolution of the CB_het source zone. The initial condition immediately prior to dissolution (i.e., 0% DNAPL mass reduction) is presented in Figure 4-9a (same as Figure 4-8a). Figure 4-9b through Figure 4-9e illustrates the scenario following increments of 20% DNAPL mass (i.e., 1 m^3) reduction. The mass removal behaviour was similar to that described in studies that explored the evolution of DNAPL source zones in 2D simulations (e.g., Christ et al., 2006; Grant and Gerhard, 2007b). DNAPL was preferentially removed from the upgradient edge of the source zone, where the concentration of CB in groundwater was low and the driving force for mass transfer was high. DNAPL also dissolves first from the higher permeability pathways where groundwater velocities are greatest. Furthermore, DNAPL residual dissolves faster than DNAPL pools because of the higher interfacial area for mass transfer and the higher groundwater velocities possible within these higher relative permeability regions. For example, observe the rapid dissolution of the isolated DNAPL branch that penetrated to the bottom of the domain due to a combination of these factors.

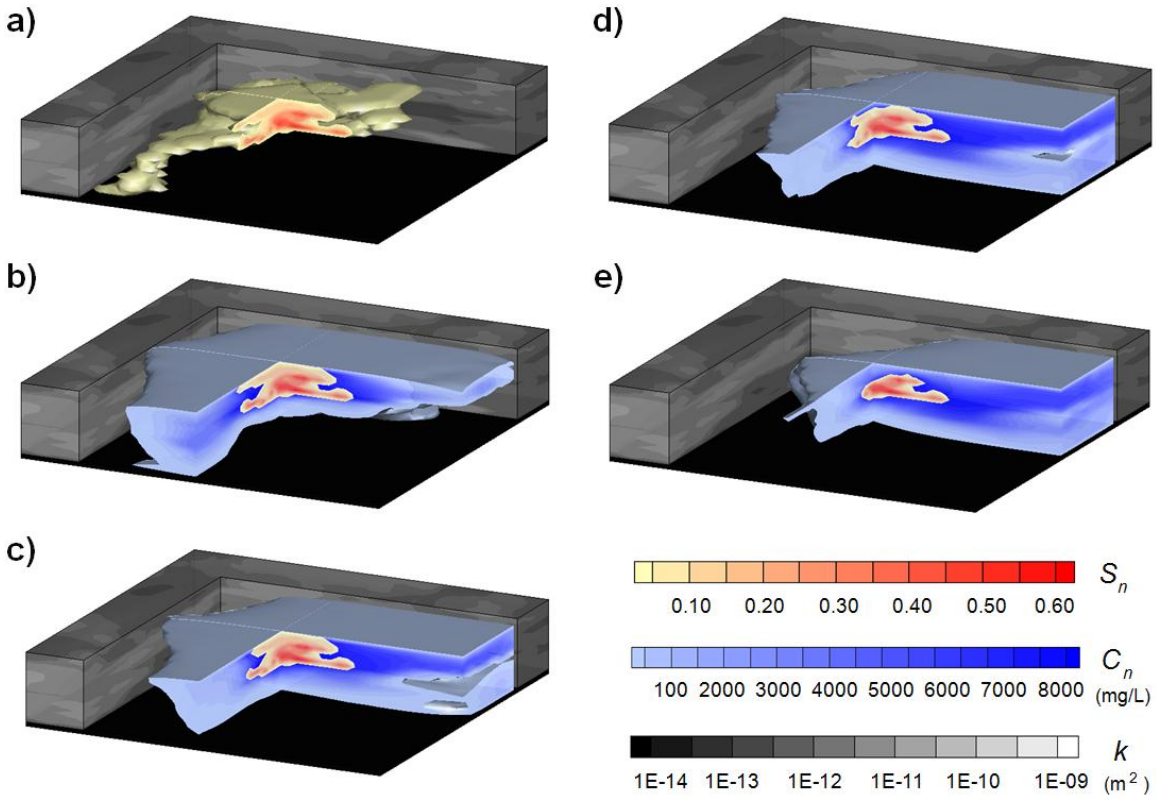

Figure 4-9: Evolution of the chlorobenzene DNAPL source zone in the heterogeneous domain (CB_het). DNAPL saturations shown in yellow-to-red scale (minimum isosurface = 0.01) and dissolved phase concentrations shown in light-to-dark blue scale (minimum isosurface = 100 mg/L). Snapshots shown after the initial 5 m3 DNAPL mass was reduced (a) 0%, (b) 20%, (c) 40%, (d) 60%, and (e) 80%. Cutout of the spatially correlated random permeability field is shown with grayscale.

All of the DNAPL source zones exhibited remediation patterns similar to the CB_het spill. Figure 4-10 plots the decrease in DNAPL volume remaining over time for all four source zones. Since the same aqueous solubility was assigned to each solvent, this variation in remediation times was mainly a function of the interplay of DNAPL architecture and the effective permeability field. As expected, all of the source zones showed decreasing rates of mass loss over time (i.e., tailing) as the most accessible DNAPL subregions were successively removed. The more heterogeneous DNAPL bodies - in the "heterogeneous" domain – formed a distinct set in Figure 4-10 compared

to the releases in the "layered" domain due to the rapid removal of isolated pools and residual zones. The releases in the layered domain, as well as the PCE release in the heterogeneous domain, all exhibit significant tailing because those source zones were characterized by substantial DNAPL pools resting on capillary barriers (middle depth in Figures 4-8c and 4-8d and bottom in Figures 4-8b and 4-8d) which dissolve most slowly.

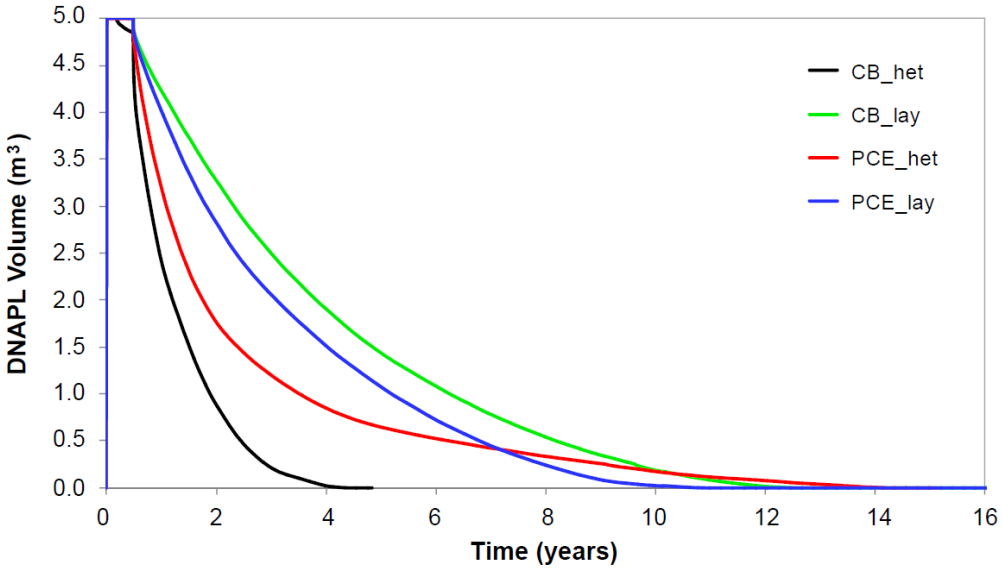

Figure 4-10: Evolution of DNAPL source zone volume over time for all four DNAPL source zones. Note that in all cases, a DNAPL solubility of 8520 mg/L was used as well as a hydraulic gradient of 0.01.

4.4.3 ERT Forward Modelling and Inversion

ERT surveys began when remediation was started and were conducted after each 10% (0.5 m^3) reduction in DNAPL volume, producing 11 total time-lapse images during the source zone lifespan (the corresponding time for each survey varies as indicated in Figure 4-10). The conversion of the hydrogeological model domain into a corresponding bulk electrical resistivity domain for each ERT survey used the electrical properties presented in Table 4-2. The finite difference blocks of the hydrogeological domain were mapped to

the hexahedral finite elements of the electrical resistivity domain following the method used in the linkage methodology presented in Chapter 3. Note that the dissolved phase plumes were not considered of electrical consequence in this study due to the small quantities of dissolved molecules and lack of charge carriers (e.g., Sauck et al., 1998). It is acknowledged that, in some instances, these plumes may exhibit elevated electrical conductivity over time due to increased dissolved ion concentrations occurring as byproducts of biodegradation of the dissolved solvent compounds (e.g., Atekwana et al., 2005). However, even if the plumes were considered more conductive than background groundwater, this would enhance the contrast with the resistive DNAPL source zone and the conclusions of this work are expected to still apply.

The 3D ERT surveys involved parallel survey lines traversing in the *x*-direction and used the dipole-dipole array with an inline electrode spacing of 1 m (23 electrodes along each survey line) and an interline spacing of 1 m (23 survey lines). As is common practice in simulating ERT surveys, random noise with a Gaussian distribution of 3 mV/A peak-to-peak amplitude was added to the voltage difference data to increase the realism of the modelling results.

The 4D-ATC method was utilized for time-lapse inversion of the apparent resistivity data recorded for all monitoring steps to obtain the 'measured' subsurface resistivity distribution. In this study, the 4D-ATC algorithm performed L_2 norm smoothness constrained inversion and used the active constraint balancing (ACB) technique in order to calculate efficiently the spatial Lagrangian multiplier for each iteration (Yi et al., 2003). For each inversion, only the current and all previously recorded monitoring data sets were employed. As discussed in Section 2.3, the 4D inverted resistivity fields were converted to ERT-measured estimates of DNAPL saturation distribution prior to analysis of the results. For the Archie's law conversion, the known pore water resistivity of 6.5 ohm-m and the mean porosity of 0.33 were used; in other words, although S_N^{ERT} was calculated for each node, the porosity of that node was assumed to be unknown, as would be the case for real sites.

4.5 Evaluating 4D ERT for Mapping DNAPL Remediation

Figure 4-11 compares the 4D ERT measurement of the remediation of the CB_het source zone to its actual disappearance. Each coloured isosurface in Figure 4-11 represents the DNAPL volume undergoing remediation in the time interval between ERT surveys (similar in format to Figures 4-6e and 4-6j). Five intervals are shown corresponding to successive 20% increases in the total DNAPL volume remediated. For example, the red isosurface depicts the portion of the DNAPL source zone undergoing remediation (hereafter called the 'remediated body') after the first 1 m^3 of the source zone is removed (difference between DNAPL in Figures 4-9a and 4-9b), while the magenta isosurface depicts the remediated body mapped between 1 m^3 of DNAPL remaining and when the DNAPL is completely eliminated (difference between Figure 4-9e and zero DNAPL). Figure 4-11 reveals that 4D ERT provides reasonable estimates of the spatial extent of the volume of the source zone remediated at each interval. This is particularly true for the outline of the treated region in plan view at all times and for the upper half of the domain. ERT, in general, is a volume averaging technique and that effect is observed here: the geophysics captures the overall shape of the subsurface volume treated but does not resolve all the smaller scale details. The DNAPL pathway that penetrated to the base of the aquifer, and is remediated in the first time interval, is partially resolved but not in its entirety due to the reduced sensitivity of ERT at depth (Figures 4-11d vs. 4-11a). In the first three time intervals (0% - 60% DNAPL remediated) when the majority of the remediation involves shallow and low to residual DNAPL saturations, ERT most accurately resolves the remediated bodies (Figures 4-11f vs. 4-11c). However, in the latter two intervals (60% - 100% DNAPL remediated), when the DNAPL body is relatively small and composed of deeper, high saturation pools, ERT overestimates the depth of the remediated body.

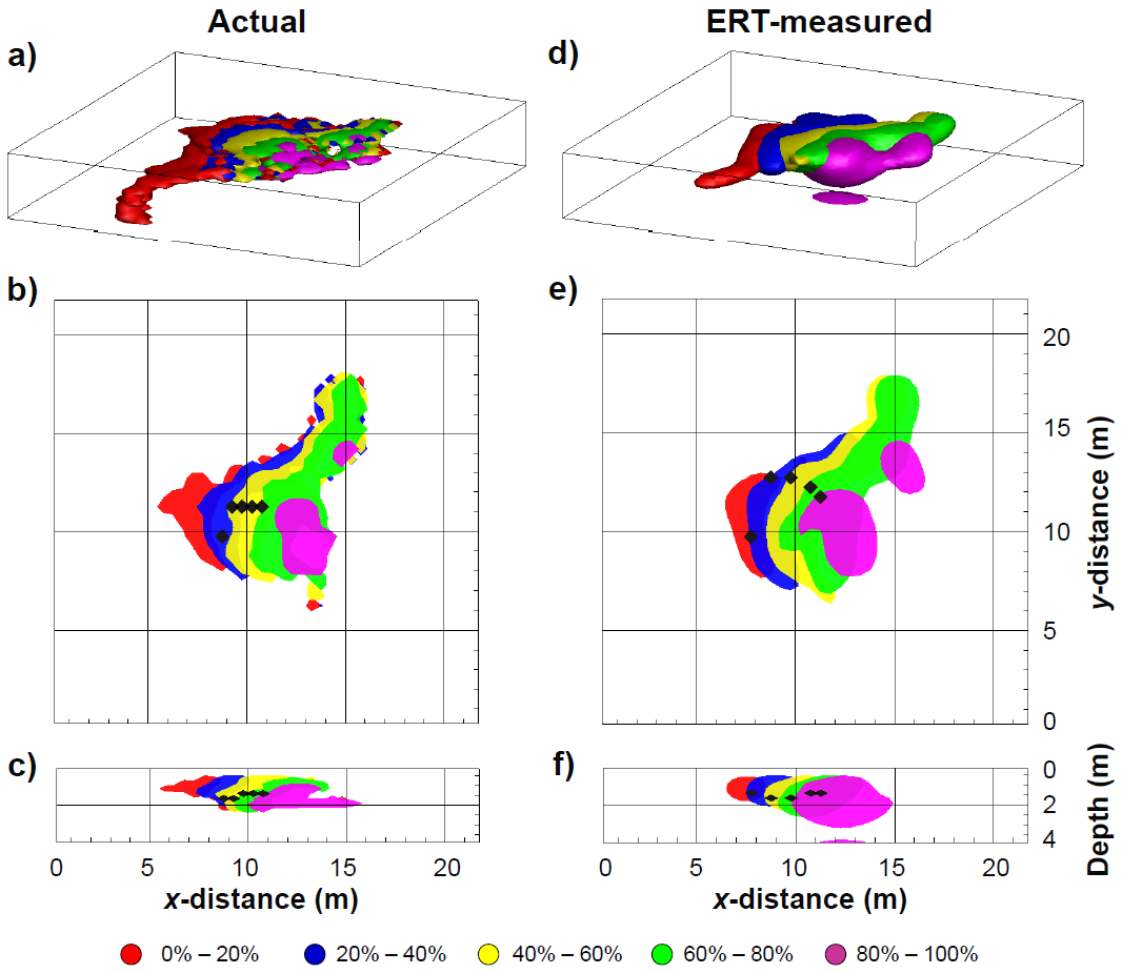

Figure 4-11: Remedial progress of chlorobenzene release in heterogeneous domain (CB_het). The left column provides the actual time-sequence of remediation while the right column provides that measured by ERT: (a,d) 3D view, (b,e) plan view section at water table (z = 1 m from top), (c,f) central cross-section parallel to groundwater flow (y = 11 m). Each isosurface encompasses all the locations where DNAPL saturations decreased more than 2% for a given time interval between ERT surveys. 5 time intervals are shown, with the isosurface colours corresponding to (numbers indicating the discrete interval of % total DNAPL volume remediated): 0-20% (red), 20-40% (blue), 40-60% (yellow), 60-80% (green), 80-100% (magenta). The center of mass for the cumulative DNAPL volume remediated (i.e., 0-20% (red), 0-40% (red + blue), 0-60% (red + blue + yellow), etc) are indicated by black markers superimposed on (b,c,e,f).

Figure 4-11 also plots the centers of mass (black markers) for the cumulative remediated body (e.g., the second marker from the left represents the center of remediated volume when 40% of the source zone has been removed). ERT reasonably locates the center of the remediated body, particularly in the *x*- and *z*-directions. It is skewed in the positive *y*-direction since ERT did not capture the deeper changes at a *y*-distance of 5 m. This limited resolution of the deeper changes is also evident in Figure 4-11f where the ERT-measured center of mass is shallower than the actual center of mass after 20% volume reduction (red). Since the center of mass is shown for the cumulative remediated body, it remains skewed in the *y*-direction. At no time is the estimated center of mass more than 3 m in error from the actual center of mass in either plan view or depth. Appendix B presents supplementary images that illustrate each stage of the modelling approach used for the CB_het, CB_lay, PCE_het and PCE_lay spill scenarios.

Figure 4-12 illustrates the time-lapse monitoring results for the CB_lay source zone. 4D ERT again captures the extent of the successive DNAPL volumes remediated. This more simplified DNAPL source zone configuration allows for relatively accurate 4D ERT mapping. Improved correlation between the center of mass of the actual and ERT-measured remediated body is evident in comparison to the CB_het spill. Once again, ERT shows increased artifacts at later times when the DNAPL remaining exists in a single high saturation pool at 2 m depth. This reduced sensitivity (and corresponding overestimation) with depth is enhanced by the existence of the clay layer directly beneath the pool which adds complexity in the structure to be resolved.

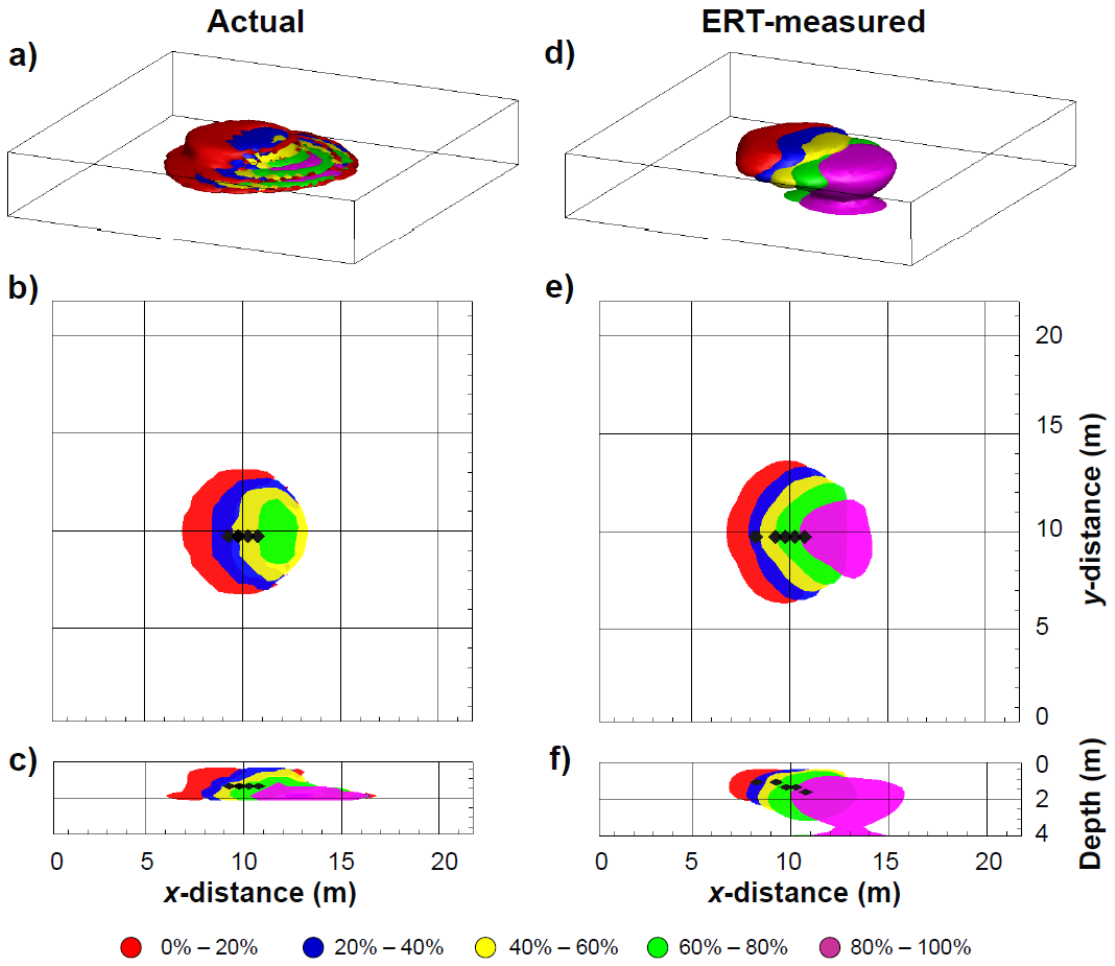

Figure 4-12: Remedial progress of chlorobenzene in layered domain (CB_lay) depicted by isosurfaces encompassing saturation decreases greater than 2%: (a) 3D view of actual changes, (d) 3D view of ERT-measured changes; (b, c) actual changes in cross-section and plan view; (e, f) corresponding ERT-measured changes. Full details in Figure 4-11 caption.

Figures 4-13 and 4-14 illustrate the time-lapse monitoring results for the PCE_het and PCE_lay source zones, respectively. The majority of both source zone volumes have migrated to depth (see Figures 4-8b and 4-8d), forming two distinct, high saturation pools at 2 m and 4 m depths, respectively. As illustrated by Figures 4-13a and 4-13c, the majority of the first 80% DNAPL volume remediated of the PCE_het source zone occurs in the shallow subsurface (0 – 2.5 m depth), with the last 20% DNAPL volume removed from the high saturation pool residing at the base of the domain at 4 m. This progression towards 'deeper' remediation is also indicated by the center of mass indicated in Figure 4-

13c. It is evident from the time-lapse ERT changes in Figure 4-13d that ERT is unable to capture the complex distribution of these deeper spills. While it does locate the central location of the remediated body, it does underestimate its horizontal extent.

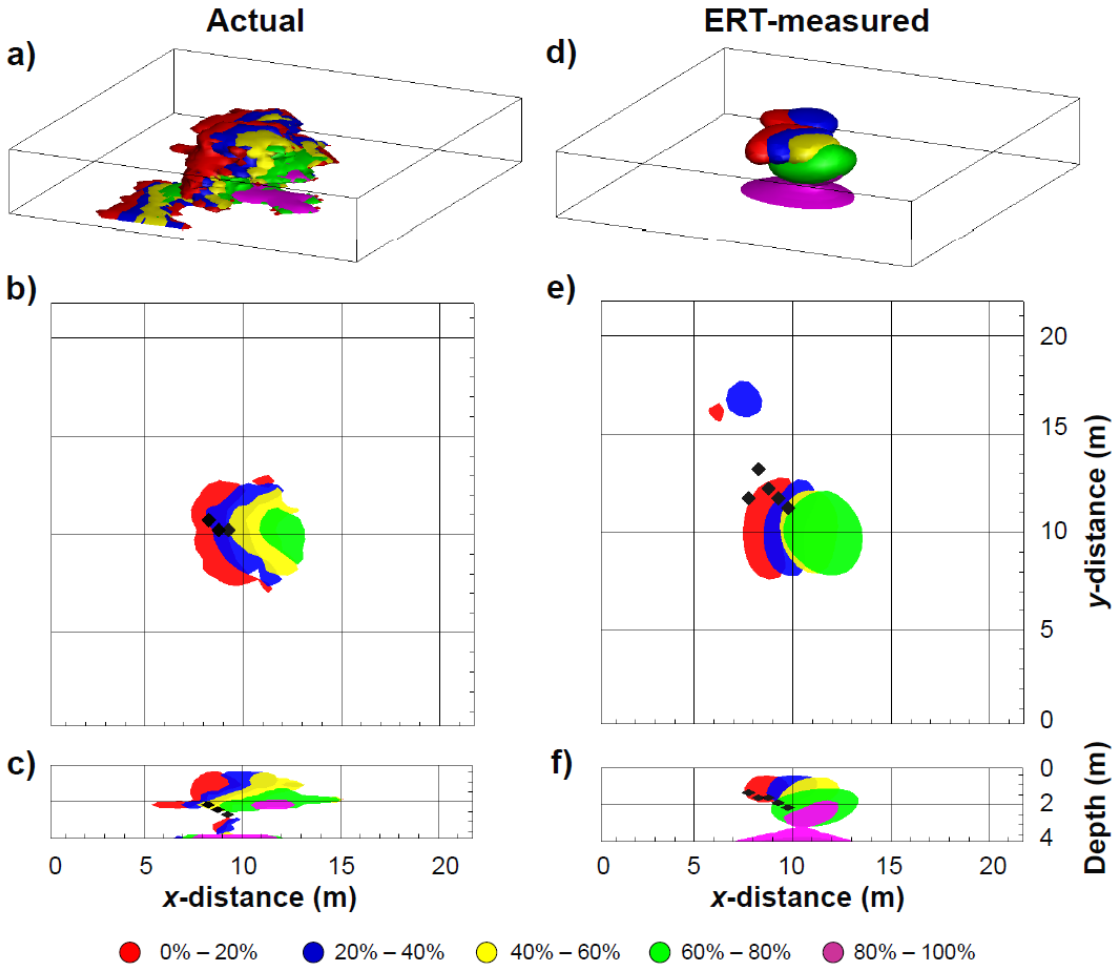

Figure 4-13: Remedial progress of tetrachlorethylene in heterogeneous domain (PCE_het) depicted by isosurfaces encompassing saturation decreases greater than 2%: (a) 3D view of actual changes, (d) 3D view of ERT-measured changes; (b, c) actual changes in cross-section and plan view; (e, f) corresponding ERT-measured changes. Full details in Figure 4-11 caption.

As illustrated in Figure 4-14, time-lapse ERT of the PCE_lay source zone also reasonably delineates the shape and location of the changes, but does not capture their horizontal

extent. Unlike the PCE_het source zone, where only late time changes existed at depth, the PCE_lay source zone also exhibits both shallow and deep changes at early time (e.g., red isosurface in Figures 4-14a and 4-14c). It is evident from Figures 4-14d and 4-14f that ERT only detected the shallow changes at these early time steps; the deeper changes went undetected as they were overlain and masked by shallower changes of similar magnitude. At late time steps (magenta isosurface), the overlying saturations were remediated and the saturation changes at depth had larger magnitudes, and ERT was able to reasonably resolve the changes at depth.

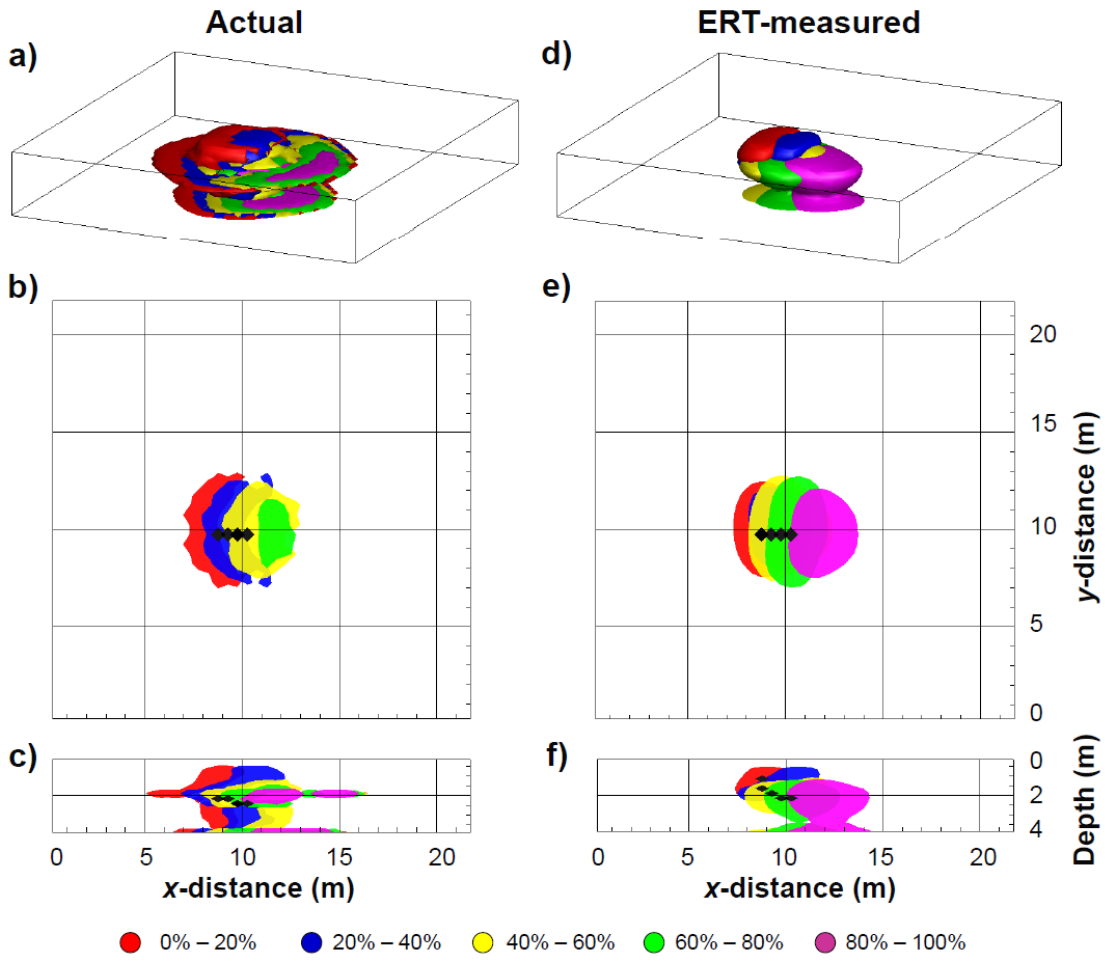

Figure 4-14: Remedial progress of tetrachlorethylene in layered domain (PCE_lay) depicted by isosurfaces encompassing saturation decreases greater than 2%: (a) 3D view of actual changes, (d) 3D view of ERT-measured changes; (b, c) actual changes in cross-section and plan view; (e, f) corresponding ERT-measured changes. Full details in Figure 4-11 caption.

The actual and ERT-measured cumulative DNAPL volume remediated as a function of depth is presented in Figure 4-15 for two of the simulations (a shallow and deep source zone). Figure 4-15a presents the CB_het source zone remediation at five times, corresponding to 20% increments in DNAPL volume reduction. The actual DNAPL volume remediated is highly variable with depth and the various pool locations are indicated by the high magnitude saturation changes. In addition, it should be noted that the DNAPL pathway that penetrates to depth comprises a relatively small volume of DNAPL and it is expected that ERT would have difficulty in mapping this deeper, small saturation pathway. As expected, the ERT-measured volume remediated does not capture the actual variability, necessarily producing a smoother envelope, which underestimates the actual volume. This underestimation increases with depth due to the reduced resolution and diminished resistivity response which, as discussed earlier, affects accurate estimation of DNAPL saturation changes. However, Figure 4-15a suggests overall that 4D-ERT can effectively quantify the DNAPL volume remediated as a function of depth for the shallow source zones.

Figure 4-15b presents the volume of DNAPL remediated for the PCE_het source zone which is characterized by highly saturated DNAPL pools at depths of 2 m and 4 m and, consequently, this is where the majority of the DNAPL remediation occurs. Time-lapse ERT is unable to effectively distinguish between these two pools, thereby averaging both pools. The magnitude of the ERT response is diminished with depth causing severe underestimation of the high DNAPL volumes at depth. This quantitative analysis of the ERT-mapped remediation of the two source zones supports the qualitative observations obtained from Figures 4-11 to 4-14.

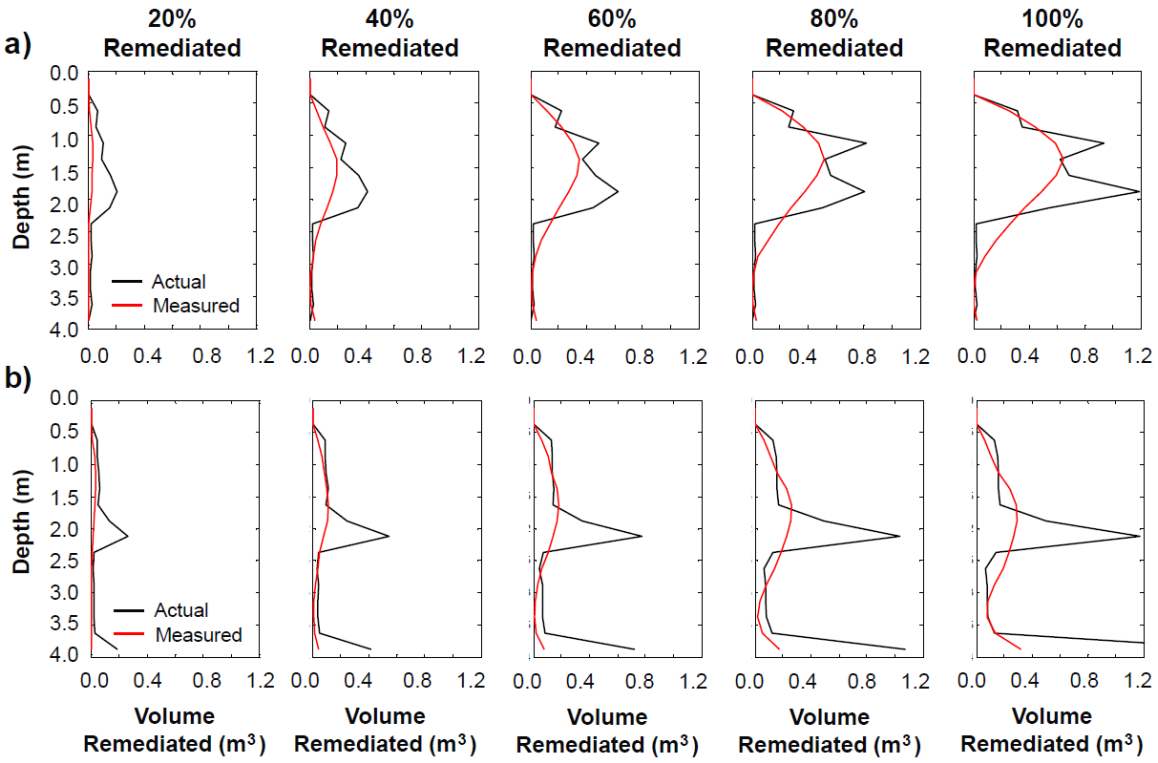

Figure 4-15: Plots of actual and ERT-measured cumulative volume remediated as a function of depth (computed as horizontal slices in the 3D domain) for 5 times corresponding to increments of 20% total volume remediated for (a) CB_het, and (b) PCE_het source zones.

One key question is: can ERT quantify how much DNAPL has been remediated? ERT-measured and actual total cumulative DNAPL volume remediated (i.e., integrated over the depth of the domain) are compared after every survey for all four source zones in Figure 4-16. It is evident that the DNAPL volume remediated is reasonably well predicted but that underestimation (points lying to the right of the 1:1 line) occurred in all cases to some degree. The CB source zones, in which at least 85% or more of the DNAPL mass is in the upper 2 m of the domain, demonstrate relatively uniform 25% underestimation at all monitoring steps. The PCE source zones, where 50% or more of the DNAPL is below 2 m depth, demonstrate increasing underestimation over time with a maximum of 50% discrepancy at the end of remediation. This is consistent with earlier figures: at later time, DNAPL remediation in the PCE source zones is primarily at depth where ERT is less sensitive.

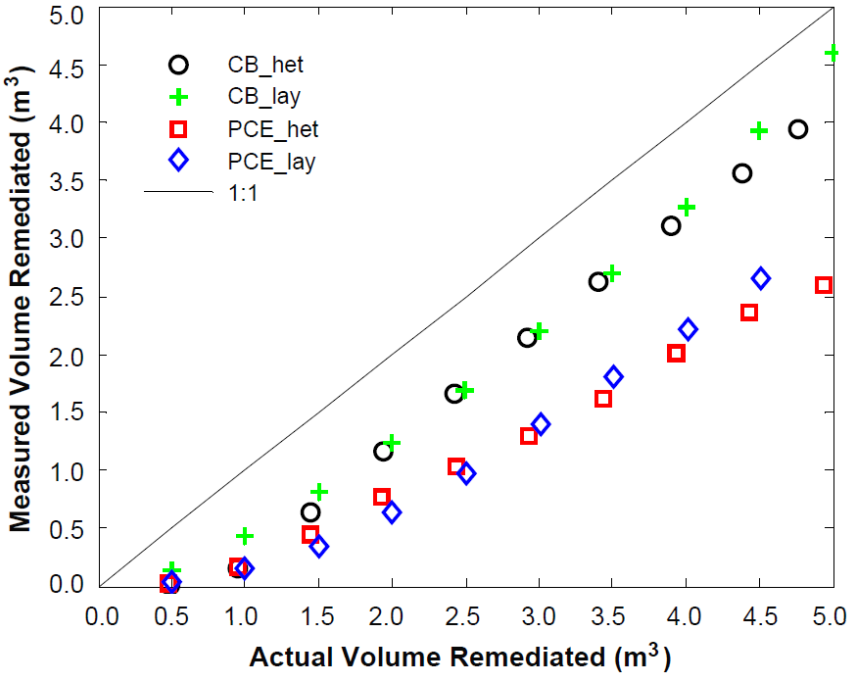

Figure 4-16: Plot of actual versus ERT-measured cumulative DNAPL volume remediated at each monitoring step for all four source zones.

A second key question is: can ERT quantify where DNAPL remediation is occurring? Figure 4-17 compares the ERT-measured and actual center of mass of the cumulative remediated DNAPL body in the mean direction of groundwater flow (i.e., positive *x*-direction) for the five monitoring steps spaced over the lifespan of each source zone. Figure 4-17 reveals that, despite the challenges with complexity and depth described, time-lapse ERT accurately predicts the progression of the remediated region across the site for all source zones. Some discrepancy exists between the ERT-measured and actual *x*-coordinate of the center of mass, but at no time is this discrepancy more than 1 m, even for the deeper PCE source zones.

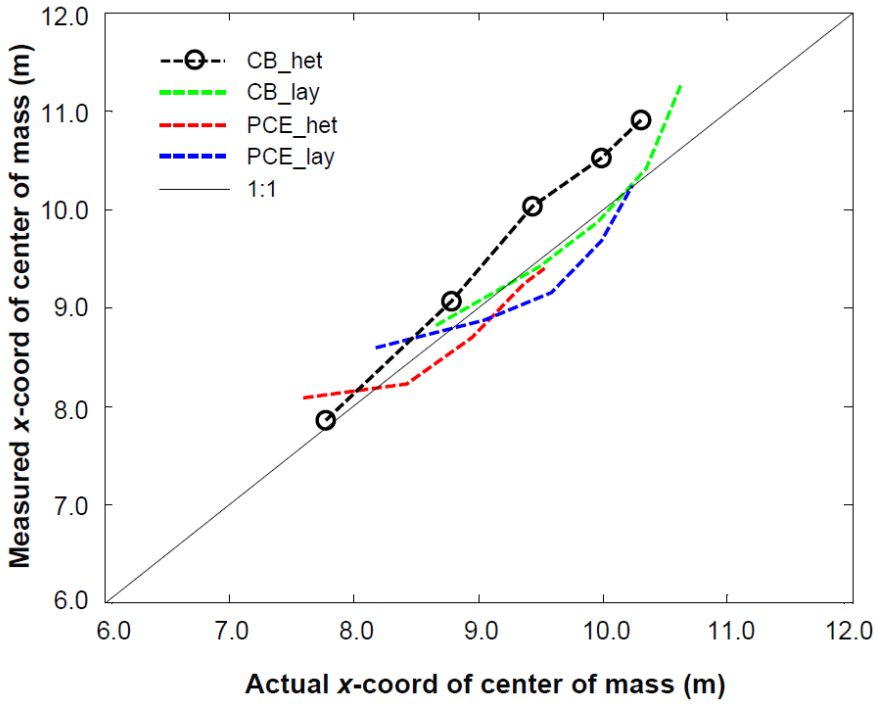

Figure 4-17: Actual versus ERT-measured *x*-coordinate of the center of mass of the cumulative remediated region. Shown are 5 monitoring steps at 20% intervals cumulative volume remediated for all four source zones. The 20% cumulative volume intervals are indicated by black circles for the CB_het source zone, but symbols are eliminated from the other plots to improve clarity.

4.6 Summary and Conclusions

This work suggests that time-lapse ERT, in particular surface ERT coupled with 4D-ATC inversion, has potential as a non-destructive approach for monitoring DNAPL remediation. A controlled laboratory experiment demonstrated the success of 4D ERT for identifying changes in NAPL distribution in a physical system. Independent simulation of the experiment with a DNAPL-ERT model provided confidence in model predictions of two coupled processes: (i) evolving NAPL distribution and (ii) time-lapse ERT monitoring of that evolution.

The DNAPL-ERT model was then employed to investigate the potential of 4D ERT monitoring of complex DNAPL source zones at the field scale. Although identifying the

detailed geometry of a complex DNAPL body is challenging for a volume averaging method like ERT, this work suggests that valuable spatial and temporal information may be available to assess and inform remedial strategies. Time-lapse ERT provided a conservative estimate of the volume of DNAPL remediated, with increased underestimation for deeper source zones. This underestimation is partly related to the limited utility and accuracy of Archie's law as it does not compensate for the diminishing resistivity response with depth. However, delineation of the DNAPL region remediated, in terms of its bulk outline and center of mass in plan view, is particularly promising. Therefore, while the effectiveness of quantitative DNAPL mass reduction estimates is dependent on the geometry and depth of the treated region, time-lapse ERT can provide valuable qualitative information (e.g., outline and center of mass) across the full range of DNAPL source zones investigated in this work.

This work corroborated the finding that 4D-ATC inversion provided improved stability and resolution of all inverted tomograms and removed the majority of artifacts that traditional independent inversion introduce. This is particularly important for monitoring complex, highly variable targets such as DNAPL source zones, where artifacts would be mistaken for clean-up. Further improvements to these 4D algorithms, such as active spatial constraints (e.g., Karaoulis et al., 2014) and L_1-norm minimizations (e.g., Kim et al., 2013), may further optimize time-lapse monitoring performance.

Overall, these conclusions are valid for relatively shallow DNAPL source zones (i.e., within several meters of the surface). In general, it is expected that sites contaminated with lower density DNAPLs such as coal tar and chlorobenzene would be more amenable to ERT monitoring than sites with higher density DNAPLs such as trichloroethylene and tetrachloroethylene. It is acknowledged that ERT applied at the surface, while technically simple and relatively inexpensive, exhibits reduced sensitivity and resolution with depth. The depth of penetration is affected by several factors, such as the average clay content and the thickness of the vadose zone. In general, the depth of investigation is approximately $1/5^{th}$ the survey length (e.g., in this study, an array spread of 22 m provided reasonable resolution to 4 m depth). In some cases, extension of the spread length will increase the depth of investigation. However, it will not increase the resolving

ability with depth; any changes at larger depth need to be considerably more significant in size and magnitude in order to be resolved. Monitoring DNAPL remediation at greater depths likely requires non-metallic boreholes (e.g., cross-hole or surface-to-borehole surveys). Future work will examine these configurations and consider the benefits against the costs (e.g., invasive drilling at relatively tight spacing).

Practical, non-invasive tools do not currently exist for mapping DNAPL remediation. For the range of source zones and site conditions considered in this work, 4D time-lapse ERT implemented at the surface may provide valuable estimates of the extent of DNAPL remediation achieved, both in terms of the spatial extent and the corresponding volume removed in real time. A critical next step is validating these findings by conducting pilot tests of 4D ERT monitoring at suitable field sites.

4.7 References

Archie, G.E. 1942. The electrical resistivity log as an aid in determining some reservoir characteristics. Transactions of the AIME, 146: 54–62.

Atekwana, E.A., E. Atekwana, F.D. Legall, and R.V. Krishnamurthy. 2005. Biodegradation and mineral weathering controls on bulk electrical conductivity in a shallow hydrocarbon contaminated aquifer. Journal of Contaminant Hydrology, 80(3–4): 149-167.

Bear, J. 1972. Dynamics of fluids in porous media. Dover, Mineola, New York.

Berg, C. 2007. An effective medium algorithm for calculating water saturations at any salinity or frequency. Geophysics, 72(2): E59-E67.

Breen, S.J., C.R. Carrigan, D.J. LaBrecque, and R.L. Detwiler. 2012. Bench-scale experiments to evaluate electrical resistivity tomography as a monitoring tool for geologic CO2 sequestration. International Journal of Greenhouse Gas Control, 9(0): 484-494.

Brewster, M.L., A.P. Annan, J.P. Greenhouse, B.H. Kueper, and G.R. Olhoeft. 1995. Observed migration of a controlled DNAPL release by geophysical methods. Ground Water, 33: 977-987.

Cardarelli, E., and G. Di Filippo. 2009. Electrical resistivity and induced polarization tomography in identifying the plume of chlorinated hydrocarbons in sedimentary formation: a case study in Rho (Milan—Italy). Waste Management & Research, 27: 595–602.

Chambers J.E., M.H. Loke, R.D. Ogilvy, and P.I. Meldrum. 2004. Noninvasive monitoring of DNAPL migration through a saturated porous medium using electrical impedance tomography. Journal of Contaminant Hydrology, 68: 1–22.

Chambers, J.E., P.B. Wilkinson, G.P. Wealthall, M.H. Loke, R. Dearden, R. Wilson, D. Allen, and R.D. Ogilvy. 2010. Hydrogeophysical imaging of deposit heterogeneity and groundwater chemistry changes during DNAPL source zone bioremediation. Journal of Contaminant Hydrology, 118: 43-61.

Christ, J.A., C.A. Ramsburg, K.D. Pennell, and L.M. Abriola. 2006. Estimating Mass Discharge from DNAPL Source Zones using Upscaled Mass Transfer Coefficients: An Evaluation using Multiphase Numerical Simulations. Water Resources Research, 42: W11420.

Daily, W., and A. Ramirez, A. 1995. Electrical resistance tomography during in-situ trichloroethylene remediation at the Savannah River Site. Journal of Applied Geophysics, 33: 239–249.

Doetsch, J., N. Linde, T. Vogt, A. Binley, and A.G. Green. 2012. Imaging and quantifying salt-tracer transport in a riparian groundwater system by means of 3D ERT monitoring. Geophysics, 77(5): B207-B218.

Gasperikova, E., S.S. Hubbard, D.B. Watson, G.S. Baker, J.E. Peterson, M.B. Kowalsky, M. Smith, and S. Brooks. 2012. Long-term electrical resistivity monitoring of recharge-induced contaminant plume behavior. Journal of Contaminant Hydrology, 142–143: 33-49.

Gerhard, J.I., and B.H. Kueper. 2003a. Capillary pressure characteristics necessary for simulating DNAPL infiltration, redistribution, and immobilization in saturated porous media. Water Resources Research, 39: 1212.

Gerhard, J.I., and B.H. Kueper. 2003b. Relative permeability characteristics necessary for simulating DNAPL infiltration, redistribution, and immobilization in saturated porous media. Water Resources Research, 39: 1213.

Gerhard, J.I., and B.H. Kueper. 2003c. Influence of constitutive model parameters on the predicted migration of DNAPL in heterogeneous porous media. Water Resources Research, 39: 1279.

Gerhard, J.I., T. Pang, and B.H. Kueper. 2007. Time scales of DNAPL migration in sandy aquifers. Ground Water, 45: 147-157.

Grant, G.P., and J.I. Gerhard. 2007a. Simulating the dissolution of a complex dense non-aqueous phase liquid source zone: 1. model to predict interfacial area. Water Resources Research, 43: W12410.

Grant, G.P., and J.I. Gerhard. 2007b. Simulating the dissolution of a complex dense non-aqueous phase liquid source zone: 2. experimental validation of an interfacial area-based mass transfer model. Water Resources Research, 43.

Grant, G.P., J.I. Gerhard, and B.H. Kueper. 2007a. Field scale impacts of spatially correlated relative permeability in heterogeneous multiphase systems. Advances in Water Resources, 30: 1144-1159.

Grant, G.P., J.I. Gerhard, and B.H. Kueper. 2007b. Multidimensional validation of a numerical model for simulating a DNAPL release in heterogeneous porous media. Journal of Contaminant Hydrology, 92: 109-128.

Hadley, P., and C. Newell. 2012. Groundwater Remediation, the Next 30 Years. Ground Water, 50(5): 669-678.

Johnson, T.C., L.D. Slater, D. Ntarlagiannis, F.D. Day-Lewis, and M. Elwaseif. 2012. Monitoring groundwater-surface water interaction using time-series and time-frequency analysis of transient three-dimensional electrical resistivity changes. Water Resources Research, 48(7): W07506.

Karaoulis, M.C., J.H. Kim, and P.I. Tsourlos. 2011a. 4D active time constrained resistivity inversion. Journal of Applied Geophysics, 73: 25-34.

Karaoulis, M., A. Revil, D.D. Werkema, B.J. Minsley, W.F. Woodruff, and A. Kemna. 2011b. Time-lapse three-dimensional inversion of complex conductivity data using an active time constrained (ATC) approach. Geophysical Journal International, 187: 237-251.

Karaoulis, M., A. Revil, P. Tsourlos, D.D. Werkema, and B.J. Minsley. 2013. IP4DI: A software for time-lapse 2D/3D DC-resistivity and induced polarization tomography. Computers & Geosciences, 54(0): 164-170.

Karaoulis, M., P. Tsourlos, J.H. Kim, and A. Revil. 2014. 4D time-lapse ERT inversion: introducing combined time and space constraints. Near Surface Geophysics, 12(1): 25-34.

Kavanaugh, M.C., P.S.C. Rao, L. Abriola, C. Newell, J. Cherry, T. Sale, G. Destouni, S. Shoemaker, R. Falta, R. Siegrist, D. Major, G. Teutsch, J. Mercer, and K. Udell. 2003. The DNAPL remediation challenge: is there a case for source depletion? US Environmental Protection Agency, Washington DC.

Kim, J.H., M.J. Yi, S.G. Park, and J.G. Kim. 2009. 4-D inversion of DC resistivity monitoring data acquired over a dynamically changing earth model. Journal of Applied Geophysics, 68: 522-532.

Kim, J.H., R. Supper, P. Tsourlos, and M.J. Yi. 2013. Four-dimensional inversion of resistivity monitoring data through L*p* norm minimizations. Geophysical Journal International, 195(3): 1640-1656.

Kueper, B.H., and E.O. Frind. 1991a. Two-phase flow in heterogeneous porousmedia, 1 Model development.Water Resources Research, 27(6): 1049–1057.

Kueper, B.H., and E.O. Frind. 1991b. Two-phase flow in heterogeneous porousmedia, 2 Model application.Water Resources Research, 27(6): 1058–1070.

Kueper, B.H., G.P. Wealthall, J.W.N. Smith, S.A. Leharne, and D.N. Lerner. 2003. An illustrated handbook of DNAPL transport and fate in the subsurface. Environment Agency R&D Publication 133. EA, Bristol.

Loke, M.H. 2013. Tutorial: 2-D and 3-D electrical imaging surveys. http://www.geotomosoft.com/downloads.php, accessed 20 August 2013.

Loke, M.H., and R.D. Barker. 1996. Rapid least-squares inversion of apparent resistivity pseudosections using a quasi-Newton method. Geophysical Prospecting, 44(1): 131–152.

Loke, M.H., J.E. Chambers, D.F. Rucker, O. Kuras, and P.B. Wilkinson. 2013. Recent developments in the direct-current geoelectrical imaging method. Journal of Applied Geophysics, 95: 135-156.

Lucius, J.E., G.R. Olhoeft, P.L. Hill, and S.K. Duke. 1992. Properties and hazards of 108 selected substances - 1992 edition. Open-File Report 92-527, U. S. Geological Survey.

MacPhee, S.L., J.I. Gerhard, and G. Rein. 2012. A novel method for simulating smoldering propagation and its application to STAR (Self-sustaining treatment for active remediation). Environmental Modelling and Software, 31: 84-98.

Mercer, J.W., and R.M. Cohen. 1990. A review of immiscible fluids in the subsurface: properties, models, characterization, and remediation. Journal of Contaminant Hydrology, 6: 107-163.

Naudet, V., J.C. Gourry, F. Girard, F. Mathieu, and A. Saada. 2013. 3D electrical resistivity tomography to locate DNAPL contamination around a housing estate. Near Surface Geophysics, (In Press).

Nenna, V., A. Pidlisecky, and R. Knight. 2011. Informed experimental design for electrical resistivity imaging. Near Surface Geophysics, 9: 469-482.

Nguyen, F., A. Kemna, A. Antonsson, P. Engesgaard, O. Kuras, R. Ogilvy, J. Gisbert, S. Jorreto, and A. Pulido-Bosch. 2009. Characterization of seawater intrusions using 2D electrical imaging. Near Surface Geophysics, 7: 377-390.

Newmark R.L., W.D. Daily, K.R. Kyle, and A.L. Ramirez. 1998. Monitoring DNAPL pumping using integrated geophysical techniques. Journal of Environmental and Engineering Geophysics, 3: 7–13.

Ogilvy R.D., O. Kuras, P.I. Meldrum, P.B. Wilkinson, J.E. Chambers, M. Sen, A. Pulido-Bosch, J. Gisbert, S. Jorreto, I. Frances, and P. Tsourlos. 2009. Automated monitoring of coastal aquifers with electrical resistivity tomography. Near Surface Geophysics, 7: 367–375.

Oldenborger, G.A., M.D. Knoll, P.S. Routh, and D.J. LaBrecque. 2007. Time-lapse ERT monitoring of an injection/withdrawal experiment in a shallow unconfined aquifer. Geophysics, 72(4): F177–F187.

Pankow, J.F., S. Feenstra, J.A. Cherry, and M.C. Ryan. 1996. Dense chlorinated solvents in groundwater: Background and history of the problem. In: Pankow, J.F., and J.A. Cherry (Eds.), Dense Chlorinated Solvents and other DNAPLs in Groundwater, History, Behavior, and Remediation. Waterloo Press, Portland, Oregon, United States, pp. 1-52.

Papadopoulos N.G., P. Tsourlos, G.N. Tsokas, and A. Sarris. 2007. Efficient ERT measuring and inversion strategies for 3D imaging of buried antiquities. Near Surface Geophysics, 5: 349–362.

Power C., J.I. Gerhard, P. Tsourlos, and A. Giannopoulos. 2013. A new coupled model for simulating the mapping of dense nonaqueous phase liquids using electrical resistivity tomography. Geophysics, 78(4): EN1-EN15.

Revil, A., and L.M. Cathles. 1999. Permeability of shaly sands. Water Resources Research, 35: 651-662.

Robert, T., D. Caterina, J. Deceuster, O. Kaufmann, and F. Nguyen. 2012. A salt tracer test monitored with surface ERT to detect preferential flow and transport paths in fractured/karstified limestones. Geophysics, 77(2): B55-B67.

Robin, M.J.L., E.A. Sudicky, R.W. Gillham, and R.G. Kachanowski. 1991. Spatial variability of Strontium distribution coefficients and their correlation with hydraulic conductivity in the Canadian Forces Base Borden aquifer. Water Resources Research, 27: 2619–2632.

Sauck, W.A., E.A. Atekwana, and M.S. Nash. 1998. Elevated conductivities associated with an LNAPL plume imaged by integrated geophysical techniques. Journal of Environmental and Engineering Geophysics, 2-3: 203-212.

Seferou, P., P. Soupios, N.N. Kourgialas, Z. Dokou, G.P. Karatzas, E. Candasayar, N. Papadopoulos, V. Dimitriou, A. Sarris, and M. Sauter. 2013. Olive-oil mill wastewater transport under unsaturated and saturated laboratory conditions using the geoelectrical resistivity tomography method and the FEFLOW model. Hydrogeology Journal, 21(6): 1219-1234.

Singha, K., and S.M. Gorelick. 2006. Hydrogeophysical tracking of three-dimensional tracer migration: The concept and application of apparent petrophysical relations. Water Resources Research 42(6): W06422.

Slater, L., A. Binley, R. Versteeg, G. Cassiani, R. Birken, and S. Sandberg. 2002. A 3D ERT study of solute transport in a large experimental tank. Journal of Applied Geophysics, 49: 211-229.

Tsourlos, P., and R. Ogilvy. 1999. An algorithm for the 3-D inversion of tomographic resistivity and induced polarization data: preliminary results. Journal of the Balkan Geophysical Society, 2: 30-45.

Tsourlos, P., R.D. Ogilvy, P.I. Meldrum, and G.M. Williams. 2003. Time-lapse monitoring in single boreholes using electrical resistivity tomography. Journal of Environmental and Engineering Geophysics, 8(1): 1–14.

West, M.R., G.P. Grant, J.I. Gerhard, and B.H. Kueper. 2008. The influence of precipitate formation on the chemical oxidation of TCE DNAPL with potassium permanganate. Advances in Water Resources, 31: 324-338.

Wilson, V.C., C. Power, A. Giannopoulos, J.I. Gerhard, and G.P. Grant. 2009. DNAPL mapping by ground penetrating radar examined via numerical simulation. Journal of Applied Geophysics, 69: 140-149.

Yi, M.J., J.H. Kim, and S.H. Chung. 2003. Enhancing the resolving power of least-squares inversion with active constraint balancing. Geophysics, 68: 931-941.

Zheng, C. 1990. MT3D, A Modular Three-Dimensional Transport Model for Simulation of Advection, Dispersion and Chemical Reactions of Contaminants in Groundwater Systems, 170 pp., U.S. Environ. Prot. Agency, Washington, D. C.

Zhou, Q.Y., J. Shimada, and A. Sato. 2001. Three-dimensional spatial and temporal monitoring of soil water content using electrical resistivity tomography. Water Resources Research, 37(2): 273–285.

5 IMPROVED TIME-LAPSE ELECTRICAL RESISTIVITY TOMOGRAPHY MONITORING OF DENSE NON-AQUEOUS PHASE LIQUIDS WITH SURFACE-TO-HORIZONTAL BOREHOLE ARRAYS

5.1 Introduction

Cleaning up sites contaminated with non-aqueous phase liquids (NAPLs) presents an ongoing challenge in the field of environmental remediation. Denser-than-water NAPLs (DNAPLs), such as chlorinated solvents and coal tar, are a class of hazardous industrial organic liquids often introduced into the subsurface by uncontrolled releases (Pankow et al., 1996). Following a release, DNAPLs migrate through the subsurface as an immiscible 'oil' phase in response to gravity and capillary forces. Typically a release will penetrate the water table and the majority of the mass will occupy the saturated zone for decades if not remediated. The resulting DNAPL body can exhibit a wide range of forms, from a laterally extensive pool (i.e., highly saturated accumulation) to a complex, heterogeneous distribution of both pools and residual (i.e., disconnected blobs) (Gerhard et al., 2001, 2007). This DNAPL source zone can serve as a long-term source of groundwater contamination posing significant risks to human health and the environment.

One of the most challenging and important components of a successful DNAPL remediation program is effective characterization and temporal monitoring strategies (Kavanaugh et al., 2003). Conventional techniques, which typically rely on geochemical analysis and sampling from a sparse network of intrusive boreholes, are expensive and provide limited spatial and temporal resolution. Non-invasive geoelectrical methods, particularly electrical resistivity tomography (ERT), have long been proposed to improve characterization and monitoring at contaminated sites (e.g., Brewster et al., 1995; Chambers et al., 2010). ERT is well-established and widely employed in hydrogeological applications (e.g., Slater, 2007; Loke et al., 2013). Time-lapse ERT is a strongly emerging branch in applied geophysics (Supper et al., 2014), monitoring dynamic

processes such as salt-water intrusion (e.g., Nguyen et al., 2009), groundwater-surface water interaction (e.g., Johnson et al., 2012) and CO_2 migration (e.g., Sauer et al., 2014). In the context of DNAPL site investigations, ERT exhibits significant potential due to the typically highly resistive nature of DNAPLs relative to groundwater (Lucius et al., 1992). Thus, a DNAPL occupying the saturated zone at a contaminated site is expected to provide an electrical target amenable to ERT detection, with changes in DNAPL distribution, either by migration or remediation processes, providing electrical changes that can be monitored by time-lapse ERT.

The application of ERT for mapping DNAPL in the subsurface has been suggested by a number of studies (e.g., Newmark et al., 1998; Power et al., 2013). However, ERT electrodes applied at the surface to detect static DNAPL is difficult (e.g., Cardarelli and Di Filippo, 2009). One reason is the complexity of the electrical target: an intricate, unknown distribution of DNAPL in heterogeneous soil. Thus, surface ERT used in time-lapse mode to monitor temporal changes associated with DNAPL has more potential. This is particularly true with recent advancements in time-lapse ERT data acquisition (e.g., Wilkinson et al., 2013) and inversion (e.g., Karaoulis et al., 2013). Chapter 4 (i.e., Power et al., 2014) demonstrated the potential of four-dimensional (4D) surface ERT to monitor the remediation of various DNAPL spills. This study revealed that the technique showed promise, providing reasonable delineation of the remediated DNAPL region and estimates of remediated DNAPL volumes. However, reduced effectiveness was evident in field scale scenarios with DNAPL located at depth (e.g., greater than 2 m). DNAPL at depth is expected when significant volumes are released, soils are highly permeable, and/or the DNAPL has a high density (Gerhard et al., 2007). In such cases, surface ERT is hampered by a limited investigation depth and reduced vertical resolution with distance from the surface (Chambers et al., 2010).

ERT electrodes have been deployed in vertical boreholes at DNAPL sites to achieve superior depth resolution relative to surface ERT. Chambers et al. (2004) used cross-hole ERT to monitor the migration of DNAPL through a saturated porous medium in a laboratory column. Daily and Ramirez (1995) used cross-hole ERT to image the injection of methane as a metabolic carbon source at a trichloroethylene (TCE) site. At another

TCE site, Newmark et al. (1998) used time-lapse cross-hole ERT comparison images to successfully monitor decreasing resistivity changes associated with the pumping of the pooled TCE. Goes and Meekes (2004) used cross-hole ERT to delineate DNAPL at two contaminated field sites, demonstrating a correlation between DNAPL presence and high electrical resistivity. Chambers et al. (2010) used high-resolution, cross-hole ERT in a pilot-scale experiment to map groundwater chemistry changes associated with the bioremediation of a DNAPL source zone. However, cross-hole ERT also has practical constraints. To achieve sufficient resolution, the spacing between the vertical boreholes is constrained by the depth of the borehole (i.e., borehole depth / borehole spacing ≈ 1.5). Therefore, to provide adequate coverage of a DNAPL source zone, a large number of vertical boreholes may be required. This would be expensive and vertical boreholes in a source zone might induce DNAPL remobilization downwards into pristine aquifer.

Directional drilling and horizontal borehole technology, originally utilized sparingly at environmental sites (e.g., Miller, 1996; Plummer et al., 1997), has become increasingly popular due to improved installation, performance and cost (e.g., Lehr, 2004; English, 2010). At DNAPL sites, horizontal remediation wells are being increasingly incorporated into remedial strategies including soil vapour extraction, air sparging, bioremediation and horizontal soil sampling (e.g., Moran and Losonsky, 2008; Van Heest et al., 2013). Although individually more expensive to install than vertical wells, horizontal wells provide increased efficiency and performance with one well replacing a network of vertical wells due to the greater zone of influence and contact length between horizontal screen and contamination (Van Heest, 2013). The same benefit is expected to apply to ERT, namely electrode placement in proximity to the DNAPL target at depth.

Recent ERT work has applied electrodes in horizontal tunnels (i.e., tunnel-to-tunnel) to image geological conditions in advance of tunnel boring (Danielsen and Dahlin, 2010) and mining (van Schoor and Binley, 2010). Harro and Kruse (2013) used direct push technology to implant electrodes horizontally at depths to improve the resolution of ERT-imaged limestone boundaries. Simyrdanis (2013) presented an initial exploration of the surface-to-tunnel ERT arrangement by means of numerical and experimental studies on a variety of subsurface targets with relatively simple geometries. Although surface-to-

tunnel ERT shares many similarities with cross-hole ERT and can use the same electrode arrays (e.g., Bing and Greenhalgh, 2000), the main difference relates to the different sensitivities provided by surface electrodes compared to borehole electrodes. Simyrdanis (2013) examined a number of electrode arrays and proposed a geometrical factor threshold to ensure viable electrode arrays with a sufficient signal-to-noise ratio. Simyrdanis (2013) recommended an optimum vertical separation of seven times the electrode spacing between surface and tunnel electrodes for resolving resistive targets.

In this work, surface-to-horizontal borehole (S2HB) ERT is proposed by recording ERT measurements in a combined mode using electrodes on the surface and within a horizontal borehole to obtain increased resolution in the area between them. While the spacing between the vertical boreholes in cross-hole ERT is constrained by borehole depth, greater coverage of the subsurface can be obtained with S2HB ERT due to the larger distances permitted between the surface and horizontal borehole (Simyrdanis, 2013). It is expected that a single horizontal borehole could replace a large number of vertical boreholes. To the authors' knowledge, geophysical arrays have never been considered for horizontal boreholes in environmental applications.

The objective of this study is to evaluate the potential of time-lapse surface-to-horizontal borehole ERT, in comparison to a traditional surface ERT survey, as a means for monitoring changes in DNAPL distribution. These changes may correspond to DNAPL migration or remediation. Both numerical simulations and laboratory experiments were conducted to accomplish this objective. A published DNAPL-ERT model was employed to provide an initial, theoretical evaluation of the performance of time-lapse S2HB ERT for monitoring the remediation of a realistic, field scale DNAPL source zone. A laboratory experiment was then performed to demonstrate the S2HB ERT approach for a real system involving a changing NAPL distribution over time. The experimental results were then compared to an independent simulation of the experiment using the DNAPL-ERT model. In all cases, surface ERT surveys were also conducted to provide a reference to evaluate the performance of S2HB ERT. All experimental and simulated ERT surveys were analyzed with newly developed 4D ERT inversion algorithms to provide spatial and volume estimates of NAPL change as a function of time.

5.2 Numerical Modelling

5.2.1 Numerical model

First, a field scale DNAPL scenario was simulated to provide an initial, theoretical estimate of the potential improvement of the S2HB ERT approach over surface ERT. This was simulated using 'DNAPL-ERT', a numerical model described in Chapter 3 (i.e., Power et al. (2013)).

DNAPL-ERT, which couples two models, DNAPL3D-MT and IP4DI, simulates a realistic initial distribution of DNAPL at a contaminated site and the complex pattern of DNAPL removal as it is dissolved by flowing groundwater, and then simulates periodic ERT surveys to predict the electrical resistivity in both space and time. The multiphase flow component of DNAPL-ERT is DNAPL3D-MT (Grant and Gerhard, 2007a,b), a three-dimensional (3D), finite-difference, multiphase flow model that simulates the infiltration and redistribution of DNAPL below the water table as well as DNAPL dissolution and transport of the dissolved phase species in groundwater. It combines the DNAPL migration model DNAPL3D (Gerhard and Kueper, 2003a,b,c) and the dissolved phase transport model MT3D (Zheng, 1990), linked by a mass transfer module based on interfacial area between the immiscible phases (Grant and Gerhard, 2007a,b). Complete details on the model formulation, and the validation of all of its processes against multidimensional, heterogeneous laboratory experiments, are provided by Gerhard and Kueper (2003a,b,c), Grant and Gerhard (2007a,b) and Grant et al. (2007a,b).

The ERT component of DNAPL-ERT is IP4DI (Karaoulis et al., 2013), a 3D numerical model that performs both steps of geoelectrical forward modelling and inversion. Forward modelling uses the finite element method with hexahedral elements to numerically solve Poisson's equation and mathematically predict the response from an ERT survey. The forward modelling scheme used in IP4DI is based on the 3D algorithm fully described by Tsourlos and Ogilvy (1999) and used in a number of studies, including archeological investigations and salt tracer mapping (e.g., Papadopoulos et al., 2007; Karaoulis et al., 2011b). The inversion schemes available in IP4DI will be discussed in Section 5.2.3.

Central to the development of the coupled DNAPL-ERT model was the conversion of the local, spatially variable hydrogeological properties from the DNAPL3D-MT model domain to the local, spatially variable electrical resistivity that defines the IP4DI forward model domain. A sophisticated linkage was achieved by a novel integration of a variety of established petrophysical and geoelectrical relationships (e.g., Revil and Cathles, 1999; Berg, 2007), with the electrical resistivity field accounting for both the spatial heterogeneity of subsurface soils (intrinsic permeability, porosity and clay content) and the evolving spatial distribution of fluids in the pore space (water, DNAPL and air). A full description of the development and testing of the coupled DNAPL-ERT model is provided in Chapter 3.

5.2.2 Field Scale DNAPL Scenario

As discussed, ERT surveys implemented at the surface suffer from decreasing resolution with depth, meaning source zones with DNAPL located at depth will not be fully resolved. Therefore, to effectively evaluate the S2HB ERT approach, and compare it to traditional surface ERT, a realistic contamination scenario comprising DNAPL at various depths was required. A chlorinated solvent DNAPL commonly found at contaminated sites, tetrachloroethylene (PCE), typically exhibits this type of source zone architecture (e.g., Gerhard et al., 2007). The PCE spill scenario, one of a suite of complex DNAPL spill scenarios simulated in Chapter 4, was utilized for this study.

This field scale contamination scenario was simulated in a 3D model domain with a surface area of 22 m long (*x*-direction) by 22 m wide (*y*-direction), and a depth of 4 m (*z*-direction), as illustrated in Figure 5-1. The domain was discretized into 30,976 nodes with a nodal spacing of 0.50 m in the *x*- and *y*-directions and 0.25 m in the *z*-direction. The domain employed a random, spatially-correlated, intrinsic permeability field generated using the algorithm of Robin et al. (1991) to represent the heterogeneous aquifer. This domain employed a mean permeability of 4.8 $x10^{-12}$ m^2 and variance of ln(*k*) of 2.9, representing an aquifer with significant heterogeneity characterized by grain sizes from coarse sand to clay. Correlated to the variation in the permeability field was a

variation in clay content, Cl, (mean Cl = 0.085 and variance Cl = 0.003) and porosity ϕ (mean ϕ = 0.33 and variance ϕ = 0.001). The water table was established at 0.5 m below ground surface, below which the domain was initially fully saturated with water. The capillary fringe is assumed to be negligible and the vadose zone was assigned a single (average) water content of 50%. While it is acknowledged that explicitly incorporating a capillary fringe may provide a more gradual transition in electrical properties, it is not expected to significantly impact the conclusions of this work. The side boundaries were characterized by fixed, hydrostatic water pressures such that an average hydraulic gradient of 0.01 was established with groundwater flowing in the *x*-direction, as indicated in Figure 5-1. The bottom boundary was set as impermeable to both DNAPL and water.

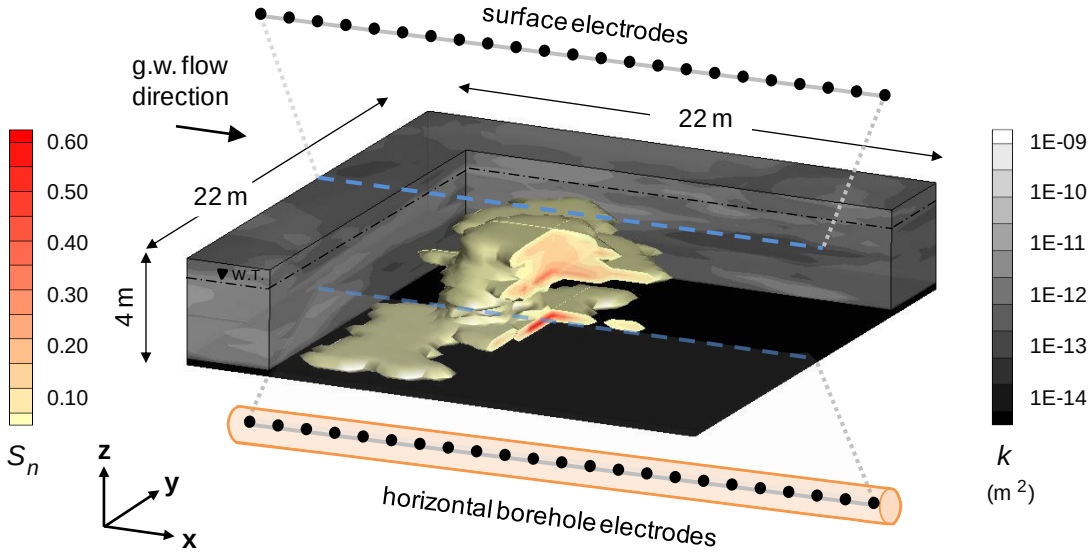

Figure 5-1: 3D view of the simulated DNAPL distribution corresponding to t = 6 months following the release of 5 m^3 of tetrachloroethylene (both the DNAPL and permeability fields are partially cutaway to assist visibility). DNAPL saturations are shown above 1%, with deeper red corresponding to higher DNAPL saturations. The permeability field is shown in grayscale with darker shades of gray representing lower permeability. The horizontal borehole (magnified and displayed below the domain) is positioned 4 m directly beneath the surface array and both arrays are located at *y*-distance = 10 m.

The release of PCE was simulated through a 3 m^2 patch area located between 8.5 m and 11.5 m in both horizontal directions and located coincident with the water table. The aim was to mimic a leaking underground storage tank or waste lagoon located at the water table. Table 5-1 provides the hydrogeological and electrical properties employed. The release boundary was specified by a constant total DNAPL flux (1 m^3/day), with the fraction of total DNAPL flux through each source node weighted according to the node's permeability to mimic the realistic inflow of DNAPL (e.g., from a leaking lagoon or tank) (Grant et al., 2007a). The source was initiated at time t = 0 days and was turned off at t = 5 days, representing the release of 5 m^3 (5,000 litres) of DNAPL. The released DNAPL was allowed to redistribute for t = 6 months to create a realistic initial subsurface distribution of DNAPL prior to remediation and time-lapse ERT monitoring. At this point, all DNAPL had stopped moving or moved very slowly and the configuration of the contaminant source zone was essentially fixed. To ensure that the full 5 m^3 of DNAPL was retained, no DNAPL was permitted to dissolve prior to the end of this redistribution stage.

Figure 5-1 illustrates the 3D spatial distribution of the 5 m^3 DNAPL at t = 6 months (i.e., prior to remediation). The figure reveals that the PCE, due to its much higher density than water, quickly penetrated to 4 m depth. The DNAPL body is characterized by a complex network of pools and residual, exhibiting a range of DNAPL saturations from 1% to 74% of the pore space. Two distinct pools of high DNAPL saturation exist at 2 m and 4 m depths, with only 44% of the DNAPL mass retained in the upper 2 m.

The configuration of DNAPL at the end of the release/redistribution period (i.e., Figure 5-1) represented the initial DNAPL source zone subject to remediation. At this time (t = 6 months), DNAPL dissolution was enabled and the simulation was continued until t = 14 years, by which time all of the released DNAPL mass had dissolved into the ambient groundwater flowing through the source zone. While dissolution of a DNAPL source zone normally takes on the order of decades, here the DNAPL solubility was enhanced (8520 mg/L versus 150 mg/L for PCE) and gradient was increased (0.01 versus ~0.001-0.005 which is ambient conditions). This represents an aggressive remediation scenario, for example active flushing with surfactants.

Table 5-1: Field scale simulation model parameters

Parameter	Value	Units
Hydrogeological parameters		
Sand porosity [1]	0.32 (saturated); 0.46 (vadose)	-
Clay porosity [1]	0.42 (saturated); 0.56 (vadose)	-
Water density [2]	1000	kg/m^3
Water viscosity [2]	0.001	Pa·s
DNAPL density[2]	1630	kg/m^3
DNAPL viscosity[2]	0.0009	Pa·s
DNAPL-water interfacial tension[3]	0.0444	N/m
DNAPL solubility[3]	8520	mg/L
Electrical parameters		
Sand resistivity [4]	1000	ohm·m
Clay resistivity [4]	30	ohm·m
Water resistivity [5]	6.5	ohm·m
DNAPL and air resistivity [6]	1.0×10^6	ohm·m

[1] Bear (1972)

[2] Gerhard et al. (2007)

[3] Mercer and Cohen (1990)

[4] Loke (2013)

[5] Calculated from Equation 3-9 in Chapter 3

[6] Chambers et al. (2004)

5.2.3 ERT Data Acquisition and Inversion

Site investigation and remediation of DNAPL sites invariably begins subsequent to a known or discovered release. For this study, it was assumed that site investigation by ERT was initiated after DNAPL emplacement and just prior to starting remediation. The first ERT survey was simulated at t = 6 months (Figure 5-1), with subsequent surveys conducted after each 20% reduction in DNAPL mass. As indicated by the survey lines and electrode locations in Figure 5-1, the ERT surveys were conducted along a single 2D

vertical cross-section located at *y*-distance = 10 m (the centerline of the release area). Full 3D forward modelling was performed to realistically account for the 3D, heterogeneous nature of the DNAPL target in the survey measurements, with 2D inversion used to invert this vertical cross-section.

The surface ERT survey consisted of a single survey line applied along the surface, with the dipole-dipole electrode array (current electrodes A, B and potential electrodes M, N: AB-MN) being used with an inline spacing of 1 m (23 surface electrodes). The S2HB ERT survey consisted of this same surface survey line combined with a second survey line in a parallel horizontal borehole located at 4 m depth (as shown in Figure 5-1). This vertical separation distance is well within the maximum proposed by Simyrdanis (2013). After careful evaluation of possible electrode arrays and their performance in other studies (e.g., Goes and Meekes, 2004; Simyrdanis, 2013), the pole-tripole array (AMN-B) was selected. Like the surface array, an inline spacing of 1 m was used for the horizontal borehole line. In all surveys, random noise with a Gaussian distribution of 5 mV/A peak-to-peak amplitude was added to the synthetic potential difference data to render modelling results more realistic (e.g., Miller et al., 2008).

IP4DI comprises a number of schemes to perform iterative L_2 smoothness-constrained inversion on the acquired apparent resistivity data to obtain the "true" subsurface resistivity distribution. For the static (i.e., time-invariant) detection of the 2D cross-section of the DNAPL source zone at t = 6 months, independent inversion was used. In terms of time-lapse monitoring, independent inversion has also been traditionally used, with the ERT data recorded at each monitoring step independently inverted and used to reconstruct differential time-lapse images. Recently, a number of 4D time-lapse inversion algorithms have been developed (e.g., Kim et al., 2009; Karaoulis et al., 2014; Loke et al., 2014). In these approaches, the subsurface model and the entire monitoring datasets are defined in a space-time domain; multiple monitoring datasets recorded at different times are simultaneously inverted. Regularizations are introduced in both space and time domains which stabilize the inversion and effectively reduce inversion artifacts evident in independent inversion (Karaoulis et al., 2011a).

For this study, the 4D active time constraint (4D-ATC) inversion introduced by Karaoulis et al. (2011a) was used. In this method, the time Lagrangian is expressed as a variable diagonal matrix with the temporal Lagrangian values varying between different monitoring steps proportionally to the expected degree of spatial resistivity changes occurring (i.e., areas of significant changes are assigned low time regularization values and vice versa). One method proposed by Karaoulis et al., (2011a) to pre-estimate regions of change and assign appropriate time Lagrangian values is based on a preliminary analysis of the data through differential imaging of initial independent inversion; this is the method used in this work. With the appropriate time Lagrangian, the 4D-ATC algorithm was then applied to the entire dataset recorded from all monitoring steps with improved sensitivity now on the spatial and temporal changes of resistivity. The application and benefits of this algorithm, which is described in detail by Karaoulis et al. (2011a), have been demonstrated in a number of studies (e.g., Karaoulis et al., 2011a,b; 2014).

5.2.4 ERT Static Detection of DNAPL Body

Figure 5-2a shows the vertical cross-sectional image (*y*-direction = 10 m) of the simulated DNAPL spill scenario at the start of the ERT investigation. Figure 5-2b illustrates the corresponding actual resistivity distribution (i.e., directly converted from Figure 5-2a using the DNAPL-ERT linkage methodology). The soil matrix variability is realistically represented in the electrical model domain, with the lowest resistivities (dark-blue) in Figure 5-2b corresponding to higher clay contents associated with the lowest permeabilities in Figure 5-2a. And the high resistivity regions (dark-red in Figure 5-2b) correspond to either high air saturations in the vadose zone or high DNAPL saturations in the source zone (red in Figure 5-2a).

Figures 5-2c and 5-2d illustrate the 2D inverted resistivity distributions from the surface ERT and S2HB ERT surveys, respectively. As illustrated in Figure 5-2c, the surface ERT response provides reasonable delineation of the soil matrix variability and the general

outline of the DNAPL in the near-surface soil but is unable to resolve deeper DNAPL due to reduced sensitivity with depth.

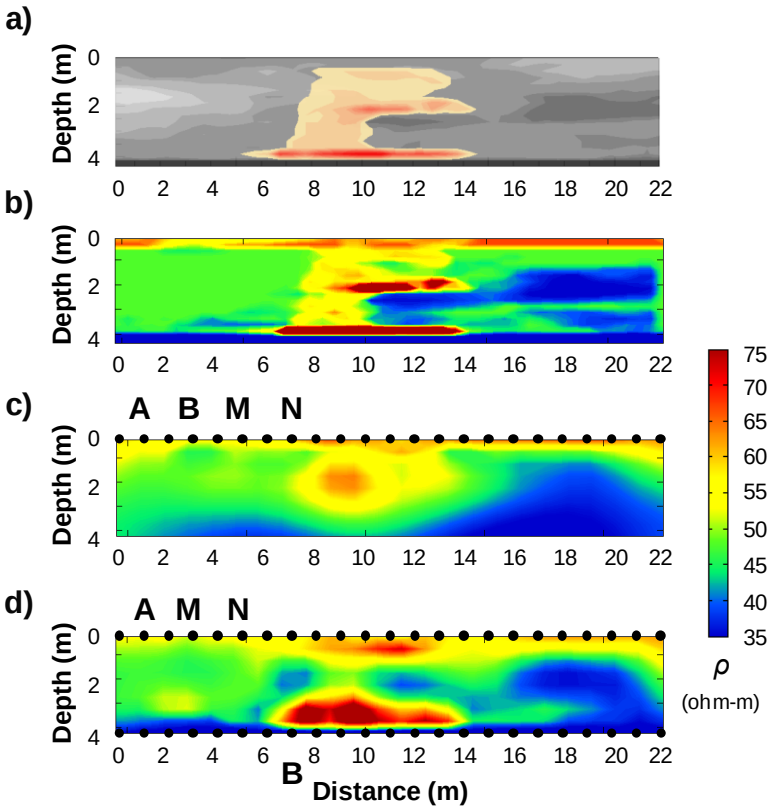

Figure 5-2: (a) vertical cross-section of the simulated DNAPL spill scenario at *y*-distance = 10 m (same colourbar as Figure 5-1), (b) actual resistivity distribution corresponding to the hydrogeological model domain in (a), (c) inverted resistivity distribution obtained from the surface ERT survey, and (d) inverted resistivity distribution obtained from the surface-to-horizontal borehole ERT survey. The electrode indexes A, B, M and N have been superimposed on (c) and (d) to highlight the electrode array used (i.e., dipole-dipole, AB-MN; pole-tripole, AMN-B).

As illustrated in Figure 5-2d, S2HB ERT provides improved delineation of the DNAPL source zone with the most significant improvement evident between 2.5 m and 4 m depths where superior sensitivity and resolution is achieved. However, Figures 5-2c and 5-2d also underscore the challenge in static detection of a complex DNAPL distribution

in heterogeneous porous media; in absence of alternative lines of evidence, these would be hard to interpret. Hence, the rest of this work focuses on time-lapse ERT. It is important to note, however, that since time-lapse monitoring relies first on static inversion at each monitoring step, the improvements shown here are relevant to improved time-lapse monitoring with S2HB ERT.

5.2.5 Time-lapse Monitoring of DNAPL Remediation

In this DNAPL scenario, time-lapse ERT is investigated for monitoring changes in the DNAPL distribution during remediation. Figure 5-3a shows the evolving actual resistivity distribution corresponding to each successive 20% reduction of the initial DNAPL mass (i.e., t0). As expected, the DNAPL mass was removed over time in a heterogeneous manner. For example, most of the residual DNAPL was dissolved first, as is common (e.g., Grant and Gerhard, 2007b), and this is illustrated by the progressive removal of the low DNAPL resistivities (yellow) in the initial monitoring steps (i.e., t1 and t2) in Figure 5-3a. Ratio images are used to highlight the actual resistivity difference between each sequential monitoring step (e.g., between t1 and t2) during remediation, as illustrated in Figure 5-3b. In the first four difference images (i.e., t1/t0 – t4/t3), resistivity changes occur in a realistic manner: (a) throughout the entire depth of the subsurface always at the upgradient end of the source zone, and (b) removing the low saturation (residual) DNAPL first. The final difference image (i.e., t5/t4) highlights resistivity changes related to the eventual remediation of the two high saturation pools remaining at late time at 2 m and 4 m depths.

The sequential difference images of the 4D-ATC inverted resistivity distributions obtained from the surface ERT and S2HB ERT surveys are illustrated in Figures 5-3c and 5-3d, respectively. In Figure 5-3c, surface ERT provides reasonable delineation of the changes in DNAPL distribution over time; however, it is evident that the diminished response with depth of surface ERT again impedes the imaging of changes occurring in the deeper subsurface (below 2 m). In contrast, S2HB ERT exhibits improved imaging of DNAPL changes at all depths across the entire monitoring period, as shown in Figure 5-

3d. This is particularly evident at later times (i.e., t4/t3 and t5/t4), where the two high saturation pools at 2 m and 4 m depths are remediated; surface ERT provides a low magnitude envelope of the changes, while S2HB ERT improves the delineation of the changes and the captures their corresponding magnitudes.

This field scale modelling result suggests that S2HB ERT may have potential for mapping DNAPL remediation. However, it is acknowledged that the model has not been validated for this specific application and a real system involving S2HB and NAPL has never been performed. An experiment is required to develop confidence in this approach and in the reliability of the model.

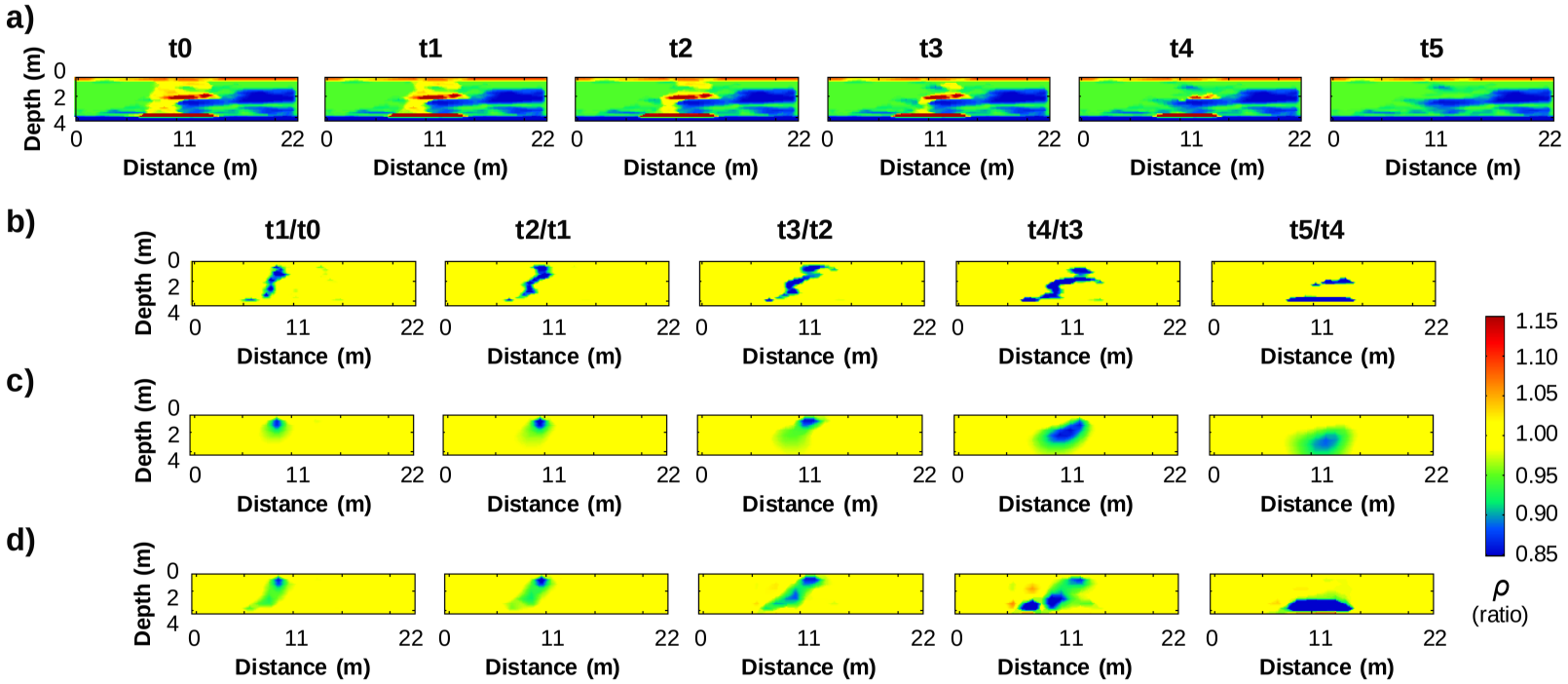

Figure 5-3: (a) actual resistivity distributions corresponding to each monitoring step during remediation of the simulated DNAPL spill scenario (same colourbar as Figure 5-2), (b) actual resistivity ratio images between sequential time steps, with 4D time-lapse inverted ratios images from (c) surface ERT and (d) surface-to-horizontal borehole ERT.

5.3 Bench Scale Proof of Concept Experiment

A controlled laboratory experiment was conducted to validate the S2HB and 4D ERT methods for mapping evolving NAPL distributions in a physical system. In addition, independent simulation of the experiment with the DNAPL-ERT model allowed direct comparison of the model to a known system under controlled conditions and provide confidence in the model for simulating a physical system. Although the experiment involved temporal changes in NAPL distribution related to NAPL injection, the findings are equally applicable to NAPL remediation; the principle of time-lapse ERT monitoring is identical whether the NAPL is added (injection) or removed (remediation).

5.3.1 Experimental Procedure

The experiment was conducted in a 3D experimental tank constructed of plexiglass with dimensions 1 m x 1 m x 1 m (e.g., Simyrdanis et al., 2012; Seferou et al., 2013). The experiment was performed within a central subvolume of the tank to minimize possible boundary effects on the ERT measurements. As illustrated in Figure 5-4, this subvolume was 0.60 m and 0.40 m in the *x* and *y* dimensions, respectively, and 0.25 m in the *z* (vertical) dimension. As shown in Figure 5-4, the tank was packed with a homogeneous 'staircase' of medium sand, consisting of three staggered steps of dimensions 0.22 m x 0.16 m x 0.05 m, surrounded by fine sand. The medium quartz sand was sieved to retain only a single mesh size to obtain a narrow particle size distribution (mean grain size of 0.58 mm, coefficient of uniformity of 1.36) The fine quartz sand also exhibited a narrow particle size distribution (mean grain size of 0.23 mm, coefficient of uniformity = 1.56).

The tank was initially packed with fine sand in lifts of 0.01 m to an elevation of 0.50 m (0.25 m depth from the proposed surface) to provide uniformity in the background sand throughout the full tank volume while also permitting easier accessibility during preparation of the 'experimental subvolume'. At this elevation, the horizontal borehole and electrodes (i.e., bottom section of the S2HB frame shown in Figure 5-5a and

described in more detail below) were installed and carefully backfilled with fine sand, as illustrated in Figure 5-5b.

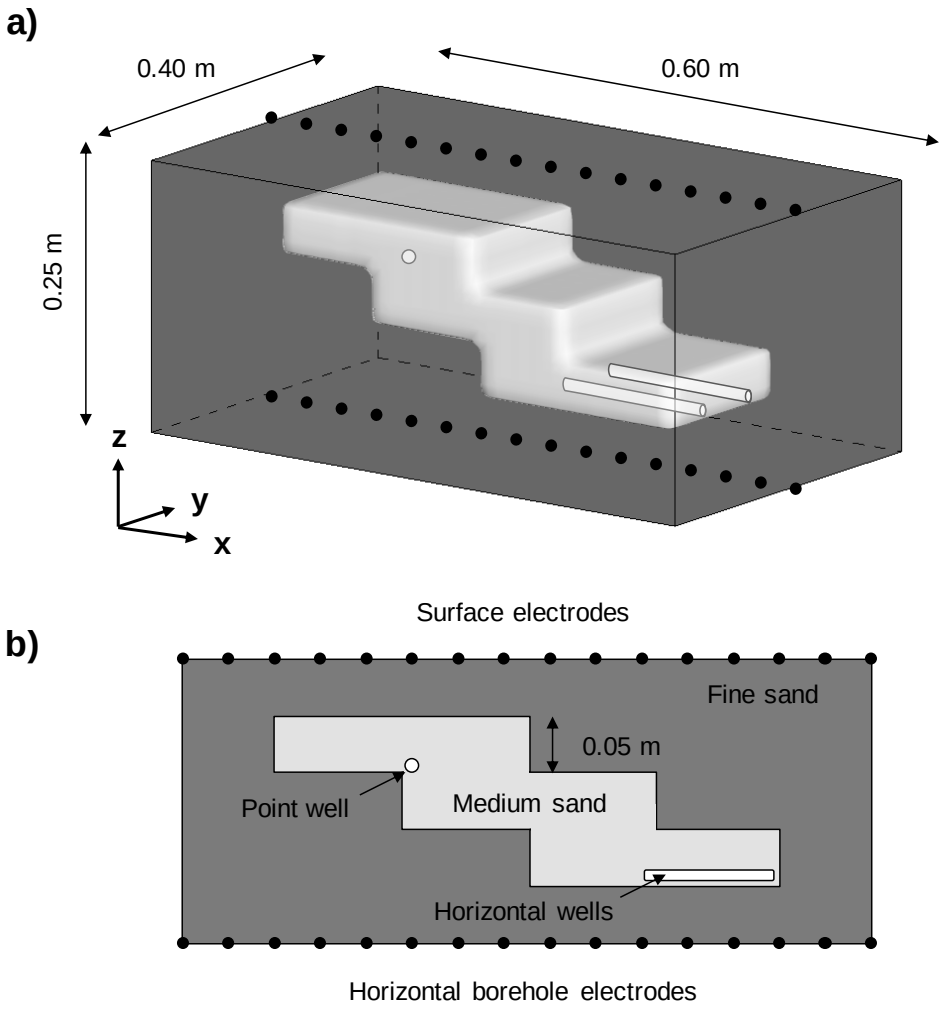

Figure 5-4: Schematic diagram of (a) 3D experimental domain showing the medium sand 'staircase' (light gray) surrounded by fine sand (dark gray), (b) cross-sectional view along the centerline (*y*-distance = 0.20 m).

At the base of the bottom medium sand step (i.e., 0.20 m depth), two horizontal NAPL injection wells, constructed from 10 mm diameter PTFE tubes, were installed in parallel. As shown in Figure 5-5c, these wells were initially filled with NAPL to ensure that no air existed in the wells immediately prior to NAPL injection. A rectangular stainless steel

frame, constructed the size of each medium sand step, was used to provide accurate and simultaneous packing of the medium sand and fine sand during the installation of each step, after which the frame was removed. Figure 5-5d shows the installation of the bottom medium sand step within the fine sand. This sand packing procedure was repeated for installation of the remaining steps, with Figure 5-5e illustrating the installation of a point injection well (2 mm diameter PTFE tube) at the base of the top step. At the surface, the surface electrodes (i.e., top section of the S2HB frame) were installed, with the full tank shown in Figure 5-5f. The dry sands were then saturated by the slow injection of tap water into the base of the tank over 24 hours. A small concentration of salt was added to the water to provide moderate water conductivity (10 ohm-m).

Corn oil (Minerva, Greece) was used in this experiment as a non-toxic surrogate for toxic industrial NAPLs. The key property of corn oil relevant to this study is that, like most NAPLs, it is an insulating fluid that displaces the more conductive water in the pore spaces of the saturated zone. The density of the corn oil was 920 kg/m^3, meaning it was essentially neutrally buoyant and migration was expected to be negligible when the injection pump was off during the short (24 hour total) timescale of this experiment. The corn oil was dyed with Oil Blue N powder (Sigma-Aldrich) to permit mapping of the final NAPL distribution during tank excavation. The properties of the sand, water and NAPL used in this experiment are shown in Table 5-2 (note that all parameters without superscripts were measured directly).

A surface-to-horizontal borehole electrode frame was constructed matching the experimental design illustrated in Figure 5-4. The frame was made from polyvinyl chloride pipes and is shown inside the tank (water-filled only) in Figure 5-5a. The key components of the frame include two parallel sections traversing horizontally: the top section contains a series of small steel electrodes that are located at the surface, while the bottom section contains electrodes that mimic a water-filled horizontal borehole scenario. A vertical separation distance of 0.25 m (i.e., approximately six times the electrode spacing of 0.04 m) was used between the surface and horizontal borehole; this again satisfies the allowable separation distance suggested by Simyrdanis (2013).

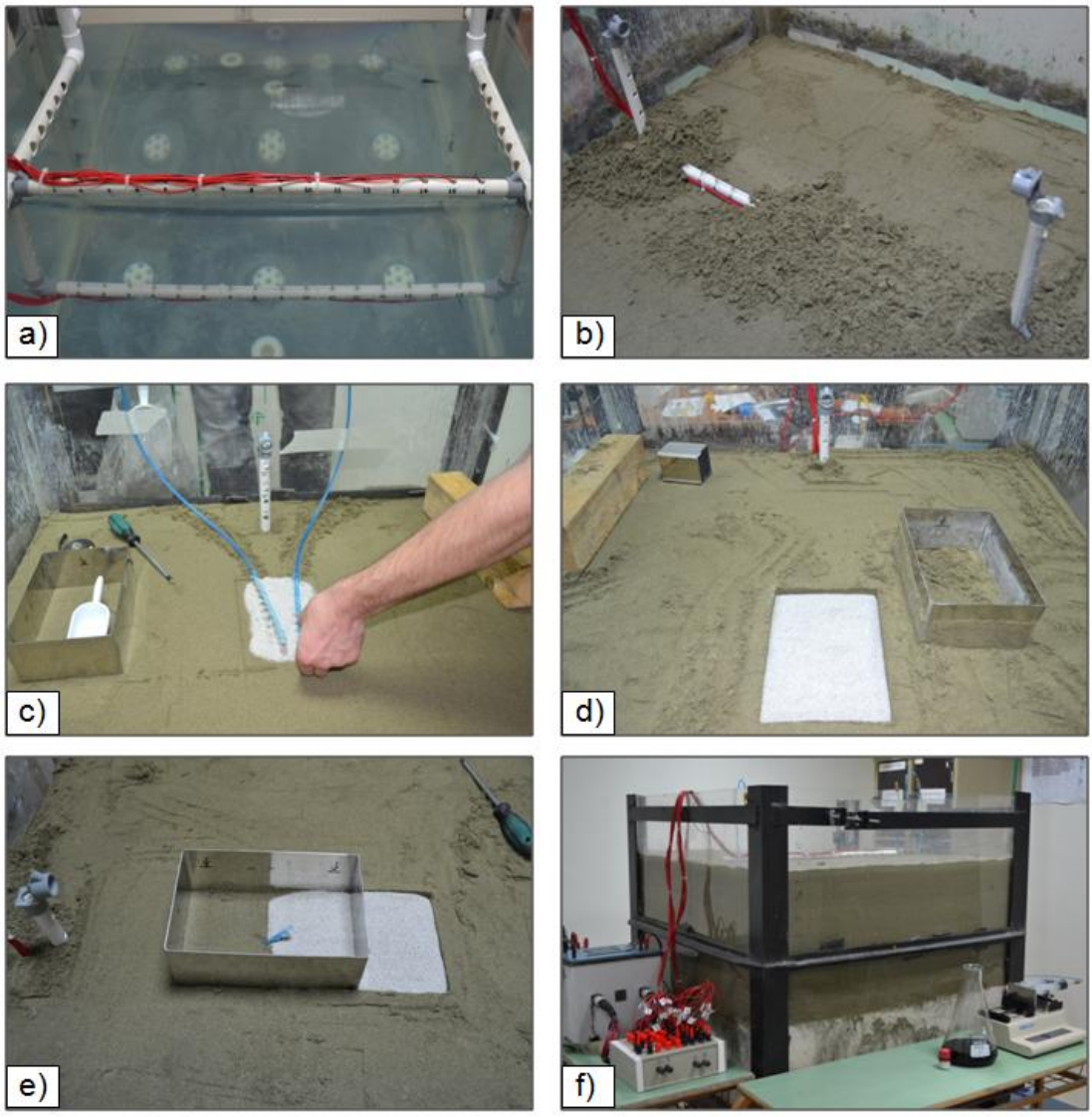

Figure 5-5: (a) surface-to-horizontal borehole frame placed inside tank filled with water only, (b) installation of horizontal borehole electrodes frame segment in the fine sand, (c) two horizontal injection wells installed parallel at the base of the bottom medium sand step, (d) construction of bottom medium sand step showing the stainless steel frame used to separate the fine sand and medium sand, (e) installation of point source well at the base of the top medium sand step, (f) 3D experimental tank set-up showing the resistivity meter and the injection of NAPL through the syringe pump.

5.3.2 Measurement Procedure

A total volume of 1600 mL of NAPL was injected into the medium sand using a syringe pump at a constant injection rate of 2 mL/min. The NAPL volume was injected in periodic intervals of 200 mL to provide 8 time-lapse ERT monitoring steps of total volume injected: 200 mL, 400 mL, 600 mL, 800 mL, 1000 mL, 1200 mL, 1400 mL and 1600 mL. The first 1400 mL of NAPL was evenly and simultaneously injected through the 0.10 m screened lengths of the two horizontal wells in the bottom step ('primary source'), while the final 200 mL was injected through the point source well in the top step ('secondary source'). Upon release through the primary source at the base of the staircase, the NAPL was expected to preferentially migrate through the more permeable medium sand, with the high entry pressure of the fine sand ensuring NAPL containment within the staircase. It was expected that each medium sand step would progressively 'fill up', with the NAPL invading each step, from bottom to top, in sequence.

Prior to the injection of oil, a surface ERT and S2HB ERT survey (i.e., 2D survey performed along the centerline, as shown in Figure 5-4) was conducted in order to characterize the static water saturated conditions within the experimental tank, and to provide baseline sections with which to produce differential time-lapse images from subsequent surveys. The dipole-dipole electrode array was used for the surface survey while the pole-tripole array was used for the S2HB survey. In both arrays, an inline spacing of 0.04 m was used, with 16 electrodes along both the surface and horizontal borehole lines. A resistivity meter (Syscal R1 Plus, Iris Instruments) was used to record the ERT measurements. Following the injection of NAPL, subsequent surveys were conducted at each injected NAPL volume interval to provide time-lapse monitoring of the NAPL migration. The low density contrast between NAPL and water (i.e., 80 kg/m^3) meant that the NAPL was essentially neutrally buoyant; therefore, NAPL movement was expected to be minimal during the short intervals required for ERT data acquisition (40 mins). 4D-ATC inversion, in 2D mode, was used to simultaneously invert all monitoring steps and obtain optimized time-lapse images of the subsurface experiencing NAPL volume increases with time. Preliminary tests were conducted prior to the NAPL experiment to investigate the effects of possible noise sources from the finite tank

boundaries. The high repeatability, stability and lack of artifacts in the inversion results suggested that the tank, with the specified tank subvolume, array configuration and experimental procedure (i.e., time-lapse), can be adequately modelled using the standard 'infinite' Dirichlet boundary condition.

Table 5-2: Experimental parameters

Parameter	**Value**	**Units**
Hydrogeological parameters		
Medium sand porosity	0.40	-
Medium sand permeability	2.35×10^{-11}	m^3
Medium sand mean grain size	0.00058	m
Fine sand porosity	0.43	-
Fine sand permeability	8.07×10^{-13}	m^3
Fine sand mean grain size	0.00023	m
Water density	1000	kg/m^3
Water viscosity	0.001	Pa·s
NAPL density	920	kg/m^3
NAPL viscosity	0.065	Pa·s
NAPL-water interfacial tension[1]	0.0233	N/m
Electrical parameters		
Water resistivity	10	ohm-m
NAPL resistivity	1×10^6	ohm-m
Sand resistivity[2]	1000	ohm-m
Cementation exponent[3]	1.5	-
Saturation exponent[3]	2.0	-

[1] Gaonkar (1989)

[2] Loke (2013)

[3] Berg (2007)

Following the ERT surveys at the final monitoring step (i.e., 1600 mL of NAPL volume), the experimental test area was excavated to confirm the actual final distribution of NAPL. The excavation was carried out in 0.01 m depth intervals from 0 m depth to 0.25 m depth, with high resolution photographs taken of the plan-view extent of the blue-dyed NAPL invasion at each interval. These images were later magnified and the boundary of the NAPL was traced. Although variations in blue, corresponding to variations in NAPL saturation, were observed, no attempt to quantify these differences was undertaken. A soil sample was taken from each of the three medium steps (depth intervals of 0.8 m, 0.12 m and 0.16 m) and these were then analyzed to calculate water and NAPL contents. Appendix C presents a number of photographs to illustrate the excavation procedure.

5.3.3 Numerical Simulation of the NAPL Evolution Experiment

The DNAPL-ERT model and associated modelling approach described earlier in Section 5.2.1 was employed to independently simulate the experiment, simulating both (i) the NAPL migration, and (ii) the response of the ERT surveys to the simulated NAPL distribution. The numerical model domain used the same *x, y, z* dimensions as the experimental subvolume (Figure 5-4), with a grid resolution of 0.02 m in the *x*- and *y*-dimensions and 0.01 in the *z*-dimension. The experimental design, associated parameters and measurement procedure all described in previous sections were used in the simulation. NAPL injection through the horizontal wells was simulated by fixing the NAPL flux (2 mL/min) through two 0.10 m wide sources located just above the base of the bottom step (i.e., depth = 0.19 m) as indicated by the horizontal well locations in Figure 5-4. Similarly, NAPL injection through the point well was simulated by fixing the NAPL flux at a single node located in the center of the top step just above the base. The domain was initially water-saturated. The side boundaries were characterized by constant water pressures and constant water saturations (allowing water displaced by NAPL to flow out of the domain) with the top and bottom boundaries being no flux.

The simulated NAPL distribution is shown here to provide insight into the experimental and ERT imaging results presented in the next section. Figure 5-6 illustrates the distribution of NAPL following the release of the full 1600 mL of NAPL into the medium

sand. The NAPL is predicted to invade the whole of the medium sand staircase. It is evident that high saturations (60 % < S_n < 95%) exist throughout the entire NAPL body, which is expected since the total volume injected approximately equaled the total pore space volume of the staircase. Figure 5-6 illustrates that the highest saturations exist at both the primary and secondary NAPL release locations (Figure 5-4).

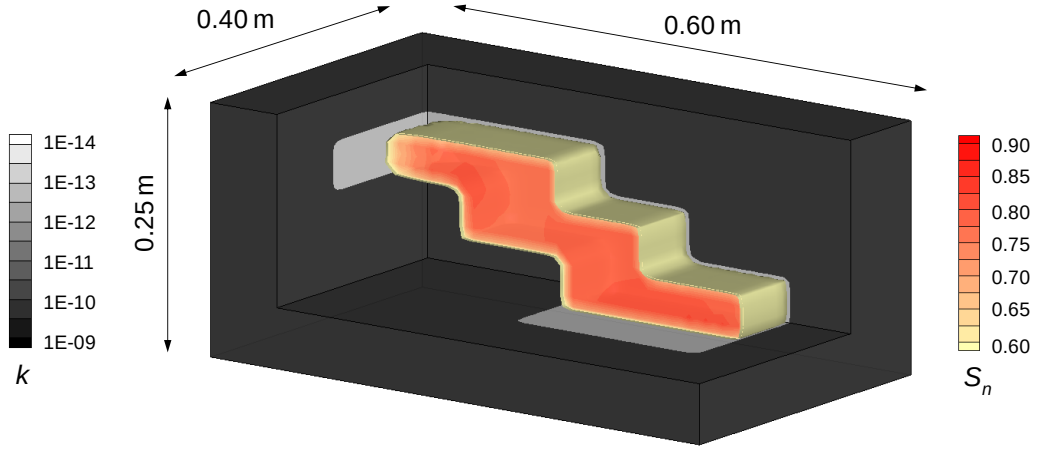

Figure 5-6: Simulated distribution of NAPL following the release of 1600 mL of NAPL into the medium sand. Shown are NAPL saturations above 60%, with deeper red corresponding to higher NAPL saturations. Dark gray represents the fine sand and light gray represents the medium sand. Both NAPL and permeability fields are partially cutaway to see inside the NAPL body.

Figure 5-7 presents the simulated NAPL distribution at each 200 mL volume injected interval, illustrating the evolving distribution of NAPL within the medium sand. The NAPL injected from the two horizontal wells was predicted to redistribute, spreading laterally and vertically within the bottom step. As expected, the fine sand acts as a capillary barrier and contains the NAPL within the medium sand. Over time, the increasing volume of NAPL injected results in the progressive invasion of the staircase from the bottom (injection location) to the top, as expected. The results shown in the next section focus on the ability of the simulated ERT surveys to resolve the changes illustrated in Figure 5-7, and the ability of actual ERT surveys to resolve the corresponding changes in the physical experiment.

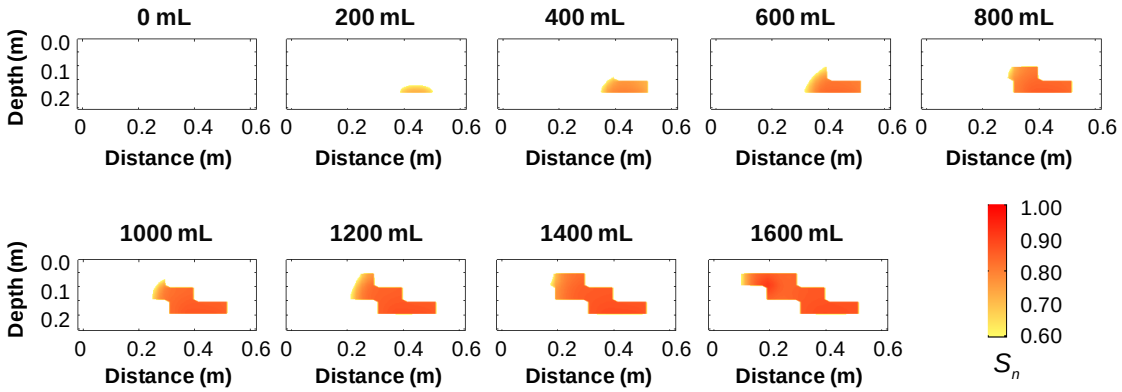

Figure 5-7: Cross section along the centerline (*y*-distance = 0.20 m) of the simulated NAPL spill scenarios at 200 ml volume intervals following the injection of NAPL into the medium sand 'staircase'.

5.4 Results and Discussion

5.4.1 Experimental Results

Figure 5-8 illustrates the inverted resistivity images from both surface ERT and S2HB ERT surveys at each monitoring step of the actual experiment. From the baseline image (i.e., 0 mL volume injected) of both surveys, it is evident that ERT measures some variability which is likely associated with the contrast between the medium and fine sands and their associated porosities, along with some noise contributions. Surface ERT shows slight variability at near-surface which is associated with the medium sand, but only the top step, whereas S2HB ERT shows a non-uniform background throughout the entire medium sand staircase.

After the first 200 mL NAPL is injected, it is evident that surface ERT showed no change in imaging due to the poor resolution at the depth of the injection well. In contrast, S2HB ERT shows a distinct high resistivity response corresponding to injected NAPL surrounding the location of the horizontal well source. Subsequent 200 mL volume injections up to a total of 600 mL injected (first row), show little to no variability in the surface ERT responses, while S2HB ERT (second row) shows increasing lateral and

vertical extent of high resistivities related to the evolving invasion of NAPL through the staircase. Surface ERT begins to show resistivity variations in the near surface (top 0.15 m) after 800 mL, with this high resistivity region continuing to gradually increase in extent and magnitude in the remaining monitoring steps (third row) to a total of 1600 mL. This coincides with the invasion of NAPL to shallower depths where surface ERT exhibits its highest resolution. The results show similarity to the expected ERT response of the simulated NAPL migration illustrated in Figure 5-7. S2HB ERT continues to show increasing resistivities as the NAPL penetrates from deeper to shallower regions (bottom row), with the 1600 mL image providing evidence of a fully invaded staircase.

Figure 5-9 illustrates the 4D-ATC difference images between sequential monitoring steps in the experiment. From surface ERT, it is evident that small changes were first detected after 600 mL which coincide with the upward migration of the NAPL into the middle step. From this volume until the total 1600 mL injected, surface ERT captures the NAPL invasion into the top half of the staircase, with the changes exhibiting increasing magnitudes over time. In terms of the S2HB survey, Figure 5-9 illustrates clearly that S2HB ERT captures the entire invasion of NAPL through the staircase. Furthermore, at volume intervals between 800 mL and 1400 mL, it is evident that S2HB ERT is detecting some unexpected changes beneath the bottom step. Upon excavation of the experimental tank, it was confirmed that some NAPL actually invaded the fine sand beneath the horizontal wells. This was likely due to excessive capillary pressures generated in the area immediately surrounding the horizontal wells during this time interval when injection was still occurring but the bottom step was fully saturated with NAPL. The final difference image (i.e., 1600 mL / 1400 mL) no longer shows changes in this area since the NAPL was no longer injected in the horizontal wells, instead being injected through the point source in the top step.

Appendix C compares the time-lapse images obtained by 4D-ATC inversion (illustrated in Figure 5-9) to the corresponding time-lapse images obtained from the traditional independent inversion approach.

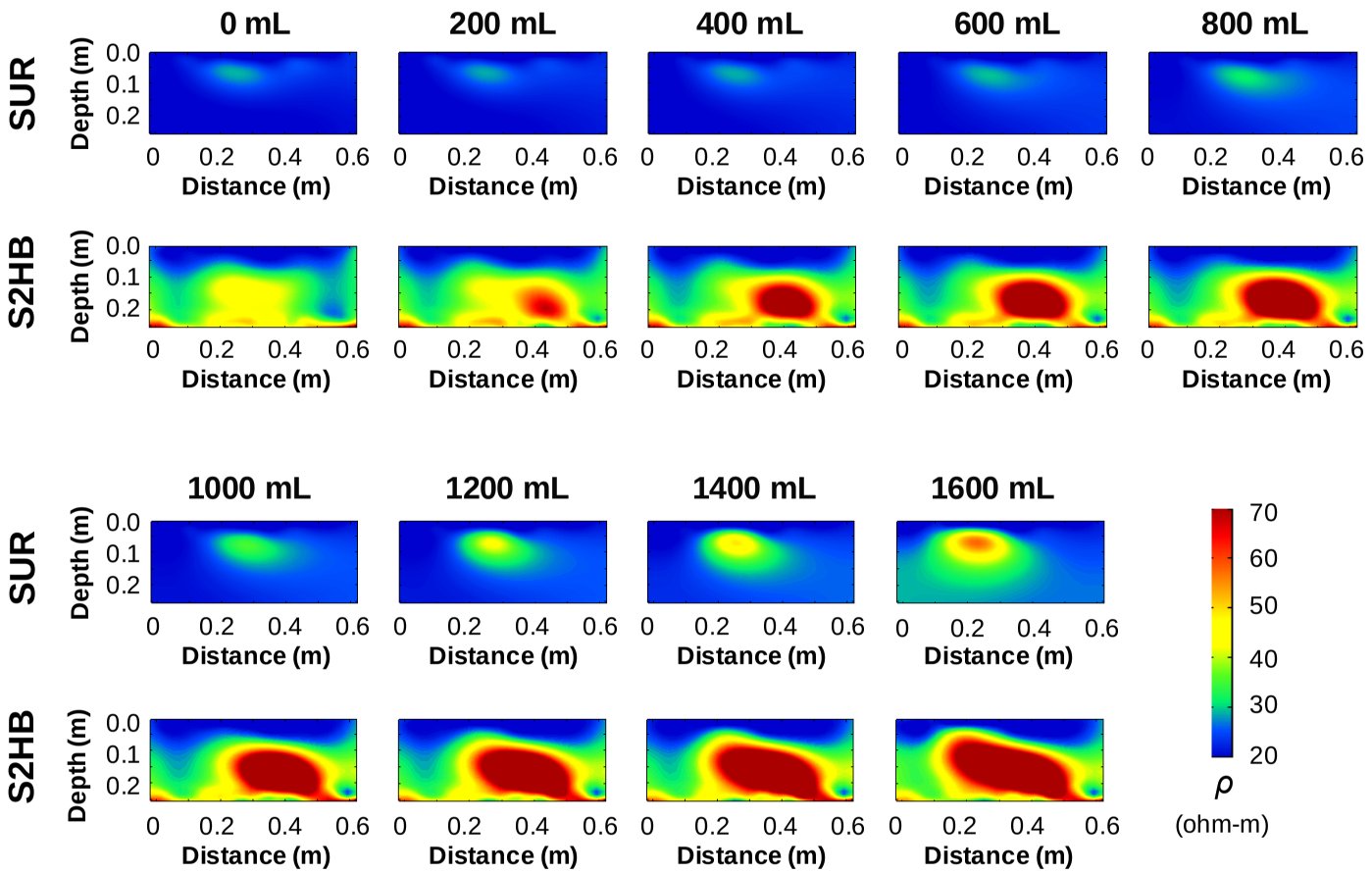

Figure 5-8: Experimental results showing the 2D inverted resistivity images from surface ERT ('SUR') and surface-to-horizontal borehole ERT ('S2HB'). Each monitoring step corresponds to a 200 mL volume injected interval.

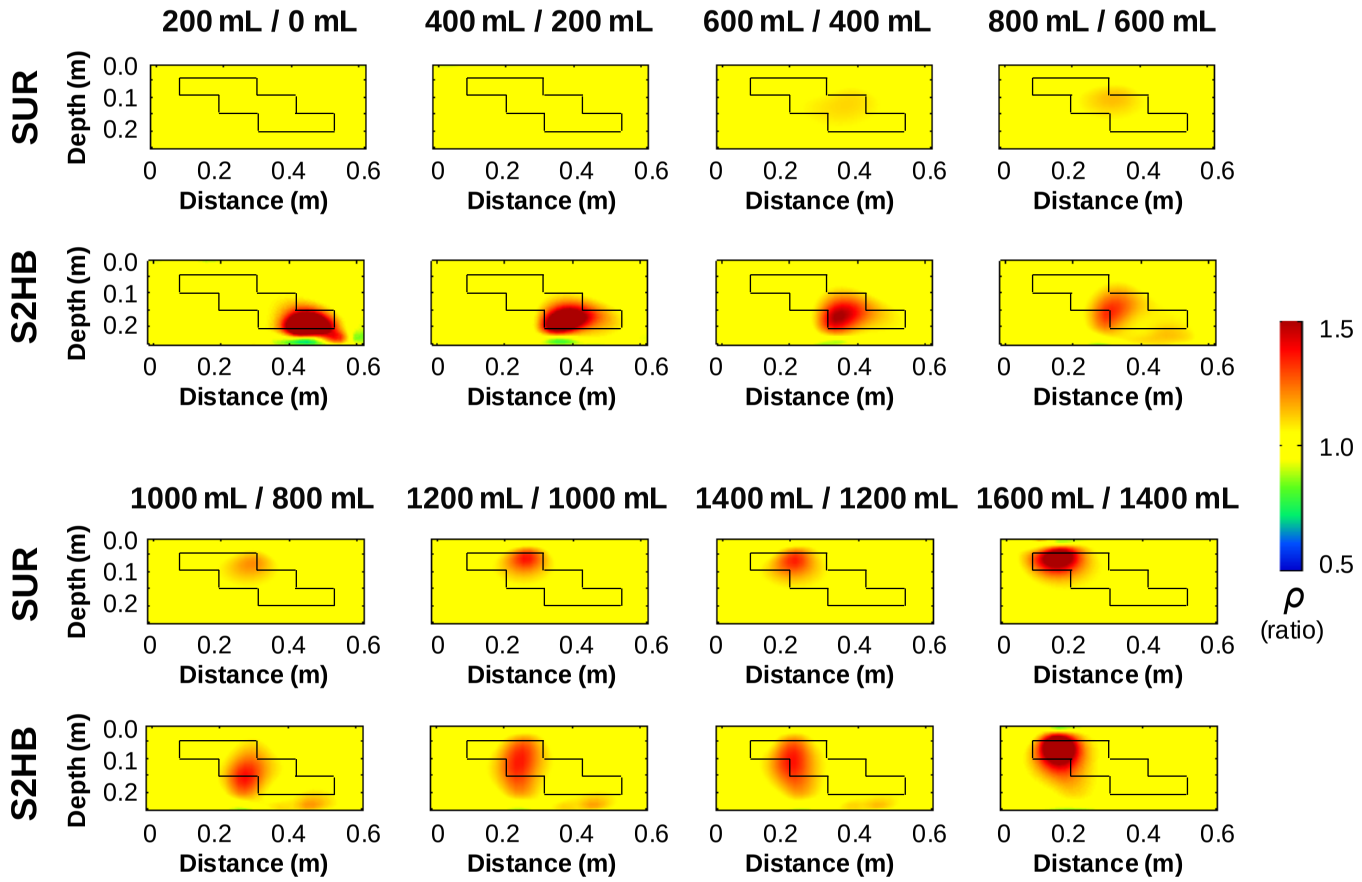

Figure 5-9: Experimental results showing the 2D ratio resistivity images between sequential monitoring steps from surface ERT ('SUR') and surface-to-horizontal borehole ERT ('S2HB').

5.4.2 Actual NAPL Distribution

Following the injection of the 1600 mL NAPL volume, the difference image between the baseline (0 mL) and final (1600 mL) resistivity images was obtained for both surface ERT and S2HB ERT, as illustrated in Figures 5-10a and 5-10b, respectively. While surface ERT captured the invasion of NAPL in the top and middle steps, S2HB ERT resolves the invasion of NAPL through the entire medium sand staircase. The dashed contour lines shown in each figure represent the general envelope of each respective response. A resistivity ratio threshold value of 1.2 was used to demark the more measurable changes from the background.

During excavation of the experimental test area, the blue-dyed NAPL was easily distinguishable within the sand. The excavation confirmed that the NAPL invaded the entire plan view section of the staircase at all depths. The NAPL was completely contained within the medium sand laterally, with a small volume of NAPL observed within the fine sand directly beneath the horizontal wells as mentioned above. From the three soil samples, an average NAPL saturation of 72% was determined. Figure 5-10c illustrates the actual final distribution by hashed layers showing the extent of the NAPL at each 0.02 m depth interval (from photographs), and a solid line indicating the outline of the original medium sand. The dashed contour lines of the surface and S2HB ERT response envelopes shown in Figures 5-10a and 5-10b are super-imposed on the actual final distribution in Figure 5-10c and demonstrate the significantly improved performance of S2HB ERT relative to surface ERT.

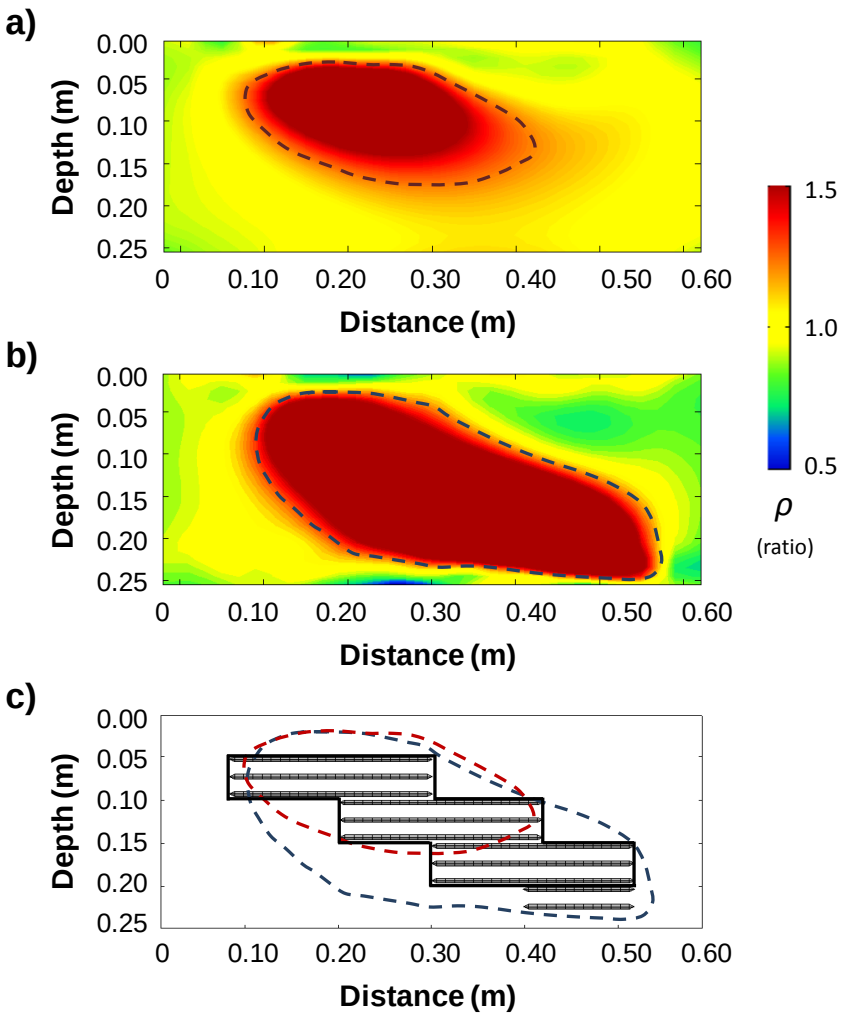

Figure 5-10: Experimental ratio image between the final monitoring step and the baseline step (i.e., 1600 mL / 0 mL) for (a) surface ERT and (b) surface-to-horizontal borehole ERT. (c) actual distribution of NAPL at the end of the experiment, based on visual analysis of photographs taken at various depths during excavation (hashed layers). The black soil outline shows the staircase boundary, while the contour lines show the envelope of the surface ERT response (dashed red) and surface-to-horizontal borehole ERT response (dashed blue) at a resistivity ratio of 1.2.

5.4.3 Comparison of Experimental and Simulated Results

As discussed in Section 5.3.3, the experiment was simulated by the DNAPL-ERT model, with ERT surveys simulated at all monitoring steps illustrated in Figure 5-7. 4D-ATC time-lapse inversion was again used to obtain the inverted resistivity of all simulated monitoring steps. The simulated and experimental images for NAPL volume intervals (only 400 mL intervals shown) for both surface ERT and S2HB ERT are shown in Figure 5-11. It is evident that the simulated results provide reasonable correlation with the experimental results and are able to image the evolving NAPL distribution at each monitoring step. A main difference between the simulated and experimental results is the background variability, where the simulated data provides a more uniform response and the experimental data exhibits more variability, as illustrated by the background image at 0 mL. This likely corresponds to the different sources of noise between the simulated data (synthetic noise added) and the experimental data (real noise).

A difference also exists between the average background resistivity of the simulated data (28 ohm-m) and experimental data (20 ohm-m). Since no model calibration was employed during independent simulation of the experiment, the DNAPL-ERT model linkage is directly influenced by the measurements of the hydrogeological parameters (Table 5-2), with particular sensitivity to pore water resistivity and porosity (Archie, 1942). While the pore water resistivity was directly measured in the experimental tank, porosity was measured by the water evaporation method on an extracted soil sample. Therefore, the simulated background resistivity may be affected by inaccuracies in the measurements of hydrogeological parameters and also the selection of literature values for parameters that were not measured directly (e.g., cementation exponent).

Aside from some differences in background variability, it is evident that the simulated response closely matches the experimental response in mapping the NAPL invasion at later time steps. Some mismatch does exist due to the higher magnitude of the simulated response. Also, the experiment observed the real migration of NAPL into the fine sand beneath the bottom step, whereas the simulation did not predict this unintentional occurrence. This difference is particularly evident in the S2HB ERT responses in Figure 5-11.

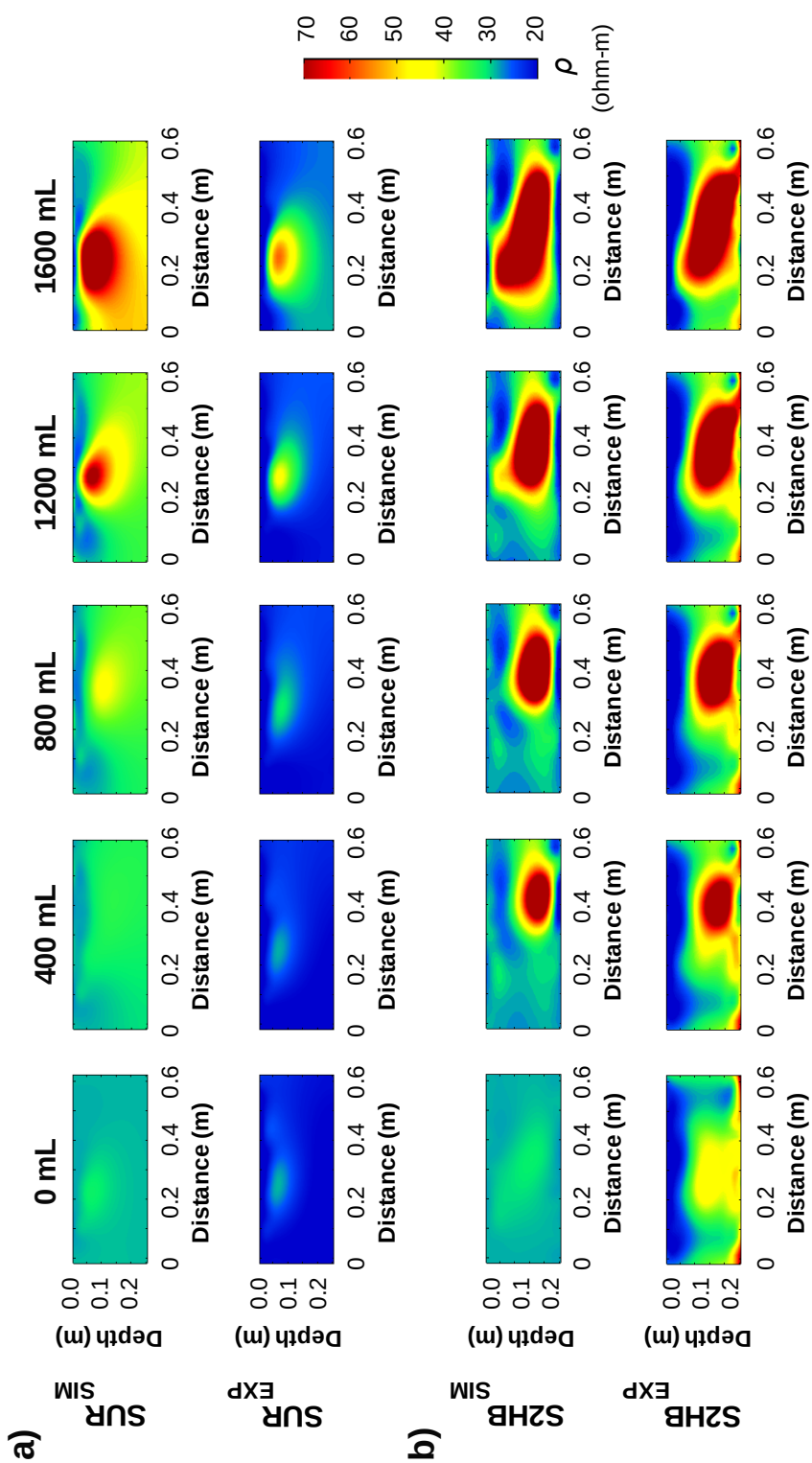

Figure 5-11: Comparison of simulated and experimental ERT images from (a) surface ERT, and (b) surface-to-horizontal borehole ERT for every 400 mL volume injected intervals.

Figure 5-12 presents the ratio images between each successive 400 mL volume interval, comparing both the simulated and experimental data. It is even more evident that the simulated data closely matched the experimental data, especially now that the background variability is removed. Some differences exist, including the penetration of NAPL into the fine sand beneath the horizontal wells that are not predicted in the simulated data. And slight differences in the strength of the response changes can be detected between simulated and experimental data. However, overall, it is evident that both datasets are closely matched.

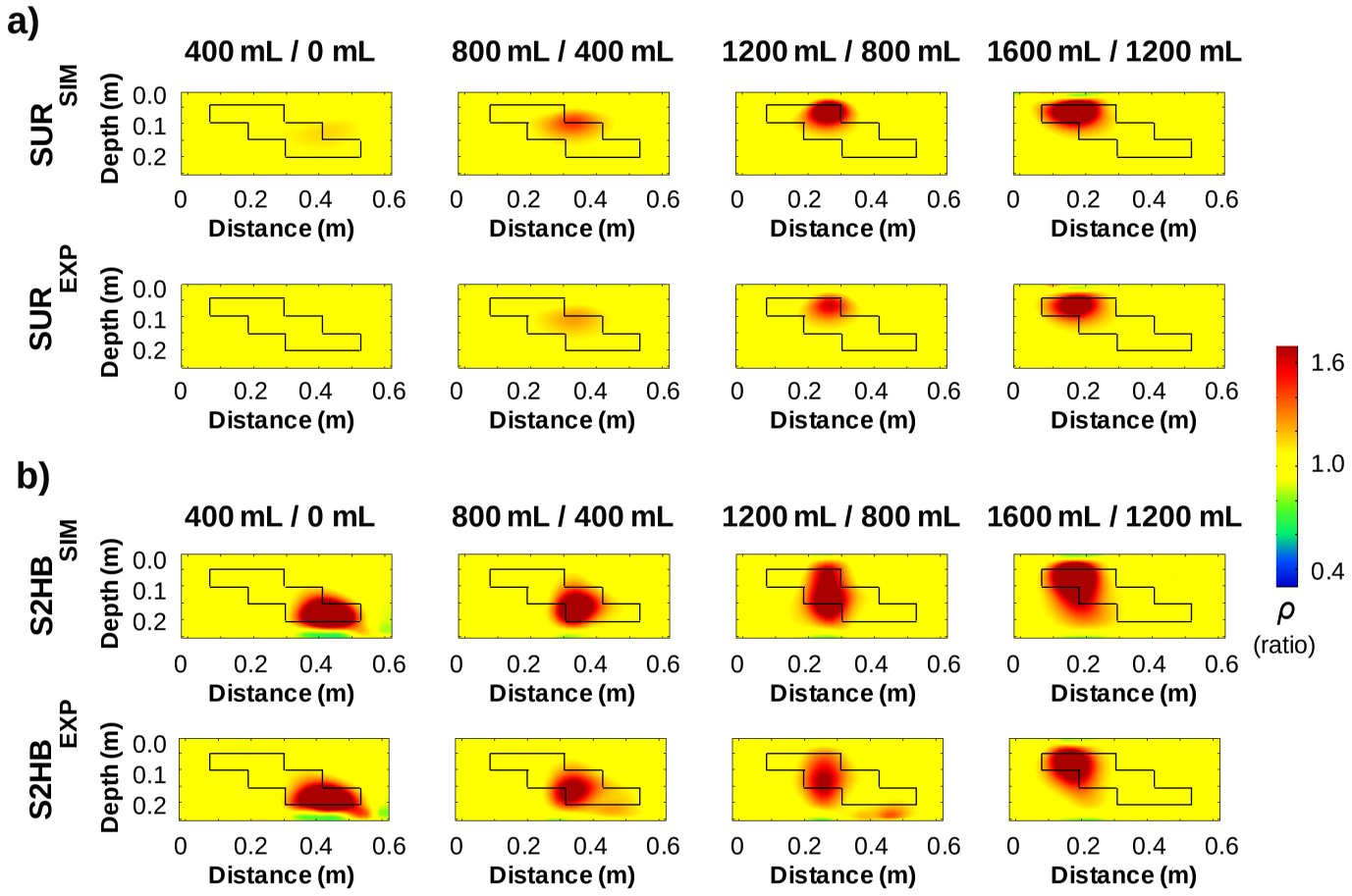

Figure 5-12: Comparison of simulated and experimental ERT ratio images between sequential monitoring steps from (a) surface ERT, and (b) surface-to-horizontal borehole ERT.

5.5 Conclusions

This work introduced the new concept of surface-to-horizontal borehole (S2HB) ERT for improved mapping of evolving DNAPL distributions relative to surface ERT. It was proposed that S2HB ERT would exhibit superior resolution with depth. This was confirmed at the laboratory scale and predicted to also apply at the field scale.

Coupled with 4D inversion, S2HB ERT was demonstrated to well resolve successive remediation intervals over the entire 4 m height of a simulated field scale DNAPL source zone undergoing remediation. This provided significant improvements over surface ERT where delineation of remediation occurring below 2 m was inhibited by limited resolution at depth. Using the DNAPL-ERT model to forecast this improvement was a straightforward way to estimate the potential benefit of S2HB ERT, with a controlled laboratory experiment subsequently conducted as a necessary validation procedure.

The laboratory experiment confirmed that the 4D S2HB ERT approach provided improved time-lapse monitoring of NAPL changes in a real system. The experiment corroborated the field scale numerical findings: time-lapse NAPL changes occurring at depth unresolved by surface ERT were mapped by S2HB ERT. The experimental findings were then validated by comparison to the actual final distribution of NAPL confirmed from excavation of the tank. The resolution of the new ERT method was such that even unexpected NAPL migration in the deepest part of the tank was correctly mapped.

Independent simulation of the experiment – predicting NAPL migration and predicting ERT surveys of simulated NAPL distributions – revealed an excellent correlation between the numerical predictions and actual observations. This provides validation of the coupled DNAPL-ERT model for surface ERT in a more complex physical system than ever previously used and, for the first time, for S2HB ERT of evolving NAPL. These validations provide confidence in the model as a reliable tool for simulating real systems. In particular, it suggests that the type of improvement shown in the field scale simulation shown likely provides a reasonable approximation of the benefit of the S2HB ERT approach.

While this work demonstrates the potential benefits of S2HB ERT for mapping DNAPLs, it is acknowledged that this is an initial study of a new concept and a number of simplifying assumptions were made. The experiment was performed at the tank scale and does not incorporate the field scale complexities that exist at contaminated sites. The homogeneity in the background soil matrix provided favourable conditions for improved static delineation of the NAPL distribution that is not usually possible at field sites. Although static detection is not a focus of this work, it is acknowledged that the time-lapse approach takes advantage of improved static images in generating the time-lapse result. Although some improvements with S2HB ERT in the static delineation of a DNAPL body may be possible in favourable conditions, time-lapse S2HB ERT monitoring of evolving NAPL changes remains the most promising application.

A number of factors may impact the vertical distance and image resolution in the region between the surface and horizontal borehole including the thickness of the vadoze zone, soil heterogeneity and clay volume, and the depth of the DNAPL source zone. Simyrdanis (2013) demonstrated that the allowable vertical distance between the surface and horizontal borehole is approximately seven times the electrode spacing. Therefore, to image deep DNAPL source zones, the electrode spacing could be increased; however, image resolution will be affected. In instances where the DNAPL source zone is particularly far from the surface, the surface electrodes could instead be implanted in a horizontal line below the ground surface using direct push technology (e.g., Harro and Kruse, 2013) or deployed in a second, shallower horizontal borehole. Alternatively, an ERT survey could be conducted using just the electrodes in the deep horizontal borehole below the remediation zone, in the form of an ‘in-borehole’ configuration.

The application of S2HB ERT aims to take advantage of the increasing usage and effectiveness of horizontal boreholes at contaminated sites; however, to the authors’ knowledge, ERT electrodes have never been placed inside horizontal boreholes at environmental sites. It is expected that electrode installation will be similar to the well-established methods used for vertical boreholes in cross-hole ERT. Careful construction and installation of the electrode cables will be required to ensure correct placement of the electrodes. In the case where some electrode displacement exists between the surface and

horizontal borehole electrodes, filters can be used to correct for displacement errors (e.g., Simyrdanis et al., 2012).

While cross-hole ERT also provides resolution at depth, S2HB should be unique in its ability to achieve sufficient coverage of a typical DNAPL source zone at reasonable expense. It is expected that a single horizontal borehole could replace a large number of vertical boreholes. In addition, although 2D cross-section ERT was shown here, the surface component of S2HB permits the acquisition of ERT measurements from a 2D surface grid to a single horizontal borehole providing a trapezoidal 3D mapping of the subsurface. This is extremely beneficial as 3D ERT measurements are usually preferred to capture the highly heterogeneous nature of DNAPL distributions at field sites. Future work will investigate this '3D surface to horizontal borehole' configuration.

Time-lapse S2HB ERT exhibits significant potential as a practical, non-invasive tool for mapping a much wider range of DNAPL source zone geometries, site conditions, and remediation activities than surface ERT, and perhaps also cross-hole ERT. An important next step would be using the validated model to simulate a range of DNAPL scenarios and site conditions to explore the limits within which S2HB is expected to be successful. A pilot test may also be conducted to investigate the application of 4D S2HB ERT monitoring of DNAPL remediation at a contaminated site.

5.6 References

Archie, G.E. 1942. The electrical resistivity log as an aid in determining some reservoir characteristics. Transactions of the AIME, 146: 54–62.

Bear, J. 1972. Dynamics of fluids in porous media. Dover, Mineola, New York.

Berg, C. 2007. An effective medium algorithm for calculating water saturations at any salinity or frequency. Geophysics, 72(2): E59-E67.

Bing, Z., and S.A. Greenhalgh. 2000. Cross-hole resistivity tomography using different electrode configuration. Geophy. Prosp., 48: 887-912.

Brewster, M.L., A.P. Annan, J.P. Greenhouse, B.H. Kueper, and G.R. Olhoeft. 1995. Observed migration of a controlled DNAPL release by geophysical methods. Ground Water, 33: 977-987.

Cardarelli, E., and G. Di Filippo. 2009. Electrical resistivity and induced polarization tomography in identifying the plume of chlorinated hydrocarbons in sedimentary formation: a case study in Rho (Milan—Italy). Waste Management & Research, 27: 595–602.

Chambers J.E., M.H. Loke, R.D. Ogilvy, and P.I. Meldrum. 2004. Noninvasive monitoring of DNAPL migration through a saturated porous medium using electrical impedance tomography. Journal of Contaminant Hydrology, 68: 1–22.

Chambers, J.E., P.B. Wilkinson, G.P. Wealthall, M.H. Loke, R. Dearden, R. Wilson, D. Allen, and R.D. Ogilvy. 2010. Hydrogeophysical imaging of deposit heterogeneity and groundwater chemistry changes during DNAPL source zone bioremediation. Journal of Contaminant Hydrology, 118: 43-61.

Christ, J.A., C.A. Ramsburg, K.D. Pennell, and L.M. Abriola. 2006. Estimating Mass Discharge from DNAPL Source Zones using Upscaled Mass Transfer Coefficients: An Evaluation using Multiphase Numerical Simulations. Water Resources Research, 42: W11420.

Daily, W., and A. Ramirez, A. 1995. Electrical resistance tomography during in-situ trichloroethylene remediation at the Savannah River Site. Journal of Applied Geophysics, 33: 239–249.

Danielsen B.E, and T. Dahlin. 2010. Numerical modeling of resolution and sensitivity of ERT in horizontal boreholes. Journal of Applied Geophysics, 70: 245–254.

English, J. 2010. HDD: An Environmental Home Run. Underground Construction Magazine, 65(12).

Gerhard, J.I., and B.H. Kueper. 2003a. Capillary pressure characteristics necessary for simulating DNAPL infiltration, redistribution, and immobilization in saturated porous media. Water Resources Research, 39: 1212.

Gerhard, J.I., and B.H. Kueper. 2003b. Relative permeability characteristics necessary for simulating DNAPL infiltration, redistribution, and immobilization in saturated porous media. Water Resources Research, 39: 1213.

Gerhard, J.I., and B.H. Kueper. 2003c. Influence of constitutive model parameters on the predicted migration of DNAPL in heterogeneous porous media. Water Resources Research, 39: 1279.

Gerhard, J.I., T. Pang, and B.H. Kueper. 2007. Time scales of DNAPL migration in sandy aquifers. Ground Water, 45: 147-157.

Goes, B.J.M., and J.A.C. Meekes. 2004. An effective electrode configuration for the detection of DNAPLs with electrical resistivity tomography. Journal of Environmental and Engineering Geophysics, 9(3):127-141.

Grant, G.P., and J.I. Gerhard. 2007a. Simulating the dissolution of a complex dense non-aqueous phase liquid source zone: 1. model to predict interfacial area. Water Resources Research, 43: W12410.

Grant, G.P., and J.I. Gerhard. 2007b. Simulating the dissolution of a complex dense non-aqueous phase liquid source zone: 2. experimental validation of an interfacial area-based mass transfer model. Water Resources Research, 43.

Grant, G.P., J.I. Gerhard, and B.H. Kueper. 2007a. Field scale impacts of spatially correlated relative permeability in heterogeneous multiphase systems. Advances in Water Resources, 30: 1144-1159.

Grant, G.P., J.I. Gerhard, and B.H. Kueper. 2007b. Multidimensional validation of a numerical model for simulating a DNAPL release in heterogeneous porous media. Journal of Contaminant Hydrology, 92: 109-128.

Harro, D., and S. Kruse. 2013. Improved imaging of covered karst with the multi-electrode resistivity implant technique. NCKRI Symposium 2. Proceedings of the 13th Multidisciplinary Conference on Sinkholes and the Engineering and Environmental Impacts of Karst. Carlsbad, New Mexico, US.

Johnson, T.C., L.D. Slater, D. Ntarlagiannis, F.D. Day-Lewis, and M. Elwaseif. 2012. Monitoring groundwater-surface water interaction using time-series and time-frequency analysis of transient three-dimensional electrical resistivity changes. Water Resources Research, 48(7): W07506.

Karaoulis, M.C., J.H. Kim, and P.I. Tsourlos. 2011a. 4D active time constrained resistivity inversion. Journal of Applied Geophysics, 73: 25-34.

Karaoulis, M., A. Revil, D.D. Werkema, B.J. Minsley, W.F. Woodruff, and A. Kemna. 2011b. Time-lapse three-dimensional inversion of complex conductivity data using an active time constrained (ATC) approach. Geophysical Journ. Int., 187: 237-251.

Karaoulis, M., A. Revil, P. Tsourlos, D.D. Werkema, and B.J. Minsley. 2013. IP4DI: A software for time-lapse 2D/3D DC-resistivity and induced polarization tomography. Computers & Geosciences, 54(0): 164-170.

Karaoulis, M., P. Tsourlos, J.H. Kim, and A. Revil. 2014. 4D time-lapse ERT inversion: introducing combined time and space constraints. Near Surface Geophysics, 12(1): 25-34.

Kavanaugh, M.C., P.S.C. Rao, L. Abriola, C. Newell, J. Cherry, T. Sale, G. Destouni, S. Shoemaker, R. Falta, R. Siegrist, D. Major, G. Teutsch, J. Mercer, and K. Udell. 2003. The DNAPL remediation challenge: is there a case for source depletion? US Environmental Protection Agency, Washington DC.

Kim, J.H., M.J. Yi, S.G. Park, and J.G. Kim. 2009. 4-D inversion of DC resistivity monitoring data acquired over a dynamically changing earth model. Journal of Applied Geophysics, 68: 522-532.

Kim, J.H., R. Supper, P. Tsourlos, and M.J. Yi. 2013. Four-dimensional inversion of resistivity monitoring data through L*p* norm minimizations. Geophysical Journal International, 195(3): 1640-1656.

Kueper, B.H., G.P. Wealthall, J.W.N. Smith, S.A. Leharne, and D.N. Lerner. 2003. An illustrated handbook of DNAPL transport and fate in the subsurface. Environment Agency R&D Publication 133. EA, Bristol.

Lehr, J. H. 2004. Wiley's remediation technologies handbook: major contaminant chemicals and chemical groups. John Wiley & Sons, Inc., Hoboken, New Jersey.

Loke, M.H. 2013. Tutorial: 2-D and 3-D electrical imaging surveys. http://www.geotomosoft.com/downloads.php, accessed 20 August 2013.

Loke, M.H., J.E. Chambers, D.F. Rucker, O. Kuras, and P.B. Wilkinson. 2013. Recent developments in the direct-current geoelectrical imaging method. Journal of Applied Geophysics, 95: 135-156.

Loke, M.H., T. Dahlin, and D.F. Rucker. 2014. Smoothness-constrained time-lapse inversion of data from 3-D resistivity surveys. Near Surface Geophysics, 12(1): 5-24.

Lucius, J.E., G.R. Olhoeft, P.L. Hill, and S.K. Duke. 1992. Properties and hazards of 108 selected substances - 1992 edition. Open-File Report 92-527, U. S. Geological Survey.

MacPhee, S.L., J.I. Gerhard, and G. Rein. 2012. A novel method for simulating smoldering propagation and its application to STAR (Self-sustaining treatment for active remediation). Environmental Modelling and Software, 31: 84-98.

Mercer, J.W., and R.M. Cohen. 1990. A review of immiscible fluids in the subsurface: properties, models, characterization, and remediation. Journal of Contaminant Hydrology, 6: 107-163.

Miller, R.R. 1996. Horizontal wells. GWRTAC Series Technology Overview Report TO-96-O2. Prepared for Ground-Water Remediation Technologies Analysis Center, October 1996.

Miller, C.R., P.S. Routh, T.R. Brosten, and J.P. McNamara. 2008. Application of time-lapse ERT imaging to watershed characterization. Geophysics, 73(3): G7-G17.

Moran, W., and G. Losonsky. 2008. Enhanced Delivery of Potassium Permanganate Using Horizontal Wells. In Proceedings of the Sixth International Conference on Remediation of Chlorinated and Recalcitrant Compounds, Monterey, California, USA, May 19-22, 2008.

Nenna, V., A. Pidlisecky, and R. Knight. 2011. Informed experimental design for electrical resistivity imaging. Near Surface Geophysics, 9: 469-482.

Nguyen, F., A. Kemna, A. Antonsson, P. Engesgaard, O. Kuras, R. Ogilvy, J. Gisbert, S. Jorreto, and A. Pulido-Bosch. 2009. Characterization of seawater intrusions using 2D electrical imaging. Near Surface Geophysics, 7: 377-390.

Newmark R.L., W.D. Daily, K.R. Kyle, and A.L. Ramirez. 1998. Monitoring DNAPL pumping using integrated geophysical techniques. Journal of Environmental and Engineering Geophysics, 3: 7–13.

Pankow, J.F., S. Feenstra, J.A. Cherry, and M.C. Ryan. 1996. Dense chlorinated solvents in groundwater: Background and history of the problem. In: Pankow, J.F., and J.A. Cherry (Eds.), Dense Chlorinated Solvents and other DNAPLs in Groundwater, History, Behavior, and Remediation. Waterloo Press, Portland, Oregon, United States, pp. 1-52.

Papadopoulos N.G., P. Tsourlos, G.N. Tsokas, and A. Sarris. 2007. Efficient ERT measuring and inversion strategies for 3D imaging of buried antiquities. Near Surface Geophysics, 5: 349–362.

Plummer, C.R., J.D. Nelson, and G.S. Zumwalt. 1997. Horizontal and vertical well comparison for in situ air sparging. Ground Water Monitoring and Remediation, 17: 91-96.

Power C., J.I. Gerhard, P. Tsourlos, and A. Giannopoulos. 2013. A new coupled model for simulating the mapping of dense nonaqueous phase liquids using electrical resistivity tomography. Geophysics, 78(4): EN1-EN15.

Power, C., J.I. Gerhard, M. Karaoulis, P. Tsourlos, and A. Giannopoulos. 2014. Evaluating four-dimensional time-lapse electrical resistivity tomography for monitoring DNAPL source zone remediation. Journal of Contaminant Hydrology, (In Press).

Revil, A., and L.M. Cathles. 1999. Permeability of shaly sands. Water Resources Research, 35: 651-662.

Robin, M.J.L., E.A. Sudicky, R.W. Gillham, and R.G. Kachanowski. 1991. Spatial variability of Strontium distribution coefficients and their correlation with hydraulic conductivity in the Canadian Forces Base Borden aquifer. Water Resources Research, 27: 2619–2632.

Sauer, U., N. Watanabe, A. Singh, P. Dietrich, O. Kolditz, and C. Schutze. 2014. Joint interpretation of geoelectrical and soil-gas measurements for monitoring CO2 releases at a natural analogue. Near Surface Geophysics, 12(1): 165-187.

Seferou, P., P. Soupios, N.N. Kourgialas, Z. Dokou, G.P. Karatzas, E. Candasayar, N. Papadopoulos, V. Dimitriou, A. Sarris, and M. Sauter. 2013. Olive-oil mill wastewater transport under unsaturated and saturated laboratory conditions using the geoelectrical resistivity tomography method and the FEFLOW model. Hydrogeology Journal, 21(6): 1219-1234.

Simyrdanis, K. 2013. Development of surveying geophysical techniques for the study of geotechnical and environmental problems. PhD thesis. Aristotle University of Thessaloniki, Greece.

Simyrdanis, K., P. Tsourlos, P. Soupios, and J.H. Kim. 2012. Optimizing surface-to-tunnel ERT measurements. Near Surface Geoscience 2012, 18th European Meeting of Environmental and Engineering Geophysics, Paris, France, September 2012.

Supper, R., J. Chambers, P. Tsourlos, and J.H. Kim. 2014. Foreword on the Special Topic of Geoelectrical Monitoring. Near Surface Geophysics, 12(1): 1-3.

Tsourlos, P., and R. Ogilvy. 1999. An algorithm for the 3-D inversion of tomographic resistivity and induced polarization data: preliminary results. Journal of the Balkan Geophysical Society, 2: 30-45.

Van Heest, G., M. Sequino, and G. Losonsky. 2013. Directional drilled horizontal wells and engineering horizontal remediation wells screens accelerate site closure. 29th Annual International Conference on Soils, Sediments, Water, and Energy, Oct 21–24 2013, University of Massachusetts at Amherst, MA, USA.

Van Heest, G. 2013. Horizontal wells for groundwater remediation: How a technology that revolutionized the oil industry is used to remediate groundwater. The Magazine for Environmental Managers. Air and Waste Management Association. June 2013 Edition.

van Schoor, M., and A. Binley. 2010. In-mine (tunnel-to-tunnel) electrical resistance tomography in South African platinum mines. Near Surface Geophysics, 8: 563-574.

West, M.R., G.P. Grant, J.I. Gerhard, and B.H. Kueper. 2008. The influence of precipitate formation on the chemical oxidation of TCE DNAPL with potassium permanganate. Advances in Water Resources, 31: 324-338.

Wilkinson, P.B., S.S. Uhlemann, J.E. Chambers, P.I. Meldrum, L.S. Oxby, and O. Kuras. 2013. Optimised sequential experimental design for geoelectrical resistivity monitoring surveys. Near Surface Geoscience 2013, 19th European Meeting of Environmental and Engineering Geophysics, Bochum, Germany, September 2013.

Yi, M.J., J.H. Kim, and S.H. Chung. 2003. Enhancing the resolving power of least-squares inversion with active constraint balancing. Geophysics, 68: 931-941.

Zheng, C. 1990. MT3D, A Modular Three-Dimensional Transport Model for Simulation of Advection, Dispersion and Chemical Reactions of Contaminants in Groundwater Systems, 170 pp., U.S. Environ. Prot. Agency, Washington, D. C.

6 CONCLUSIONS

6.1 Summary

Practical, non-invasive tools do not currently exist for identifying the volume and distribution of soil impacted by DNAPL. For many years, ERT has been proposed as an attractive and viable technique to assist in the characterization and monitoring activities at DNAPL contaminated sites. While the potential has been demonstrated by a number of studies, ERT has not become a standard technique for DNAPL site investigations. The behaviour of DNAPLs in the subsurface is a particularly complex field of research with years of systematic and controlled studies being performed. The application of ERT imaging to this problem also requires a systematic and controlled approach but this has not been possible due to controlled field experiments largely prohibited and laboratory experiments rarely reproducing the field scale heterogeneity critical to DNAPL behaviour. Therefore, it was evident that an updated evaluation of the potential for DNAPL mapping by ERT was timely, particularly to coincide with the recent advancements in the ERT technique.

The goal of this research was to explore the potential of ERT for application as a non-invasive DNAPL site investigation tool with specific emphasis on evaluating the potential of 4D time-lapse ERT for monitoring the remediation of DNAPL source zones.

The first objective was to develop a coupled DNAPL-ERT numerical model that would form the fundamental and theoretical basis of this research. The coupled model integrates a multiphase flow model, which generates realistic DNAPL scenarios, with an ERT forward model that predicts the corresponding resistivity response. The model creates a link between the main hydrogeological parameters of interest at DNAPL sites (including hydraulic permeability, porosity, clay content, groundwater quality, and air, water, and DNAPL contents evolving with time) and the corresponding bulk electrical resistivity distribution that is measured by an ERT survey. The model was then employed for an evaluation of ERT under a range of DNAPL scenarios. Sensitivity studies conducted at a range of scales, from a single location to an entire domain, demonstrated that the DNAPL-ERT model is robust and sensitive to both variations in DNAPL distribution and

subsurface heterogeneity. The DNAPL-ERT model was then used to independently simulate two laboratory experiments involving ERT mapping of NAPL with two different electrode configurations. Close correlation between the experimental and simulated data provided confidence in the DNAPL-ERT model for (i) simulating changing NAPL distributions, and (ii) predicting the results of ERT surveys. The DNAPL-ERT model provides a valuable and cost-effective avenue for simulating and testing ERT mapping of DNAPL spills at the field scale.

The second objective was to explore the potential of four-dimensional (4D) time-lapse ERT implemented at the surface to monitor DNAPL source zone remediation. Static delineation of complex electrical target presented by an intricate, unknown DNAPL distribution in a heterogeneous, unknown permeability field is not easily remedied. However, time-lapse ERT monitoring may remain promising even in complex, heterogeneous environments because the background soil matrix is removed in the time-lapse ERT response with the evolving signal directly corresponding to changes in DNAPL mass and distribution. A controlled laboratory experiment demonstrated the success of 4D ERT implemented at the surface for identifying changes in NAPL distribution in a physical system. The model was then employed to investigate the potential of the 4D ERT approach for monitoring DNAPL source zones at the field scale. Four DNAPL source zones, exhibiting a range of complexity, were simulated, followed by modelled time-lapse ERT monitoring of complete DNAPL mass removal. Results demonstrated that 4D time-lapse ERT provides effective mapping of both the outline and the center of mass of the treated portion of the source zone as a function of time to within a few metres in each direction. In addition, the technique provided a reasonable, albeit conservative, estimate of the DNAPL volume removed with time: 25% underestimation in the upper 2 m and up to 50% underestimation at late time between 2 and 4 m depth. The technique is less reliable for identifying cleanup of relatively thin DNAPL branches located outside the main DNAPL body and DNAPL cleanup at depth due to reduced sensitivity.

The third objective was to evaluate the potential of surface-to-horizontal borehole (S2HB) ERT as an improved configuration for monitoring the remediation of DNAPL source

zones. S2HB ERT was proposed as an alternative ERT configuration due to its superior depth resolution and to coincide with the upsurge in horizontal wells being incorporated into remedial strategies in recent years. Results from a controlled laboratory experiment and simulation of a complex field scale DNAPL remediation scenario demonstrate that S2HB ERT provides improved mapping of DNAPL distributions at the laboratory and field scale. As expected, significant improvement occurs at larger depth which demonstrates the superior depth resolution and sensitivity of S2HB ERT. Confirmation of the final NAPL distribution was obtained by excavation of the tank at the end of the experiment, providing validation of the corresponding surface and S2HB ERT results. This initial study demonstrates significantly improved resistivity imaging with S2HB ERT and its potential as a non-invasive DNAPL site tool for mapping DNAPL mass changes during remediation of deeper DNAPL source zones.

6.2 Implications

This work implies that time-lapse ERT has significant potential for providing valuable spatial and temporal subsurface information during the remediation of DNAPL source zones. Although some elements of this work have demonstrated that static delineation of a DNAPL source zone may be possible with ERT in some highly favourable environments (e.g., homogeneous soil matrix, cohesive DNAPL body with high saturation pools), overall this work confirms that static detection of a DNAPL source zone at a typical field site remains a challenging problem that is not easily remedied. However, time-lapse ERT – in particular 4D ERT – is promising as a DNAPL site tool for monitoring subsurface changes related to DNAPL mass removal over time.

Although ERT applied at the surface is affected by limited resolution at depth, it is still widely employed as it is inexpensive, practical and provides significant and rapid spatial coverage. Due to the number of advancements in ERT, surface ERT surveys are also providing more reliable and higher quality subsurface information. In the context of DNAPL investigations, this work has shown that 4D ERT applied at the surface may provide valuable qualitative information across a range of DNAPL source zones

undergoing remediation. The limited sensitivity and resolution at depth of surface ERT is mainly evident when inferring quantitative information such as DNAPL mass removed. Therefore, while the accuracy of quantitative information may be site-specific and dependent on field conditions and the geometry of the DNAPL source zone, time-lapse ERT exhibits potential to be utilized more widely as a valuable qualitative mapping (e.g., bulk outline and center of mass of the evolving treated region) tool at DNAPL sites.

At sites where electrodes may be deployed inside boreholes, superior depth resolution and more accurate quantitative information may be obtained. Cross-hole ERT is well-established and widely used as an alternative to surface ERT across a wide range of hydrogeological applications. Although it can provide superior imaging, it is however limited by the separation distance between the borehole pair. Therefore, a large number of vertical boreholes may be required to provide adequate spatial coverage of a typical DNAPL source zone undergoing remediation. In addition, drilling vertical boreholes in the vicinity of a DNAPL source zone could lead to unintentional DNAPL remobilization downwards into pristine aquifer.

To overcome these constraints, S2HB ERT may be an extremely attractive option. Although it has not yet been considered at environmental sites, this work has demonstrated that S2HB ERT provides significantly improved imaging of subsurface changes. Horizontal remediation wells are becoming more commonplace at DNAPL sites due to a number of benefits, such as improved access and contact with contaminants. These benefits are analogous to the benefits of ERT electrode placement in proximity to the prospected DNAPL target. Although S2HB ERT may be more expensive to implement, it has the potential to provide significant cost savings in the long-term.

Throughout this work, recently developed 4D time-lapse inversion algorithms were employed and provided significantly improved imaging of time-lapse changes compared to previously used inversion algorithms. These improvements, which include the reduction of inversion artifacts and improved sensitivity in regions of change, are particularly valuable in the context of DNAPL remediation monitoring where even small artifacts can mask, or be mistaken, for changes of interest. These improvements have

also demonstrated that the recent advancements evident in the ERT technique are having an impact on the reliability and quality of information obtained from ERT.

6.3 Recommendations for Future Work

Despite the potential shown in this work, time-lapse ERT will not become a standard monitoring technique at real sites until the knowledge obtained from this work is applied at a real field site undergoing remediation. Although time-lapse monitoring of DNAPL remediation is proposed, it is acknowledged that the DNAPL source zone requires some general characterization prior to remediation. Conventional intrusive techniques, which are also continually improving, can still be used for this purpose with ERT possibly providing complementary geological or DNAPL source zone information prior to remediation. The information gathered from this initial characterization is then typically used to develop a site conceptual model. Depending on the detail of this conceptual model, the DNAPL-ERT numerical model could be used to predict the resistivity response of an ERT survey at this site, and provide a cost-effective avenue to test optimum ERT data acquisition and inversion methods.

This work demonstrated that the DNAPL-ERT model provides an extremely valuable and cost-effective avenue to investigate many aspects of the ERT technique and its application to DNAPL scenarios. A wide range of additional studies are possible with the DNAPL-ERT model. For example, the S2HB ERT configuration could be compared to cross-hole ERT for monitoring a wider range of field scale DNAPL remediation scenarios. This study could also evaluate the benefits of ERT surveys utilizing a single horizontal borehole in S2HB compared to a network of vertical boreholes that may be required in cross-hole ERT. The optimum vertical separation distance between surface and horizontal borehole could be further investigated in the context of DNAPL targets. The S2HB ERT configuration could also be examined in 3D, with a surface ERT grid combined with a single horizontal borehole.

As discussed, ERT is a rich field of research with ongoing advancements continually improving the technique. Sequential optimized ERT survey design has been proposed to obtain improved data quality during time-lapse monitoring surveys. Further developments to 4D inversion algorithms have occurred that propose further improvements in time-lapse imaging. Additional subsurface information obtained from other geoelectrical techniques can be incorporated into ERT inversions to provide improved imaging, while joint hydrogeological-ERT inversions have also demonstrated improved mapping of subsurface features. The DNAPL-ERT model could be used to evaluate the performance of the latest 4D inversion algorithms and optimized electrode array designs.

The multiphase flow component of the DNAPL-ERT model can also be extended to permit reactive transport processes and allow investigation of biogeochemistry signatures and alternative remediation technologies such as chemical oxidation and bioremediation. Alternative geoelectrical techniques could also be investigated for mapping DNAPLs including induced polarization (IP) and ground penetrating radar (GPR). The coupled DNAPL-ERT model can also handle complex conductivities and dielectric permittivities, meaning the model can be extended to study these alternative techniques.

APPENDIX A – SURFACE ERT EXPERIMENT

The following photos illustrate the preparation and data acquisition of the laboratory tank experiment described in Chapter 4:

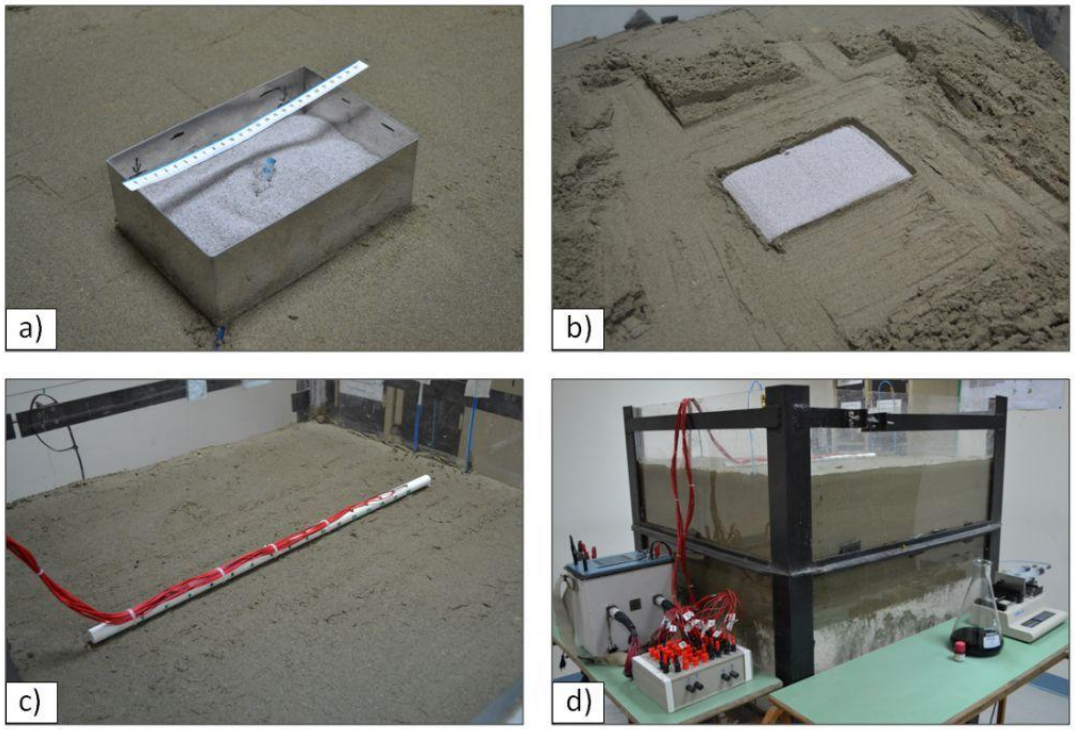

Figure A-1: (a) placement of the medium sand block showing the stainless steel divider (used to separate the fine sand and medium sand) and the location of the DNAPL release point, (b) top of the medium sand block following removal of the stainless steel divider, (c) mobile ERT survey line unit which holds the electrodes, and (d) 3D experimental tank set-up showing the resistivity meter and the syringe pump used to inject the DNAPL.

APPENDIX B – COMPLETE TIME-LAPSE ERT APPROACH

The 4D time-lapse modelling approach described in Chapter 4 (schematic presented in Figure 4-2) was used to evaluate the potential of time-lapse ERT to monitor DNAPL remediation at the field scale. In Chapter 4, Figures 4-11 to 4-14 present the actual versus ERT-measured DNAPL saturation changes for four DNAPL remediation scenarios: CB_het, CB_lay, PCE_het and PCE_lay. Additional images are presented in this section to illustrate the complete time-lapse modelling approach for each DNAPL remediation scenario.

B.1 Chlorobenzene (CB_het) Remediation Scenario

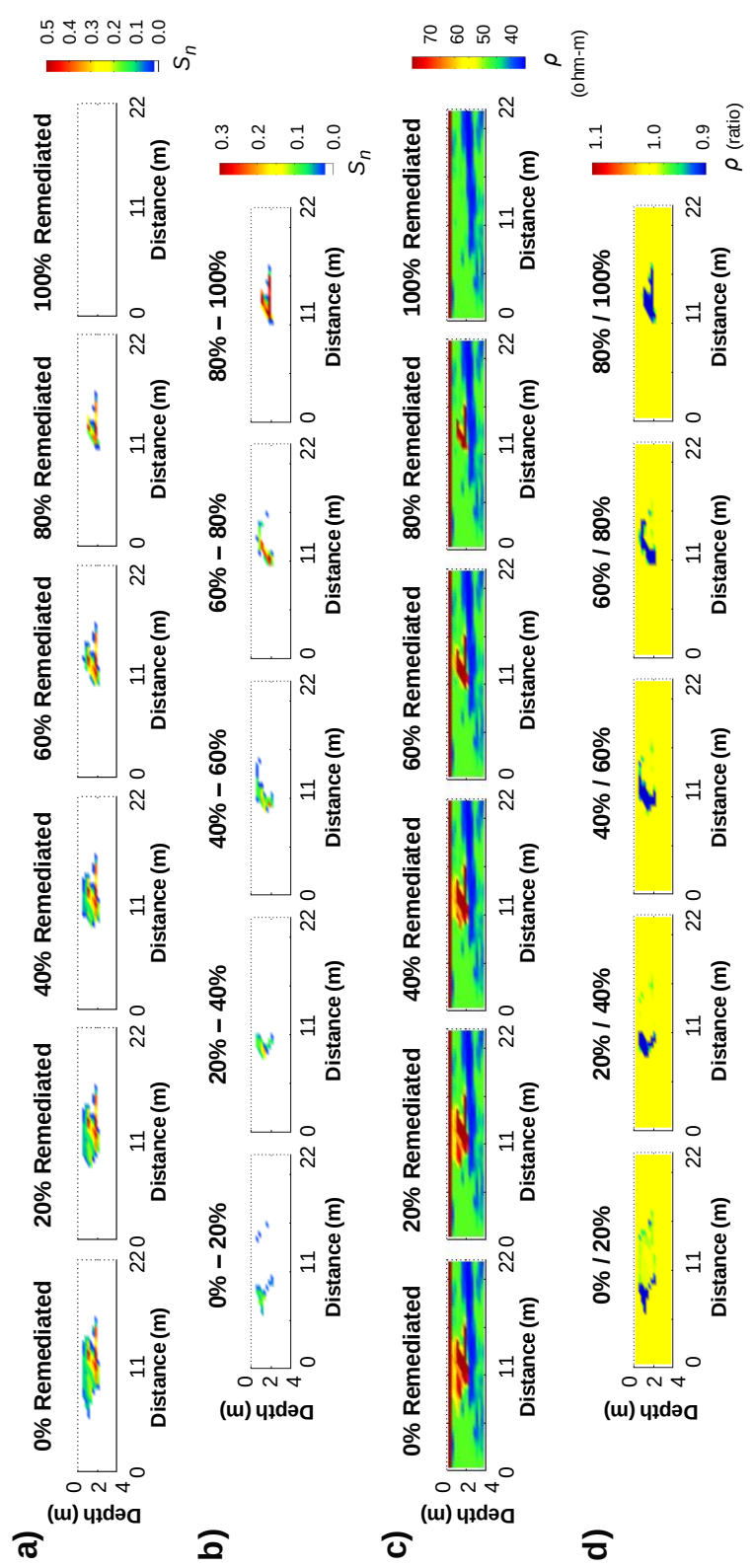

Figure B-1: (a) DNAPL saturation distributions at each monitoring step during remediation of the simulated chlorobenzene (CB_het) spill scenario, (b) DNAPL saturation changes between sequential monitoring steps, (c) actual resistivity distributions corresponding to each monitoring step during remediation, (d) actual resistivity ratio images between sequential monitoring steps.

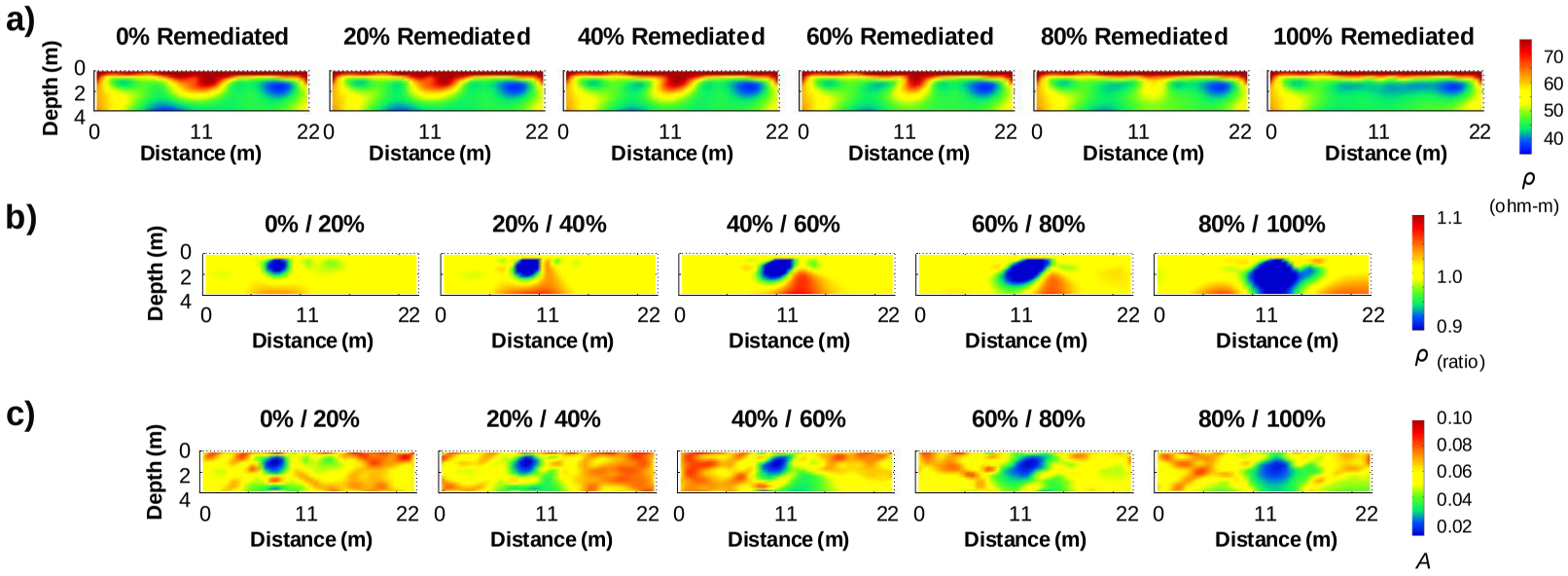

Figure B-2: (a) independently inverted resistivity distributions at each monitoring step during remediation of the simulated chlorobenzene (CB_het) spill scenario, (b) independently inverted ratio images between sequential monitoring steps, (c) temporal Lagrangian distribution between sequential monitoring steps.

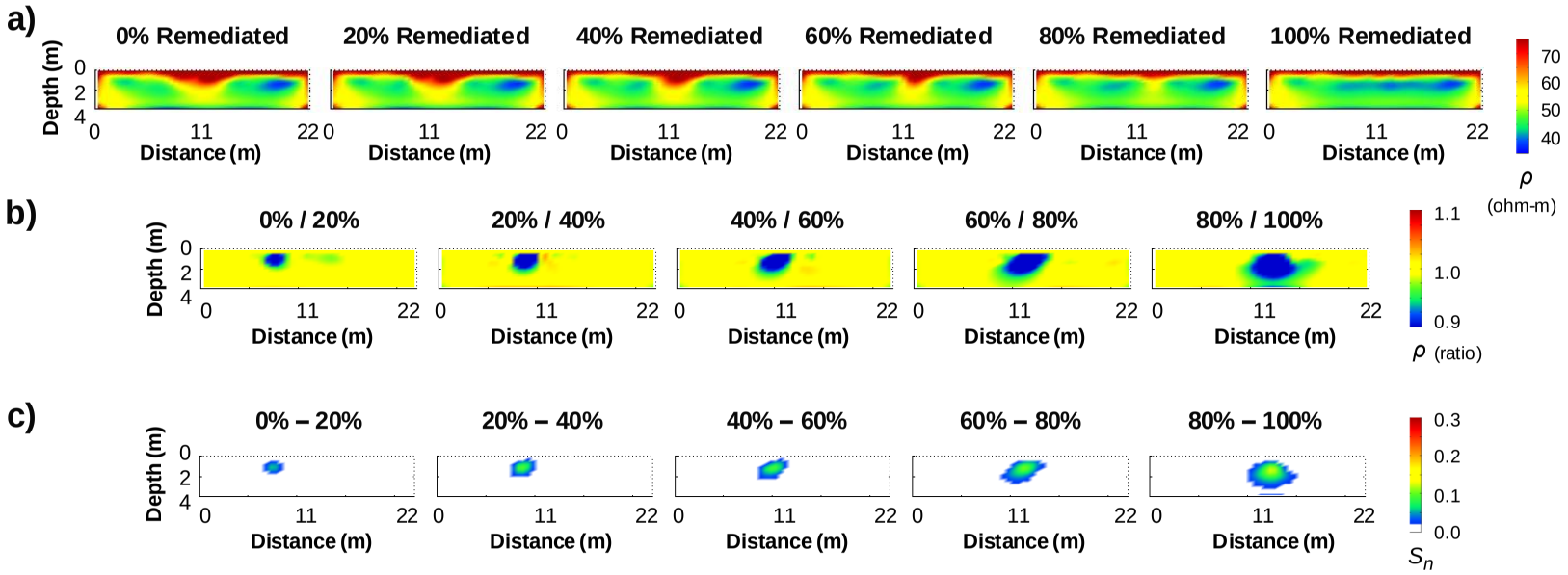

Figure B-3: (a) 4D-ATC inverted resistivity distributions at each monitoring step during remediation of the simulated chlorobenzene (CB_het) spill scenario, (b) 4D-ATC inverted ratio images between sequential monitoring steps, (c) ERT-measured DNAPL saturation changes between sequential monitoring steps.

B.2 Chlorobenzene (CB_lay) Remediation Scenario

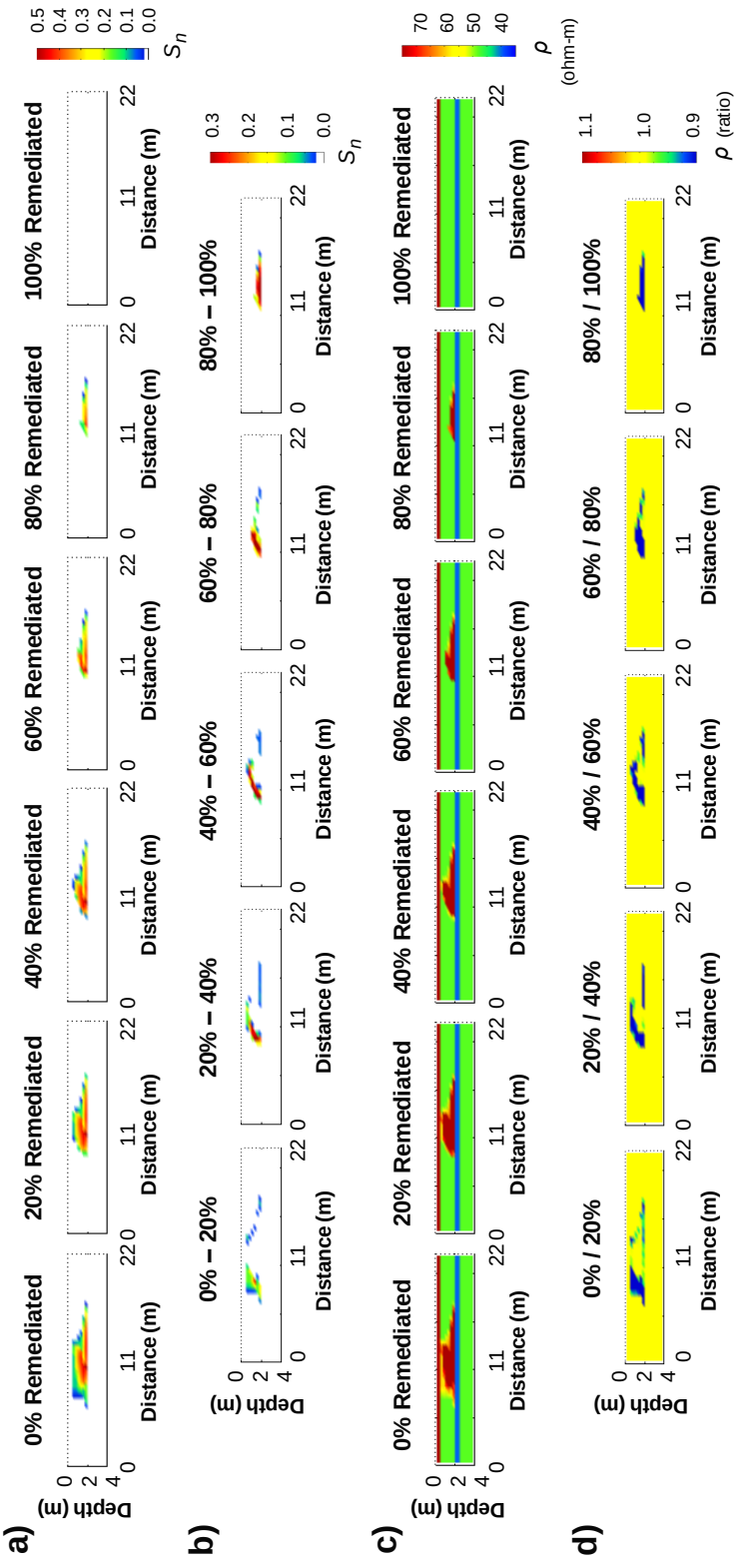

Figure B-4: (a) DNAPL saturation distributions at each monitoring step during remediation of the simulated chlorobenzene (CB_lay) spill scenario, (b) DNAPL saturation changes between sequential monitoring steps, (c) actual resistivity distributions corresponding to each monitoring step during remediation, (d) actual resistivity ratio images between sequential monitoring steps.

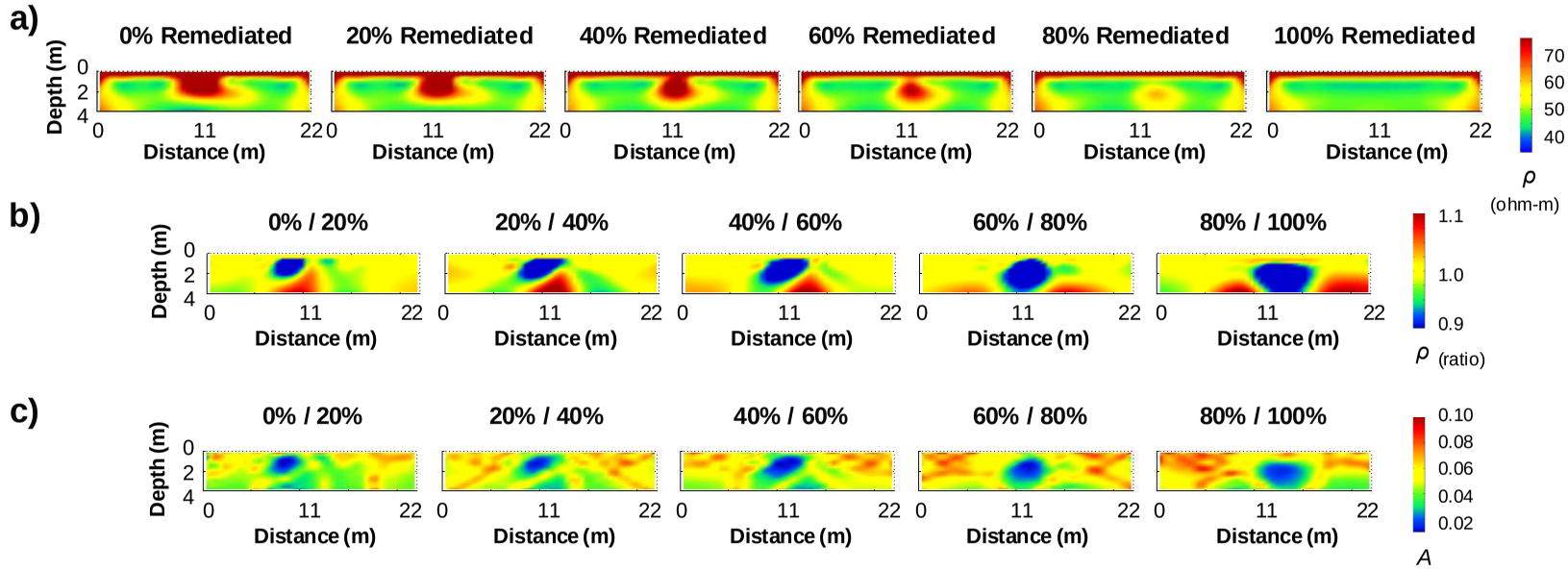

Figure B-5: (a) independently inverted resistivity distributions at each monitoring step during remediation of the simulated chlorobenzene (CB_lay) spill scenario, (b) independently inverted ratio images between sequential monitoring steps, (c) temporal Lagrangian distribution between sequential monitoring steps.

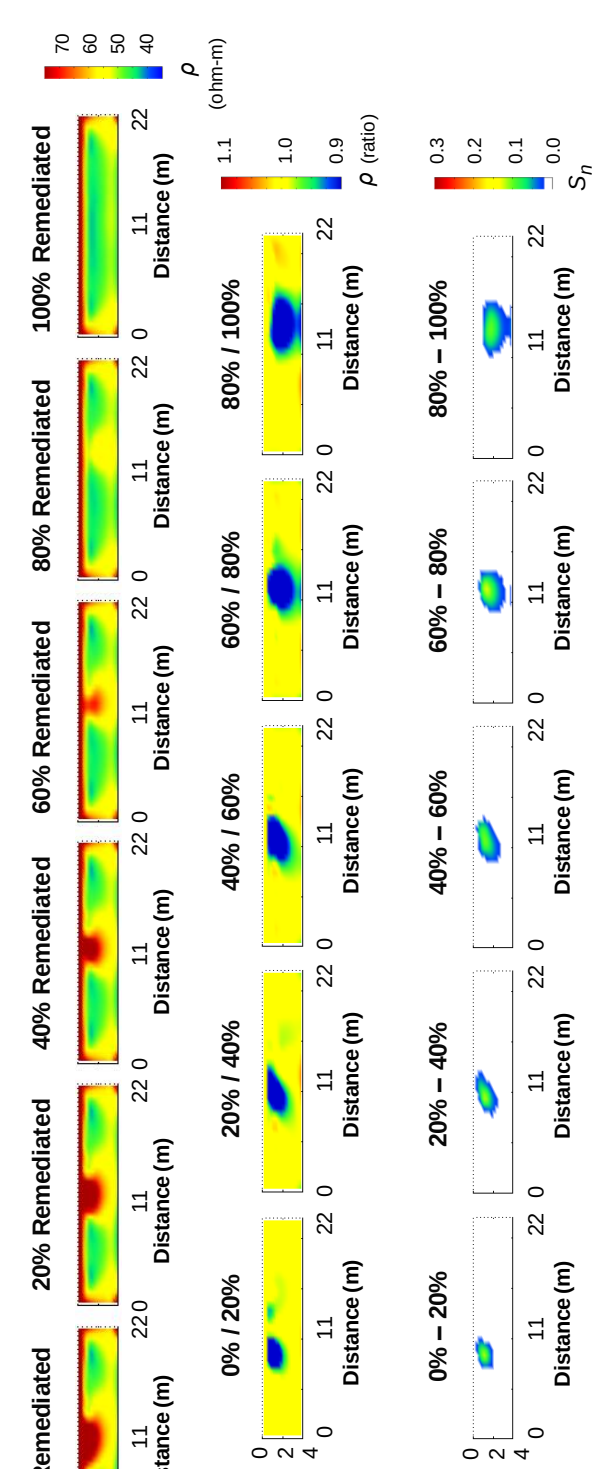

Figure B-6: (a) 4D-ATC inverted resistivity distributions at each monitoring step during remediation of the simulated chlorobenzene (CB_lay) spill scenario, (b) 4D-ATC inverted ratio images between sequential monitoring steps, (c) ERT-measured DNAPL saturation changes between sequential monitoring steps.

B.3 Tetrachloroethylene (PCE_het) Remediation Scenario

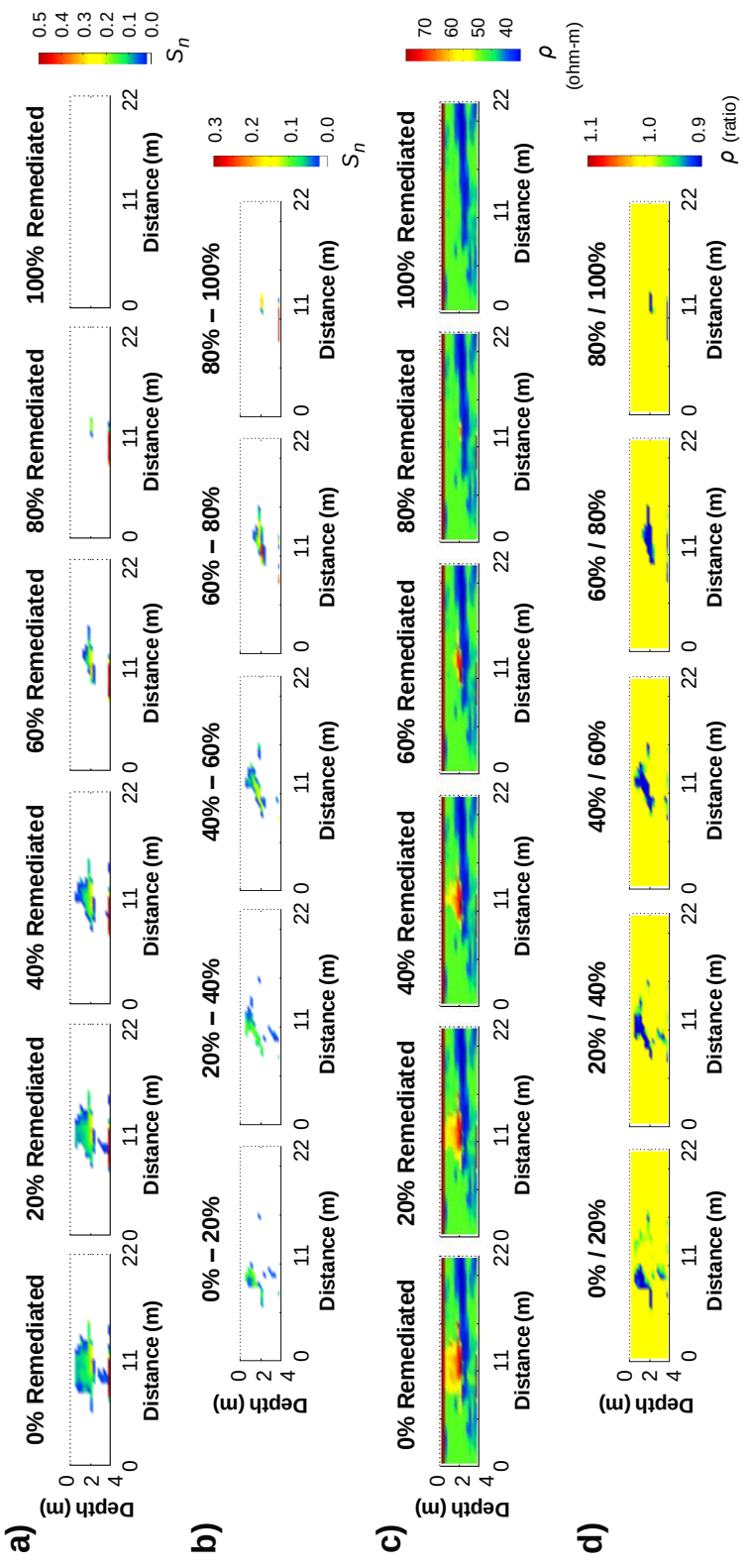

Figure B-7: (a) DNAPL saturation distributions at each monitoring step during remediation of the simulated tetrachloroethylene (PCE_het) spill scenario, (b) DNAPL saturation changes between sequential monitoring steps, (c) actual resistivity distributions corresponding to each monitoring step during remediation, (d) actual resistivity ratio images between sequential monitoring steps.

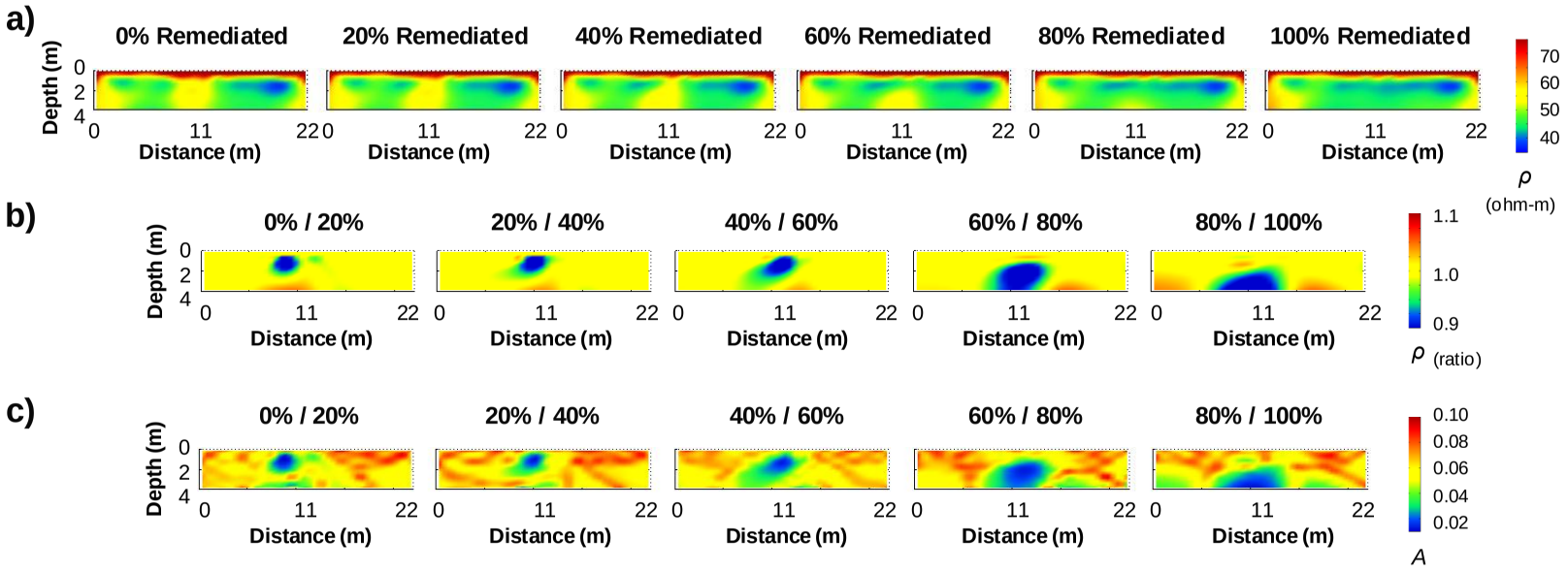

Figure B-8: (a) independently inverted resistivity distributions at each monitoring step during remediation of the simulated tetrachloroethylene (PCE_het) spill scenario, (b) independently inverted ratio images between sequential monitoring steps, (c) temporal Lagrangian distribution between sequential monitoring steps.

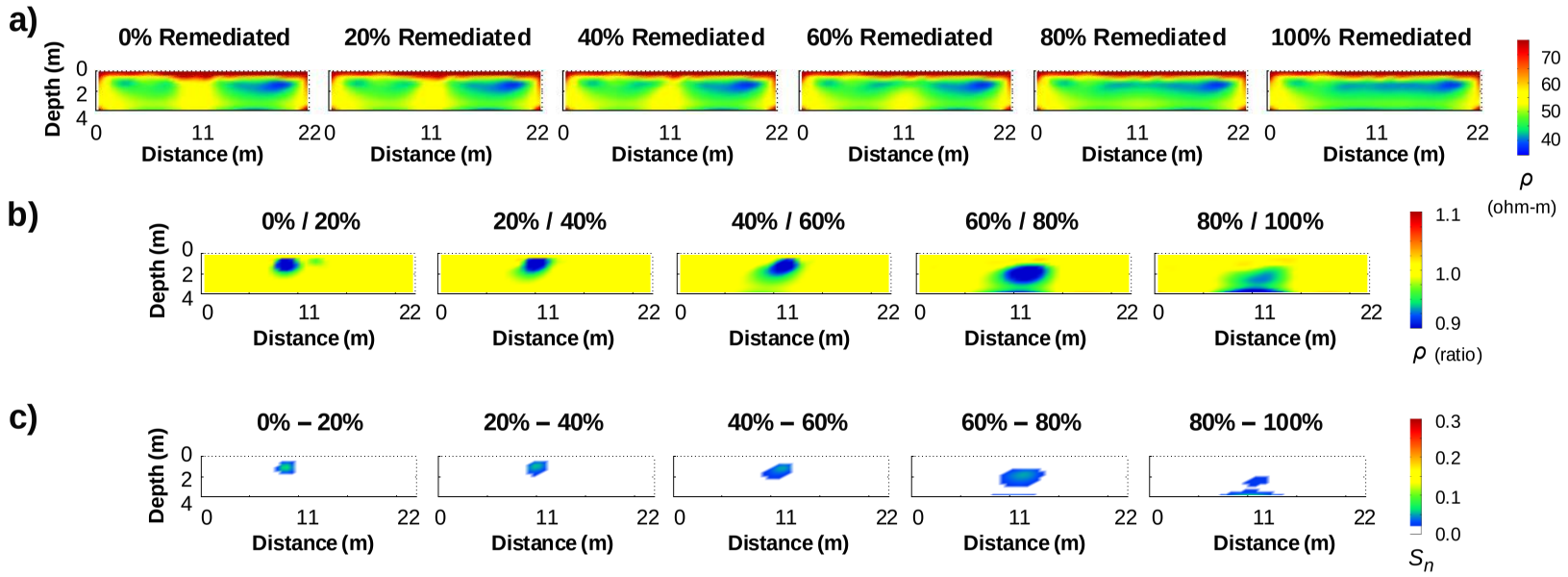

Figure B-9: (a) 4D-ATC inverted resistivity distributions at each monitoring step during remediation of the simulated tetrachloroethylene (PCE_het) spill scenario, (b) 4D-ATC inverted ratio images between sequential monitoring steps, (c) ERT-measured DNAPL saturation changes between sequential monitoring steps.

B.4 Tetrachloroethylene (PCE_lay) Remediation Scenario

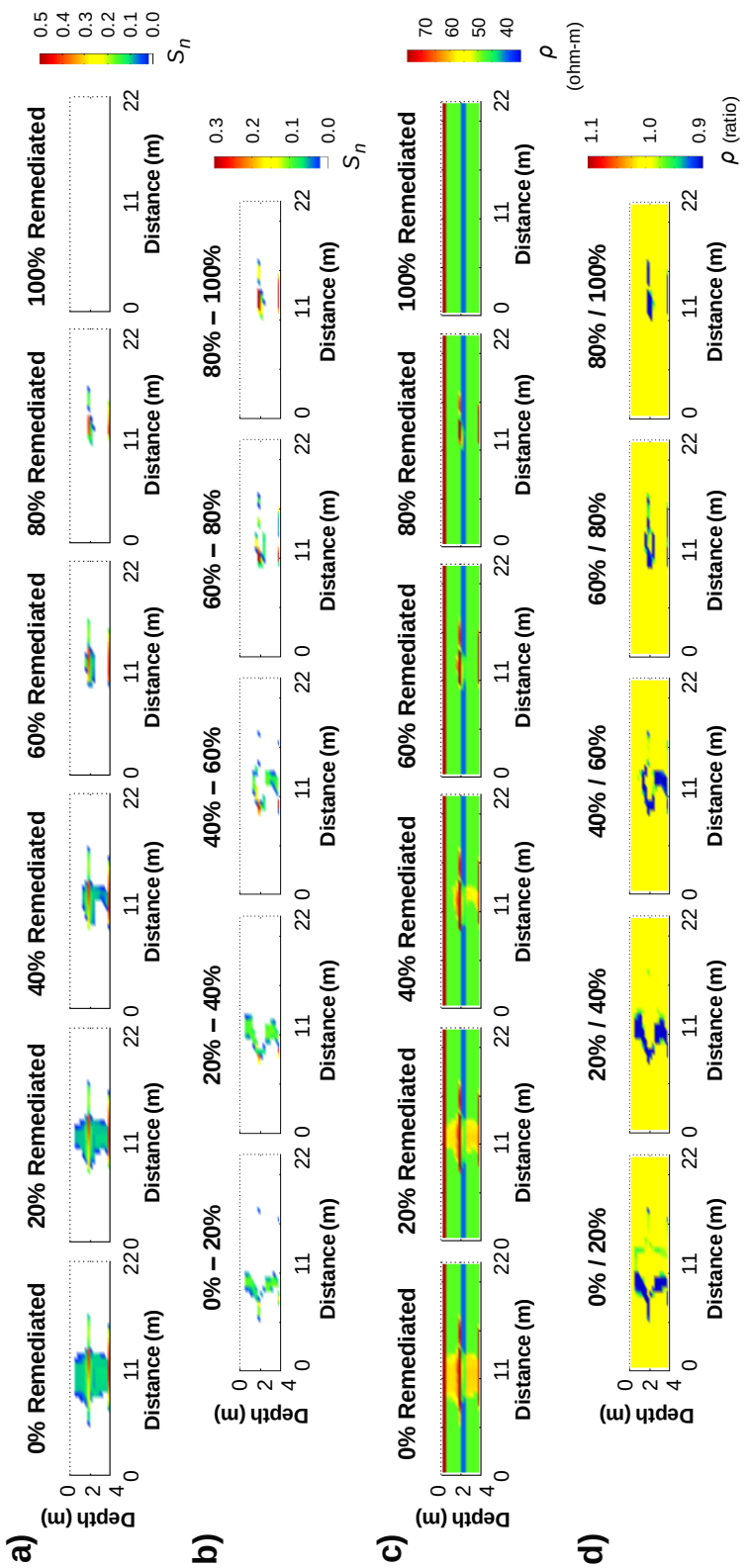

Figure B-10: (a) DNAPL saturation distributions at each monitoring step during remediation of the simulated tetrachloroethylene (PCE_lay) spill scenario, (b) DNAPL saturation changes between sequential monitoring steps, (c) actual resistivity distributions corresponding to each monitoring step during remediation, (d) actual resistivity ratio images between sequential monitoring steps.

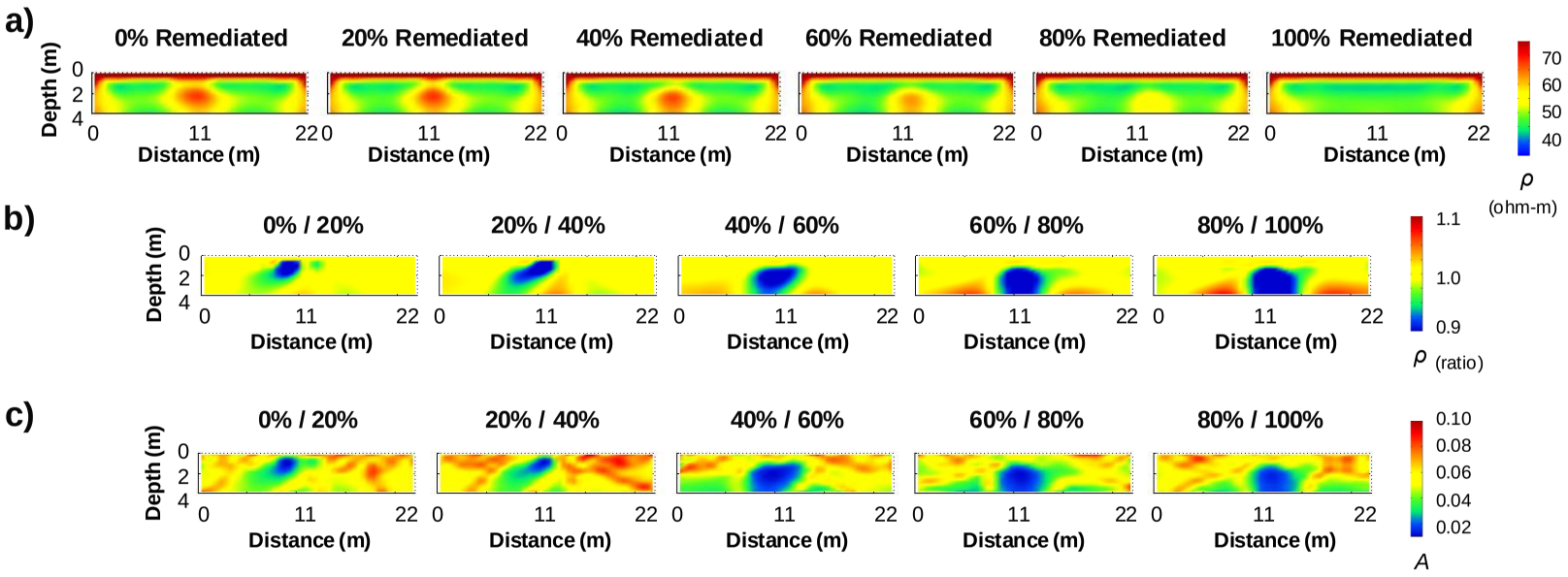

Figure B-11: (a) independently inverted resistivity distributions at each monitoring step during remediation of the simulated tetrachloroethylene (PCE_lay) spill scenario, (b) independently inverted ratio images between sequential monitoring steps, (c) temporal Lagrangian distribution between sequential monitoring steps.

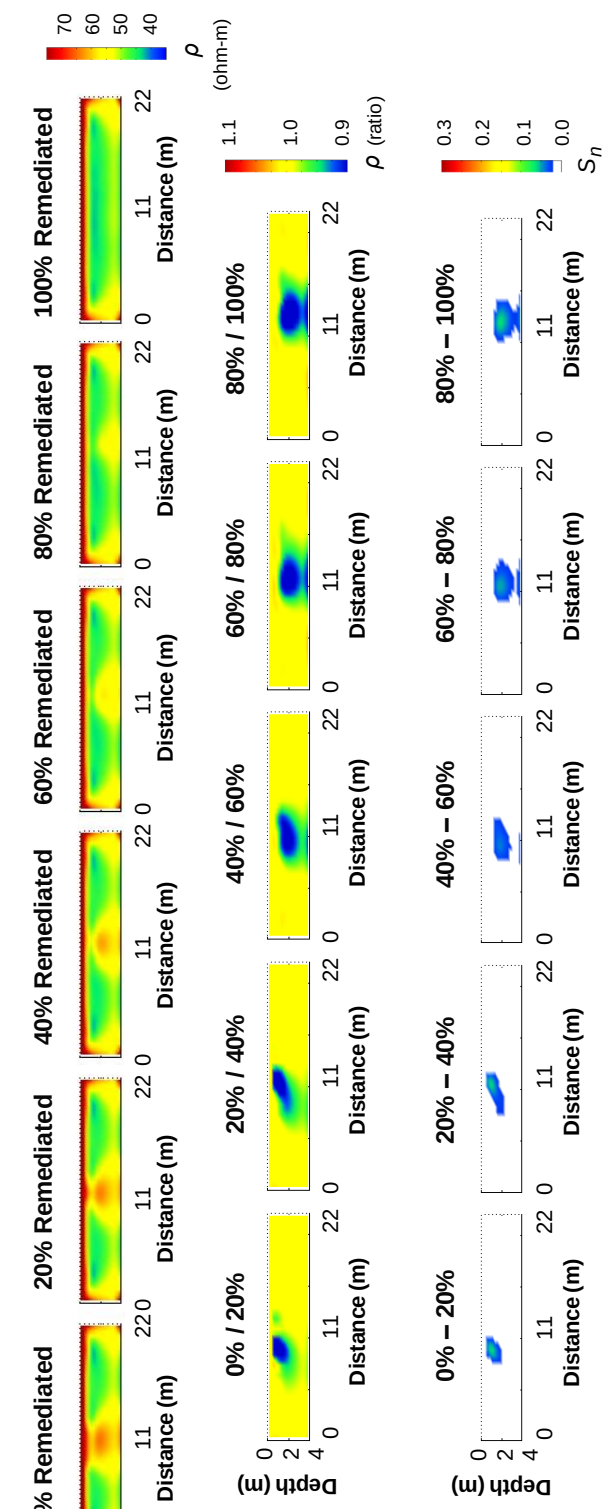

Figure B-12: (a) 4D-ATC inverted resistivity distributions at each monitoring step during remediation of the simulated tetrachloroethylene (PCE_lay) spill scenario, (b) 4D-ATC inverted ratio images between sequential monitoring steps, (c) ERT-measured DNAPL saturation changes between sequential monitoring steps.

APPENDIX C – SURFACE-TO-BOREHOLE ERT EXPERIMENT

This section provides supplementary material to the surface-to-horizontal borehole ERT experiment described in Chapter 5.

C.1 – Supplementary Photos

The following photos illustrate the preparation and data acquisition of the laboratory tank experiment described in Chapter 5:

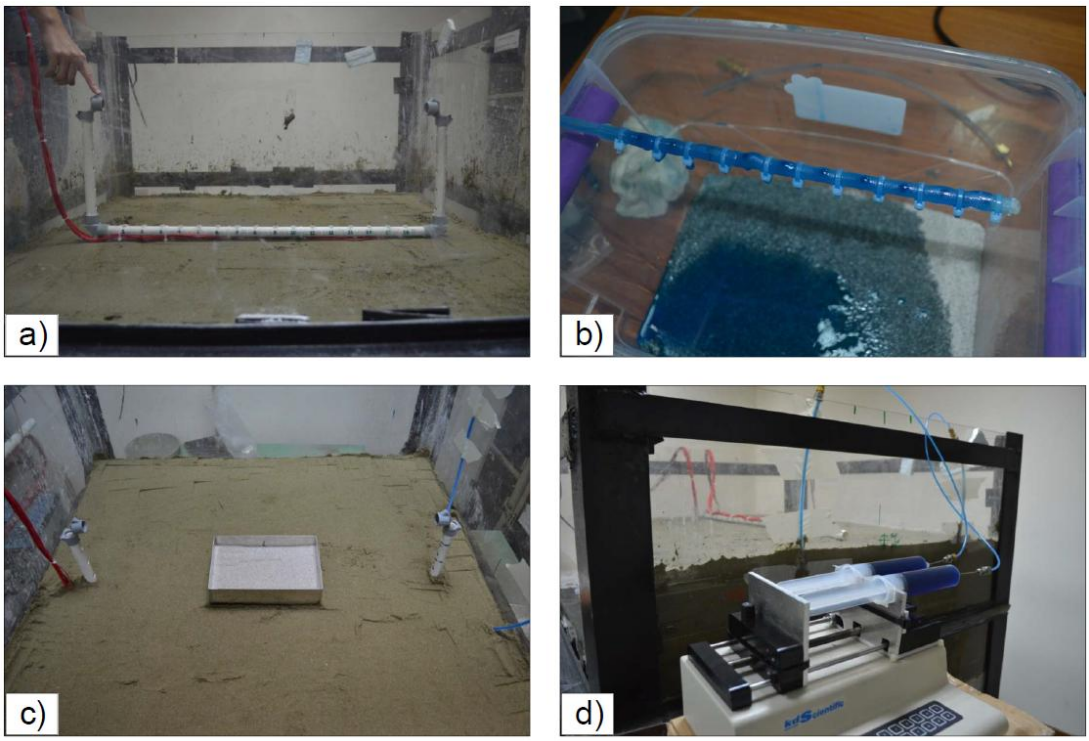

Figure C-1: (a) placement of the horizontal borehole electrode unit into the fine sand, (b) testing the horizontal well for NAPL injection, (c) construction of the middle step with the stainless steel divider, (d) syringe pump holding two 60 mL syringes to simultaneously inject NAPL into the parallel horizontal wells.

The following photos illustrate the excavation of the laboratory tank after the experiment was completed as described in Chapter 5:

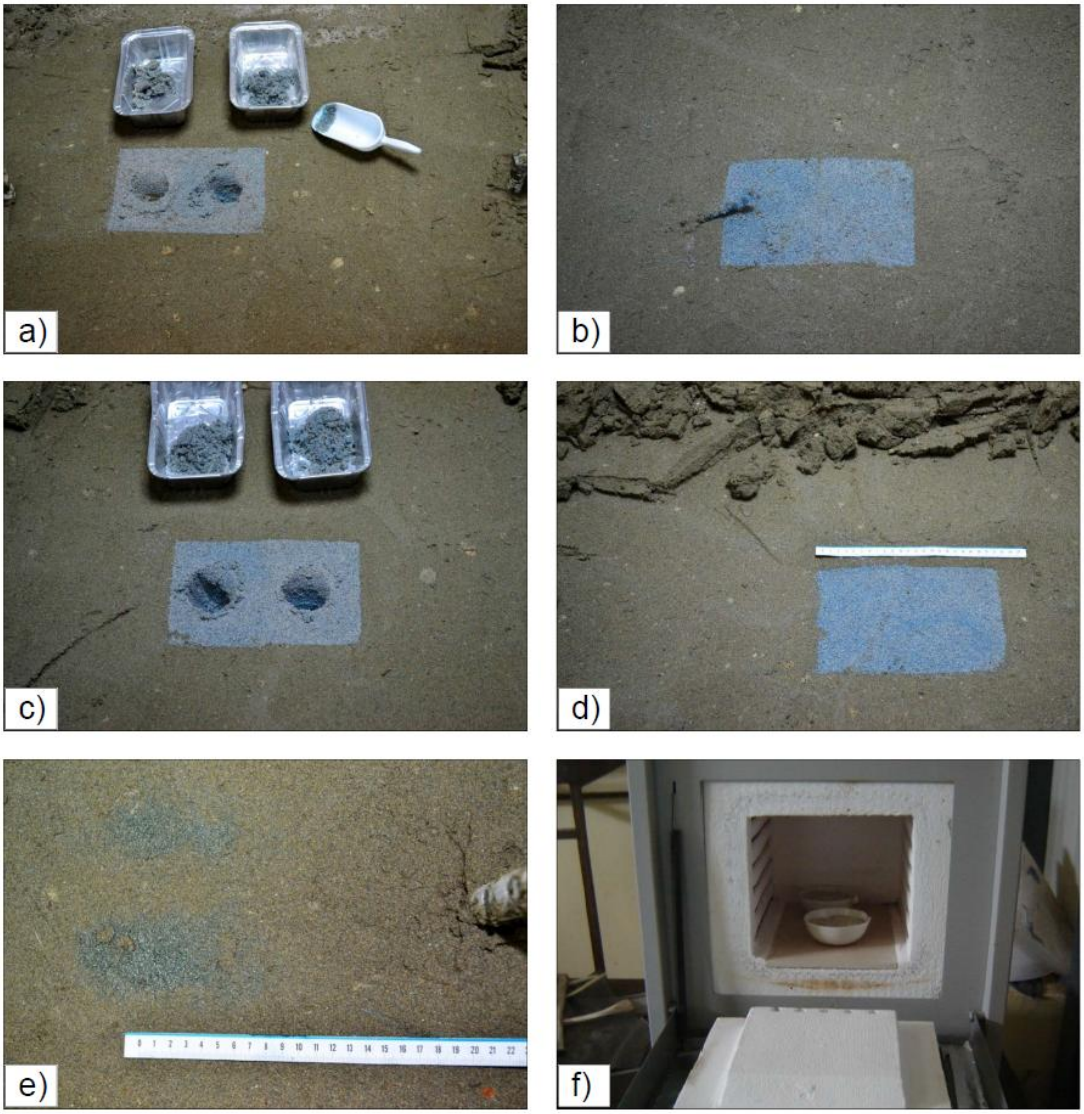

Figure C-2: (a) extracting soil samples at the 8 cm depth interval during excavation, (b) excavation around the point injection well at 10 cm depth, (c) extracting soil samples at the 12 cm depth interval, (d) visualization of the NAPL invasion at the 16 cm depth interval, (e) evidence of NAPL penetration into the fine sand beneath the base of the bottom step (22 cm depth interval), and (f) removal of NAPL from excavated soil samples in a high temperature muffle-furnace.

C.2 – Time-lapse Inversion Imaging

Throughout this thesis, only the 4D-ATC inversion time-lapse images have been presented. To illustrate the performance of the 4D-ATC inversion versus the traditional independent inversion, this section presents both the independent inversion and the 4D-ATC inversion results for monitoring the time-lapse changes in the NAPL experiment described in Chapter 5.

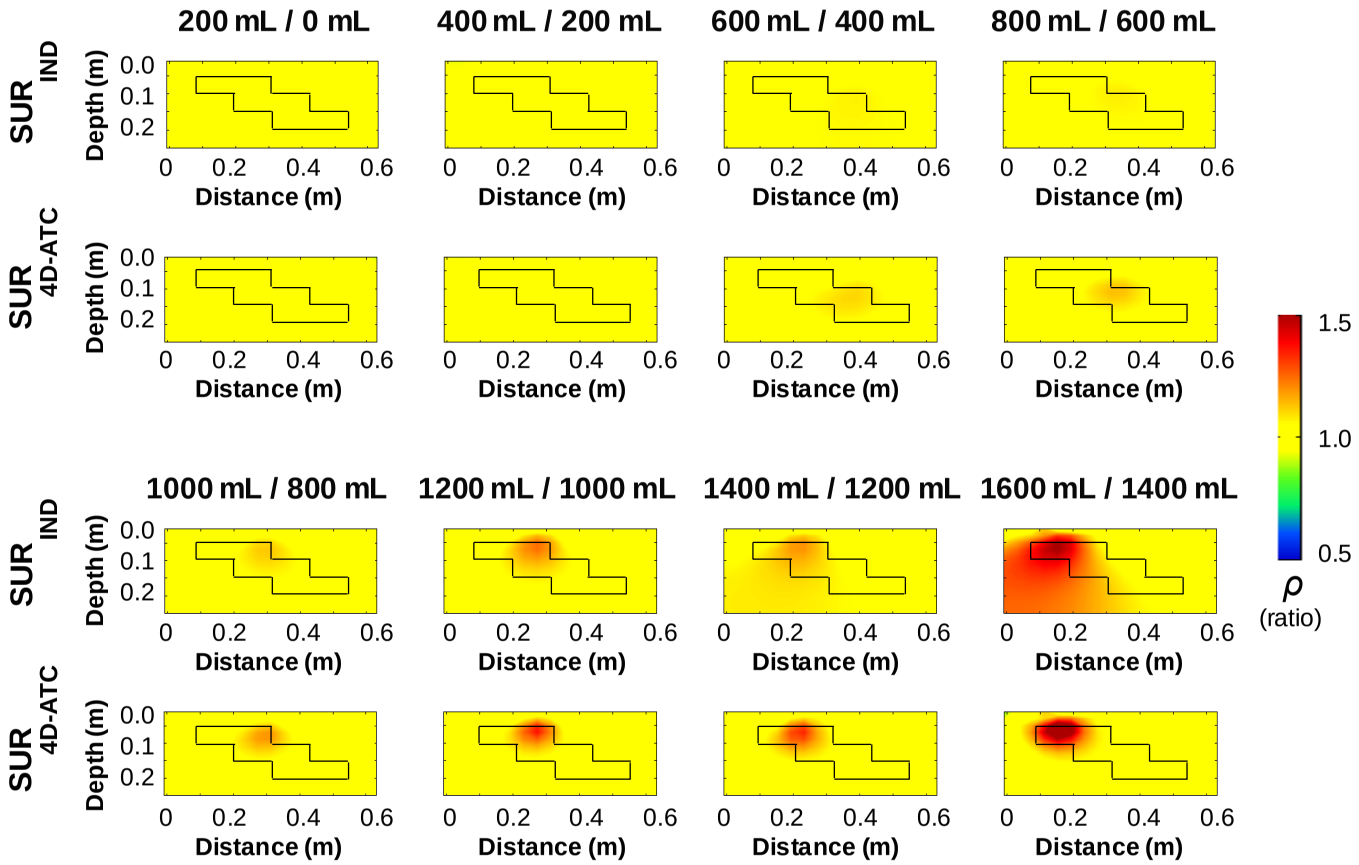

Figure C-3: sequential ratio inverted resistivity images from surface ERT array comparing traditional independent inversion (first and third rows) and 4D-ATC inversion (second and fourth rows).

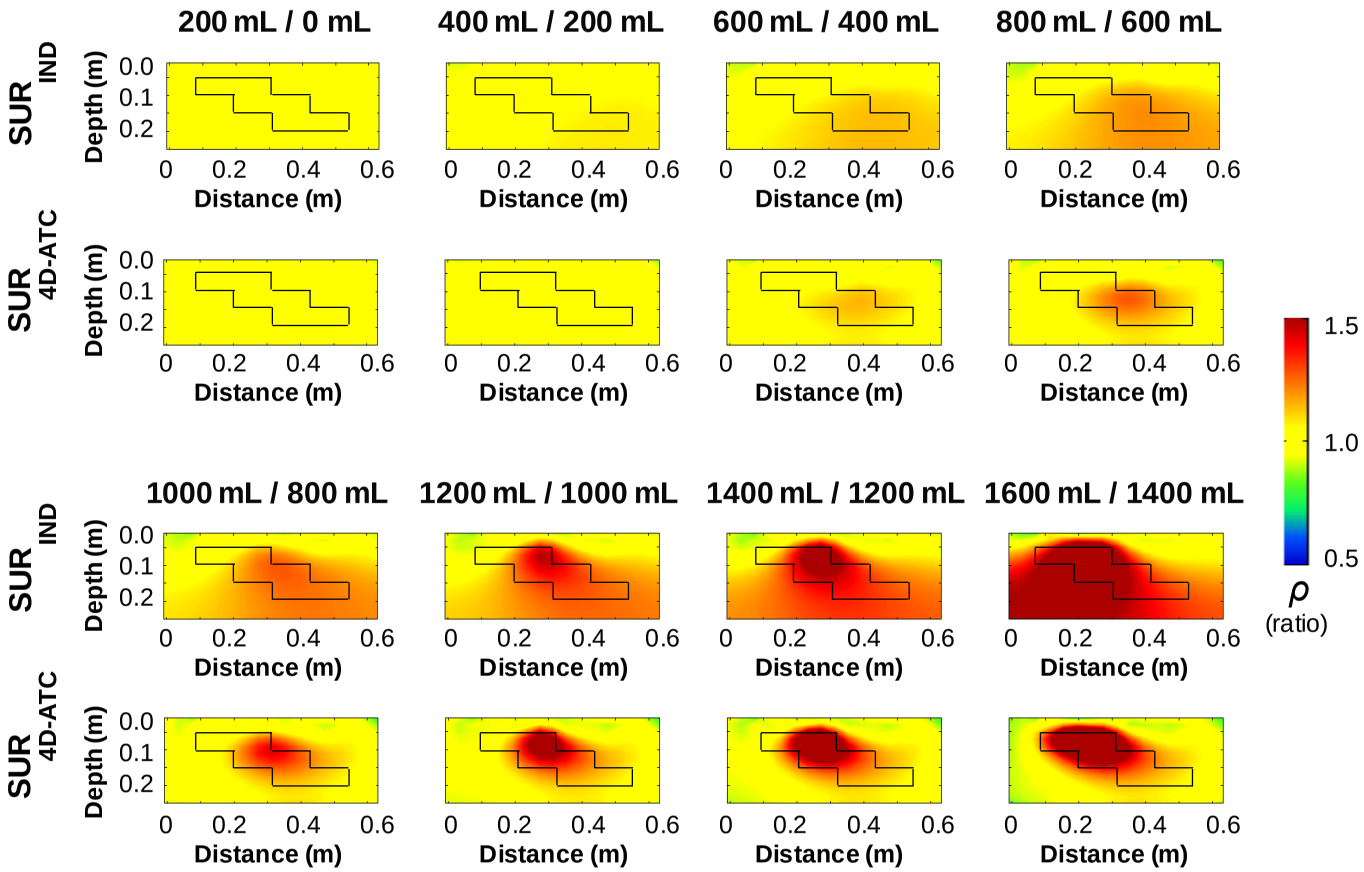

Figure C-4: cumulative ratio inverted resistivity images from surface ERT array comparing traditional independent inversion (first and third rows) and 4D-ATC inversion (second and fourth rows).

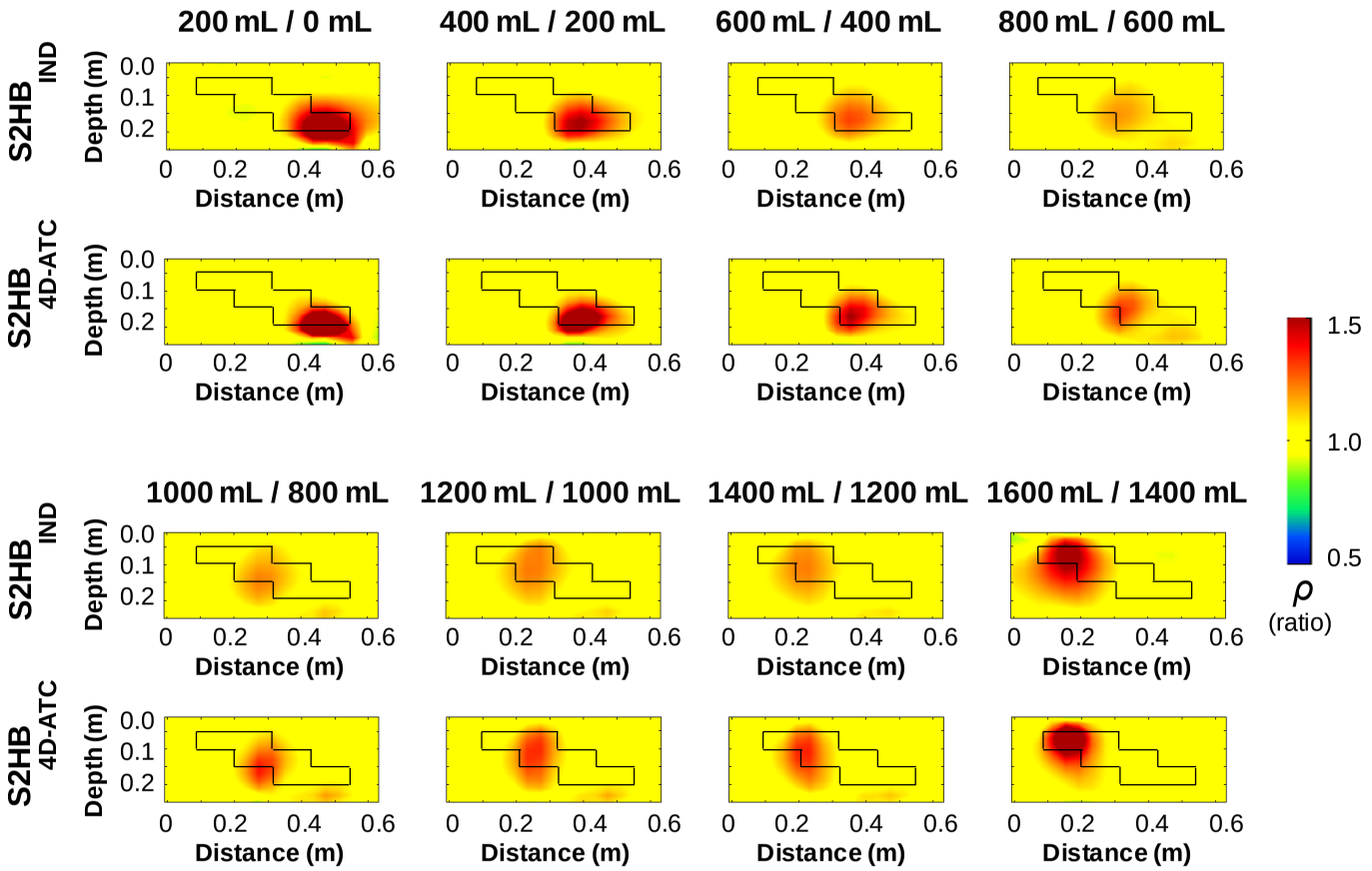

Figure C-5: sequential ratio inverted resistivity images from surface-to-horizontal borehole ERT array comparing traditional independent inversion (first and third rows) and 4D-ATC inversion (second and fourth rows).

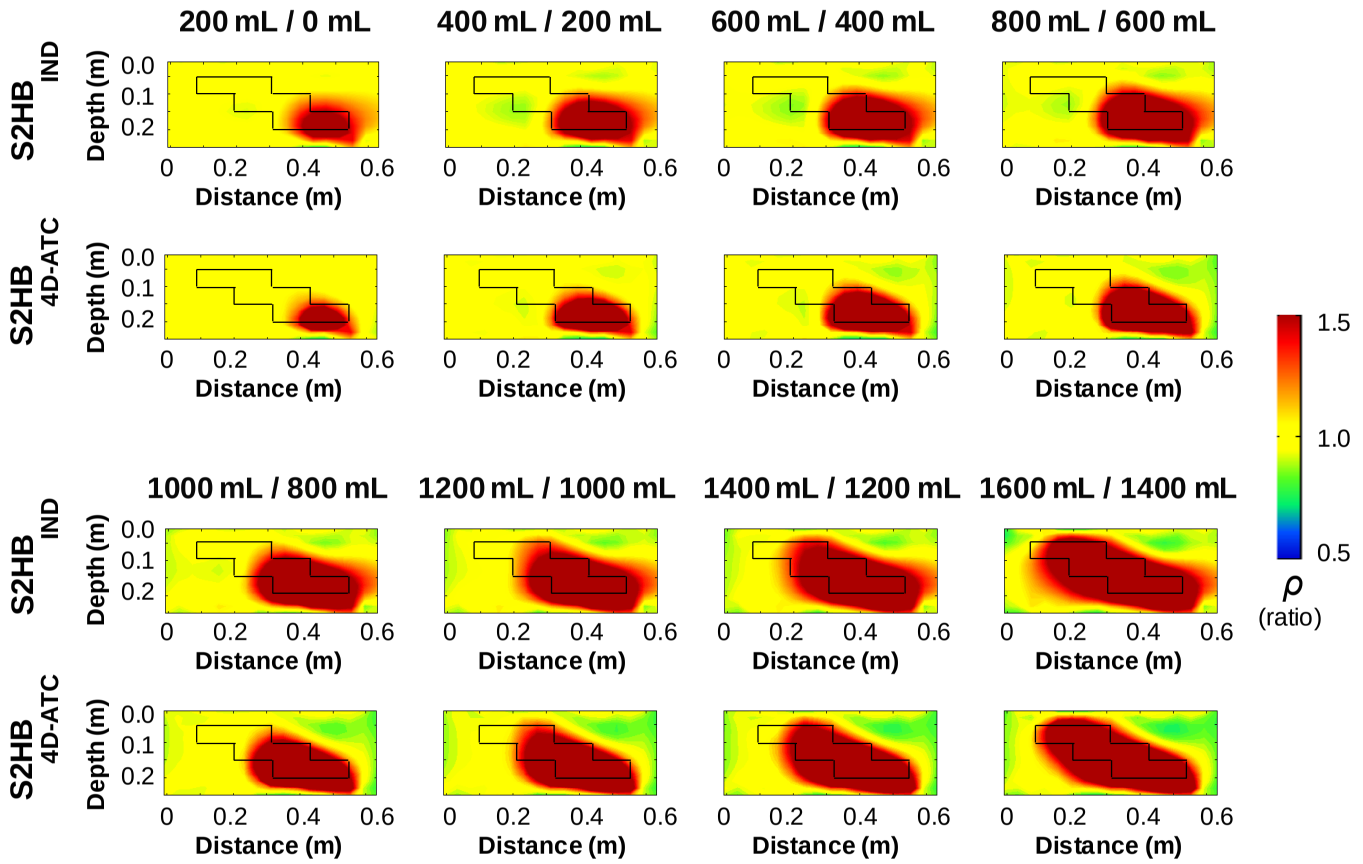

Figure C-6: cumulative ratio inverted resistivity images from surface-to-horizontal borehole ERT array comparing traditional independent inversion (first and third rows) and 4D-ATC inversion (second and fourth rows).

APPENDIX D – COPYRIGHT PERMISSION

Chapter 3 of this thesis has been published in Geophysics journal. The copyright agreement and permissions are indicated below:

SOCIETY OF EXPLORATION GEOPHYSICISTS
P.O. Box 702740, Tulsa, Oklahoma 74170-2740 USA
Physical Address: 8801 S. Yale Ave., Tulsa, OK 74137 USA

GEO-2012-0395
Manuscript Number
(GEOPHYSICS only)

Transfer of Copyright Agreement

Agreement must be signed by lead or corresponding author and returned to SEG Business Office before article is published.

Article title: A new coupled model for simulating the mapping of dense nonaqueous phase liquids using electrical resistivity tomography

Names of all authors: Christopher Power, Jason I. Gerhard, Panagiotis Tsourlos, and Antonis Giannopoulos

Journal: ☑ GEOPHYSICS ☐ THE LEADING EDGE **(check one)**

For and in consideration of the potential publication of the article listed above (the "Work") by the Society of Exploration Geophysicists ("SEG"), I, the undersigned, as lead and/or corresponding author and acting on behalf of all authors and/or owners of copyright in the Work, hereby transfer, assign, and convey all right, title, interest, and worldwide copyright in the Work to SEG, effective if and when the paper is accepted for publication, subject only to limitations expressed in this Transfer of Copyright (the "Agreement"). The Agreement includes all material to be published as part of the article, in any medium, including but not limited to tables, figures, graphs, source code, movies, and other multimedia. Responses to discussions of the Work, errata, and other similar material directly related to the Work which may arise subsequent to publication also are considered part of the Work. In the event the Work incorporates copyrighted material of others, all required permissions or releases have been secured.

Authors shall retain the following royalty-free rights: (1) the right to reproduce the Work, including figures, drawings, tables, and abstracts of the Work, with proper copyright acknowledgment, for any purpose; (2) the nonexclusive right, after publication by SEG, to authorize third parties to republish the Work or translations or portions thereof, provided the SEG-formatted version is not used (SEG permission is required if the SEG-formatted version is used); (3) all proprietary rights in the Work that are not transferred to SEG in the Agreement, including the right to any patentable subject matter that may be contained in the Work; (4) the right to make oral presentation of the same or similar information as that contained in the Work provided acknowledgment is made of SEG copyright ownership and publication status; (5) the right to post the article or portions thereof on authors' own Web pages or, in the case of a Work Made for Hire, to post the article on the employer's Web site, in either case with acknowledgment of SEG copyright. If the posting is a modification of what SEG has published, an accompanying notification stating this is required.

SEG may republish the Work or portions thereof in any future SEG publication or complilation in any form and in any language, and SEG retains nonexclusive right to license third parties to do the same.

This Agreement entitles the undersigned (or in the case of a Work Made for Hire, the employer) to retain all other rights. I confirm that this article has not been published previously elsewhere, nor is it under consideration by any other publisher, that the Work does not infringe any copyright or invade any right of privacy or publicity, and that I have the full power to enter into this Agreement and to make the grants contained herein. This Agreement shall be binding on my heirs, executors, administrators, and assigns, and shall be construed in accordance with the laws of the State of Oklahoma.

IN WITNESS WHEREOF, I have executed this Transfer of Copyright on this ____ day of _____,20____

Christopher Power
Name of author (print or type)

Signature

Company for which work was performed (if applicable)

Authorized by:_____

Title:_____

SIGN HERE IF U.S. GOVERNMENT EMPLOYED ALL AUTHORS WHEN WORK WAS PREPARED.

I certify that the article named above was prepared solely by a U.S. government employee(s) as part of his/her (their) official duties and therefore legally cannot be copyrighted.

Name (print or type)

Signature Date

CURRICULUM VITAE

Name: Christopher Power

Post-secondary Education and Degrees:

Waterford Institute of Technology, Waterford, Ireland
2001-2003 National Certificate

Waterford Institute of Technology, Waterford, Ireland
2003-2004 National Diploma

The University of Edinburgh, Edinburgh, United Kingdom
2004-2007 M.Eng

The University of Western Ontario, London, Ontario, Canada
2008-2014 Ph.D

Honours and Awards: William Dudgeon Scholarship (2006), M E B Lindsay Prize (2007), Edmund Nuttal Prize (2007), Geosyntec Consultants Student Research Competition Winner (2008), John Booker Award (2009), NSERC Industrial Postgraduate Scholarship (2011), R.M. Quigley Award (2012)

Related Work Experience:

2011-2013 Hydrogeophysical Student Researcher
Geosyntec Consultants, Guelph, Ontario, Canada

2008-2013 Teaching Assistant
The University of Western Ontario, London, Ontario, Canada

2008-2014 Research Assistant
The University of Western Ontario, London, Ontario, Canada

Publications:

Wilson, V.C, C. Power, A. Giannopoulos, J.I. Gerhard, G.P. Grant. 2009. DNAPL mapping by ground penetrating radar examined via numerical simulation. Journal of Applied Geophysics, 69(3-4): 140-149.

Power, C., J.I. Gerhard, P. Tsourlos, A. Giannopoulos. 2013. A new coupled model for simulating the mapping of dense non-aqueous phase liquids using electrical resistivity tomography. Geophysics, 78(4): EN1-EN15.

Power, C., J.I. Gerhard, M. Karaoulis, P. Tsourlos, A. Giannopoulos. 2014. Evaluating four-dimensional time-lapse electrical resistivity tomography for monitoring DNAPL source zone remediation. Journal of Contaminant Hydrology, 162-163: 27-46.